Characterisation of the subglacial environment using geophysical constrained Bayesian inversion techniques

Siobhan Killingbeck

Submitted in accordance with the requirements for the degree of
Doctor of Philosophy

The University of Leeds
School of Earth and Environment

March 2020

The candidate confirms that the work submitted is his/her own, except where work which has formed part of jointly-authored publications has been included. The contribution of the candidate and the other authors to this work has been explicitly indicated below. The candidate confirms that appropriate credit has been given within the thesis where reference has been made to the work of others.

The work presented in Chapter three of this thesis has appeared in the following publication:

Killingbeck, S. F., Livermore, P. W., Booth, A. D., and West, L. J. (2018). Multimodal layered transdimensional inversion of seismic dispersion curves with depth constraints. *Geochemistry, Geophysics, Geosystems*, 19, 4957– 4971. doi.org/10.1029/2018GC008000

SK was responsible for the acquisition, processing and interpretation of the dataset, preparation of all the figure and manuscript. SK and PL developed MuLTI. PL contributed to writing the methodology section. All authors commented on early drafts of the manuscript.

The work presented in Chapter four of this thesis has appeared in the following publication:

Killingbeck, S., Booth, A., Livermore, P., West, L., Reinardy, B., and Nesje, A. (2019). Subglacial sediment distribution from constrained seismic inversion, using MuLTI software: Examples from Midtdalsbreen, Norway. *Annals of Glaciology*, 60(79), 206-219. doi:10.1017/aog.2019.13

SK was responsible for the acquisition, processing and interpretation of the datasets, preparation of all the figure and manuscript. SK and AB acquired the data. All authors commented on early drafts of the manuscript.

The work presented in Chapter five of this thesis has appeared in the following publication:

Killingbeck, S. F., Booth, A. D., Livermore, P. W., Bates, C. R., and West, L. J.: Characterisation of subglacial water using a constrained transdimensional Bayesian Time Domain Electromagnetic Inversion, *Solid Earth Discuss*., doi.org/10.5194/se-2019-126, accepted, 2019.

SK was responsible for the acquisition, processing and interpretation of the dataset, preparation of all the figure and manuscript. SK and AB acquired the data. SK and PL developed MuLTI TEM. RB provided advice and support while using the TEM equipment. All authors commented on early drafts of the manuscript.

Acknowledgements

This thesis was funded by the UK NERC SPHERES DTP, grant NE/L002574/1 and supervised by Dr Adam Booth, Dr Phil Livermore and Dr Jared West. They are thanked for their fantastic support, guidance, time and energy spent during this project, and always provided expert advice and feedback when asked.

In the 2017 field campaign, GPR equipment was generously provided by Jostein Bakke (University of Bergen). Fieldwork was part-funded by the EVOGLAC project (University of Bergen, University of Oslo), and greatly assisted by the support and local expertise of Atle Nesje and Kjell Magne Tangen. In the 2018 field campaign, fieldwork was part-funded by the research project 'Snow Accumulation Patterns on Hardangerjøkulen Ice Cap (SNAP)', itself funded by the European Union's Horizon 2020 project INTERACT, under grant agreement No 730938. Fieldwork was greatly assisted by Emma Pearce and James Killingbeck, and again the support and local expertise of Atle Nesje and Kjell Magne Tangen. The time domain electromagnetic equipment was supplied by NERC Geophysical Equipment Facility, loan 1090. Alan Hobbs and all NERC GEF staff are thanked for their support and advice throughout the loan.

Richard Bates is thanked for his support and advice in preparation for the TEM acquisition, during TEM deployment in the field, and analysis of the TEM results and interpretations.

Richard Rigby is thanked for creating the gpdc and Leroi mex files enabling MuLTI and MuLTI-TEM to be run in Matlab (on Windows and Linux) and all his extra computing and IT support.

Benedict Reinardy is thanked for his advice on the geomorphology of the field site, Midtdalsbreen, and surrounding area.

Roger Clark is thanked for being my transfer chair, including his guidance and suggestions for progression of this work during the project.

David Harbottle, Worldwide University Network, is thanked for funding a visit to Professor Doug Schmitt's petrophysics labs in Edmonton, Alberta.

This thesis benefited from discussions at the 2017 Glacial Seismology Summer School held at Colorado State University, sponsored by POLENET, SCAR, IGS and IACS.

IAG is thanked for part-funding a glaciology training course in Svalbard in 2017.

Abstract

An accurate characterization of the inaccessible subglacial environment is key to accurately modelling the dynamic behaviour of ice sheets and glaciers, crucial for predicting sea-level rise. The composition and water content of subglacial material can be inferred from measurements of shear wave velocity (*Vs*) and bulk electrical resistivity (*R*), themselves derived from Rayleigh wave dispersion curves and transient electromagnetic (TEM) soundings.

Conventional Rayleigh wave and TEM inversions can suffer from poor resolution and non-uniqueness. In this thesis, I present a novel constrained inversion methodology which applies a Markov chain Monte Carlo implementation of Bayesian inversion to produce probability distributions of geophysical parameters. MuLTI (Multimodal Layered Transdimensional Inversion) is used to derive *Vs* from Rayleigh wave dispersion curves, and its TEM variant, MuLTI-TEM, for evaluating bulk electrical resistivity. The methodologies can include independent depth constraints, drawn from external data sources (e.g., boreholes or other geophysical data), which significantly improves the resolution compared to conventional unconstrained inversions. Compared to such inversions, synthetic studies suggested that MuLTI reduces the error between the true and best-fit models by a factor of 10, and reduces the vertically averaged spread of the *Vs* distribution twofold, based on the 95% credible intervals.

MuLTI and MuLTI-TEM were applied to derive *Vs* and *R* profiles from seismic and TEM electromagnetic data acquired on the terminus of the Norwegian glacier Midtdalsbreen. Three subglacial material classifications were determined: sediment ($Vs < 1600$ m/s, $50\ \Omega m < R < 500\ \Omega m$), permafrost ($Vs > 1600$ m/s, $R > 500\ \Omega m$) and weathered/fractured bedrock containing saline water ($Vs > 1900$ m/s, $R < 50\ \Omega m$). These algorithms offer a step-change in our ability to resolve and quantify the uncertainties in subsurface inversions, and show promise for constraining the properties of subglacial aquifers beneath Antarctic ice masses. MuLTI and MuLTI-TEM have both been made publicly available via GitHub to motivate users, in the cryosphere and other environmental settings, for continued advancement.

Table of Contents

List of Tables

List of Figures

Figure 4.6 1D block models created to simulate snow and ice thicknesses expected at Lines A, B and C (a-d). Blue, red and brown lines represent base snow, ice and soft substrate boundaries; DWM synthetic wavefield shot gathers (e-h); corresponding dispersion curves picked with an estimate of associated uncertainty derived from the width of the dispersion image (i-l).

Figure 4.7 Posterior Vs distributions determined from MuLTI inversion (a-d) without depth constraints and (e-h) with depth constraints; the models correspond to those shown in figure 6 a-d. Colour scale represents the probability density distribution of Vs values within the 95% credible interval, red highlighting most likely. Black line shows the true synthetic Vs profiles. Blue, red and brown correlation lines highlight the snow, ice and soft substrate depths respectively.

Figure 4.8 Mid-line C, B and A CMPCC gathers (a-c), corresponding dispersion images (d-f) and Vs distribution profiles (g-i), with the average of the distribution plotted in black.

Figure 4.9 2D inversion outputs for Lines A-D. Left column: approximate 2D depth resolution, characterised by the range of phase velocity picks. Central column: most likely 2D Vs profiles output from multiple 1D MuLTI inversions. Diverging colour scale centred, in white, on Vs of ice (1750-1900 m/s). Right column: estimated uncertainty (half the interquartile range of the posterior distribution). Snow and ice depth horizons are plotted in blue and red respectively.

Figure 4.10 a) 3D cross-section of lines A-D, showing the Vs mode solution and interpreted locations of sediment and bedrock. The black semi-transparent overlay shows where L_{max} is exceeded, hence where results could be unreliable. b) Schematic 3D cross-section interpretation of Lines A-D. c) Base map annotated with line locations and the interpretations from (a).

Figure 5.1 a) Location of Hardangerjølken ice cap in Norway and Google Earth image of Midtdalsbreen, survey area, with nearest sources of TEM noise (town and railway line) highlighted. b) Survey lines acquired during 2018 field season with the seismic Vs results obtained at the top rock horizon displayed. The orange border around (b) identifies the same area as the orange box in (a), note (b) is rotated away from North to enable optimal data comparison in later figures.

Figure 5.2 Survey configuration testing at the intersection of B and D. a) 37m x 37m transmitter coil with receiver in the centre. b) 10m x 10m transmitter coil with receiver 15m offset. c) 5m x 5m transmitter coil with receiver 12.5m offset. d) Raw data acquired at the intersection of B and D (237.5Hz), from each survey configuration, plotted with background noise recorded with transmitter turned off.

Figure 5.3 a) Survey configuration used for acquiring lines A, B, C and D on the glacier. b) Image of the receiver unit on top of a rug to protect unit from snow and easily drag along the lines. c) Image of transmitter unit sitting in bubble-wrap pocket used to protect unit and batteries from snow and cold.

Figure 6.3 Results of synthetic models a - e inverted using MuLTI with fixed depth constraints at base-ice, 2 km. i) *Vs* posterior probability distributions with the true model plotted in the black dashed line and mode solution plotted in the black solid line. ii) Comparison of the observed data with the forward model of the best fitting ensemble model. iii) Posterior distribution of number of nuclei.

Figure 6.4 Results of synthetic models a - e inverted using MuLTI-TEM with fixed depth constraints at base-ice, 2 km. i) resistivity posterior probability distributions with the true model plotted in the black dashed line and mode solution plotted in the black solid line. ii) comparison of the observed data with the forward model of the best fitting ensemble model. iii) posterior distribution of number of nuclei.

Figure 7.1 Left column: Facies classifications for lines A-D at Midtdalsbreen (Chapter 5), colour bar on the left. Right column: joint probability of *Vs* and *R* calculated from the product of the normalised PDF values (Equation 7.1), assuming *Vs* and *R* are independent. Note this is calculated for the subglacial material only with colour bar on the right.

Figure 7.2 2D model parameters input to the petrophysical four phase model for lines A-D. Left column: estimated *Vp* profiles derived from the smoothed modal *Vs* profiles (Chapter 4) and estimated ν (Table 6.1) using equation 7.12. Centre column: modal resistivity profiles, detailed in Chapter 4. Right column: estimated porosity model using the facies classifications shown in Figure 4.9, Chapter 4, for subglacial material only. Blue and red lines are the base snow and ice horizons, respectively.

Figure 7.3 Petrophysical four-phase model outputs for lines A-D at Midtdalsbreen. Left column: fraction of water content. Centre column: fraction of ice content. Right column: fraction of air content. The arrows in the right column point to anomalously high air content at depth, arising from anomalously low *Vp* values derived from observed low *Vs*, using equation 7.12. Note only the subglacial material is included in this analysis, the white snow and ice layers are not representative of the colour bars shown.

Figure 7.4 Illustration of MuLTI III model parameterization using Voronoi nuclei (floating and confined) and prior distributions, reformed from the original MuLTI parameterization shown in figure 2.1. a) Prior distribution of *Vs* without depth constraints; b) prior distribution of *Vs* with depth constraints; c) prior distribution of both *Vp* and density.

Figure 7.5 Illustration of six possible perturbations to a current model in MuLTI III, adapted from the original MuLTI perturbations shown in figure 2.2. a) change *Vs* of a nucleus, b) change *Vp* of a nucleus, c) change density of a nucleus, d) move a nucleus to a different depth, e) give birth to a new floating nucleus, and f) remove a floating nucleus.

List of abbreviations

AMIRA - Australian Mineral Industries Research Association

AVO – Amplitude Verses Offset

CMPCC – Common Midpoint Cross-Correlation

CMP - Common Midpoint

CSIRO - Commonwealth Scientific and Industrial Research Organisation

DWM – Discrete Wavenumber Method

GPR – Ground Penetrating Radar

MASW – Multichannel Analysis of Surface Waves

MCMC – Markov Chain Monte Carlo

MuLTI – Multimodal Layered Transdimensional Inversion

MuLTI-TEM - Multimodal Layered Transdimensional Inversion of Transient Electromagnetics

PDF – Probability Density Function

R – Resistivity

TEM - Transient Electromagnetics

TWT – Two Way Travel-time

Vp – P wave velocity

Vs – Shear wave velocity

Chapter 1 Introduction

The cryosphere is changing rapidly under the impact of climatic warming. Glaciers store 70 percent of the world's fresh water supply and are rapidly retreating in many areas (Vaughan et al., 2013), exposing a once concealed subglacial environment. Glacier melting has been one of the dominant contributors to 20th century global mean sea level rise (Church et al. 2013). Mounting evidence from satellite records and global temperature trends suggest the contribution of glaciers and ice-sheets to global sea level will increase in the coming decades (e.g., Meier et al., 2007; Bamber and Riva 2010; Kopp et al., 2014, 2017; Larour et al., 2017).

Prediction of sea level rise relies on large scale ice sheet models having the best possible parameterisation of the ice sheets and their subglacial environment (Christoffersen et al., 2014). Characterising the subglacial environment and its hydrology is important for these models as it dictates the speed at which ice sheets slide over their beds (Bell 2008; Siegert et al., 2018). Through a complex system of interactions, water at the ice/bed interface can significantly modify glacier flow; it can act either as a lubricant to accelerate ice motion (e.g., Iken and Bindschadler, 1986; Mair et al., 2002; Bartholomaus et al., 2008; Bartholomew et al., 2010; Hoffman et al., 2011), or can lead to reductions in flow velocity by carving efficient drainage networks (e.g., Sundal et al., 2011). Glacio-geophysical methods are therefore needed for monitoring, imaging and mapping the remote and inaccessible subglacial environment and its drainage system.

Geophysicists have developed a wide range of methods for investigating the physical properties of the broad glacier system. Many geophysical methods are well-suited to assessing the englacial and basal properties of glaciers and ice masses (e.g., seismic reflection, refraction and ground penetrating radar methods), but these can be problematic for characterising material much beyond the immediate vicinity (~2 m) of the glacier bed (Booth et al., 2012). Although much of the control on ice dynamics may be effectively located at such depths, sediment bodies such as subglacial aquifers and permafrost may extend to much greater depths (e.g., Mikucki et al., 2015; Hauck et al., 2001). The influence of such features on glacier dynamics may become increasingly important as they are modified and progressively exposed through deglaciation (Siegert et al., 2018; Haeberli et al., 2017; Cooper et al., 2017).

A further problem in the analysis of geophysical data, in glaciology and pervasively throughout geophysical surveying, is non-uniqueness in interpretations and a lack of

constraints on layer boundary depths and parameters. The problem is exacerbated in the glaciological environment where ground-truth datasets are so seldom available. While interpretations may often draw on the potential of several co-located geophysical datasets, these are typically comparisons of the available data and do not blend them quantitatively. Joint inversions using multiple independent datasets can constrain the model space, combining and improving the depth sensitivity and resolution from each component. Additionally, the use of probabilistic Bayesian sampling-based inversion methods can provide a comprehensive quantitative uncertainty analysis.

Glaciological surveying has benefitted widely from the experience of processing in other geophysical fields, notably by importing seismic analysis methods from the hydrocarbon industry (Anandakrishnan et al., 1998; Horgan et al., 2008; Holland & Anandakrishnan, 2009). Seismic surface wave methods and electromagnetic methods have been used extensively in environmental/geotechnical investigations (Buselli et al., 1988; Stokoe et al., 2000; Auken et al., 2003; Penumadu and Park 2005; Pedersen et al., 2017) but have seen relatively little use within the glaciological field. In the geotechnical setting, they are used because of their sensitivity to water content and material type. Of particular relevance here is that shear wave velocities (*Vs*), estimated from surface wave methods, are sensitive to material stiffness; and electrical resistivity (*R*), estimated using electromagnetic methods, is sensitive to liquid water content. Such sensitivities suggest that these methods could be valuable for characterising hydrological regimes within the glaciological setting; indeed, they were identified by Siegert et al. (2018) as two promising 'next generation' geophysical methods for consideration. However, seismic and resistivity inversions are vulnerable to significant non-uniqueness issues hence could be improved using Bayesian analysis approaches.

In this thesis, I therefore focus on exploring novel geophysical methods for characterising the subglacial environment, and develop the strategies by which the data they yield are jointly inverted. Specifically, the thesis focuses on 1) multichannel analysis of surface waves (MASW) and 2) transient (time-domain) electromagnetic (TEM) methods. The analyses comprise of extensive synthetic data trials before analysing new geophysical data acquired on the Norwegian glacier Midtdalsbreen, an outlet of the Hardangerjøkulen ice cap. Finally, I present a combined analysis of the MASW and TEM results and suggest the development of a novel joint *R-Vs* constrained inversion strategy to quantify the water contents of subglacial environment.

1.1 The subglacial environment

The subglacial environment is one of our planet's last great frontiers, concealed by snow and ice for thousands of years. Menzies and Shilts (2002) define the subglacial environment as a boundary interface between ice and material: "the glacial sub-system directly underlying an ice mass in close contact with the overlying ice, including those cavities and channels beneath the ice that are not influenced by subaerial processes". The material composition and hydrology of the subglacial environment has substantial control on glacial erosional, transportational and depositional processes, affecting the flow dynamics of glaciers and ice masses (Bell 2008; Siegert et al., 2018). Subglacial erosion and deposition processes are among the most complex, yet least understood set of glacial processes. Our poor knowledge stems from the inaccessible nature of what occurs beneath an ice mass, making it difficult to explore. Measurements from direct access to the bed through ice-caves and drilling boreholes can prove accurate observations of the subglacial environment for that point in space, but data are difficult to extrapolate to larger areas and can be inefficient to acquire (and, in the case of ice-caving, potentially hazardous). In contrast, non-invasive, geophysical methods employed at or above the ice surface enable coverage of larger areas in a comparably short amount of time (Figure 1.1).

Glaciers move by either: ice deformation, basal sliding or deformation of subglacial sediments (Cuffey and Paterson, 2010). A significant control on ice motion is whether ice is underlain by hard (frozen/bedrock) or soft (unfrozen) substrate, and therefore whether motion is governed by ice/sediment deformation (Hofstede et al., 2018) or sliding (Stearns and van der Veen, 2018). Sliding and friction laws are used to predict dynamic ice motion, e.g., Weertman1957, Budd et al., 1979, Schoof 2005, Gagliardini et al., 2007, Iverson 2010, of which accurate parametrization and understanding of basal boundary conditions is needed, in particular the basal sliding velocity (*Ub*), the speed of a glacier sliding over its material base. This velocity is dependent on a number of factors, including:

- the type of drainage system (efficient or inefficient); e.g. Chandler et al., 2013
- the basal roughness (smooth or large cavities); e.g. Rippin et al., 2011
- the type and thickness of material (bedrock or deformable sediments); e.g. Murray 1997
- the presence of water acting as a lubricant (causing stick - slip); e.g. Winberry et al., 2011

An important influence on *Ub* is the presence of liquid water at the glacier bed. Changes in water inputs can cause changes in basal slip (by altering the basal drag/resistance), throughout all ice-mass scales - from mountain glaciers (e.g., Iken and Bindschadler, 1986; Mair et al., 2002; Bartholomaus et al., 2008) to ice sheets (e.g., Bartholomew et al., 2010; Hoffman et al., 2011). Water can be produced *in situ* at the glacier bed through pressure melting, or can be routed as meltwater from the glacier surface through moulins, crevasses, and fractures. Water at the ice/bed interface can be dynamic and flowing through subglacial drainage channels, or static and stored in the pores of sediments within subglacial aquifers. Either way, observations of water content, sediment type and thickness are required to accurately predict basal sliding velocities and hence future flow dynamics of glaciers and ice masses.

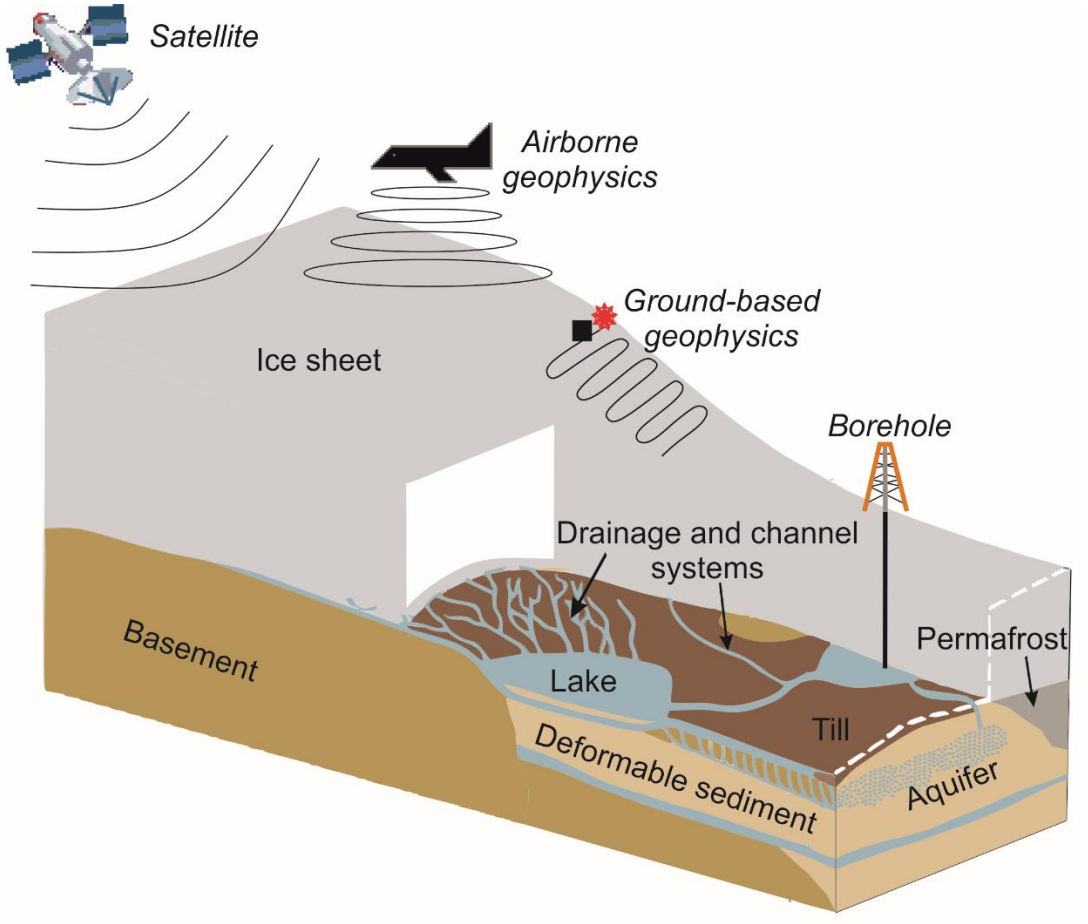

Figure 1.1 Schematic diagram of the subglacial environment including geophysical methods used to characterise and monitor it. (Schematic adapted from the WISSARD project, online at: http://www.wissard.org/science-and-operations).

1.2 Geophysical techniques used to characterise the subglacial environment

Ground-based, airborne and space-borne geophysical methods are deployed to observe targets below ice that may be difficult or impossible to measure using direct observations, providing a spatial distribution of geophysical properties of the target (Figure 1.1). Air- and space-borne methods can have particular benefit for remote and inaccessible areas. Satellite remote sensing allows for regular, regional, monitoring and mapping of glacier structures (e.g., Glasser and Scambos, 2008), glacier thinning (e.g., Holt et al., 2013), glacier velocity (e.g., Rignot et al., 2011), and many other applications. More densely sampled airborne methods have been applied, for example, to measure higher resolution ice-sheet bed topography (e.g., Blankenship et al., 2001), identify remotely located subglacial lakes (e.g., Rutishauser et al., 2018) and map the extent of permafrost and deep groundwater in polar regions (e.g., Minsley et al., 2012 and Mikucki et al., 2015). Having identified key areas of interest, ground-based techniques then provide targeted datasets at key locations. They provide a link between sparse-but-detailed glaciological observations and the spatial coverage of the satellite/airborne datasets. A general overview of some ground-based geophysical techniques used in glaciology today, along with the type of observations they provide, are presented in Table 1.1.

The most commonly used ground-based methods include ground penetrating radar (GPR), seismic reflection and seismic refraction (Figure 1.2 and see Table 1.1 for case studies); however, as stated in Section 1.1, the applicability of these can be limited given their poor penetration beyond the ice-bed interface. GPR methods are well suited to characterising englacial properties and basal topography, but glacier bed reflectivity and, in the case of temperate ice, high attenuation rates within the ice column limits the utility of subglacial radar sampling. Seismic reflection methods provide detailed englacial structure and basal topography; via amplitude-versus-offset (AVO) and anisotropy techniques, they also provide estimates of the mechanical properties of ice and glacial material (e.g., Anandakrishnan, 2003; Booth et al., 2012; Diez et al., 2015; Kulessa et al., 2017). However, they often lack the resolution and/or signal-to-noise ratio to quantify subglacial material properties. Seismic refraction methods are limited by their low depth penetration into subglacial material (e.g., Thiel and Ostenso, 1961; Bentley and Kohnen, 1976; King and Jarvis, 2007); refraction interpretations are impeded since an ice-sediment interface typically represents a velocity reduction, hence critical refraction will not occur and a head-wave will not be generated.

In this thesis, I explore the relatively novel glacio-geophysical methods of MASW and TEM (Figure 1.2), to evaluate their benefits for characterising the subglacial environment. MASW is based on the analysis of dispersion curves from surface (Rayleigh) waves. Rayleigh waves are a form of seismic wave that travels along the ground-surface (highlighted by the blue rolling surface waves in Figure 1.2), termed 'groundroll' in reflection seismology and often considered as noise. Rayleigh waves are important in engineering geophysics as their velocities are closely related to those of the shear wave in the same elastic media, and therefore can be used to estimate the shear wave velocity (*Vs*) of that media (e.g., Stokoe et al., 2000; Penumadu and Park 2005). This is of particular interest for investigating properties of the basal material as *Vs* is related to the shear modulus (μ) or stiffness of a material:

$$Vs = \sqrt{\mu/\rho} \tag{1.1}$$

where ρ is the density. Therefore, it is possible to estimate how hard or soft, rigid or deformable the subglacial material is. From the viewpoint of subglacial hydrology, this could inform the potential for the hydrological erosion of subglacial sediment (Sundal et al., 2015; Kulessa et al., 2017) or the degree to which sediments are frozen. Dispersion curves can be obtained from either passive or active seismic sources. In this thesis I report acquisition of dispersion curves from active seismic sources using the multichannel analysis of surface waves (MASW) method (Park et al., 1999), discussed further in Chapter 2 and 4.

Although *Vs* provides a good indication of the stiffness of a material, it does not inform the properties of pore water nor the degree of water saturation. Electrical methods are the only geophysical method that are directly influenced by the electrical properties of pore fluids (Archie, 1952). The state of pore water, whether liquid or frozen, can be inferred from electrical resistivity depth profiles. Electrical resistivity values increase by several orders of magnitude when water in pores freezes (Hoekstra and McNeill, 1973). Such profiles can be obtained from inversions of transient (time-domain) electromagnetic soundings (TEM). This uses electromagnetic fields to investigate subsurface resistivity structure by measuring the decay of a secondary electromagnetic field created by subsurface eddy currents, which are induced by a primary magnetic field, generated by current transmitted through a coil (highlighted in Figure 1.2). TEM methods are used extensively in environmental investigations for example, searching for groundwater (Auken et al., 2003) and mapping its vulnerability to saltwater and/or contaminant intrusions (Buselli et al., 1988; Pedersen et al., 2017). In this thesis I acquire ground-based TEM data to estimate the resistivity structure of the subglacial environment, discussed further in Chapters 2 and 5.

The MASW and TEM data acquired for this project are around the front of a glacier, where the ice is relatively thin, aiming to test the depth sensitivities of these techniques. However, in chapter 6 I present a feasibility study highlighting the potential for these techniques to be extended to thicker ice applications, by using dispersion curves from passive seismic and large loop TEM (Figure 1.2).

By characterising the seismic shear wave velocity and resistivity structure of the subsurface, I provide a promising means of distinguishing both material type and water content within the subglacial environment.

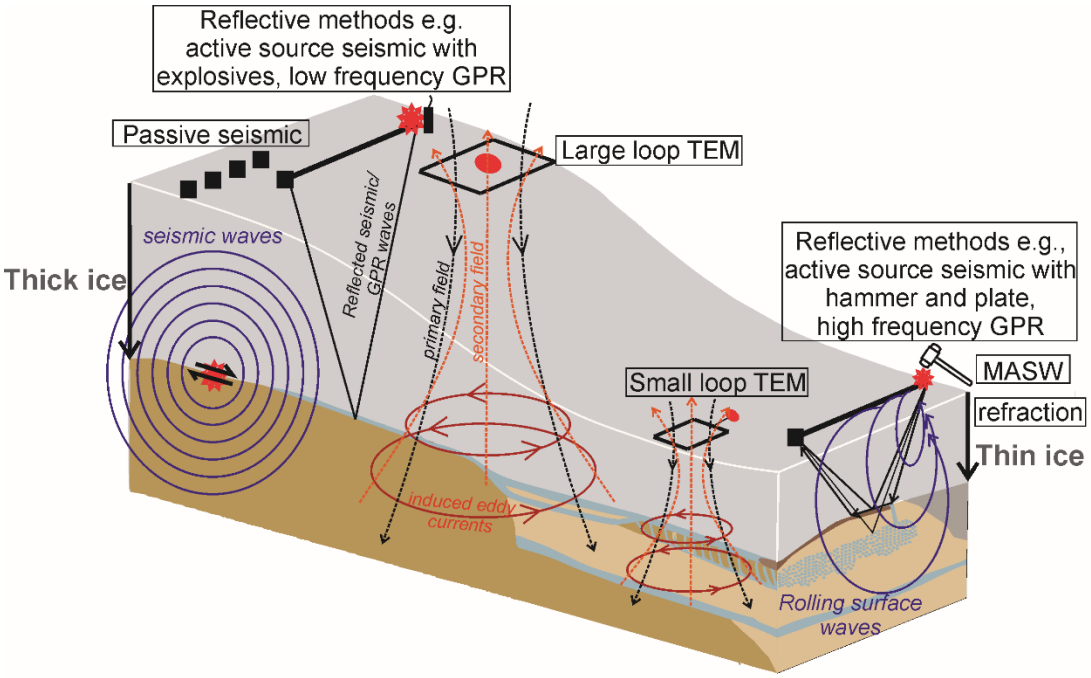

Figure 1.2 Schematic diagram of ground based geophysical methods acquired on glaciers, highlighting the different techniques used for different thicknesses of ice. The glacier and subglacial material figure is adapted from the WISSARD project, online at: http://www.wissard.org/science-and-operations.

Table 1.1 (continued overleaf) Comparison of ground-based geophysical methods used in cryosphere studies

Geophysical method	Geophysical parameter estimated	Depth penetration	Cryosphere observations from geophysical method
Ground penetrating radar (GPR)	Dielectric impedance	Depends on frequency of antenna used e.g., 200 MHz: 100-meter scale 2 MHz: km scale (through ice) The presence of water causes scattering of the waveform, making it very difficult to interpret signal below porous layers or temperate ice.	• Ice-thickness including bed topography (Young et al., 2010; Bingham et al., 2017; Lindbäck et al., 2018) • Englacial layering and properties (Murray et al., 2007; Bohleber et al., 2017) • Snow structure, density and water equivalent (Booth et al., 2013; St. Clair and Holbrook 2017)
Seismic reflection	Acoustic impedance and P and S wave velocities	Source dependant e.g., hammer and plate: m to km scale, Explosives: km scale, Vibroseis: m to km scale. Although, attenuation in the ice and off the ice-bed interface affects the depth of penetration.	• Ice-thickness including bed topography (Crary, 1963; Benjumea and Teixidó, 2001). • Investigate conditions and properties of the ice-bed interface (Smith 2007; Brisbourne et al., 2017) • Subglacial material investigation at the ice-bed interface (Vaughan et al., 2003; Booth et al., 2012; Kulessa et al., 2017); • Snow, firn and ice density profiles (Kohnen, 1972; Godio and Rege, 2015)
Seismic refraction	P wave velocity	Source dependant e.g., hammer and plate: ~ 10 m, Explosives: ~ 50 m Although, if there is a velocity reduction (e.g., ice-sediment or frozen-unfrozen interface) critical refraction will not occur.	• Shallow snow, firn and ice mechanical properties, including P wave velocity and density profiles (Bentley and Kohnen, 1976; Picotti et al 2015). • Determining frozen and unfrozen material in permafrost studies (Hauck et al., 2004; 2007 and 2008)

(continued overleaf)

Passive seismic	Rayleigh wave velocity and estimate of shear wave velocity	Low frequency source, provides km scale depths	• Cryoseismicity, using glacier-quakes to identify glacier movement and basal deformation (Winberry et al., 2011) • Glacier and ice-sheet thicknesses and estimate basal seismic properties (Diez et al., 2016; Picotti et al., 2017; Preiswerk and Walter, 2018) • Other applications discussed further in the detailed reviews Podolskiy and Walter, 2016 and Aster and Winberry, 2017.
Seismic surface waves from active seismic	Rayleigh wave velocity and estimate of shear wave velocity	Source dependant e.g., Hammer and plate: ~ 50 m, Explosives: ~ 250 m, Vibroseis: ~ 250 m.	• Firn and shallow ice velocity structure (Armstrong, 2009 and Tsoflias et al., 2008) • Anisotropy and crystalline fabric of ice sheets (Picotti et al., 2015), • Identifying unfrozen zones within subglacial material, (Tsuji et al., 2008) • Mapping low velocity zones/unfrozen zones in permafrost (Dou and Ajo-Franklin, 2014)
Time domain electromagnetics	Conductivity/ resistivity	Depends on transmitter system, loop size and current used e.g., Geonics TEM47: 5 to 150 m TEM57: 200 to 500 m, TEM67: 1000 m.	• Mapping permafrost on mountainous regions (Hauck et al., 2001) Airborne TEM: • Mapping Arctic permafrost (Minsley et al., 2012) • Mapping deep saline groundwater zones in Antarctica (Mikucki et al., 2015)

1.3 Integrating multiple geophysical observations using a Bayesian inversion framework

Inversions of isolated geophysical datasets are unconstrained and non-unique, with many models of the subsurface matching the observed dataset to some required numerical criterion. Integrating multiple geophysical observations into one inversion can constrain the model space, combining depth and resolution sensitivities from multiple datasets. This can be completed by a constrained inversion, complementing

the model space with prior information from another independent dataset (e.g., Auken and Christiansen, 2004; Socco et al., 2009), or furthermore, by a direct joint inversion approach, allowing objective testing of the independent datasets interrelationships. Some examples of joint inversions include the combination of geoelectric and seismic surface wave data (e.g., Hering et al., 1995; Gallardo and Meju, 2003; Wisén and Christiansen, 2005, Ronczka et al., 2018), to improve the definition of layered structure in near surface environments. Reflection seismic and controlled source electromagnetics have been combined to estimate fluid properties of petroleum reservoirs, which could not be obtained from one survey-type alone (Hou et al., 2006; Hoversten et al., 2006).

Isolated geophysical inversions can be vulnerable to inaccurate, insufficient or inconsistent data, causing ambiguities in the solution. They generally require a fixed number of layers and can be dependent on the starting model chosen, where inversions of the same dataset using slightly different starting parameters, can provide completely different solutions (Ellis et al., 1994; Foti et al., 2009). Furthermore, in many inversions, regularization is employed to penalize small-scale roughness to produce a single smooth solution (Auken and Christiansen, 2004). However, single solutions may not be sufficient given the non-uniqueness issues. Table 1.2 compares some of the different inversion methods used in geophysical problems. It directly compares the inversion method used (e.g. deterministic, stochastic, regularised), whether a global or local minimum is sought, the computational power needed, the form of output solution provided and an example case study, for each method detailed.

Bayesian Markov Chain Monte Carlo (MCMC) is a type of method that probabilistically quantifies the model space consistent with the observations. The application of the method results in a posterior probability distribution of the subsurface structure, numerically approximated by an ensemble of models, from which representative models such as the mean or mode can be obtained, in addition to rigorous estimates of uncertainties. Additionally, using a transdimensional Bayesian method allows each ensemble member to self-select both its model values and complexity based on the data, therefore never fixing the number of layers in the model. This inversion methodology has been exploited in deep-earth investigations, where surface wave dispersion and teleseismic P wave receiver functions both supply constraints on the crustal and upper mantle geology and efficient Bayesian algorithms for joint inversions have been developed (e.g., Bodin et al., 2012; Julià et al., 2000; Shen et al., 2012).

In this thesis I present a constrained Bayesian inversion technique, applying it to the inversion of Rayleigh wave dispersion curves and TEM datasets combined with

independent depth constraints. A pair of transdimensional Bayesian frameworks, termed "MuLTI" and "MuLTI-TEM" for MASW and TEM applications respectively, are used to probabilistically quantify the model space consistent with the observations, outputting individual *Vs* and *R* probability density functions (PDFs) allowing comprehensive uncertainty analysis. Here, I base the method on existing implementations of such a transdimensional method, which have successfully inverted both single and multiple data sets (Bodin et al., 2012; Bodin and Sambridge, 2009; Livermore et al., 2018). Further details of the methodology are presented in Chapter 3.

Using the probabilistic outputs of both *R* and *Vs*, from MuLTI and MuLTI-TEM, I consider two approaches: 1) probabilistic facies classification and 2) four- phase petrophysical modelling, for the development of a joint *R*-*Vs* constrained inversion strategy to quantify the water contents of the subglacial environment. The probabilistic facies classification follows the assumption that both methods are sensing the same underlying geology which, therefore, structurally controls the distribution of geophysical properties. This could lead to a more accurate understanding of the subsurface structure, utilizing the structural similarities between resistivity and seismic velocity (e.g., Gallardo and Meju, 2003; Wisén and Christiansen, 2005). Alternatively, petrophysical relationships could be derived to obtain and/or guide interpretations of the volumetric proportions of water, ice and air in the subsurface (e.g., Hauck et al., 2008). Further details of this discussion is presented in Chapter 7.

Table 1.2 Comparison of common geophysical inversion methodologies

Inversion method	Inversion type	Global/ local minimum	Computat-ional power	Solution output	Examples
Damped least squares (Levenberg, 1944; Marquardt,1963)	Deterministic with fixed model space. No regularisation applied	Local	low	Single best fit solution with RMS misfit	Inversion of surface wave dispersion curves (Xia et al., 1999)
Occams (Constable et al., 1987)	Deterministic with fixed model space. Regularisation applied	Potential to get caught in local minimum but generally smoothest acceptable model	low	Smoothest acceptable model to within an expected tolerance	Inversion of magnetotelluric and electromagnetic data (deGroot-Hedlin and Constable 1990; Vallée and Smith 2009)
Genetic Algorithm (Holland, 1965)	Stochastic with fixed model space. No regularisation applied	Global	High, depending on the number of iterations needed	Single best fitting model and REM misfit, with access to the misfit of other models tested	Inversion of surface wave dispersion curves (Yamanaka, and Ishida, 1996; Tsuji et al., 2012)
1D laterally constrained (Auken and Christiansen 2004)	Deterministic with fixed model space. Regularisation applied in the form of prior information.	Local minimum but prior information guides the inversion to what model space is expected.	low	Best fitting model with standard deviation analysis of the primary parameters in the model	Inversion of resistivity data (Auken et al., 2005)
Bayesian transdimensional MCMC (Sisson, 2005)	Stochastic with variable model space. Regularisation applied in the form of prior information.	Global	High, millions of iterations needed with multiple chains	PDF solution, access to mode, average, best models with full uncertainty analysis	Inversion of surface wave dispersion and teleseismic P wave receiver functions (Bodin et al., 2012; Julià et al., 2000; Shen et al., 2012)

1.4 Objectives and thesis roadmap

In this work, I aimed to further develop non-conventional geophysical techniques used in cryosphere studies highlighting their strengths and limitations, to motivate other users and continued development of these methods, thus providing more varied geophysical parameterisation of the cryosphere's subsurface. Specifically, this work focuses on the development of Rayleigh wave dispersion curves, from MASW, and TEM for characterising the subglacial environment. The objectives of the work are:

1. The development of a novel inversion methodology, easily adaptable for different geophysical techniques, enabling multiple geophysical observations to be integrated into a single inversion.
2. To evaluate the feasibility of using MASW and TEM techniques on glacier ice, to obtain the shear-wave and resistivity properties of the subglacial environment.
3. To deploy MASW, TEM and complementary GPR surveys on Midtdalsbreen, an outlet glacier of the Hardangerjøkulen ice cap in Norway, using observations from (2) to inform and optimise acquisition design.
4. To apply the novel inversion methodology developed in (1) to derived shear-wave and resistivity models of the Midtdalsbreen subglacial environment.
5. To develop a joint inversion strategy for combining observations from the seismic and TEM data.
6. In discussion, to evaluate the applicability of these approaches for characterising larger ice sheets, for example in Antarctica and Greenland, where the evolution of the subglacial environment is an important consideration in predictions of future sea-level rise.

This chapter provides an introduction and background to the research and geophysical techniques used, outlining the main aim and objectives of the thesis. Chapter 2 summarises the MASW, TEM and GPR acquisitions undertaken during two field campaigns, in spring 2017 and spring 2018.

The next three chapters are presented in the form of three papers published over the course of my studentship. Chapter 3 details the methodology, including the development of the Bayesian inversion methodology, MuLTI. Chapters 4 and 5 demonstrate the application of MuLTI and its MuLTI-TEM variant for, respectively, the inversion of Rayleigh wave dispersion curves and TEM data, using data acquired on Midtdalsbreen glacier.

In Chapter 6, I consider the feasibility of the MuLTI algorithm for characterising the subglacial environment beneath thicker ice sheets, thus evaluating its applicability for

use in Greenland and Antarctica. The discussion in Chapter 7 summarises the current strengths and limitations of the MuLTI and MuLTI-TEM techniques, and also considers the development of a joint inversion strategy by which seismic and TEM data can be numerically integrated. Finally, Chapter 8 summarises the thesis conclusions and prioritises actions for further work.

Chapter 2 Geophysical data acquisition

Ahead of describing the development of the inversion methodologies in this thesis and their application to field data, I first give an overview of the study area and review the geophysical acquisitions undertaken there.

2.1 Field site

GPR, active source seismic and TEM data acquisition was performed on Midtdalsbreen, a northeast-flowing outlet glacier of the Hardangerjøkulen ice cap in central-southern Norway (60.59°N, 7.52°E), 6.8 km^2 in area, in April-May 2017 and 2018 (Figure 2.1).

Hardangerjøkulen is Norway's 6th largest glacier (71.28 km^2) (Andreassen and Winsvold, 2012) and is an important water source for local river catchments. Annual glacier length measurements performed by A. Nesje between 1982 and 2018 show that the front of Midtdalsbreen advanced 36 m between 1982 and 2001, but retreated 219 m between 2001 and 2018 (e.g., nve.no/hydrologi/bre; Reinardy et al., 2019), thus exposing material recently melted out from beneath the glacier. Midtdalsbreen is surrounded by mountains of phyllite and crystalline granite and gneiss, with moraines on the glacier foreland primarily consisting of till with granite, gneiss and phyllite clasts. Foreland studies presented in Reinardy et al., 2019 and 2013 describe observations of debris rich ice that incorporate fine sediment (sands and clayey silts) and occasional bedrock clasts (phyllites). GPR data presented in Reinardy et al. 2019 highlights a potential subglacial reflector corresponding to the base of a subglacial permafrost layer. Direct observations of exposed material around the front of the glacier, during data acquisition, also showed soft, wet sediment (sands and clays) and hard bedrock clasts. These observations of unfrozen fine grained sediment, frozen sediment (permafrost) and bedrock were used as the lithology types expected within the subglacial environment at Midtdalsbreen.

Willis et al. in 2012 investigated the Midtdalsbreen's subglacial drainage system using dye tracing methods. They suggested that the glacier has a split drainage system, with a hydraulically efficient distributed system on the eastern section (T1; Figure 2.2) and an inefficient linked cavity system on the central and western sections (T2 and T3; Figure 2.2).

Åkesson et al. (2017) developed a numerical ice flow model of the Hardangerjøkulen ice cap, drawing on glacier and climate reconstructions, to highlight its sensitivity to climate change. They showed that the present day ice cap is highly sensitive to surface

mass balance changes and could disappear completely within a century, due to future warming climate predictions. However, the bed conditions are not well known; based on sparse sediment cover in the surrounding areas, Åkesson et al. (2017) assume Hardangerjøkulen to be hard-bedded, with no deformable sediments present. The extent to which this assumption is true is unknown, which highlights the importance of geophysical investigations to better characterise subglacial properties.

Midtdalsbreen is well-suited to methodological development since it is both logistically accessible and has a simple wedge-shaped profile (Figure 2.1c), which is valuable for this study since ice thicknesses show little cross-glacier variation. The simple profile also allows different depth sensitivities of the surface wave seismic and TEM techniques to be explored. The location of the survey lines were chosen in an area dominated by the distributed subglacial system (Figure 2.2), away from the channelized system, where the subsurface structure is more likely to be relatively homogenous with minimum variability and complexity compared to the subsurface around the channelized system. At the time of acquisition, April–May, the subsurface comprised snow (~2–4 m thick) overlying a varying thickness (0–25 m) of glacier ice and a substrate of unknown subglacial material.

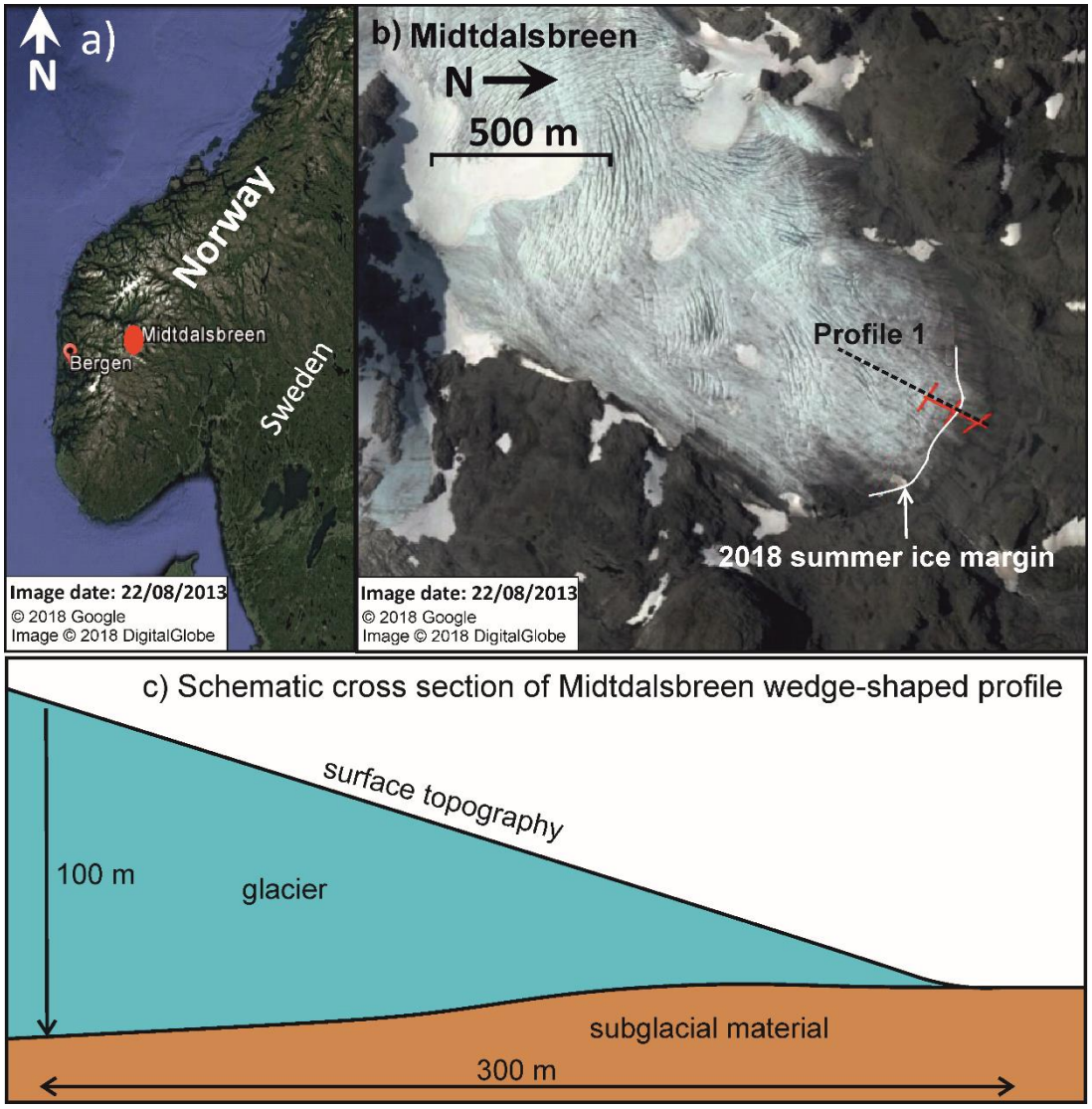

Figure 2.1 a) Location of Hardangerjøkulen ice cap, South Norway. Google Earth satellite images taken in 2013. b) Google Earth image of Midtdalsbreen, an outlet glacier of the Hardangerjøkulen ice cap, with survey lines highlighted in red at the front of the glacier and profile 1 from Reinardy et al., 2019 GPR survey highlighted in the black dashed line. c) Schematic cross section of Midtdalsbreen's wedge shaped profile, interpreted from Reinardy et al., 2019 GPR profile 1. Note that b) is orientated away from north to enable optimal data comparison in later figures throughout the thesis.

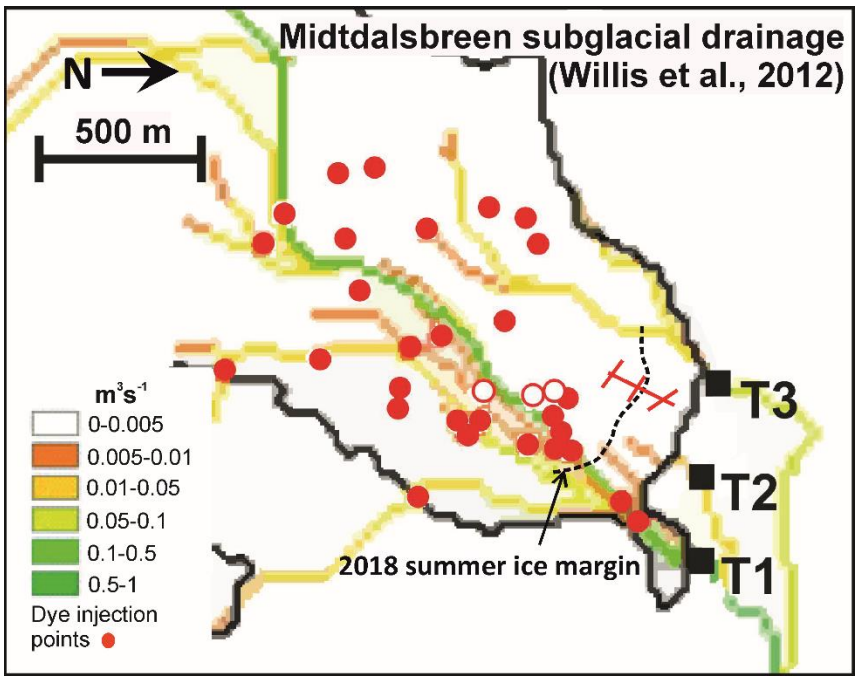

Figure 2.2 Calculated annual average subglacial water fluxes (m^3s^{-1}) beneath Midtdalsbreen presented in Willis et al., 2012, with the 2018 ice margin displayed in a black dashed line and 2018 survey lines displayed in red. Red closed/open circles are moulins yielding returns/no returns from previous dye tracing experiments detailed in Willis et al., 2012.

2.2 Data acquisition

Two field campaigns were completed during this project:

i) in April-May 2017 – a test campaign acquiring active source seismic and GPR, and.

ii) in April-May 2018 – the main field campaign, acquiring GPR, active source seismic and TEM around and over the front of the glacier.

Survey lines A-D (Figure 2.3) were surveyed with all techniques. Results and interpretations of lines A-D, from the main field session in 2018, are discussed fully in Chapter 4 and 5, providing an insight to the properties of the Midtdalsbreen subglacial material. This section shows, in more detail than presented in the following chapters, the data acquisition for each geophysical method.

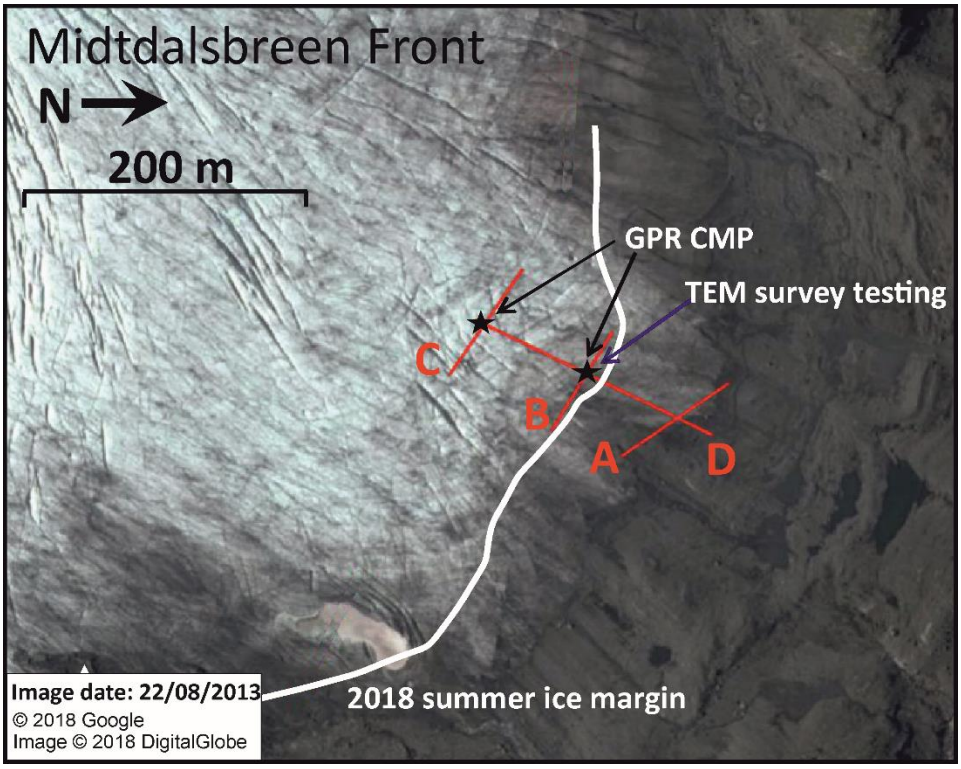

Figure 2.3 Survey lines acquired during the 2017 and 2018 field seasons at the front of Midtdalsbreen. GPR common midpoint gathers (CMP) were acquired at the black stars and 1D TEM survey testing was completed at the midpoint of line B.

2.2.1 MASW acquisition

MASW employs a linear array of geophones in line with an active seismic source acting on the ground surface. This method was initially introduced by Park et al., 1999. Field data collected in time and space are transformed into a domain (e.g. frequency-wavenumber) where the phase velocities associated with different frequencies are easily chosen by picking the spectral maxima (Foti et al., 2015). The x, y-pairs of phase velocity ($PV(f)$) and frequency (f) define the dispersion curve. At a given frequency, the phase velocity (PV) specifies the resolvable wavelength λ associated with each datum (Stokoe et al., 1994) as

$$\lambda = \frac{PV(f)}{f} \tag{2.1}$$

and its associated resolvable scale (L) is approximated using a one-third wavelength resolution criterion (Gazetas, 1982)

$$L = \frac{\lambda}{3} \tag{2.2}$$

The frequency range where the phase velocities are considered stable, where a clear spectral maxima can be picked, correspond to the minimum and maximum wavelengths of the surface waves recorded. This defines the surface waves resolvable

scale as $L_{min} \leq L \leq L_{max}$, where L_{min} is the thinnest resolvable layer and L_{max} is the maximum resolvable depth, discussed further in Chapter 3. The survey design and parameters used to acquire the seismic data can have a large effect on the resolution of the dispersion curve's spectra maxima. Larger wavelengths become well developed plane waves at longer offsets (Park et al., 2001) enabling lower frequencies to be picked, however body waves, including refractions, also become more dominant at far offsets (Park et al., 2001) and therefore a trade-off has to be considered, which will be field site specific.

A test field campaign was completed in April-May 2017 to test the general performance of subglacial MASW imaging, plus the feasibility of a portable hammer-and-plate source. Active source seismic data were acquired around the front of Midtdalsbreen along Lines A, B, C and D (Figure 2.3) with a Geometrics GEODE system and 24 10 Hz vertical-component geophones (Figure 2.4a-b), with 2 m spacing for the cross-glacier lines (A, B, C), and 4 m spacing for the wedge profile line (D). GPR profiles were also acquired along the length of the seismic lines to identify the structure and thickness of the ice. Dispersion curve analysis from the 2017 data acquisition showed the lowest frequencies generated from this survey design, above background noise levels, were 18 Hz (Figure 2.5a-c show examples from line C). This enabled imaging to an estimated 30 m depth (assuming a one-third wavelength resolution criterion, Gazetas 1982), which penetrated 10 m into the subglacial environment when the ice was ~20 m thick, estimated from the GPR data. However, identifying the low frequencies were mainly limited by poor resolution dispersion curves, most likely due to the maximum shot offset (46 m). Synthetic testing showed, using 48 geophones (doubling the offset but keeping the dense sampling to avoid spatial aliasing; Yilmaz 2001) would provide better resolved dispersion curves enabling lower frequencies to be picked (down to 14 Hz), for a greater depth penetration (~ 45 m) (Figure 2.5f).

With this knowledge, in the main field session in 2018, the seismic data were acquired with the same system but with 48 10 Hz vertical-component geophones. With more geophones available, the length of the spread was doubled for each line, providing a higher resolution dispersion curve, especially at the lower frequencies, < 20 Hz, (Figure 2.5d-e). Some P wave energy is observed in this longer offset dispersion curve at the high frequencies, > 100 Hz, high phase velocities, > 3000 m/s, highlighted in Figure 2.5e, however this is not dominant at this offset and the surface wave dispersion curve can easily be picked. Detailed analysis, results and interpretations of the 2018 MASW study is presented in Chapter 4.

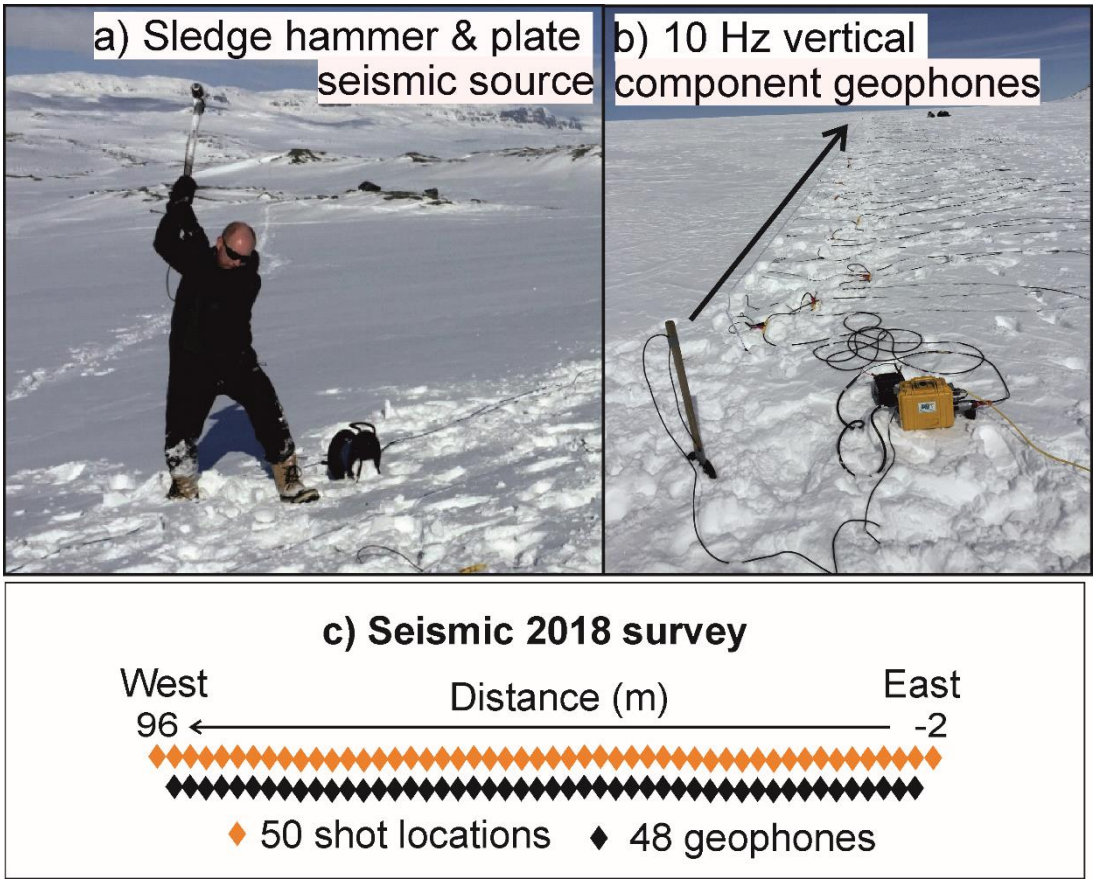

Figure 2.4 a) Active seismic data acquisition using a sledge hammer and plate as the source (left image), b) 10 Hz vertical component geophones with a Geometrics GEODE system (right image), c) schematic image of 2018 seismic survey set up for the cross-glacier lines A, B and C.

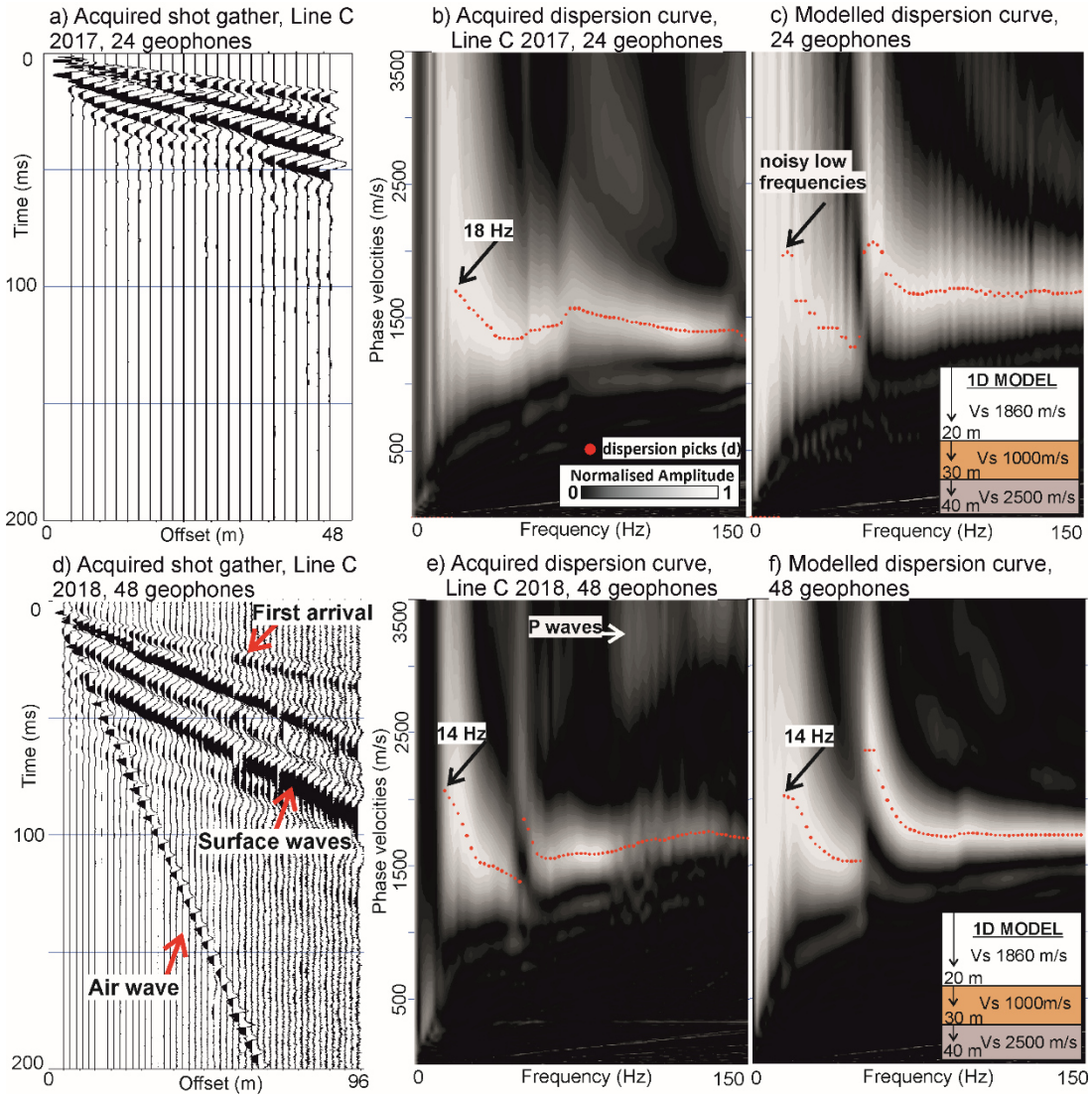

Figure 2.5 Dispersion curve analysis from the 2017 test field campaign compared to the 2018 main campaign. a) Acquired shot gather at Line C in 2017 using 24 geophones. b) Acquired dispersion curve at Line C using 24 geophones, lowest frequencies picked were 18 Hz. c) Synthetic modelled dispersion curve (using the discrete wavenumber method) with 24 geophones showing poorly resolved dispersion curve picks especially at the low frequencies. d) Acquired shot gather at Line C in 2018 using 48 geophones. e) Acquired dispersion curve at Line C using 48 geophones, lowest frequencies picked were 14 Hz. f) Synthetic modelled dispersion curve (using the discrete wavenumber method) with 48 geophones showing a much better resolved dispersion curve picked, in particular low frequencies down to 14 Hz can be clearly defined. The synthetic 1D model used in this analysis was 20 m ice, 1860 m/s, on top of a 10 m low velocity zone, 1000 m/s, above basement, 2500 m/s. Note see Chapter 3 for detail on the discrete wavenumber method (DWM).

2.2.2 Transient electromagnetics acquisition

Transient (time-domain) electromagnetics uses transient pulses of electric current to induce electric and magnetic fields in the subsurface, measuring the subsequent decay

response of the induced fields. A schematic of the transmitter waveform is shown in Figure 2.6, highlighting the transient pulses and receiver measurement windows, in the transmitter-off periods. The response of the subsurface is measured in terms of the decaying amplitude of the secondary electromagnetic field. This is recorded as a function of time, with later responses originating from greater depths. The measured voltages versus time can be inverted to provide a resistivity profile with depth. Further detail on the TEM method is detailed in Chapter 5, Section 2.

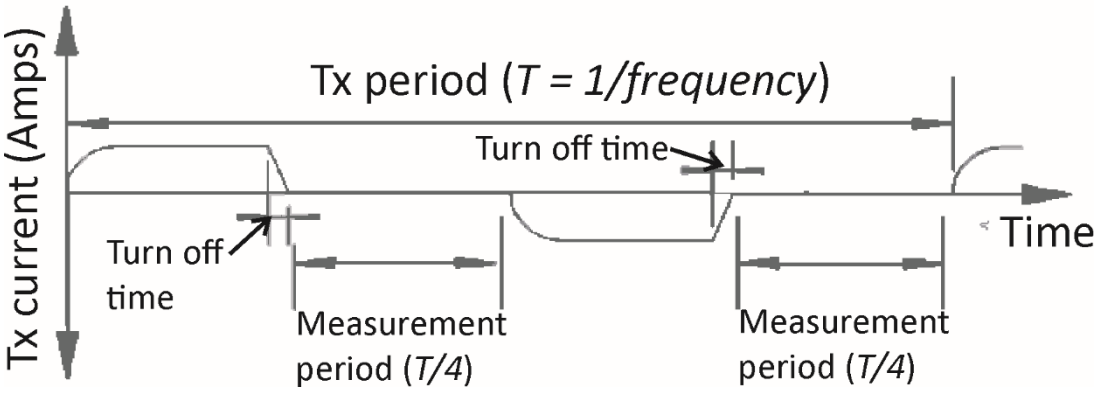

Figure 2.6 Schematic diagram of the transmitter waveform, adapted from Geonics 1994.

TEM data was acquired in the main field session in 2018, with a Geonics PROTEM 47 system, consisting of a 3 channel digital time-domain receiver, a TEM-47 battery powered transmitter and a 3D multi-turn receiver coil, loaned from the NERC GEF, Figure 2.7a-c. Multiple 1D soundings were acquired along each line with a 4 m spacing for lines A, B and C (schematic diagram shown in Figure 2.7d), and 8 m spacing for line D. Detailed analysis, results and interpretations of the 2018 TEM study is presented in Chapter 5.

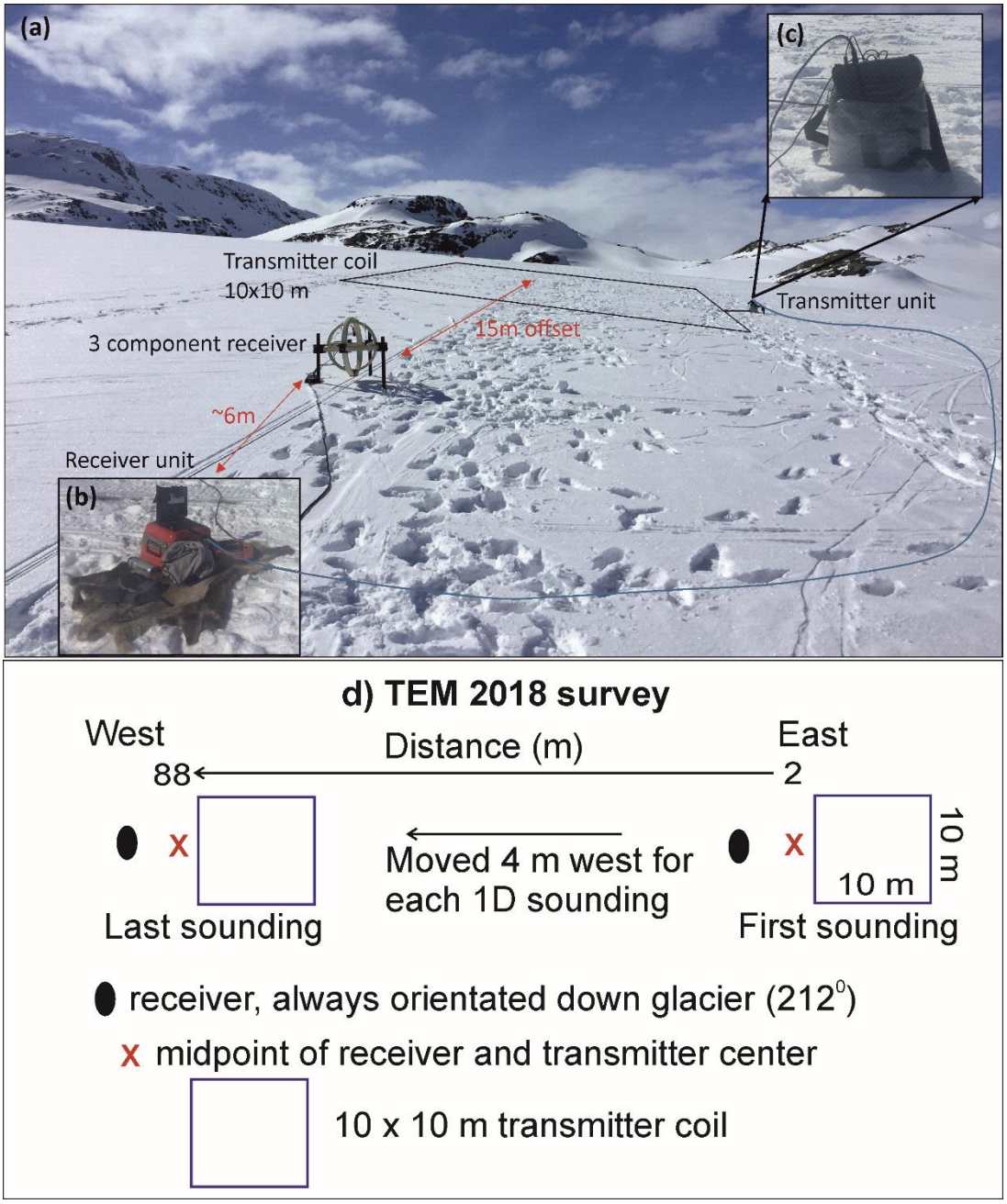

Figure 2.7 a) TEM acquisition set up. b) Image of the receiver unit on top of a rug to protect unit from snow and easily drag along the lines. c) Image of transmitter unit sitting in bubble-wrap pocket used to protect unit and batteries from snow and cold. d) Schematic image of 2018 TEM survey set up for the cross-glacier lines A, B and C.

2.2.3 Ground penetrating radar acquisition

GPR was acquired in both field sessions, 2017 and 2018, to identify the structure and thickness of the snow and ice, along all lines. The GPR was acquired with Sensors & Software PulseEKKO PRO unshielded 200 MHz antennas and towed along the back of a snowmobile, shown in Figure 2.8. Additional to these common offset profiles,

two common midpoint gathers were acquired at the midpoints of line B and C (at their intersection with Line D; highlighted in Figure 2.3) for velocity analysis to estimate snow and ice thicknesses. Results from the GPR dataset are presented in Chapter 4.

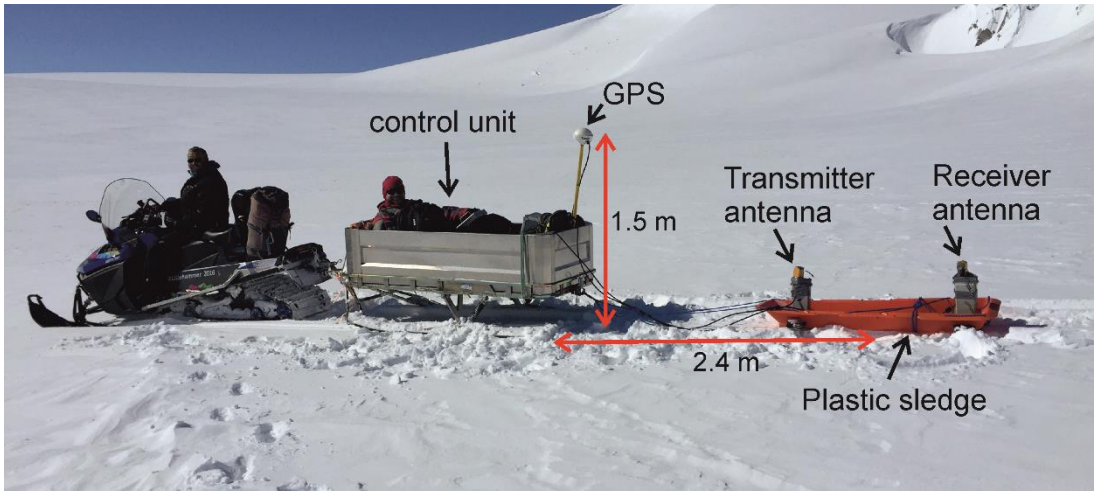

Figure 2.8 GPR acquisition set up.

Chapter 3 Multimodal Layered Transdimensional Inversion of Seismic Dispersion Curves With Depth Constraints

S. F. Killingbeck[1], P. W. Livermore[1], A. D. Booth[1], and L. J. West[1]

[1]School of Earth and Environment, University of Leeds.

Corresponding author: Siobhan Killingbeck (eespr@leeds.ac.uk)

Published in Geochemistry, Geophysics, Geosystems, doi: doi.org/10.1029/2018GC008000

3.1 Abstract

MuLTI (Multimodal Layered Transdimensional Inversion) is a Markov chain Monte Carlo implementation of Bayesian inversion for the probability distribution of shear-wave velocity (*Vs*) as a function of depth. Based on Multichannel Analysis of Surface Wave (MASW) methods, it requires as data (i) a Rayleigh-wave dispersion curve and (ii) additional layer depth constraints, the latter we show significantly improve resolution compared to conventional unconstrained inversions. Such depth constraints may be drawn from any source (e.g., boreholes, complementary geophysical data) provided they also represent a seismic interface. We apply MuLTI to a Norwegian glacier, Midtdalsbreen, in which ground-penetrating radar (GPR) was used to constrain internal layers of snow, ice and subglacial sediments, with transitions at 2 m and 25.5 m, and whose *Vs* is assumed to be in the range 500-1700 m/s, 1700-1950 m/s and 200-2800 m/s respectively. Synthetic modelling demonstrates that MuLTI recovers the true model of *Vs* variation with depth. Significantly, compared to inversions without depth constraints, in this synthetic case MuLTI not only reduces by about a factor of 10 the error between the true and the best fitting model, but also reduces by a factor of 2 the vertically-averaged spread of the distribution of *Vs* based on the 95% credible intervals. We further show that using frequencies above about 100Hz lead to unconverged solutions due to mode ambiguities associated with fine spatial structures. For our acquired data on Midtdalsbreen, we use 14-100Hz data for which MuLTI produces a large-scale converged inversion.

3.2 Plain Language Summary

Geophysical inversion is used to infer plausible subsurface features from surface measurements. However, inversions based on datasets acquired with a single geophysical technique often have poor resolution due to many different subsurface models fitting the data within the error tolerance. This study presents a novel method, *MuLTI*, for inverting seismic surface wave data with constraints on depths of internal layers to obtain a more accurate and reliable interpretation of the subsurface. Here, our depth constraints are drawn from ground-penetrating radar (GPR) horizon observations. MuLTI has been tested on an example dataset from a glaciated environment to determine the seismic wave velocity of the subglacial sediment, which has important implications for glacier flow dynamics. By constraining the subsurface with GPR depth horizons, results show the inverted solution being 2 times better resolved and 10 times more accurate within the glaciological subsurface, than without constraints applied. Thus, we demonstrate MuLTI can mitigate poor resolution of an

unconstrained inversion, particularly at increased depth. Although we present examples from a glaciated dataset, this novel methodology is applicable to any layered subsurface environment.

3.3 Introduction

Many inversions of geophysical data derived from a single type of geophysical instrument are under-constrained, a property that results from not only limitations of the size and accuracy of the dataset, but inherent non-uniqueness: many models of the subsurface may be consistent with the single class of surface-based constraints. For this reason, joint inversions using datasets of mixed types can be a powerful method of constraining the model space, where ambiguities of one methodology are mitigated by resolution in the other. Over the past few decades several different joint inversion algorithms and techniques have been developed in various geological settings to overcome such under-constrained problems. Geoelectric and seismic surface wave data have been combined (Hering et al., 1995, Wisén and Christiansen 2005) to improve the definition of layered structure in near surface environments (e.g., Ronczka et al., 2018). Similarly, reflection seismic and controlled source electromagnetics have been combined to estimate fluid properties of petroleum reservoirs, which could not be obtained from one survey-type alone (Hoversten et al., 2006). Colombo et al. (2017) used the joint inversion of seismic and airborne time domain electromagnetics to improve imaging of complex near surface structures to reduce risk in shallow petroleum exploration. In deep-Earth investigations, surface wave dispersion and teleseismic p-wave receiver functions both supply constraints on the crustal and upper mantle geology and efficient algorithms for joint inversions have been developed (e.g., Julià et al., 2000; Bodin et al. 2012; Shen et al., 2012). Our paper focuses on the use of constrained inversions to characterise a glaciated subsurface by inverting Rayleigh (surface) wave datasets in the presence of depth constraints here provided by ground-penetrating radar (GPR) data.

Rayleigh waves are a type of seismic wave that travel along the ground surface, which, in an active seismic survey, are efficiently generated by a compressional wave source: such a source typically converts more than 2/3 of the total seismic energy into Rayleigh waves (Richart et al., 1970). Using Multichannel Analysis of Surface Wave (MASW) methods, the dispersive properties of the Rayleigh waves can be utilized to infer the elastic properties of the subsurface (Park et al., 1999), often expressed in terms of shear wave velocity (*Vs*), compressional wave velocity (*Vp*) and density. The MASW technique is most sensitive to *Vs* (Xia et al., 2003), being only weakly dependent on *Vp* and density (Wathelet, 2005). When inverted with no other

constraint, Rayleigh wave dispersion curves have poor depth sensitivity (Foti et al., 2009) particularly given data collection issues including noise and finite bandwidth, the latter being problematic for resolving short length scales and near-surface structures. Indeed, a direct inversion of such data has a vertical resolution of only 1/3 of the shortest wavelengths sampled (Gazetas 1982), typically with 1-10 meter resolution in active source surveys. In view of this limitation in resolution, many models of subsurface *Vs* structure may provide an acceptable level of fit to the observed data, therefore giving an ambiguous inversion.

An independent geophysical survey technique is ground-penetrating radar, GPR, which is sensitive to changes in subsurface dielectric permittivity and can resolve the layered near-surface velocity-depth structure to centimetre accuracy (Booth et al., 2010). However, as with MASW, GPR data itself cannot unambiguously constrain subsurface structure, and often has limited depth penetration. By combining Rayleigh wave observations and depth information from GPR data, constrained inversion offers a powerful way to reduce the ambiguities inherent in single-technique inversions, provided that subsurface interfaces correspond to co-located contrasts in both elastic and electromagnetic properties. This assumption is likely appropriate in (for example): a glaciated environment with snow, ice and a subglacial substrate (Tsuji et al., 2012); a permafrost environment featuring unfrozen and frozen ground (Kneisel et al., 2008); and hydrological settings such as the imaging of shallow aquifers (Cardimona et al., 1998). Such inversions both honour the cm-scale accuracy of the GPR constraints and, assuming the layered GPR model can be interpreted, their major advantage is the narrowed range of elastic properties that is permitted for each layer within the model. This latter effect vastly reduces the space of subsurface models consistent with the data, and thus significantly improves the resolution of any inversion. Furthermore, layer constraints mean that poor surface wave resolution in one layer does not necessarily spread to the adjacent layers. Of course, this approach is only viable when the contrasts detected by the seismic and GPR methods are likely the same; in situations where a change in electromagnetic properties would produce no linked elastic contrast (e.g., a salinity horizon within an aquifer), our approach would not be useful. In this study, we use synthetic and real data examples from a glaciological setting, modelling the subsurface distribution of snow, ice and subglacial material. In this setting, we expect that elastic and electromagnetic horizons will be co-located. In practice, depth constraints could be added from any external data source – for example, from seismic reflection studies or borehole control.

Even when multiply constrained, inversions are seldom unique. In many inversions, regularisation is employed to penalise small scale roughness to produce a single

smooth solution. However, single solutions may not be sufficient given the non-uniqueness issues in surface wave inversions. Bayesian Markov Chain Monte Carlo is a type of method that probabilistically quantifies the model space consistent with the observations. The application of the method results in a posterior probability distribution of the sub-surface structure, numerically approximated by an ensemble of models, from which representative models such as the mean or mode can be obtained, in addition to rigorous estimates of uncertainties. This posterior probability distribution must lie within the bounds defined by a specified prior distribution, but is honed by the data into peaks that correspond to the most likely models. A refinement, applied here, is to use a transdimensional Bayesian method that allows each ensemble member to self-select both its model values and complexity based on the data. Averaging over the many ensemble members, to obtain a mean solution, then provides an effective smoothing. Furthermore, in the case where surface observations are weakly informative (as is often the case in surface wave dispersion), a Bayesian transdimensional approach will prefer models with fewer layers, and therefore larger length scales (MacKay, 2003), rather than models with many thin layers. Here, we base our method on existing implementations of such a transdimensional method, which have successfully inverted both single and multiple datasets (Bodin and Sambridge, 2009, Bodin et al., 2012, Livermore et al., 2018).

In this paper we present the algorithm *MuLTI* (Multimodal Layered Transdimensional Inversion), which implements a Bayesian inversion of surface wave data, honouring depth constraints. MuLTI is coded in Matlab and is freely available; we provide all datasets and scripts needed to reproduce the figures in this paper. The remainder of the paper is structured as follows. We first describe MuLTI in detail and demonstrate its ability to retrieve a known sub-surface structure using synthetic datasets within a glacial setting. We then show an application of MuLTI to image the structure, both within and under, a Norwegian glacier using a dataset which we acquired *in situ*. Although we focus on glacial environments, MuLTI can be used in any layered geological environment where electromagnetic and elastic properties change at the same depths.

3.4 The MuLTI Algorithm

MuLTI is a Bayesian method which seeks to determine the posterior distribution of the shear wave velocity (*Vs*) as a function of depth, for a prescribed profile of *Vp* and density (see also Bodin et al. (2012), Wathelet (2005)). Denoting the dataset by $\boldsymbol{d}$ and the model description of *Vs* by $\boldsymbol{m}$, using Bayes' theorem this can be written

$$p(m|d) = p(d|m)p(m)/p(d) \quad (3.1)$$

where $p(m|d)$ is the posterior probability of the model given the data, $p(m)$ is the prior information known about the model before introduction of the data, $p(d|m)$ is the likelihood (probability of observing the measured data given a particular model (m)) and $p(d)$ is the evidence. In what follows, we consider a Markov Chain Monte Carlo methodology to sample the posterior distribution, in which relative inference is sufficient: thus here the evidence does not enter our analysis. The algorithm traverses the space of admissible models, sampling with greater frequency those models that are more likely. Provided that the chain of models is long enough, the statistics of the discretised ensemble will converge to those of the underlying posterior distribution.

It is important to note what we take to mean for the data, *d*. Both GPR and Rayleigh wave datasets are 'data' in the geophysical sense but, because the GPR-derived layer depths are comparatively so well resolved, we use the two datasets in different ways. The GPR data we take to be part of our background knowledge of the system and are included in the prior, while the Rayleigh wave data we take to comprise the data (*d*), used in the likelihood. Hence, the two datasets are not treated on an equal footing.

MuLTI can run in two different modes. In the first, it conducts a constrained inversion using both seismic data and layer-depth constraints, here derived from GPR data and assuming an underlying infinite half-space. In the second mode, MuLTI runs with no pre-defined internal boundaries, and the subsurface here is described by an infinite half-space.

3.4.1 The data

Rather than using raw data from synthetic waveform models, seismograms or active seismic acquisitions, MASW uses the derived dispersion curve in the frequency-phase velocity domain. This dispersion curve is characterised by a discrete set of points that we term the data, d, by picking the phase velocity for a set of frequencies according to the spectral maximum (Foti et al. 2015). If *N* discrete points are picked in this domain, the data comprise *N* pairs of frequency (f) and Rayleigh wave phase velocity (PV) values with corresponding standard deviation σ:

$$d = [f_1 \ f_2 \ldots . f_N \, , PV_1 \ PV_2 \ldots . PV_N] \, , \quad (3.2)$$

$$\sigma = [\, \sigma_1 \ \sigma_2 \ldots . \sigma_N] \, . \quad (3.3)$$

The standard deviation of the phase velocities is a measure of uncertainty in the picked dispersion curve, which is either prescribed as a constant vector (for example, in a synthetic test), or determined as a function of frequency from the width of the waveform dispersion image. For the latter case, we note that the resolution of the

dispersion curve depends on the survey parameters used to acquire the seismic data. For example, a higher density of wavefield sampling, i.e. more receivers and longer source-receiver offset ranges, produces better resolved dispersion curves; furthermore, in general, higher frequencies are typically better resolved than lower frequencies (Park et al., 2001).

3.4.2 Model parameterisation

We describe the 1D variation of *Vs* with depth as a piecewise constant function using Voronoi nuclei (but see Dettmer et al. (2010) for an alternative), in which each layer is divided into a variable number of sub-layers with constant velocities; at each depth, the value of *Vs* is determined by its nearest nucleus within the same layer (Bodin et al. 2012), see Figure 3.1 for an illustration of this model parameterisation. To ensure that *Vs* within each pre-specified layer is always described (requiring a minimum number of nuclei of 1 within each layer), we define a set of *confined* nuclei, which are confined to the given layers but are otherwise unconstrained in depth. The number of confined nuclei is equal to the number, l, of internal layers including the half space. All other k nuclei in the model are unconstrained in depth, and are termed floating nuclei. The model vector is then

$$m = [dp_1, dp_2, \ldots., dp_k, Vs_1, Vs_2, \ldots., Vs_k, k, dpc_1, dpc_2 \ldots. dpc_l, c, Vsc_2, \ldots., Vsc_l] \quad (3.4)$$

where dp_i are the floating nuclei depths, Vs_i are the floating nuclei wave speeds, dpc_i are the depths of the confined nuclei, Vsc_i are the wave speeds of the confined nuclei, and k is the number of floating nuclei. In our transdimensional framework, the number of floating nuclei $k \geq 0$, characterising the complexity of the *Vs* profile, is a free parameter. All Voronoi nuclei are defined with depths ranging from 0 to a pre-defined maximum depth dp_{max}. We note that the lowermost Voronoi cell is unbounded in downwards vertical extent and describes an infinite half-space.

3.4.3 The likelihood

The likelihood expresses the probability of observing the data (in our case, the picked dispersion curve) given a specific model m, here achieved by running a forward calculation of the frequency-P*V* response and comparing to the observed data (d). For a given frequency, there are multiple phase velocities at which the Rayleigh wave can travel; the slowest velocity is called the fundamental mode, the next highest velocity is called the 1st higher-order mode, then the 2nd higher-order mode etc. (Park et al., 1999). Early models of surface wave inversion only considered the fundamental mode with simple near surface environments (Xia et al., 1999), although it has been shown subsequently that higher order modes are preferred over the fundamental mode in several types of velocity structures (e.g., when a high velocity layer overlies a low

velocity layer (Gucunski & Woods, 1992)). Here, we calculate all relevant modes (fundamental, 1st and 2nd higher order modes) and we assume that the probability of the *i*th datum $PV_i(f_i)$ is normally distributed about the nearest modal value, $c(f_i)$, at frequency f_i (of the three calculated) with standard deviation $\sigma_i(f_i)$. We deliberately do not specify which mode should be associated with any given datum because it is often difficult in practice to unambiguously assign the correct modal index (see section 3.5). Assuming that each datum (indexed by $i = 1, 2 \ldots N_{data}$) is independent, the likelihood $p(m|d)$ is then proportional to

$$\prod_{i=1}^{N_{data}} e^{-\frac{(PV_i - c(f_i))^2}{2\sigma(f_i)^2}} \tag{3.5}$$

We calculate the modal dispersion curves using the Geopsy dispersion curve (gpdc) algorithm of Wathelet (2005), by first converting our Voronoi cells to a layer-model. The gpdc algorithm uses a propagator matrix method to find the eigenvalues of the dispersion equation (Wathelet, 2005). This is a fast algorithm suitable for running repeatedly within MuLTI. We note that there is an option within MuLTI to limit the calculation of misfit to use either only the fundamental mode, or to use only a subset of the frequency range.

Our framework can be easily altered to include a different definition of likelihood: the choice we made above is not unique. Other definitions include a characterisation of the misfit in terms of a determinant, removing the need to calculate the modal curves (Maraschini & Foti, 2010), or use of a full wavefield inversion approach using the dispersion spectra instead of a picked curve (Dou & Ajo-Franklin, 2014).

3.4.4 Prior information

The remaining key aspect of our Bayesian method is the prior information that is assumed for the model parameters: the number (k), depth (dp) and material properties (Vs) associated with the Voronoi nuclei. By conditioning on the value of k, the prior can be written as

$$p(m) = p(dp_1, dp_2, \ldots., dp_k, Vs_1, Vs_2 \ldots. Vs_k, dpc_1, dpc_2, \ldots., dpc_l, Vsc_1, Vsc_2, \ldots., Vsc_l | k)\, p(k) \tag{3.6}$$

By further assuming that each pair (dp_j Vs_j), for both the floating and confined nodes, is independent of the others, the above probability can be written as

$$\prod_{j=1}^{k+l} p(Vs_j, dp_j|k) = \prod_{j=1}^{k+l} p(Vs_j \mid dp_j, k)\, p(dp_j) \tag{3.7}$$

We assume that k is uniformly distributed between given bounds: we commonly take $k \sim$ U[0,30], limiting the maximum number of floating nuclei to 30. We further assume that the depth of each Voronoi nucleus is independent and has a depth uniformly

distributed within given bounds: either the limits defined by GPR-defined layers for confined nuclei or dp ~ U[0, dp_{max}] for floating nuclei, with dp_{max} typically taken to be 40 m. The value of *Vs* attached to each nuclei is assumed to be uniformly distributed within bounds dependent on its assumed composition. Without GPR constraints, wide bounds are applied for the infinite half space, typically *Vs* ~ U[200,2800] m/s, but with GPR constraints the much narrower ranges are defined by the layers' composition**.**

Figure 3.1 illustrates the model geometry, and shows schematic differences between the unconstrained (Figure 3.1a) and GPR-constrained (Figure 3.1b) cases. Without GPR constraints, there is a large range of possible *Vs* values (grey shading) at any depth. The inclusion of GPR constraints reduces the model parameter space significantly, although *Vs* variability within each layer is permitted by the unconstrained number of floating Voronoi nuclei within each layer.

While all the model prior distributions are uniform, this does not mean the distributions of all diagnostics of the prior are also uniform. For example, the distribution of nuclei depths is not uniform (when using GPR constraints), because the existence of the confined nuclei that are tied to certain layers skews the distribution.

3.4.5 Numerical sampling of the posterior

We sample the posterior distribution by using the Monte Carlo Markov chain (MCMC) algorithm, in which we iteratively generate a long chain of models. The algorithm is very similar to that described in Gallagher et al. (2011) and Bodin et al. (2009) and there is no need to reproduce all the details here; we present only the key features and any differences. At each step, a new model *m'* is proposed that differs from the current model by one of four perturbations (Figure 3.2), which depend on a set of user specified parameters (σ_{change}, σ_{move} and σ_{birth}) whose values affect the speed of convergence to the posterior distribution:

- 'change *Vs*': perturb the velocity of a randomly chosen nucleus by a random amount distributed as N(0, σ_{change^2})
- 'move nucleus' : alter the depth of a randomly chosen nucleus; if it is a floating nucleus it is perturbed by an amount distributed as N(0, σ_{move^2}) and can move between the depth-derived layers; if it is a confined nucleus it is moved to a random depth distributed uniformly over that layer to which it is tied.

- 'birth' : add a floating nucleus to the existing model whose depth is uniformly distributed U[0, dp_{max}] and whose *Vs* is distributed N(v, σ_{birth^2}), where v is the value of *Vs* based on the current nuclei distribution.
- 'death': remove a floating nucleus from the existing model. Confined nuclei cannot be removed.

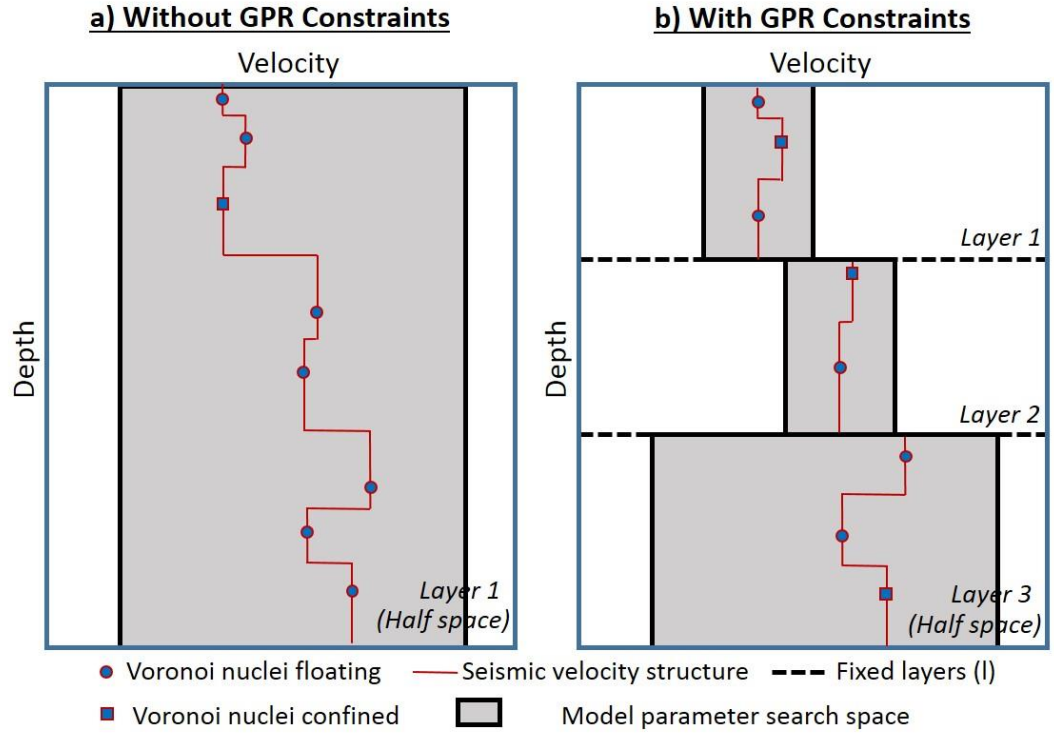

Figure 3.1 Illustration of MuLTI's model parameterisation using Voronoi nuclei (floating and confined) comparing (a) a 1-layer model with no internal layers and (b) a GPR-determined 3 layer structure assuming different ranges of *Vs* within each layer. Grey indicates the range of possible *Vs* values. Figure adapted from Bodin et al., 2012.

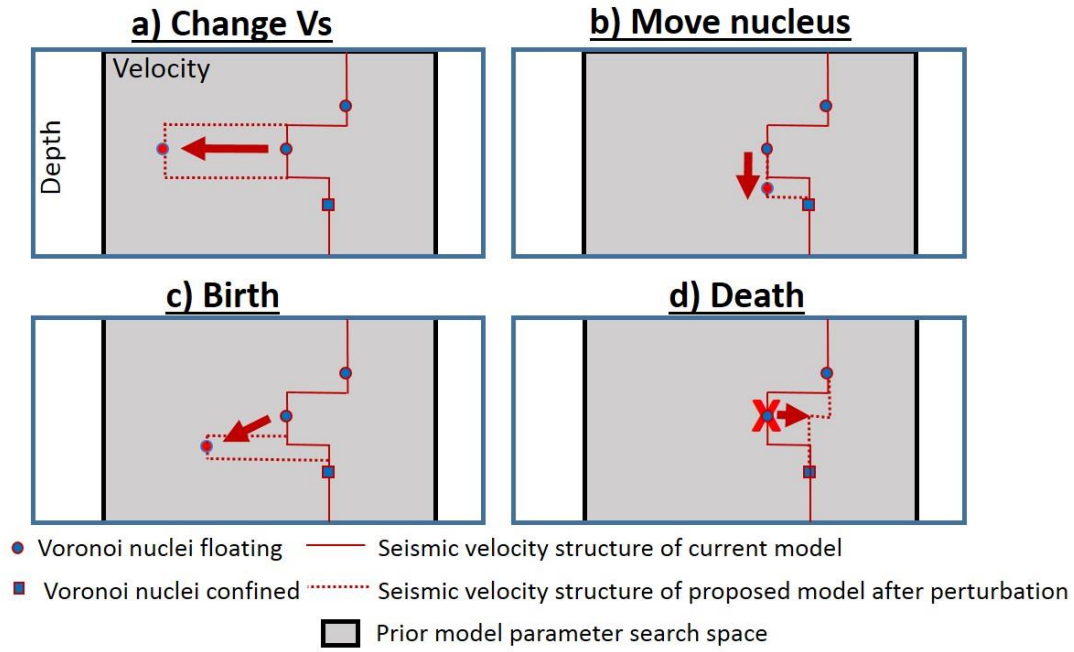

Figure 3.2 Illustration of 4 possible perturbations to a current model (a) change *Vs* of a nucleus, (b) move a nucleus to a different depth, (c) give birth to a new floating nucleus and (*d*) remove a floating nucleus.

Each proposed model is tested to see if it satisfies a certain acceptance criterion which involves the quantity

$$\alpha = \min\left[1, \frac{p(m')q(m|m')p(d|m')}{p(m)q(m'|m)p(d|m)}.|J|\right] \tag{3.8}$$

where $q(m'|m)$ is the probability of moving from model m to m'. For the type of transdimensional proposal used in this approach, the Jacobian term (J) is unity (Bodin and Sambridge, 2009). The evaluation of α for the types of perturbation shown in Figure 3.2 is standard (and is not described here) except the move perturbation when considering floating nuclei. For this case, $q(m|m') = q(m'|m)$, $p(d|m')\ p(d|m)^{-1}$ is the ratio of the two model likelihoods and $p(m')p(m)^{-1}$ is the ratio of the ranges of *Vs* between the layers that the nucleus may move between. After α is evaluated it is compared to a random number u ~ U[0,1]: if α>u the proposed model is accepted, added to the chain and becomes the current model; if it is not accepted the existing model is retained as the current model.

The method is initialized with a randomised model from the prior and the method is run for a "burn-in" period. At this point, the Markov chain is presumed independent of the initial condition and statistics of the chain are recorded from then on. This technique therefore differs fundamentally from techniques such as the Genetic Algorithm which relies on an initial reference model to start the inversion process

(Hayashi, 2012). On completion, all diagnostics must be checked to ensure sufficient iterations have been taken to achieve convergence. Perturbations that improve the data fit are mostly accepted; those which decrease the fit are most likely to be rejected but are occasionally (and randomly) accepted. Proposed models that lie outside the prior bounds give $p(m') = 0$; it follows that α=0 and such models are never accepted. Figure 3.3 shows a schematic view of the algorithmic core of MuLTI.

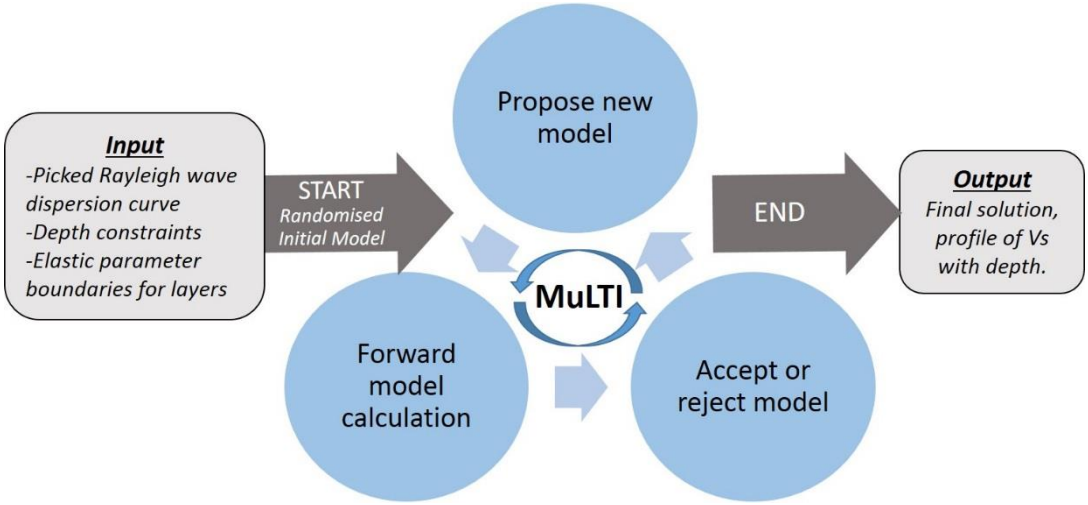

Figure 3.3 Schematic illustration of MuLTI. Grey boxes highlight the starting input data and final output model of the algorithm. The circular workflow represents the iterative inversion processes at the core of MuLTI.

MuLTI produces a variety of diagnostic statistics of the ensemble. These include: the posterior probability of the model of *Vs* as a function of depth; the best model sampled with the lowest calculated misfit; the average and modal models; 95% credible intervals on *Vs* with depth; posterior distribution of the number of nuclei; comparative plots of the observed data with dispersion curves for the best, average and modal models; and plots of the misfit against iteration count highlighting convergence of the solution. We reiterate that MuLTI can be used in any geological layered environment where electromagnetic and elastic rock property changes are co-incident.

3.5 Case Studies Using MuLTI

This section describes applications of MuLTI to both synthetic test data created assuming a simple glacial structure, and real data acquired from a Norwegian glacier. Because the output of MuLTI depends upon the resolution of the input surface wave dispersion curve, we first describe the Norwegian field setting and the data acquisition procedure in order to motivate the specific synthetic tests that will provide insight into the reliability and limitations of inversions from real data.

3.5.1 Data acquisition

Data were acquired on Midtdalsbreen, an outlet glacier of Norway's Hardangerjøkulen ice cap (60.59ºN, 7.52ºE), with the aim of characterising the *Vs* properties of the subglacial environment. These properties provide an important insight into subglacial water storage and the flow dynamics of the overlying glacier, thus motivating this study. The subsurface comprises fresh snow over ~ 25 m of glacier ice, and a substrate of unknown subglacial material (likely sediment). Midtdalsbreen is surrounded by mountains of crystalline rock, and it is thought that this hard rock lies below the subglacial material.

Seismic shots (e.g., Figure 3.4a) were recorded with 48 10 Hz vertical-component geophones at 2 m incremental offset from a hammer-and-plate source, and digitised using a Geometrics GEODE system. A GPR profile was acquired along the length of the seismic line with Malå Geosciences antennas of 200 MHz centre-frequency. The thickness of snow and ice layers were estimated from velocity analysis of a GPR common midpoint (CMP) gather located half way along the seismic spread (Figure 3.4b), using the method described in Booth et al. (2010, 2011). The GPR velocity in the snow and ice layers was 0.213 +/- 0.0014 m/ns and 0.172 +/- 0.0015 m/ns respectively, with depths to their base of 2.0 +/- 0.07 m and 25.5 +/- 0.22 m respectively. The small relative size of the layer depth uncertainties compared with resolution of surface waves (typically 1-10 metres) supports our choice of fixing the layer depths. The underlying half-space is assumed to be unconsolidated sediment and bedrock. The prior distributions on *Vs* (defining the upper and lower bounds) for each layer were defined as the values listed in Table 3.1, obtained from previous glaciological seismic studies (Peters et al., 2008; Podolskiy et al., 2016; Tsoflias et al., 2008). The shear wave speed *Vs* is narrowly constrained within the snow and ice layers but, given the uncertainty about the subglacial material properties, we permit a large range of *Vs* to encompass soft, wet sediment to hard frozen sediment and bedrock.

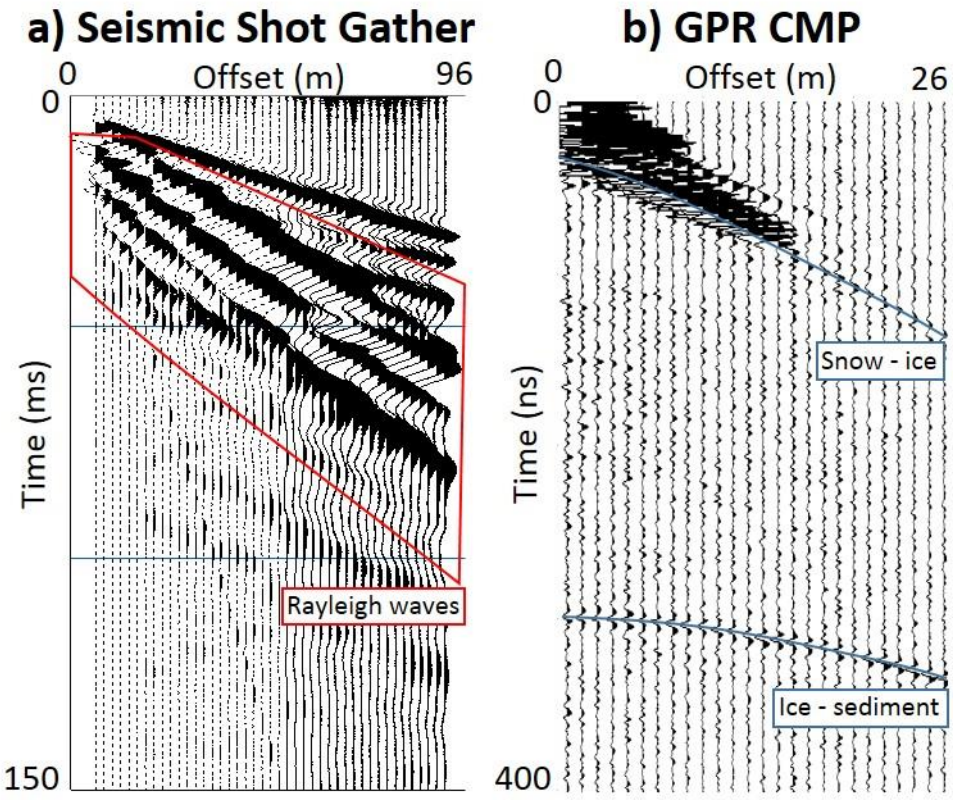

Figure 3.4 a) Seismic shot gather acquired on Midtdalsbreen; the Rayleigh wavetrain is highlighted in the red polygon. b) GPR CMP gather acquired half way along the line. GPR velocities were derived by matching the curvature of diffraction hyperbolae, highlighted in blue, which were used to determine the thickness of snow and ice layers via Dix inversion (Dix, 1955).

Table 3.1 Elastic parameter boundaries (priors) applied in MuLTI for the glaciated case study, adapted from Peters et al., 2008, Podolskiy et al., 2016 and Tsoflias et al., 2008.

Material	**Elastic Property**		
	Density (g/cm^3) Constant	***Vp* (m/s) Constant**	***Vs* (m/s) Variable**
Snow	0.47	2500	500 - 1700
Ice	0.92	3810	1700 - 1950
Subglacial material	2.5	4000	200 - 2800

3.5.2 Synthetic Data Tests

To evaluate the performance of MuLTI, we constructed a synthetic version of our acquired data, but underpinned by a simple known subsurface structure. Figure 3.5a shows our 4-layer model of snow, ice, soft sediment and hard sediment, that plausibly represents our glacial setting.

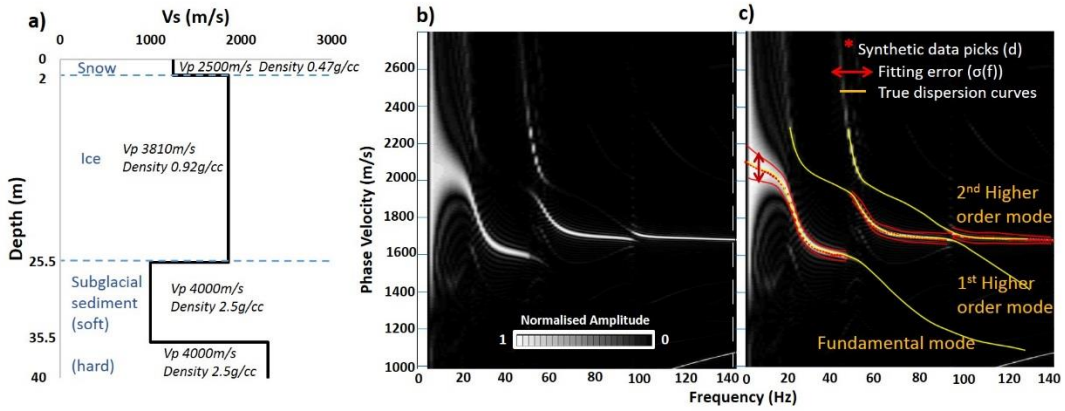

Figure 3.5 a) Synthetic *Vs* model of glaciated environment and (b) its associated Rayleigh wave dispersion curve image created from the Discrete Wavenumber Method (DWM). c) Picked dispersion curve (dotted red lines) with an estimate of the uncertainty $\sigma(f)$ (solid red lines). The yellow lines display the theoretical true dispersion curves for this model, computed using the gpdc algorithm of Wathelet (2005) implemented within MuLTI. *Vp* and density are constant in each layer.

We use the discrete wavenumber method (DWM) (Bouchon & Aki, 1977) to generate a full synthetic waveform dataset, based on the "true model" shown in Figure 3.5a. A dispersion image is calculated from the waveform created by transforming into the frequency-phase velocity domain where the dispersive pattern of the Rayleigh wave can be determined (Figure 3.5b). The maximum amplitudes of the frequency-phase velocity image are picked to create the Rayleigh wave dispersion curve, which is input into MuLTI as the "data" (d) along with an estimate of its width, the uncertainty $\sigma(f)$, Figure 3.5c. For the first two examples (Sections 3.3 and 3.4), the DWM parameters used to calculate the synthetic waveform were chosen to have a long offset and large number of receivers, in order to sample the full wavefield. However in the final synthetic example (section 3.5), we limit the DWM parameters to those used when acquiring the real Norwegian data to see the effect of a reduced dataset.

MuLTI was run with and without GPR constraints applied. With constraints, the bases of snow and ice layers were fixed at respective depths of 2 m and 25.5 m. The maximum number of floating nuclei was set at 30 and the maximum depth, dp_{max}, of the model was set to 40 m. The burn-in chain length was set to 10000. We used

parameter values σ_{change} = 20 m/s, σ_{move} = 1 m and σ_{birth} = 400 m/s, and 1 million iterations (including the burn-in) were found to be enough for convergence of the posterior distribution sampled by the single Markov chain. Convergence was also confirmed by running multiple independent chains with different initial states. To test the Markov chain was sampling correctly, the likelihood was set to unity, effectively removing the data (and rendering equivalent the posterior and prior distributions) and so the Markov chain sampled the known prior distribution against which it was benchmarked. As a preliminary test, we confirmed that MuLTI reproduced the prior distributions with the likelihood set to unity.

3.5.3 The effect of high frequencies on the inversion

We first assess whether or not MuLTI can recover the known subsurface structure from a full frequency spectrum. Figure 3.6 shows the results from MuLTI of the posterior *Vs* distribution with GPR constraints applied and frequency range of 1-140 Hz and 1-100 Hz (band-limiting the high frequencies). Although ostensibly including high frequency (>100 Hz) picks adds extra data, they cause ambiguities in higher order modes associated with these frequencies, where many different models of *Vs* can fit the observed data. This arises because we do not assign any specific mode to each frequency, an unavoidable consequence of poor resolution in real data (see section 3.5). The plethora of complex models that all have a low misfit overwhelms the natural parsimony of the Bayesian method, producing a posterior density that is far from the true model. The probability density distribution of *Vs* values within their 95 % credible interval are plotted as coloured contours alongside the true solution (black line). The highest density distribution (red) for each depth corresponds to the most likely values of *Vs*. These high frequency ambiguities are highlighted in Figure 3.6(I); even though the observed data fit the final solution, the underlying true solution is not recovered. Limiting the high frequency range to 100 Hz (Figure 3.6(II)) mitigates this problem and the true solution is almost exactly recovered (to within ~60 m/s) in this inversion.

3.5.4 Model uncertainties caused by finite bandwidth

As a second test that more closely aligns with the frequency content of real acquired data (e.g. those recorded with 10 Hz geophones), a new synthetic dataset was created with a frequency range of 14-100 Hz, avoiding the high-frequency ambiguities described above. Figure 3.7 displays the posterior *Vs* distribution respectively with and without GPR constraints applied. Figure 3.7(II) shows significant deviation between the true solution and the model ensemble particularly between 0-7 m and 25-35 m depth, without GPR constraints applied. With GPR constraints applied the

results are much improved. The density plot in Figure 3.7(I) shows that MuLTI recovers a distribution that is everywhere peaked close to the true model. This difference in resolution can be quantified by comparing the range of *Vs* values between the lower and upper 95 % credible interval boundaries. Without and with GPR constraints, respectively, this range is 1140 m/s and 618 m/s, on average over the whole depth range. Therefore, including GPR constraints yields a stark decrease in the range of *Vs* (and therefore a reduction of uncertainty) by a factor of about 2. Quantified in a different way, the inversion using GPR constraints has a depth-averaged absolute error between the modal and true values of 62 m/s, about a factor of ten smaller than the comparable error of 540 m/s associated with the inversion without GPR data.

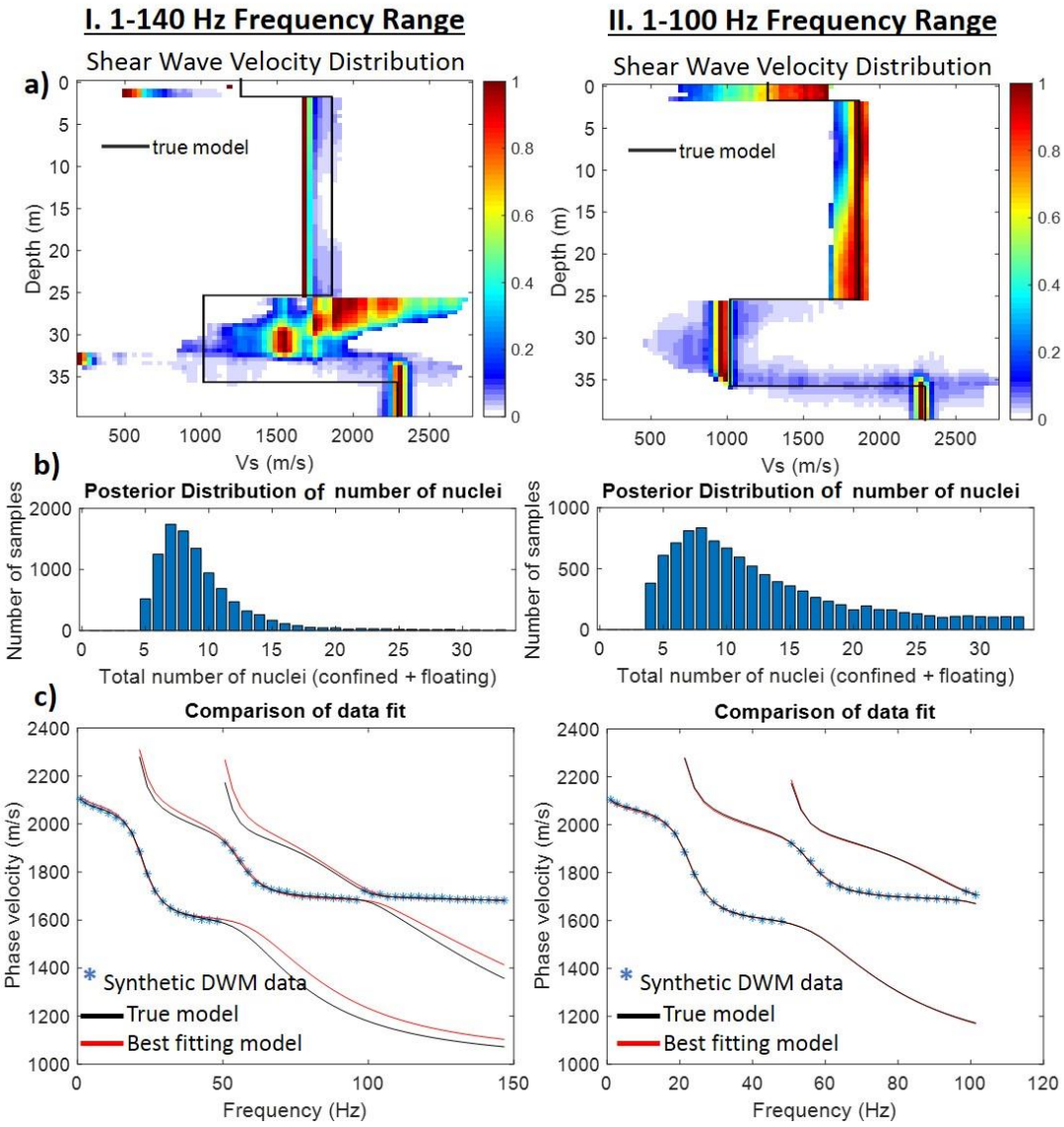

Figure 3.6 GPR-constrained shear wave velocity inversion results from MuLTI with frequency ranges 1-140 Hz (I) and 1-100 Hz (II). a) Posterior distribution of shear wave velocity solution with probability density distribution; coloured values are only shown within the 95% credible intervals, b) posterior distribution on number of nuclei, c) synthetic data and modal dispersion curves of the single ensemble member with the lowest misfit.

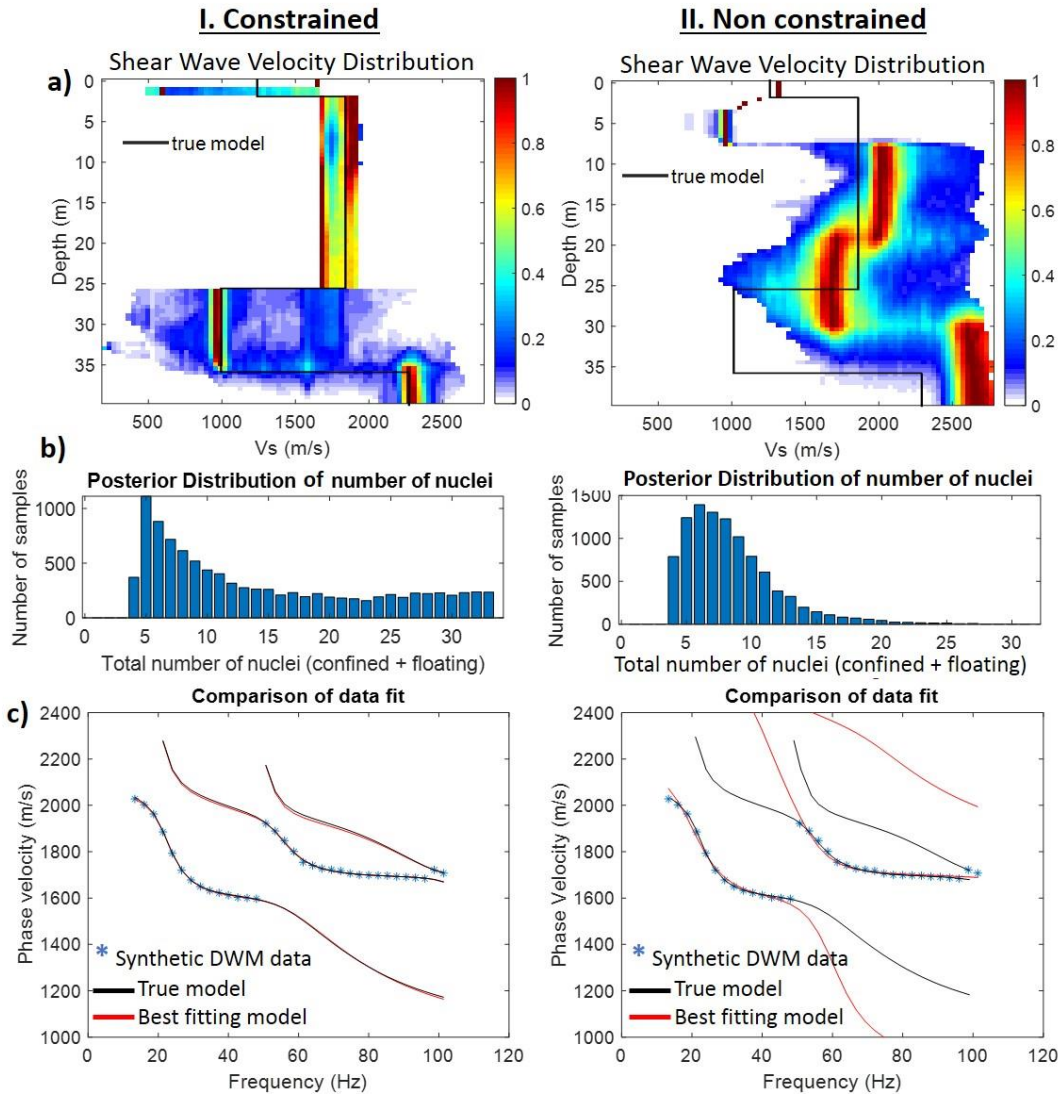

Figure 3.7 Shear wave velocity inversion results from MuLTI with (I) and without (II) GPR constraints applied, with a 14-100 Hz frequency range. a) Posterior distribution of shear wave velocity solution; coloured values are only shown within the 95% credible intervals, b) posterior distribution on number of nuclei, c) synthetic data and modal dispersion curves of the single ensemble member with the lowest misfit.

Here we briefly discuss the uncertainties in the recovered subsurface model which limit resolution at both small and large length scales. At a given frequency, the phase velocity PV specifies the resolvable wavelength λ associated with each datum (Stokoe et al., 1994) as

$$\lambda = \frac{PV(f)}{f}, \tag{3.9}$$

and its associated resolvable scale is $L = \lambda/3$, assuming a 1/3 wavelength resolution criterion (Gazetas, 1982). If the data points are bandlimited in the frequency range, which is the case for most real MASW datasets, this immediately limits the resolvable

scales by an unconstrained inversion to $L_{min} \leq L \leq L_{max}$, where L_{min} is the thinnest resolvable layer and L_{max} is the maximum resolvable depth. However, the addition of independent depth constraints will improve the resolution beyond what is possible with surface waves alone, so in the constrained inversion case these bounds will widen. Because it is not possible to easily quantify these improved resolution bounds in a simple way, in what follows we use L_{min} and L_{max} as illustrative values. For the tests shown in section 3.4, the data points were bandlimited with frequency range 14-100 Hz (Figure 3.7), illustrating the nature of any real dataset. Therefore in this example, L lies in the illustrative range 5 m $\leq L \leq$ 50 m. Which frequencies remain sufficiently clear above the noise level to be picked depends both on survey design: the dispersion curves are better resolved for a longer source-receiver offset, (Park et al., 1998, 2001) and on the specific frequency: lower frequencies have lower resolution and hence a larger error.

Although the final inverted *Vs* solution may contain shallow and layers thinner than L_{min}, the calculated *Vs* values for these layers may be considered unreliable (Park et al., 1999). An illustrative case is our first synthetic example, shown in section 3.3 (Figure 3.6b), where L_{min} = 5 m which is greater than the imposed snow depth (layer 1). The structure within that layer is therefore not well resolved, as shown by the 95% credible intervals that span the majority of the prior range in *Vs*, hence the mismatch between the true and the modal posterior distribution of *Vs* in this layer. Put another way, in the snow layer the data are relatively uninformative and do not constrain the posterior much beyond what is already assumed in the prior. It is worth remarking however that the snow layer depth of 2 m, being less than the nominal resolution limit of 5 m from the surface waves, is well resolved by the additional GPR constraints.

3.5.5 Influence of survey design on MuLTI

In addition to the issues described above, there can also be resolution difficulties at large depths caused by cut-off at long λ (low frequencies), a realistic scenario when using dispersion curves derived from active source seismic data. If the signal to noise ratio is low, the dispersion curve can be difficult to pick out over the noise, and the low frequencies then unavoidably have a higher uncertainty.

We illustrate this effect by creating a final full synthetic waveform dataset, designed to mimic as closely as possible the real data we acquired. As before, this is based on the same "true" model as in section 3.2, using the discrete wavenumber method (DWM) (Bouchon & Aki, 1977). As for the usual processing, dispersion images are calculated from these waveforms created and dispersion curves picked from the images (Figure 3.8b). The DWM parameters used to calculate the synthetic waveform

were chosen to be equal to the parameters used when acquiring our Norwegian data: 48 geophones with 2m spacing. The maximum amplitudes of the frequency-phase velocity image are picked to create the Rayleigh wave dispersion curve. It is especially noteworthy that the picked dispersion curve no longer overlies the true modal lines (as for the examples in sections 3.3, 3.4), due to the restriction to realistic survey parameters. In this synthetic example the lowest resolvable frequencies are limited to 14 Hz, where the dispersion curve becomes very wide (with large uncertainty) with no clear maxima to pick below this frequency (see Figure 3.8b). From this picked dispersion curve L_{min} is 5 m and the maximum resolvable length scale L_{max} (i.e. the maximum resolvable depth) is 49 m. The Rayleigh wave dispersion curve picked from the DWM generated synthetic waveform, along with an estimate of its width, were used as the data d and uncertainty $\sigma(f)$ (section 2.3) in MuLTI. It is also noteworthy that the poor resolution of Figure 3.8(b) makes it difficult to uniquely identify the 1st and 2nd order modes, motivating our methodological choice of defining a likelihood based on the nearest modal value.

With GPR constraints applied and using the same parameters as before, Figure 3.8b shows this DWM synthetic inversion. Within the resolvable depth interval, there is a high probability of the posterior *Vs* model (highlighted in red in the *Vs* plot) being very close to the true model. The *Vs* distribution scatter is however larger than the previous synthetic examples, due to the larger uncertainty caused by weak sensitivities of the observations to structures at 25 m depth, itself a result of the survey parameters used in this DWM synthetic. This example demonstrates MuLTI works well with dispersion curves picked from synthetic waveform data simulating a MASW dataset, within the data's resolvable depths, and accurately reflects the sensitivities of the observations.

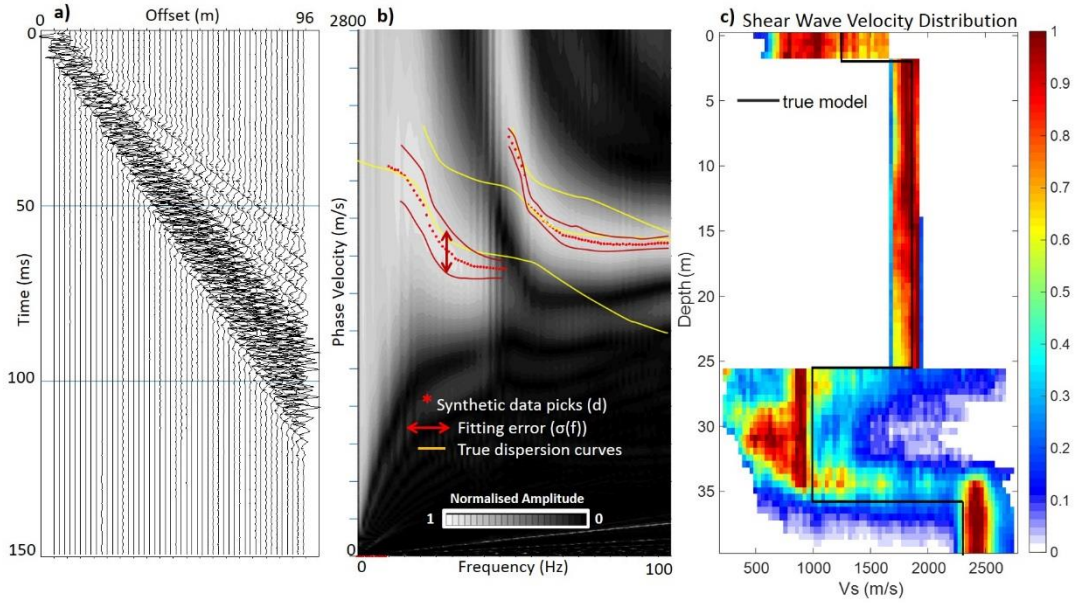

Figure 3.8 a) Synthetic wavefield created from the Discrete Wavenumber Method (DWM) of the simulated glacier model (Figure 5a). b) Corresponding dispersion image, used to pick the surface wave dispersion curve. Dotted red lines indicate the picked dispersion curve with the solid red lines showing an estimate of the uncertainty $\sigma(f)$. c) MuLTI inversion results with GPR constraints applied, showing the posterior distribution of *Vs*.

3.5.6 Application to the Midtdalsbreen dataset

Figure 3.9a shows the dispersion curve corresponding to the seismic data in Figure 3.4a, acquired on the glacier Midtdalsbreen. The dispersion curve from Figure 3.8b (derived from a synthetic model with a low velocity layer) and Figure 3.9a are visually comparable, suggesting that a low velocity zone under the glacier is plausible. From the picked dispersion curve, Equation 3.9 suggests that the thinnest resolvable layer (L_{min}) in this real dataset is 5 m, and the maximum resolvable depth (L_{max}) is 48 m. As elsewhere in this paper, we assumed 3D effects were negligible: there were no surface objects on the glacier front and we modelled the subsurface as laterally homogeneous.

The same MuLTI inversion parameters were used for this real data example as the previous synthetic examples, and results are shown in Figures 3.9b, 3.9c and 3.9d. The modal *Vs* within the ice layer is shown to be at the low end of the prior distribution, around 1700 m/s. A low velocity zone is identified directly below the glacier (at 25 m depth), roughly 7 m thick, which could be due to unfrozen wet subglacial sediment. The high *Vs* zone at 32-40 m depth could be the hard bedrock boundary, underlying the sediment layer.

Lastly, Figure 3.9(d) shows a comparison of the best-fitting model to the dataset, following comparable plots in previous sections. Although illustrative of data-fitting,

it is possible that this end-member model, which is consistent with the prior, nevertheless shows some extreme physical properties. Figure 3.9(d) shows an increase with frequency of one of the modal velocity curves, whereas it might be expected that all such curves decrease with frequency. Physically, the best-fit model is largely comparable to the modal model of Figure 3.9(b) with the exception of a rapid adjustment at 35 m depth to a low-velocity half space (of about 700 m/s), which is consistent with the prior but physically unexpected and rather exotic.

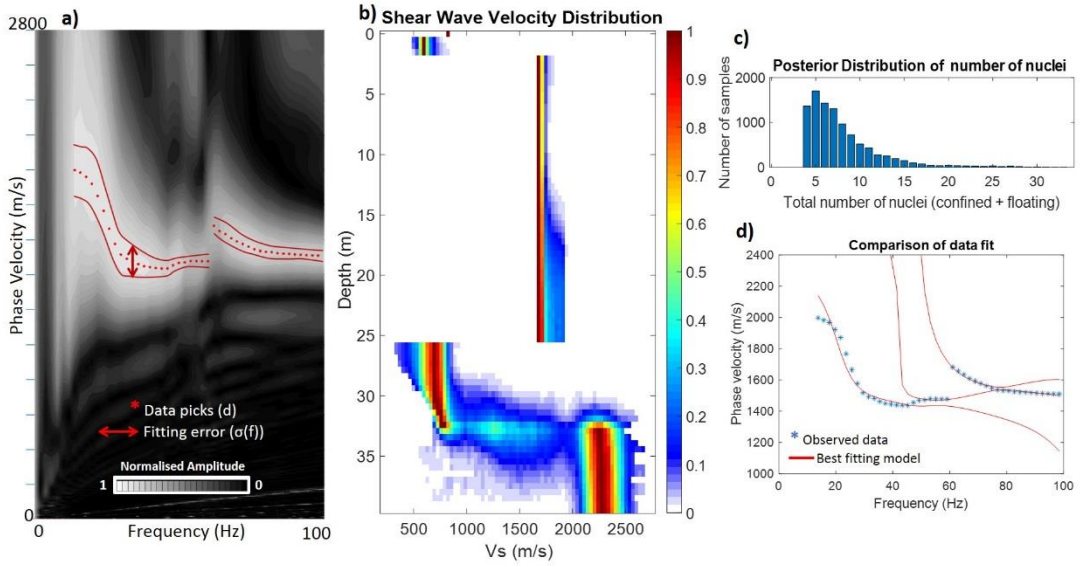

Figure 3.9 a) Calculated surface wave dispersion image from Mitdalsbreen shot gather (Figure 4a) with associated picks (*d*) and uncertainty *σ(f)*. b) Posterior distribution of shear wave velocity solution; coloured values are shown only within the 95% credible intervals. c) Posterior distribution on number of nuclei. d) Observed data and dispersion curves of the single ensemble member which has the lowest misfit.

3.6 Discussion and Conclusions

Many techniques have been recently established utilising Rayleigh wave dispersion curves to infer the seismic structure of the subsurface. However recurring problems in the inversion of Rayleigh wave dispersion curves are: poor depth sensitivity, low resolution and ambiguous, non-unique solutions. Here we have presented MuLTI (Multimodal Layered Transdimensional Inversion), a novel tool for the inversion of Rayleigh wave dispersion curves with additional depth constraints drawn from any external data source.

MuLTI implements a Bayesian formulation using a Markov chain Monte Carlo approach to explore the dependence of *Vs* with depth, and rests on the assumption that subsurface interfaces correspond to co-located contrasts in both elastic and

electromagnetic properties. It uses a new methodology to restrict the space of admissible subsurface models that are compatible with the observed Rayleigh wave data by adding fixed depth constraints, here using a GPR-derived layered structure. The uncertainty in the depth constraints applied is negligible (cm-accuracy) compared to the dispersion curve uncertainty (of m-accuracy), motivating us to fix the internal interface depths. The constraining layered structure is implemented by narrowing the *Vs* bounds for each material layer defined from the GPR, however *Vs* variability within each layer is still permissible.

The Bayesian formulation within MuLTI is employed to produce a variety of diagnostic statistics of the ensemble used to assess the reliability of the solution for interpretation. The multiple different outputs available enables a variety of marginal posterior distributions to be examined, for example, the most likely *Vs* solution along with its uncertainty range, and the distribution of the number of nuclei. A potential criticism of our methodology is that we only invert for S-wave velocity while holding *Vp* and density constant throughout the velocity model. By deriving material-layer boundaries we are able to fix the *Vp* and density appropriately in each layer according to the material expected. This is an improvement from models that have no defined layers with *Vp* and density fixed as constants throughout the model space (Hayashi, 2012). However a development of the algorithm would be, at increased computational cost, to also consider resolving *Vp* and density in each layer.

Using synthetic tests based on a glaciological snow-ice-sediment layered setting, we showed that the depth constrained inversion gives a marked improvement in accuracy (decreasing the absolute error between the best fitting and true model by a factor of 10) and depth resolution compared to inverting Rayleigh wave data in isolation. Based on the difference between the upper and lower 95% credible interval limits, the posterior distribution of *Vs* in the constrained inversion compared to the non-constrained inversion is 2 times better resolved within the glaciological subsurface. We also demonstrate that including high frequency data (>100 Hz) causes ambiguities in the higher order modes associated with spatially fine scale structure, which overwhelms the natural parsimony of the Bayesian methods, producing solutions that are far from the true model. Therefore, it is important to take caution if using frequencies >100 Hz in any multimodal Rayleigh wave dispersion curve inversion.

We present a real data application of MuLTI to a glaciated field site in Norway. However MuLTI is applicable to any layered subsurface provided depth constraints and elastic property changes are co-located at the same depths.

3.7 Code availability

MuLTI can be found at: https://github.com/eespr/MuLTI, DOI 10.5281/zenodo.1489959

3.8 Acknowledgments

The *MuLTI* algorithm including all data and examples presented in this paper can be found at: https://github.com/eespr/MuLTI, DOI 10.5281/zenodo.1489959. This project is funded by the UK NERC SPHERES DTP, grant NE/L002574/1. Richard Rigby at the University of Leeds is thanked for creating the gpdc mex file enabling this code to be run in Matlab and all his extra computing and IT support. GPR equipment was generously provided by Jostein Bakke (University of Bergen). Fieldwork was part-funded by the EVOGLAC project (University of Bergen, University of Oslo), and greatly assisted by the support and local expertise of Atle Nesje and Kjell Magne Tangen. Thomas Bodin is thanked for his advice on MCMC methods and for providing Matlab code. We also thank two anomymous referees for their constructive comments which helped improve the manuscript.

3.9 References

Bodin, T., & Sambridge, M. (2009). Seismic tomography with the reversible jump algorithm. *Geophysical Journal International*, *178*(3), 1411-1436.

Bodin, T., Sambridge, M., Tkalčić, H., Arroucau, P., Gallagher, K., & Rawlinson, N. (2012). Transdimensional inversion of receiver functions and surface wave dispersion. *Journal of Geophysical Research: Solid Earth*, *117*(B2).

Booth, A. D., Clark, R. A., & Murray, T. (2010). Semblance response to a GPR wavelet and resulting errors in velocity analysis. *Near Surface Geophysics*, *8*, 235-246.

Booth, A.D., Clark, R.A., & Murray, T. (2011). Influences on the resolution of GPR velocity analyses and a Monte Carlo simulation for establishing velocity precision. *Near Surface Geophysics*, *9*(5), 399-411.

Bouchon, M., & Aki, K. (1977). Discrete wave-number representation of seismic-source wave fields. *Bulletin of the Seismological Society of America*, *67*(2), 259-277.

Cardimona, S. J., Clement, W. P., & Kadinsky-Cade, K. (1998). Seismic reflection and ground-penetrating radar imaging of a shallow aquifer. *Geophysics*, *63*(4), 1310-1317.

Colombo, D., McNeice, G., Rovetta, D., Turkoglu, E., Sandoval-Curiel, E., & Sena, A. (2017, March). Seismic-Airborne TEM Joint Inversion and Surface Consistent Refraction Analysis: New Technologies for Complex Near Surface Corrections. In *SPE Middle East Oil & Gas Show and Conference*. Society of Petroleum Engineers.

Dettmer, J., Dosso, S. E., & Holland, C. W. (2010). Trans-dimensional geoacoustic inversion. *The Journal of the Acoustical Society of America*, *128*(6), 3393-3405.

Dix., C.H. (1955). Seismic velocities from surface measurements. *Geophysics*, 20, 68-86.

Dou, S., & Ajo-Franklin, J. B. (2014). Full-wavefield inversion of surface waves for mapping embedded low-velocity zones in permafrost. *Geophysics*, *79*(6), EN107-EN124.

Foti, S., Comina, C., Boiero, D., & Socco, L. V. (2009). Non-uniqueness in surface-wave inversion and consequences on seismic site response analyses. *Soil Dynamics and Earthquake Engineering*, *29*(6), 982–993. http://doi.org/10.1016/j.soildyn.2008.11.004.

Foti, S., Cox, B. R., Garofalo, F., Hollender, F., Bard, P. Y., Cornou, C., ... & Sicilia, D. (2015, November). Uncertainties in *VS* profiles from geophysical tests and their influence on seismic ground response analyses: results from the InterPACIFIC blind Test. In *6th International Conference on Earthquake Geotechnical Engineering, Christchurch, New-Zealand*.

Gallagher, K., Bodin, T., Sambridge, M., Weiss, D., Kylander, M., & Large, D. (2011). Inference of abrupt changes in noisy geochemical records using transdimensional changepoint models. *Earth and Planetary Science Letters*, 311(1-2), 182-194.

Gazetas, G. (1982). Vibrational characteristics of soil deposits with variable wave velocity. *International journal for numerical and analytical methods in Geomechanics*, *6*(1), 1-20.

Gucunski, N., & Woods, R. D. (1992). Numerical simulation of the SASW test. *Soil Dynamics and Earthquake Engineering*, *11*(4), 213-227.

Hayashi, K. (2012). Analysis of surface-wave data including higher modes using the genetic algorithm. In *GeoCongress 2012: State of the Art and Practice in Geotechnical Engineering* (pp. 2776-2785).

Hering, A., Misiek, R., Gyulai, A., Ormos, T., Dobróka, M., & Dresen, L. (1995). A joint inversion algorithm to process geoelectric and sutface wave seismic data. Part I: basic ideas. *Geophysical Prospecting*, *43*(2), 135-156.

Hoversten, G. M., Cassassuce, F., Gasperikova, E., Newman, G. A., Chen, J., Rubin, Y., Hou, Z., et al. (2006). Direct reservoir parameter estimation using joint inversion of marine seismic AVA and CSEM data. *Geophysics*, 71(3), C1–C13. https://doi.org/10.1190/1.2194510

Julià, J., Ammon, C. J., Herrmann, R. B., & Correig, A. M. (2000). Joint inversion of receiver function and surface wave dispersion observations. *Geophysical Journal International*, *143*(1), 99-112.

Kneisel, C., Hauck, C., Fortier, R., & Moorman, B. (2008). Advances in geophysical methods for permafrost investigations. *Permafrost and Periglacial Processes*, *19*(2), 157-178.

Livermore, P.W., Fournier, A., Gallet, Y. and Bodin, T. (2018) Transdimensional inference of archeomagnetic intensity change. *Geophysical Journal International* 215(3), 2008-2034. Doi 10.1093/gji/ggy383

MacKay, D. J. (2003). *Information theory, inference and learning algorithms*. Cambridge university press.

Maraschini, M., & Foti, S. (2010). A Monte Carlo multimodal inversion of surface waves. *Geophysical Journal International*, *182*(3), 1557-1566.

Park, C. B., Miller, R. D., & Xia, J. (1998). Imaging dispersion curves of surface waves on multi-channel record. In *1998 SEG Annual Meeting*. Society of Exploration Geophysicists.

Park, C. B., Miller, R. D., & Xia, J. (1999). Multichannel analysis of surface waves. *Geophysics*, *64*(3), 800-808.

Park, C. B., Miller, R. D., & Xia, J. (2001). Offset and resolution of dispersion curve in multichannel analysis of surface waves (MASW). In *Proceedings of the SAGEEP*.

Peters, L. E., Anandakrishnan, S., Holland, C. W., Horgan, H. J., Blankenship, D. D., & Voigt, D. E. (2008). Seismic detection of a subglacial lake near the South Pole, Antarctica. *Geophysical Research Letters*, *35*(23).Podolskiy, E. A., & Walter, F. (2016). Cryoseismology. *Reviews of Geophysics*, *54*(4), 708-758.

Richart, F. E., Hall, J. R., & Woods, R. D. (1970). Vibrations of soils and foundations. International Series in Theoretical and Applied Mechanics.

Ronczka, M., Wisén, R., & Dahlin, T. (2018). Geophysical pre-investigation for a Stockholm tunnel project: joint inversion and interpretation of geoelectric and seismic refraction data in an urban environment. *Near Surface Geophysics*, *16*(3), 258-268.

Shen, W., Ritzwoller, M. H., Schulte-Pelkum, V., & Lin, F. C. (2012). Joint inversion of surface wave dispersion and receiver functions: A Bayesian Monte-Carlo approach. *Geophysical Journal International*, *192*(2), 807-836.

Stokoe, K. H., II, Wright, G. W, James, A. B., & Jose, M. R. (1994). Characterization of geotechnical sites by SASW method. *Woods, R. D., Ed., Geophysical characterization of sites: Oxford Publ.*

Tsuji, T., Johansen, T. A., Ruud, B. O., Ikeda, T., & Matsuoka, T. (2012). Surface-wave analysis for identifying unfrozen zones in subglacial sediments. *Geophysics*, *77*(3), EN17-EN27.

Tsoflias, G. P., Ivanov, J., Anandakrishnan, S., & Miller, R. (2008). Use of active source seismic surface waves in glaciology. *21st EEGS Symposium on the Application of Geophysics to Engineering and Environmental Problems*.

Wathelet, M. (2005). Array recordings of ambient vibrations: surface-wave inversion. *PhD Diss., Liége University*, *161*.

Wisén, R., & Christiansen, A. V. (2005). Laterally and mutually constrained inversion of surface wave seismic data and resistivity data. *Journal of Environmental and Engineering Geophysics*, *10*(3), 251-262.

Xia, J., Miller, R. D., & Park, C. B. (1999). Estimation of near-surface shear-wave velocity by inversion of Rayleigh waves. *Geophysics*, *64*(3), 691-700.

Xia, J., Miller, R. D., Park, C. B., & Tian, G. (2003). Inversion of high frequency surface waves with fundamental and higher modes. *Journal of Applied Geophysics*, *52*(1), 45-57.

Chapter 4 Subglacial sediment distribution from constrained seismic inversion, using MuLTI software: Examples from Midtdalsbreen, Norway

S. F. Killingbeck[1], A. D. Booth[1], P. W. Livermore[1], L. J. West[1], B.T.I. Reinardy[2] and A. Nesje[3]

[1]School of Earth and Environment, University of Leeds

[2]Department of Physical Geography, Stockholm University and Bolin Centre for Climate Research, Stockholm

[3]Department of Earth Science, University of Bergen

Corresponding author: Siobhan Killingbeck (eespr@leeds.ac.uk)

Published in Annals of Glaciology, doi: doi.org/10.1017/aog.2019.13

4.1 Abstract

Fast ice flow is associated with the deformation of subglacial sediment. Seismic shear velocities, *Vs*, increase with the rigidity of a material and hence can be used to distinguish soft sediment from hard bedrock substrates. Depth profiles of *Vs* can be obtained from inversions of Rayleigh wave dispersion curves, from passive or active-sources, but these can be highly ambiguous and lack depth sensitivity. Our novel Bayesian transdimensional algorithm, MuLTI, circumvents these issues by adding independent depth constraints to the inversion, also allowing comprehensive uncertainty analysis. We apply MuLTI to the inversion of a Rayleigh wave dataset, acquired using active-source (MASW) techniques, to characterise sediment distribution beneath the frontal margin of Midtdalsbreen, an outlet of Norway's Hardangerjøkulen ice cap. Ice thickness (0-20 m) is constrained using co-located GPR data. Outputs from MuLTI suggest that partly-frozen sediment (*Vs* 500-1000 m/s), overlying bedrock (*Vs* 2000-2500 m/s), is present in patches with a thickness of ~4 m, although this approaches the resolvable limit of our Rayleigh wave frequencies (14-100 Hz). Uncertainties immediately beneath the glacier bed are <280 m/s, implying that MuLTI can not only distinguish bedrock and sediment substrates but does so with an accuracy sufficient for resolving variations in sediment properties.

4.2 Introduction

The subglacial environment exerts a substantial control on the flow dynamics of glaciers and ice masses (Bell, 2008; Siegert et al., 2018). A major uncertainty in ice dynamic models is the limited understanding of processes at the ice/bed interface and the composition of subglacial material. A significant control on ice motion is whether ice is underlain by hard or soft substrate, and therefore whether motion is governed by ice/sediment deformation (Hofstede et al., 2018) or sliding (Stearns and van der Veen, 2018). Such compositional variations are typically parameterised in predictive models by assuming a frictional stress coefficient (Christoffersen et al., 2014; Åkesson et al., 2017), although recent work by Stearns and Van der Veen (2018) highlights the potentially greater influence of effective basal pressure. Where underlain by sediment, the hydrological properties of the subglacial environment therefore have a profound effect on glacial flow and require proper consideration in ice dynamic modelling (Kulessa et al., 2017; Siegert et al., 2018).

Quantitative geophysical analysis of subglacial material is typically not straightforward: although many geophysical methods can assess the mechanical properties of glaciers and ice masses, they can be problematic for characterising

material much beyond the immediate vicinity (~2 m) of the glacier bed (Booth et al., 2012). Seismic reflection methods often lack the resolution or signal-to-noise ratio for quantifying subglacial material properties and, for example, may be limited to amplitude-versus-offset (AVO) studies of basal reflectivity (e.g., Anandakrishnan, 2003; Booth et al., 2012; Kulessa et al., 2017). Seismic refraction methods are limited by their low depth penetration into subglacial material (e.g., Thiel and Ostenso, 1961; Bentley and Kohnen, 1976; King and Jarvis, 2007); refraction interpretations are impeded since an ice-sediment interface typically represents a velocity reduction, hence critical refraction will not occur and a head-wave will not be generated. Ground penetrating radar (GPR) methods are well suited to characterising englacial properties (e.g., Murray et al., 2007; Young Kim et al., 2010; Booth et al., 2013; Lindbäck et al., 2018), but glacier bed reflectivity and high attenuation within the ice column limits the utility of subglacial radar sampling.

Dispersion curve analysis of surface (Rayleigh) waves presents an alternative method for characterising seismic properties of basal material, for both passive- or active-sources, by constraining the variation of shear wave velocity (*Vs*) with depth (Xia et al., 2003). Rayleigh waves are a form of seismic wave that travel along the ground surface, termed 'groundroll' in reflection seismology and although often considered as noise, they contain roughly 2/3 of the total energy of a typical surface source (Richart et al., 1970). In passive seismology, Picotti et al. (2017) used the horizontal-to-vertical spectral ratio (H*VS*R) technique to map glacier and ice sheet thicknesses and, in certain conditions, obtain reliable estimates of the basal seismic properties. Preiswerk and Walter (2018) used high frequency (>2 Hz) ambient seismic noise, collected on alpine glaciers, to estimate ice thickness and infer potential bed properties. These techniques are analogous to those used to determine the properties of the Earth's deep interior (Shen et al., 2018). Within active seismology, the use of Rayleigh wave dispersion curves is termed 'Multichannel Analysis of Surface Waves' (MASW).

Regardless of the source of the dispersion curve, characterising *Vs* offers a promising means of distinguishing material within the subglacial environment, since shear wave properties vary with rigidity (shear modulus). Various researchers have used *Vs* to distinguish between hard and soft glacier substrates (Picotti et al., 2015), or the boundary between frozen and unfrozen zones within sediment (Tsuji et al., 2012). Zimmerman and King (1986) showed that seismic velocities vary significantly with degree of pore-fluid freezing, with *Vs* increasing by as much as 90% as pore water freezes (Johansen et al., 2003). Current applications of MASW methods within cryosphere studies include: identifying velocity (*Vs*) and density structure within firn

(Armstrong, 2009; Diez et al., 2014), identifying velocity (*Vs*) structure within shallow ice (Tsoflias et al., 2008b; Young Kim et al., 2010), monitoring and mapping embedded low *Vs* zones in permafrost areas (Dou and Ajo-Franklin, 2014) and identifying unfrozen zones in subglacial sediments (Tsuji et al., 2012).

However, *Vs* depth profiles obtained from MASW suffer from poor depth resolution (Foti et al., 2015). Even for the active-source case, using frequencies that are typically higher than for passive seismology, vertical resolution can be limited to ~10 m. Indeed, at a fundamental level, the inversion of dispersion curves is also non-unique: many profiles of *Vs* (spanning a disparate set of physical structures) may be consistent with the observed data within the error tolerance. These limitations can be mitigated by constraining the MASW inversion using independent and complementary information, in our case the high resolution determination of internal horizons using co-located GPR surveys, which vastly reduces the space of acceptable models with an associated marked increase in vertical resolution. Key to this method is that the relevant subsurface horizons (e.g., the snow-ice surface and the glacier bed) represent contrasts in both electromagnetic and elastic properties.

A recently developed method for depth-constrained MASW inversion, MuLTI (Multimodal Layered Transdimensional Inversion; Killingbeck et al., 2018) is applied in this paper to characterise the subglacial environment. We invert surface wave dispersion curves to evaluate the variation of *Vs* with depth, and assess its accuracy and uncertainty. Following a synthetic study, we analyse a combined MASW-GPR dataset acquired using an active source on Midtdalsbreen, an outlet glacier of Norway's Hardangerjøkulen ice cap. Although applied here to active-source data, the seismic data enters MuLTI only through a dispersion curve, implying that MuLTI is equally valuable as a tool for passive-source seismology with associated depth constraints (which can be from any independent source: for example, airborne radar or borehole control). Thus, MuLTI is a novel methodology for investigating the subglacial environment for a range of glacier settings and seismic data types.

4.3 Method

4.3.1 Multichannel analysis of surface waves

MASW surveys use an array of geophones in-line with an active seismic source located on the ground surface, similar to the acquisition performed for a 2D seismic reflection survey. The original field records, in the time-space domain, are transformed into the frequency-wavenumber domain, where the dispersive pattern of the Rayleigh waves can be determined by picking the spectral maximum (Park et al., 1998).

The above process requires the following detailed steps. Dispersion curves are calculated from the seismic data using common midpoint cross-correlation (CMPCC) gathers (Hayashi and Suzuki, 2004) and the MASW method introduced by Park et al. (1999). CMPCC gathers are created by cross-correlating every pair of traces in each shot gather before sorting into CMP gathers. In each CMP gather, the equally spaced traces were stacked in the time domain to yield CMPCC gathers. To image dispersion curves in the phase velocity-frequency domain, phases of the cross-correlated data were shifted and stacked in the frequency domain, as described in Park et al. (1999).

The dispersion curve depends upon the near-surface elastic properties (compressional wave velocity (*Vp*), *Vs* and density), assumed horizontally homogeneous beneath the geophone spread, although with the strongest sensitivity to *Vs* (Xia et al., 2003). The frequency range over which phase velocity is considered reliable corresponds to the minimum and maximum wavelengths recorded. For any given frequency (f), the wavelength (λ) is specified as

$$\lambda = \frac{PV(f)}{f} \tag{4.1}$$

where *PV* is the phase velocity of any frequency component (Stokoe et al., 1994). The resolvable scale of a given frequency component, L, is approximately $\lambda/3$ (Gazetas, 1982), implying that the finite bandwidth f_{min} to f_{max} is associated with a range of resolution from $L_{max} \geq L \geq L_{min}$, where L_{min} is the thinnest resolvable layer and L_{max} is the maximum resolvable depth. This maximum depth is considered conservative, as other researchers (e.g., Park et al., 1999; Tsuji et al., 2012) base this estimate on a $\lambda/2$ approximation. However, MuLTI incorporates additional independent depth constraints (elaborated in the next section) which widen these bounds and improves the resolution beyond what is possible with surface waves alone (Killingbeck et al., 2018). The useful bandwidth of the survey depends on the signal-to-noise ratio in the dataset, the frequency output of the source, and the length of the survey line. A long survey line is favourable for long wavelengths and hence large L_{max}, but this risks invalidating the assumption of horizontal homogeneity; furthermore, lateral resolution is governed by the range of offsets in each CMPCC gather, hence longer offsets imply greater smearing of horizontal structure (Park, 2005). However, the resolution of dispersion curves improves as the ratio of wavelength to source-receiver offset increases; hence, for any fixed geophone spread, the low frequencies have a poorer resolution in the dispersion image and their interpretation is less precise (Park et al., 2001).

In layered media, inversion for subsurface structure is complicated by the fact that the observed dispersion curve is the combined effect of the different modes of

propagation (Foti et al., 2015), ultimately filtered by the physical survey itself which depends upon the survey design parameters. To ensure a good fit, models need to account for not only the fundamental mode (Park et al., 1999) but all its higher-order harmonics, referred to as 'modes' of propagation. Early models of surface wave inversion only considered the fundamental mode with simple near surface environments (Xia et al., 1999). However, higher order modes have shown to dominate in several types of velocity structures, for example when a high velocity layer overlays a low velocity layer (Gucunski and Woods, 1992). Therefore multimodal analysis of surface waves is important when anticipating these complex velocity profiles. Our MuLTI algorithm is compatible with such multimodal inversions.

4.3.2 MuLTI

MuLTI is a Bayesian inversion method that seeks to determine the posterior distribution of *Vs*, as a function of depth, for a prescribed profile of *Vp* and density, which is fully described in Killingbeck et al. (2018). The method does not require the number of subsurface layers to be fixed but rather, in a 'transdimensional' framework, allows the data to self-determine the required complexity of the distribution (e.g., Bodin and Sambridge, 2009; Bodin et al., 2012; Livermore et al., 2018). Its particular utility here is the ability to include subsurface depth constraints, mitigating poor resolution and non-uniqueness of inversions from surface wave dispersion curves alone.

MuLTI is initiated with frequency-phase velocity picks of Rayleigh wave dispersion curves, together with a measure of their uncertainty derived from the half width of the dispersion curve, accounting for the resolution of the dispersion curve acquired. This depends on the survey parameters used to acquire the seismic data e.g., a higher density of wavefield sampling, i.e. more receivers and longer source-receiver offset, produces better resolved dispersion curves with a smaller half-width and hence smaller uncertainty. The depth constraints determined here from GPR data fix particular layer boundaries in the inversion, a self-consistent procedure as the GPR-derived depths are accurate to the decimeter scale: about a factor of 100 more accurate than the sensitivity of the Rayleigh waves.

Figure 4.1 illustrates MuLTI's model geometry, and shows schematic differences between the unconstrained (Figure 4.1a) and depth-constrained (Figure 4.1b) cases. If no depth constraints of the subsurface interfaces are available, the unconstrained substructure is characterized (before the introduction of seismic data) by wide bounds on *Vs* (e.g., *Vs* between ~200 to 2800 m/s). However, when using co-located GPR

data, layer boundaries (e.g., snow/ice) can be identified and the constraints on *Vs* can be tightened assuming each layer can be attributed to a known material. For example, in this paper, we assume that the upper two layers within the glacier are snow and ice, each with known depth and assumed *Vs* range (500-1700 m/s for the snow layer and 1700-1950 m/s for the ice layer), thus significantly reducing the model parameter space.

MuLTI uses the Geopsy theoretical modal dispersion curve algorithm of Wathelet et al. (2004), Wathelet (2005) as a forward model to compare any proposed substructure model to the observed data (picked Rayleigh wave dispersion curve). It numerically approximates the posterior distribution by an ensemble of models (a Markov chain), traversing the space of admissible models (shaded boxes shown in Figure 4.1), sampling the models with greater likelihood more often. Provided the ensemble size is large enough, the statistics of the ensemble will converge to those of the underlying posterior distribution. MuLTI produces a variety of diagnostic statistics of the *Vs* ensemble that can be analyzed to quantify uncertainty in the subsurface properties. In our analysis, we mainly use the mode and average *Vs* profiles to visualize our preferred structure, along with the 95% credible interval as an estimate of uncertainty.

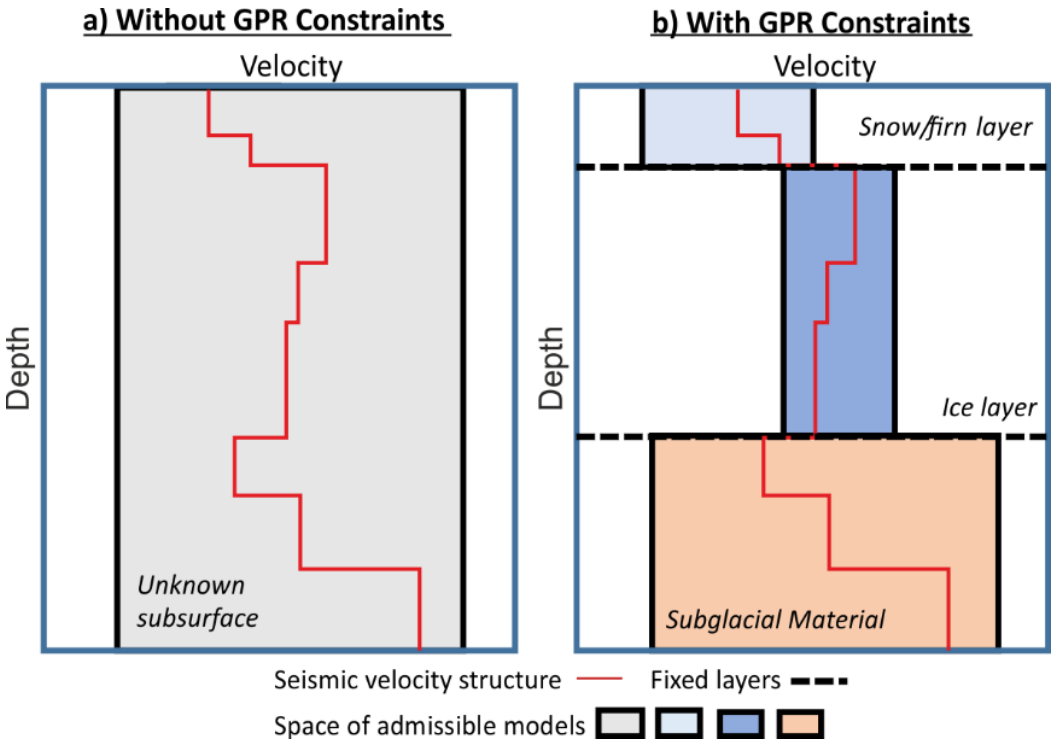

Figure 4.1 Illustration of MuLTI's model parameterisation comparing (a) a 1-layer model with no internal layers and (b) a GPR-determined 3 layer structure assuming different ranges of *Vs* within each layer. Shaded boxes indicate the range of possible *Vs* values. Figure adapted from Killingbeck et al. (2018).

4.4 Field site: Midtdalsbreen

Midtdalsbreen, 6.8 km^2 in area, is a NE-flowing outlet glacier of the Hardangerjøkulen ice cap in central-southern Norway (60.59ºN, 7.52ºE; Figure 4.2). Hardangerjøkulen is Norway's 6th largest glacier (71.28 km^2) (Andreassen and Winsvold 2012) and is an important water source for local river catchments. Annual glacier length measurements performed by A. Nesje between 1982-2018 show that the front of Midtdalsbreen advanced 36 m between 1982-2001, but retreated 219 m between 2001-2018 (e.g., nve.no/hydrologi/bre; Reinardy et al., 2019), thus exposing material recently melted out from beneath the glacier. At the time of acquisition, April-May 2018, the subsurface comprised snow (~2-4 m thick) overlying a varying thickness (0-25 m) of glacier ice, and a substrate of unknown subglacial material. Midtdalsbreen is well-suited to methodological development since it is both logistically accessible and has a simple wedge-shaped profile (Figure 4.3), which is valuable for this study since ice thicknesses show little cross-glacier variation.

Previous GPR data acquisitions show the glacier to have a 40 m wide cold-ice zone within the majority of the glacier tongue, where ice thickness is <10 m (Reinardy et al., 2019). The glacier thickens beyond its tongue, and primarily consists of warm ice within the ablation area surveyed in this study. Midtdalsbreen is surrounded by mountains of phyllite and crystalline granite and gneiss. Little Ice Age marginal moraines (post-1750 CE) on the glacier foreland primarily consist of subglacial traction till with both granite, gneiss and phyllite clasts indicating the glacier has a debris-rich basal ice layer probably underlain by sediments and areas of eroded subglacial bedrock (Reinardy et al., 2013).

Several studies have inferred subglacial erosion, transport and depositional processes at Midtdalsbreen from sedimentological and geomorphological observations made in the foreland (Andersen and Sollid, 1971; Etzelmüller and Hagen, 2005; Reinardy et al., 2013, 2019; Willis et al., 2012). Repeated observations indicate >50 cm thick sequences of highly saturated till, clay to silt-rich deposits linked to ponding meltwater, and comparatively lower volumes of sand/gravel meltwater stream deposits along with highly polished and striated phyllite. Directly in front of the glacier, end moraines and flutes are occasionally ice-cored while some till-covered areas of the foreland may also be underlain by dead-ice (ice disconnected from the glacier). However, the distribution of sediments can be highly variable, in both space and time, given the melting of ice cores and the erosion and reworking of sediment by

meltwater (Reinardy et al., 2013; 2019). The general lower limit of permafrost in this area is estimated to be 1550 m a.s.l., however DC-resistivity soundings at 1450 m a.s.l. and thermistor measurements of cold-ice (<0° C) at the glacier front of Midtdalsbreen indicate permafrost at lower elevations (Etzelmüller et al., 2003).

To explore the subglacial extent of sediment, Willis et al. (2012) investigated the Midtdalsbreen's subglacial drainage system using dye tracing methods. They suggested that the glacier has a split drainage system, with a hydraulically efficient distributed system on the eastern section and an inefficient linked cavity system on the central and western sections. In addition to demonstrating the performance of the MuLTI algorithm, we anticipate that our results will offer additional insight into sediment and ice flow characteristics at the site.

Figure 4.2 a) Location of Hardangerjøkulen ice cap, South Norway. b) Google Earth image of Midtdalsbreen, an outlet glacier of the Hardangerjøkulen ice cap. c) Survey lines acquired during the 2018 field season at the front of Midtdalsbreen. Google Earth satellite images taken in 2013. Note that (b) and (c) are orientated away from north to enable optimal data comparison in later figures.

4.5 Data acquisition

Seismic acquisitions were performed around and over the glacier front (Figure 4.2c) with a Geometrics GEODE system and 48 10 Hz vertical-component geophones. For cross-glacier lines A, B and C, the source and geophone locations had 2 m intervals; for the down-glacier line D, these were increased to 4 m. GPR profiles were acquired along the length of the seismic lines with Sensors & Software PulseEKKO PRO unshielded 200 MHz antennas. Figure 4.3 displays the processed GPR lines and the interpreted position of snow-ice and ice-bed horizons. These horizons are generally well defined and can be picked with confidence, although the signal-to-noise ratio at

the glacier bed is low below the cold-warm transition surface (where the ice is >20 m thick).

The thickness of snow and ice layers was estimated from velocity analysis of GPR common midpoint gathers (CMP) located half way along the seismic spreads B and C (Booth et al., 2011). Figure 4.4 shows CMP gathers B and C with their associated semblance responses, also marking the picked velocities and their corresponding reflection hyperbolae following velocity corrections using the method described in Booth et al. (2010). GPR velocities and their uncertainties are expressed as probability density functions in Figure 4.5, using a Monte Carlo method (Booth et al., 2011). For the snow layer (Figure 4.5b), the CMP analyses yielded a similar median, hence a single average interval velocity (0.2100 ± 0.0029 m/ns) is assumed in depth conversions. For the ice layer (Figure 4.5a), analysis from CMP B and CMP C determines differing velocities by ~6%, possibly related to the greater englacial water content at CMP C and therefore more intense radar scattering at this site. However, the velocity estimate from CMP C (0.1724 ± 0.0015 m/ns) is more consistent with ice from other locations (Murray et al., 2007; Saintenoy et al., 2013; Temminghoff et al., 2018) hence this value is used to evaluate ice thickness. It is noted a more complex 2D velocity model of the ice could be used to determine the ice thicknesses, representative of warm and cold ice, however this uncertainty is small (~1 m) compared to the thinnest resolvable layer of the surface waves (~ 5 m).

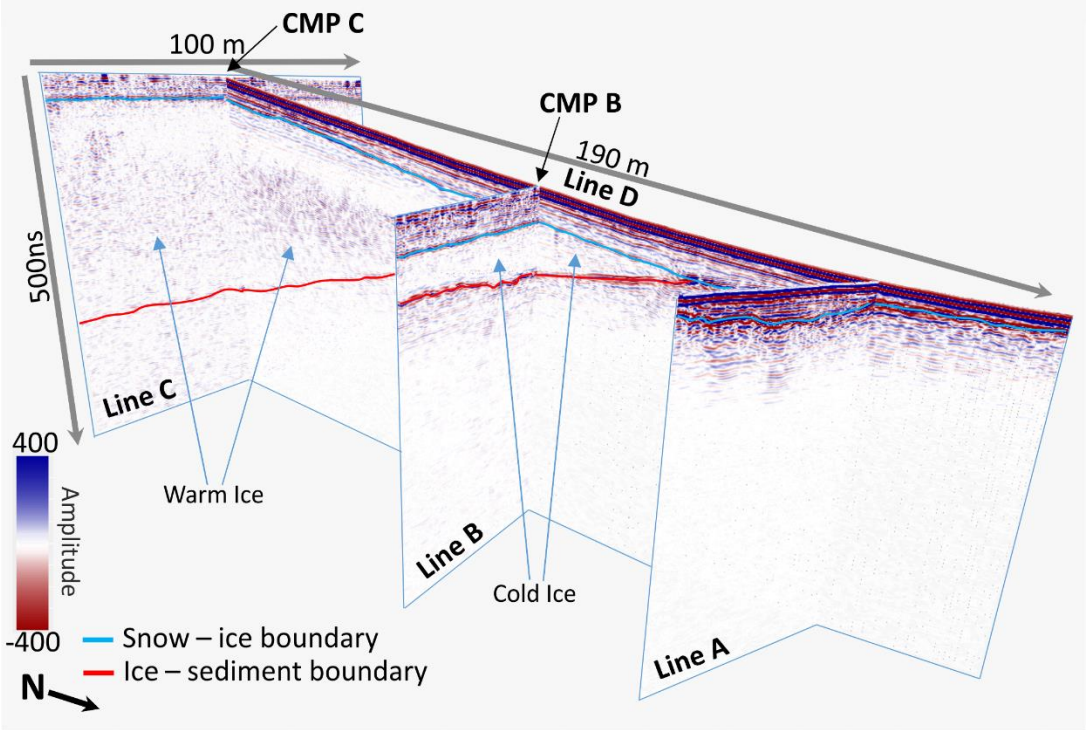

Figure 4.3 GPR lines acquired at the front of Midtdalsbreen directly along the 2D seismic survey lines: A, B, C and D. Snow (blue) and ice (red) horizons were picked in two-way traveltime (TWT).

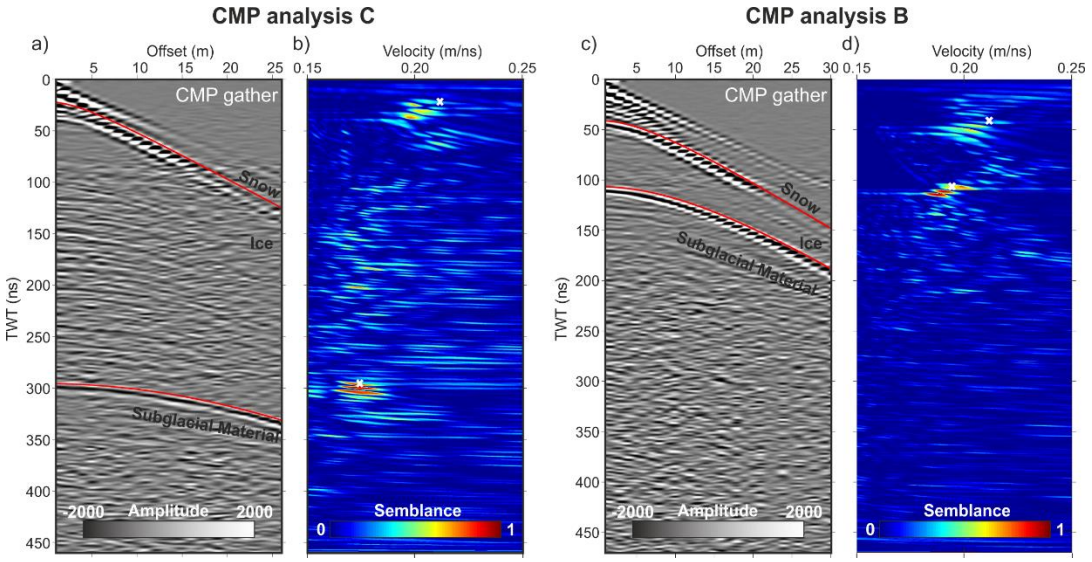

Figure 4.4 GPR CMP gathers acquired at the midpoint of lines B and C with corresponding semblance plots in two-way traveltime (TWT). a) CMP analysis for the midpoint of line C and b) CMP analysis for midpoint of line B. Picked velocities are highlighted by the white 'X' and their corresponding hyperbolae are shown in red (Booth et al., 2010).

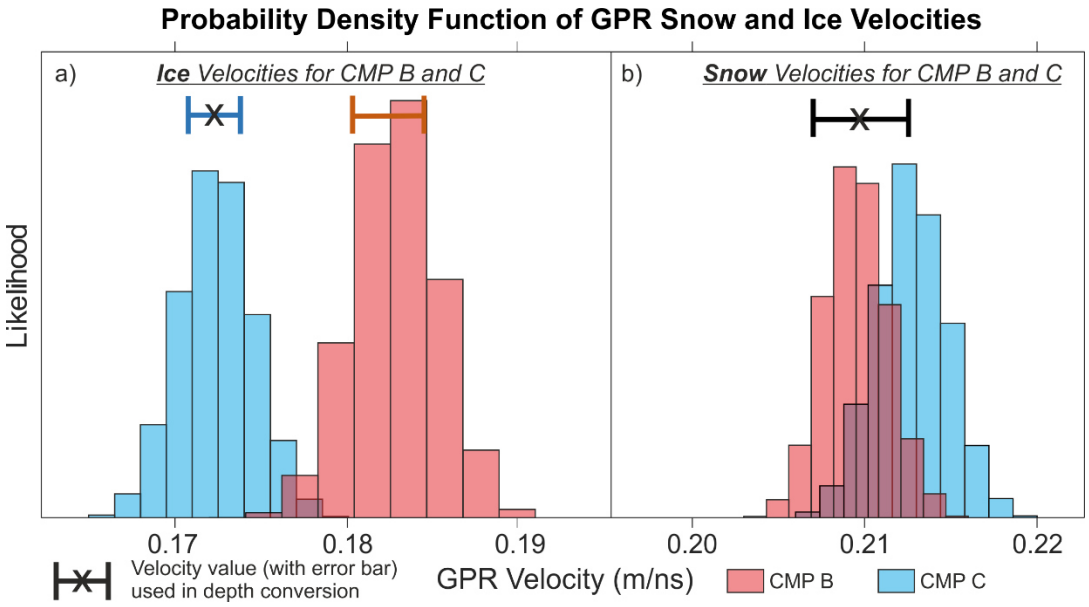

Figure 4.5 GPR velocity precision results, using Booth et al. (2011) Monte Carlo simulation method, displaying probability density functions of a) ice and b) snow GPR velocities derived from CMP B and C.

4.6 Synthetic study

A synthetic study was conducted to validate MuLTI based on a likely target subsurface and to determine inversion parameters for the acquired data. Various 1D-block models, shown in Figure 4.6; a-d (note a-d are unrelated to the seismic lines denoted A-D) were created to represent different glacial and subglacial environments which may be expected at Midtdalsbreen glacier, including: snow, glacier ice, water saturated till (low *Vs* zone) and bedrock. Each layer was populated with *Vp*, *Vs* and density values representative of each layer (Figure 4.6), obtained from example glaciological seismic studies (Peters et al., 2008; Tsoflias et al., 2008a; Podolskiy and Walter, 2016). Inversion parameters are documented in Table A1 in the appendix, and explained fully in Killingbeck et al. (2018).

Synthetic waveforms were calculated from the 1D block models using the Discrete Wavenumber Method (DWM) (Bouchon and Aki, 1977). This calculates the full waveform, which can be considered an analogue of the observed data in terms of phase velocity and amplitude (Figure 4.6e-h). The DWM parameters used to calculate the synthetic waveforms are the same as those used for acquisition of our cross-glacier lines: 48 geophones with 2 m spacing. The maximum amplitudes of the frequency-phase velocity images were picked to create the Rayleigh wave dispersion curves which were used as input to MuLTI together with an estimate of their uncertainty, $\sigma(f)$, approximated from the half width of the peak, in velocity, at each given frequency (red lines in Figure 4.6i-l); this is seen to decrease with increasing frequency. The synthetic dispersion images clearly display a fundamental mode along with first and second higher order modes (higher order modes being induced by the low velocity layer immediately underlying the high velocity ice). Comparing reference models (Figure 4.6i and 4.6l), with increasing velocity structure, to the complex velocity models (Figure 4.6j, k), shows that the presence of a sharp decrease in velocity causes a break in the fundamental mode and higher order modes become more dominant. The depth of the velocity change is directly related to the frequency at which the change in dominant mode (from fundamental to higher order) occurs.

The resolution of the dispersion curve, and the precision with which its maxima can be picked, is influenced by survey parameters. Longer source-receiver offsets sharpen the dispersion curve, and clarify the transition between different modes. However, long offsets in real data become dominated by body waves (e.g., reflections and refractions) hence there is a compromise between dispersion resolution and signal-to-noise ratio (Park et al., 2001; Park, 2005). This issue becomes evident in our real data and is considered in our discussion section.

In this synthetic example, picking of dispersion curves is restricted to frequencies of 14-100 Hz, representative of the bandwidth in our real data. Killingbeck et al. (2018) show that including higher frequencies (>100 Hz) causes instabilities related to the appearance of higher-order modes hence we deliberately omit them in our analysis. Using Equation (1) and the $\lambda/3$ wavelength sampling approximation (Gazetas, 1982), the dispersion curves picked in these examples have a thinnest resolvable layer (L_{min}) of 3 m (corresponding to no ice model, Figure 4.6d), 4.5 m (6 m ice model) and 5.6 m (23.5 m ice models); and maximum resolvable depth (L_{max}) of 30 m (no ice model), 45 m (6 m ice model) and 46 m (23.5 m ice models).

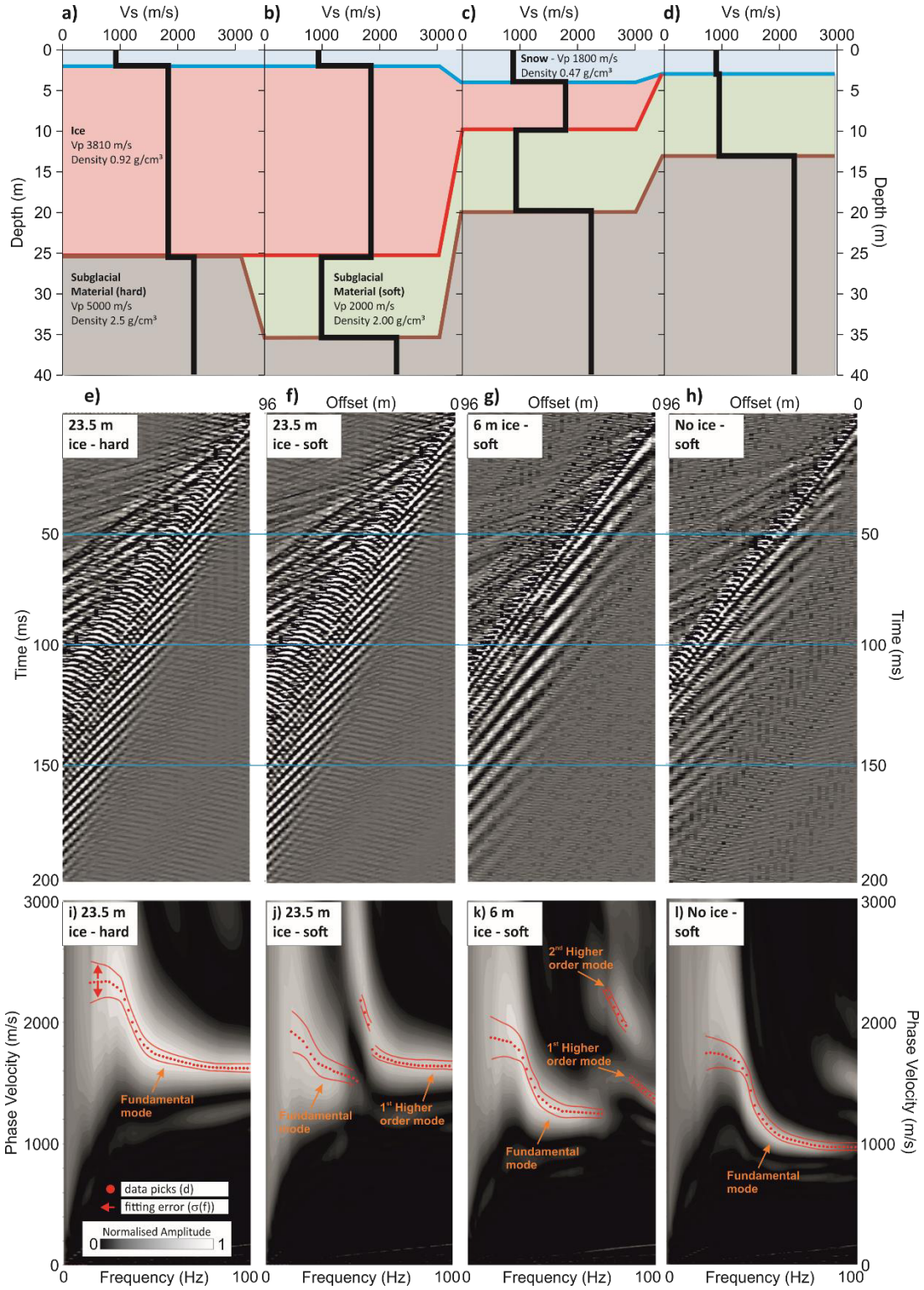

Figure 4.6 1D block models created to simulate snow and ice thicknesses expected at Lines A, B and C (a-d). Blue, red and brown lines represent base snow, ice and soft substrate boundaries; DWM synthetic wavefield shot gathers (e-h); corresponding dispersion curves picked with an estimate of associated uncertainty derived from the width of the dispersion image (i-l).

The inversions were run using *Vs* boundaries, and corresponding *Vp* and density values, set to the parameters stated in Table 4.1. Tests on varying *Vp* and density on modal dispersion curves show small variations but these are mostly within the fitting error tolerance (σ) used in MuLTI, Figure A1 in the appendix. Given the maximum resolvable depth of 46 m (from purely surface wave data), inversions were performed for a maximum depth of 40 m. To highlight the benefit of additional depth constraints (e.g., derived from GPR), MuLTI is first run for an unconstrained case and thereafter with fixed depths of the snow-ice and ice-bed layers. One million iterations were ran and found to be sufficient for convergence of the posterior distribution sampled; more detailed inversion parameters used are documented in Table A1 in the Appendix and explained further in Killingbeck et al. (2018).

Table 4.1 Elastic parameter boundaries applied in MuLTI for the glacier feasibility study. The parameters are taken from Peters et al. (2008); Tsoflias et al. (2008a); Podolskiy and Walter (2016).

Material	**Elastic Property**		
	Density (g/cm^3) Constant	***Vp* (m/s) Constant**	***Vs* (m/s) Variable**
Snow	0.47	1800	500 - 1700
Ice	0.92	3810	1700 - 1950
Subglacial material	2.5	3000	200 - 2800

Posterior *Vs* distributions produced from MuLTI are shown in Figure 4.7. The probability density distribution of *Vs* profiles within their 95% credible interval are plotted as coloured contours alongside the true solution (black line). The highest density distribution (red) for each depth corresponds to the most likely *Vs* model. The unconstrained inversions in Figures 4.7a-c show significant deviation between the true model and inversion output, with respective depth-averaged *Vs* errors of 680 m/s, 1046 m/s and 567 m/s respectively based on the modal model; although the fit is better (240 m/s error) for 4.7d (and 4.7a in the ice layer only), given the simpler underlying parameter distribution, there are multiple *Vs* distribution peaks between 20-33 m. The addition of depth constraints improves the match throughout, and Figures 4.7e-h show errors of 256 m/s, 99 m/s, 164 m/s and 138 m/s respectively (factors of 2.7, 10, 3.5 and 2 improved on their unconstrained equivalents).

More complex synthetic modelling, including an additional ice debris layer (high *Vs*) at the base of the glacier which may not be detected by GPR data, shows MuLTI can

reliably resolve unconstrained layers not accounted for in the GPR depth constraints applied within MuLTI (Figure A2 and A3 in the appendix).

This feasibility study demonstrates MuLTI works well for the expected geometries and parameter distributions for the Midtdalsbreen dataset. It also highlights the significant added value of depth constraint when a complex velocity profile is expected.

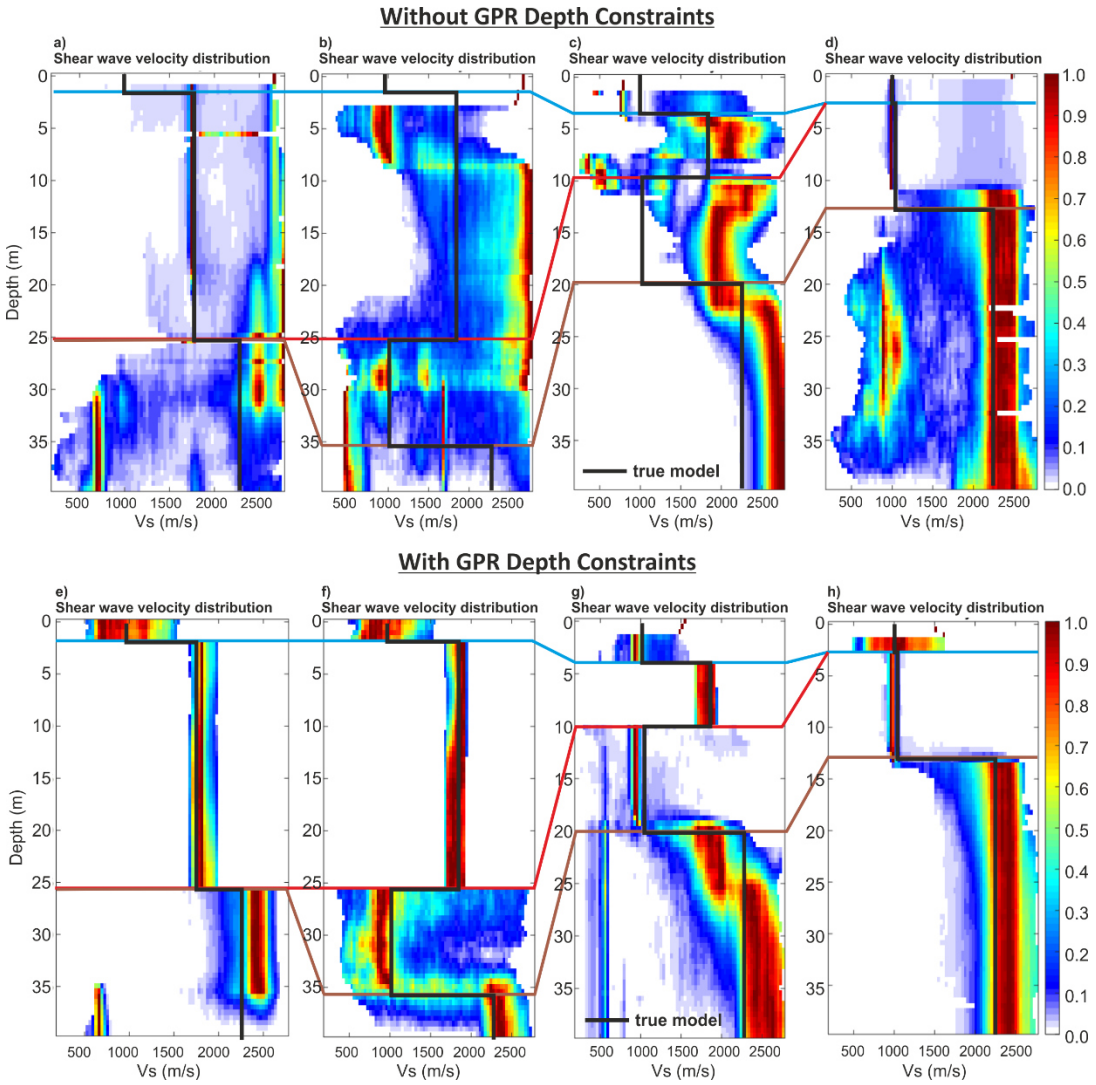

Figure 4.7 Posterior *Vs* distributions determined from MuLTI inversion (a-d) without depth constraints and (e-h) with depth constraints; the models correspond to those shown in Figure 4.6 a-d. Colour scale represents the probability density distribution of *Vs* values within the 95% credible interval, red highlighting most likely. Black line shows the true synthetic *Vs* profiles. Blue, red and brown correlation lines highlight the snow, ice and soft substrate depths respectively.

4.7 Results

4.7.1 1D shear wave velocity profiles

We first produce 1D velocity profiles for CMPCC gathers (Hayashi and Suzuki, 2004) located at the centre of lines A, B and C (Figure 4.8). A different range of source-receiver offsets was used in each gather due to differences in data quality and subsurface complexity. This minimises the spatial averaging affect beneath the geophone spread, particularly where the subsurface is not horizontally homogeneous (Park 2005). Line A shows significant interference between Rayleigh and body waves for offsets >50 m, whereas co-located GPR data suggest that the subsurface can only be described as 1D for offsets <60 m at Line B. However, data from Line C suffers from no such restrictions, hence its CMPCC gather uses the full 92 m offset range for this 1D analysis.

The dispersion images shown in Figure 4.8a-c are similar to the synthetic dispersion images (Figure 4.6i-l) giving an initial insight into the structure expected at Midtdalsbreen. The dispersion curves, which have high signal-to-noise ratio, are picked for frequencies between 14-100 Hz, implying that the thinnest resolvable layers (L_{min}) are 4.0 m (Line A), 3.8 m (Line B) and 5.7 m (C) and the maximum resolvable depths (L_{max}) are 19.5 m (Line A), 33.5 m (Line B) and 45.7 m (Line C).

The dispersion picks and their estimated uncertainty were supplied to MuLTI, together with the GPR depth constraints. The inversions used the same parameters used in the synthetic study. Posterior *Vs* distributions are shown in Figure 4.8g-i, the highest density velocities (coloured red) corresponding to the most likely (modal) solution. The average solution (black line) is the average of all accepted models, displaying a smoothed *Vs* solution, and its uncertainty is expressed as one-half of the 95% credible interval range at each depth. These uncertainties are typically ±~600 m/s for the snow layer, ±~120 m/s for the ice layer and ±~1100 m/s for the subglacial material. The estimated uncertainty for the mode solution is one-half of the interquartile range at each depth, accounting for the skewed probability densities highlighted in Figures 4.8 g-i. This convention implies smaller uncertainties: ± ~250 m/s in the snow layer, ± ~75 m/s in the ice layer, and ± 320-560 m/s in the subglacial material.

The 1D inversions show low shear wave velocities, 500-1000 m/s beneath the constrained snow-ice horizon in Line A and the constrained ice-bed horizon in Line B; both are in turn underlain by a high *Vs* zone, 2000-2500 m/s. In contrast, high velocities, ~2400 m/s, occur directly below the thicker ice in Line C. This analysis

suggests a spatially variable pattern of subglacial *Vs* from the front of the glacier to Line C, 150 m up-glacier.

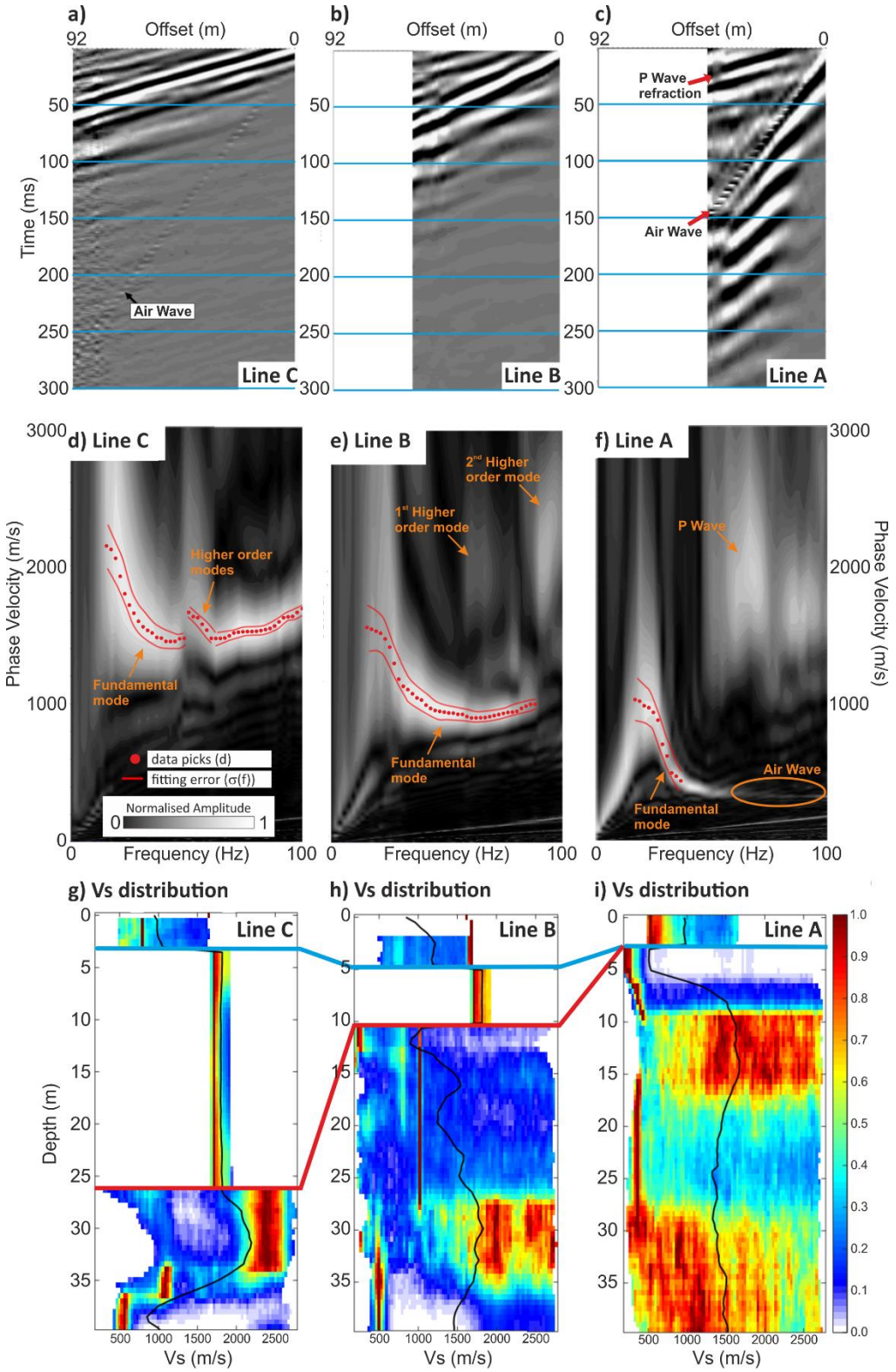

Figure 4.8 Mid-line C, B and A CMPCC gathers (a-c), corresponding dispersion images (d-f) and *Vs* distribution profiles (g-i), with the average of the distribution plotted in black.

4.7.2 2D shear wave velocity profiles

MuLTI is used to invert multiple independent 1D dispersion curves picked from all CMPCC gathers along each seismic line. Offsets are limited either to mitigate body wave contamination or prevent lateral smearing (particularly in line D where the thickness of ice decreases along the line and therefore we do not assume lateral homogeneity of *Vs* along this line). Dispersion patterns and the implied depth of penetration vary with ice thickness and the likely subglacial *Vs*, as shown by the depth range of input velocity picks in Figure 4.9 (leftmost column). These plots represent all 1D dispersion curves, picked at each CMPCC location along the line, indicate the maximum depth at which inversion results may be considered reliable.

Consistent with initial observations in the 1D analysis, the 2D *Vs* profiles (Figure 4.9, central column) highlight a wide range of subglacial *Vs* values, ~500-2500 m/s. The 2D profiles highlight spatial variability in *Vs* for the study region, both along- and cross- glacier profile (the latter evidenced in particular in Line B). The estimated uncertainties for the mode *Vs* solutions are displayed in Figure 4.9 (rightmost column). Consistent with the previous analysis, the estimated uncertainties in the average solution are generally very large, especially where input dispersion curve picks are absent (highlighted in Figure A4 in the appendix). The corresponding uncertainties in the mode solution are generally smaller, but still increase at depth, to ± ~1000 m/s where *Vs* constraints are lacking.

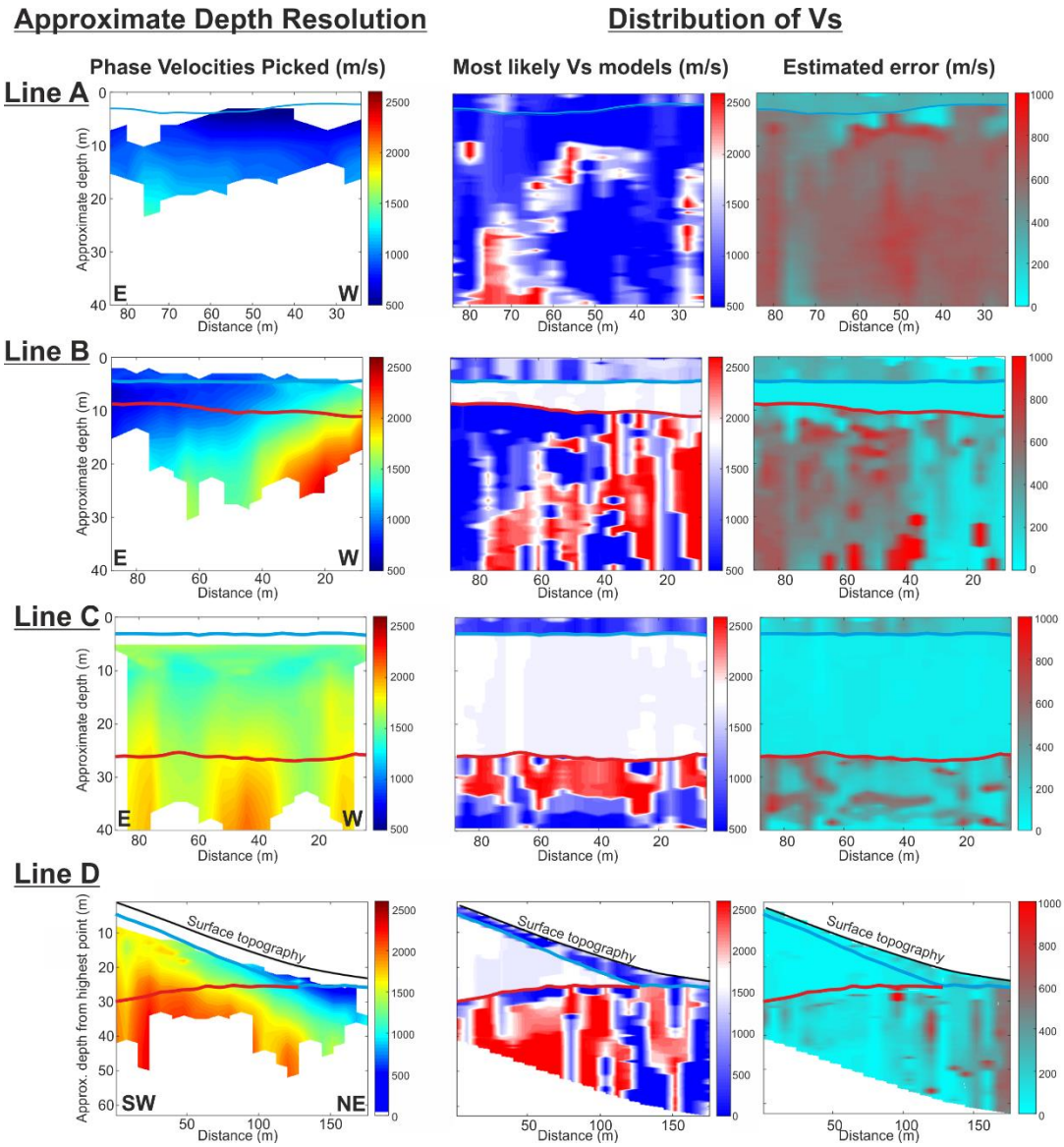

Figure 4.9 2D inversion outputs for Lines A-D. Left column: approximate 2D depth resolution, characterised by the range of phase velocity picks. Central column: most likely 2D *Vs* profiles output from multiple 1D MuLTI inversions. Diverging colour scale centred, in white, on *Vs* of ice (1750-1900 m/s). Right column: estimated uncertainty (half the interquartile range of the posterior distribution). Snow and ice depth horizons are plotted in blue and red respectively.

4.8 Interpretation and discussion

4.8.1 Interpretation of *Vs* profiles

Several studies have inferred subglacial erosion, transport and depositional processes at Midtdalsbreen, based on sedimentological and geomorphological evidence from the glacier foreland (Andersen and Sollid, 1971; Etzelmüller and Hagen, 2005; Reinardy et al., 2013, 2019; Willis et al., 2012). However, the type and distribution of

subglacial substrate is largely unknown, having not been directly imaged beneath the glacier.

The variability of *Vs* (500-2500 m/s) in our MASW records points to a complex subglacial structure, comprising local accumulations of bedrock and softer material, potentially permafrost and/or till, overlying bedrock (Figure 4.10). We consider the abrupt lateral variations in the outputs to be noise (since a pseudo-2D inversion is used by running multiple independent 1D inversions only along the line) rather than genuine structure, and instead interpret the broader variation in lateral character as representative velocity structure. The lateral resolution in our imaging varies along each line, given the changing offset range in our CMPCC gathers. In Lines A-C, the limit of lateral resolution is between ± 4-30 m, and is between ± 8-40 m in Line D; the poorest resolution is observed in the centre of each line, where the offset range in the CMPCC is greatest. The key structures we interpret in Figure 4.10 are larger in spatial extent than these limits, hence we consider our lateral resolution to be sufficient. However, the vertical velocity structure is more resolved due to the addition of GPR depth constraints, hence we consider our vertical resolution to be sufficient without smoothing.

Our slower velocities (500-1000 m/s) are interpreted to diagnose various types of partially frozen subglacial sediment, potentially the subglacial continuation of till and silt-rich deposits observed during summer on the glacier foreland. The higher velocities (2000-2500 m/s) are suggestive of phyllite or granite bedrock, with intermediate values (1000-1700 m/s) suggestive of frozen zones or weathered bedrock. Kneisel et al. (2008) suggest that a small increase in the unfrozen water content of sediment, from 10% to 13%, can cause *Vs* to decrease from 1400 m/s to 600 m/s, implying *Vs* is potentially a good means of distinguishing frozen and partially-frozen sediment. Although there is potentially some overlap in our velocity ranges, we use:

- *Vs* <1000 m/s to indicate partly-frozen sediment with water content >13%,
- 1000< *Vs* <2000 m/s to indicate partly-frozen material with water content <13%, and
- *Vs* >2000 m/s to indicate bedrock.

Line C suggests that Midtdalsbreen is directly underlain by bedrock 150 m from its terminus, but Line D suggests a transition to a sediment under-burden towards the glacier front. The eastern half of Line B, parts of Line D and all of Line A (on the foreland) are likely underlain by soft (partially frozen) sediment deposits (Figure 4.10) with a maximum thickness of 4 m. This thickness approaches our limit of vertical

resolution, but uncertainties at the associated depth are low: ± 100 m/s in Line D and ± 280 m/s in Lines A-C (Figure 4.9). Each inversion also indicates a return to high *Vs* at depth, consistent with underlying bedrock, although the greater uncertainties at these depths would motivate additional validation (e.g., from a lower-frequency seismic source or an alternate geophysical method such as time domain electromagnetics).

The presence of both bedrock and sediment at the glacier bed suggests that flow both by sliding and substrate deformation is at least possible at Midtdalsbreen, although sub-resolution layers of deforming till may be present where a bedrock substrate is inferred. The implication of zones of basally-frozen and unfrozen regions is consistent with the complex basal thermal regime inferred by Reinardy et al. (2019), who also suggest that the entrainment and elevation of debris into the glacier requires the substrate to contain both soft and unfrozen material. The presence of thick patches of frozen sediment in the Midtdalsbreen foreland also concur with permafrost models for this area (Etzelmüller et al. 2003). In addition to adding constraint to controls on the Midtdalsbreen flow regime, this study may have implications for other valley glaciers and presents a method by which they could be explored.

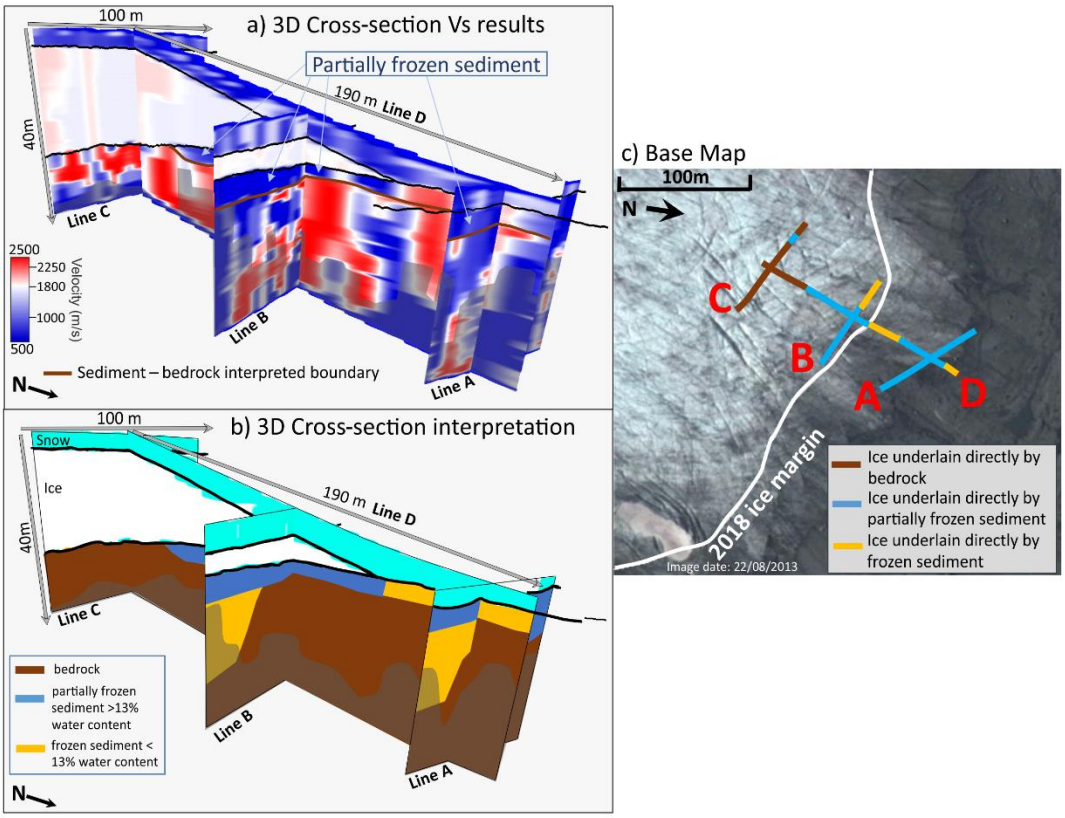

Figure 4.10 a) 3D cross-section of lines A-D, showing the *Vs* mode solution and interpreted locations of sediment and bedrock. The black semi-transparent overlay shows where L_{max} is exceeded, hence where results could be unreliable. b) Schematic 3D cross-section interpretation of Lines A-D. c) Base map annotated with line locations and the interpretations from (a).

4.8.2 Discussion and further work

Recurrent problems in Rayleigh wave inversions include poor depth sensitivity, low resolution and ambiguous, non-unique solutions. MuLTI combines a probabilistic approach with external depth constraints, mitigating many of these issues and reducing the size of the solution space. Our probabilistic method allows the uncertainty in any chosen model to be quantified at all depth levels. The addition of depth constraints also improves vertical resolution (Killingbeck et al., 2018), and further work is required to quantify this improvement.

Nonetheless, the success of MuLTI depends inherently on the quality of the input data and their suitability for the specific target. MASW analyses fundamentally require data to be observed across an array of some minimum length, in order that low frequencies can be faithfully characterised and adequate depth sampling achieved. As such, there is always a loss of lateral resolution for the low frequency Rayleigh wave

related to the array length over which they are observed. This is why we rule out the abrupt lateral variations from our interpretation of Figure 4.9. We minimise this impact by reducing, where appropriate, the maximum offset in our CMPCC gathers, but the link between lateral resolution and spread-length requires refinement. Any geophysical data are also vulnerable to noise, and we note this for the low frequencies between 50-90 m in Line B. If these noisy data were neglected, we would severely restrict the data available for the inversion (Figure A5 in the appendix). Instead, we adopt the Bayesian paradigm in which all data are kept but with enhanced error budgets where relevant. Even with their increased uncertainties, these noisy data still provide important depth constraints to the posterior distribution. We note that our data acquisition used 10 Hz geophones, if we corrected our data for the instrument response we may have picked lower frequencies (<10 Hz) which could improve the posterior distribution at depth.

Although this paper focuses exclusively on Rayleigh wave dispersion curves derived from active source seismology, with high-frequency sources and shallow depth penetration, MuLTI can be equivalently applied to dispersion curves from passive sources (e.g., Picotti et al., 2017; Walter et al., 2014) as the Geopsy forward modelling code, used in MuLTI, has the capability to model dispersion curves with frequencies <1 Hz. Being richer in low frequencies (<20 Hz), these may enable enhanced imaging of structure beneath polar ice sheets (Aster and Winberry, 2017; Siegert et al., 2018; Yan et al., 2018). MuLTI would allow such data to be inverted with depth constraints drawn from radio echo sounding (RES) datasets, thereby highlighting areas of large ice masses with a dynamic sediment underburden, although the algorithm would likely require adaptation to accommodate anisotropic effects.

The MuLTI framework also lends itself well to other geophysical inverse problems, where a theoretical geophysical response for a proposed model can be evaluated and compared probabilistically to observed data. An example of such an inverse problem would be the inclusion of time-domain electromagnetic (TEM) data to the existing approach, to which MuLTI could be readily adapted. Such a combined approach will be the subject of further investigations around the Midtdalsbreen margin, leading to a framework by which aquifer properties beneath large ice masses could be quantified (Hauck et al., 2011; Siegert et al., 2018).

4.9 Conclusions

The material properties of the subglacial environment exert a fundamental influence on glacier flow dynamics. These properties can be characterized by considering their

shear wave velocity, *Vs*, obtained by inverting Rayleigh wave dispersion curves. However, conventional dispersion curve inversions lack depth sensitivity and provide solutions that are highly non-unique. Such problems are overcome with the use of our algorithm MuLTI, a transdimensional Bayesian inversion approach, which reduces the ambiguity in the solution space by incorporated independent depth constraints. When trialed for synthetic *Vs* data representing a small glacier underlain by sediment, inclusion of such constraints results in an order-of-magnitude improvement in the depth-averaged uncertainty in the output model, reducing it for our thickest-ice case from ~1050 m/s to ~100 m/s. While an uncertainty of ~1000 m/s may not impede the value of conventional inversions for distinguishing sediment and bedrock substrates, the reduced range would be critical if observations of *Vs* were to be used to quantify detailed variations in sediment properties. As such, MuLTI is an important advance in the application of Rayleigh wave inversions.

We apply MuLTI to a Rayleigh wave dataset acquired around the terminus of Midtdalsbreen, complementing it with depth-constraints derived from co-located GPR surveys. Although widely underlain by bedrock (*Vs* ~2500 ± 280 m/s), our data reveal that a patchy distribution of sediment is present directly beneath the glacier. These sediments are only partly frozen (*Vs* ~500 m/s ± 280 m/s), and exist in pockets that may be up to 4 m thick; the sediment under-burden extends to ~150 m up-glacier from the terminus. Our interpretation is consistent with recent studies of Midtdalsbreen, which highlight the supply of sediment to the glacier foreland and identify regions of basal sediment around the glacier front.

The seismic data used by MuLTI is supplied in the form of a dispersion curve, hence the algorithm is compatible with Rayleigh wave data obtained from either active- or passive-source surveys. Equally, depth constraints are provided as numerical inputs and can therefore be drawn from any external source. MuLTI is therefore applicable for a broad spectrum of seismic data types, as a means of improving the quantitative analysis for a range of contemporary glaciological problems.

4.10 Acknowledgements

The *MuLTI* algorithm can be found at: https://github.com/eespr/MuLTI, DOI 10.5281/zenodo.1489959. This project is funded by the UK NERC SPHERES DTP, grant NE/L002574/1. Fieldwork was part-funded by the EVOGLAC project (University of Bergen, University of Oslo) and the research project 'Snow Accumulation Patterns on Hardangerjøkulen Ice Cap (SNAP)', itself funded by the European Union's Horizon 2020 project INTERACT, under grant agreement No

730938. Fieldwork was greatly assisted by Emma Pearce and James Killingbeck, and the support and local expertise of Kjell Magne Tangen. Richard Rigby at the University of Leeds is thanked for creating the gpdc mex file. Thomas Bodin is thanked for his advice on MCMC methods and for providing Matlab code. This paper benefited from discussions at the 2017 Glacial Seismology Summer School held at Colorado State University, sponsored by POLENET, SCAR, IGS and IACS. B. Reinardy gratefully acknowledges the support of a Bolin Centre for Climate Research grant.

4.11 References

Anandakrishnan S (2003) Dilatant till layer near the onset of streaming flow of Ice Stream C, West Antarctica, determined by AVO (amplitude *Vs* offset) analysis. *Annals of Glaciology*, 283-286.

Andersen JL and Sollid JL (1971) Glacial chronology and glacial geomorphology in the marginal zones of the glaciers Midtdalsbreen and Nigardsbreen, south Norway, *Norsk Geogr. Tidsskr.* 25, 1–38.

Andreassen LM and Winsvold H (2012) Inventory of Norwegian Glaciers. *Norwegian Water Resources and Energy Directorate*. 236 pp.

Armstrong M (2009) Multichannel Analysis of Surface Waves (MASW) determined surface-wave velocity profile and its relation to observation of the near-surface polar firn layers. Supervised Project Report, University of Canterbury, https://ir.canterbury.ac.nz/handle/10092/14187 (Accessed: December 2018).

Aster RC and Winberry PJ (2017) Glacial seismology. *Reports on progress in physics*.

Bell R (2008) The role of subglacial water in ice-sheet mass balance. *Nature Geoscience*, 297.

Bentley CR and Kohnen H (1976) Seismic refraction measurements of internal friction in Antarctic ice. *Journal of Geophysical Research*, 1519-1526.

Bodin T and Sambridge M (2009) Seismic tomography with the reversible jump algorithm. *Geophysical Journal International*, 1411-1436.

Bodin T, Sambridge M, Tkalčić H, Arroucau P, Gallagher K and Rawlinson N (2012) Transdimensional inversion of receiver functions and surface wave dispersion. *Journal of Geophysical Research: Solid Earth*.

Booth AD, Clark RA and Murray T (2011) Influences on the resolution of GPR velocity analyses and a Monte Carlo simulation for establishing velocity precision. *Near Surface Geophysics,* 399-411.

Booth AD, Clark RA, Kulessa B, Murray T, Carter J, Doyle S and Hubbard A (2012) Thin-layer effects in glaciological seismic amplitude-versus-angle (AVA) analysis: implications for characterising a subglacial till unit, Russell Glacier, West Greenland. *The Cryosphere*, 909-922.

Booth AD, Clark RA and Murray T (2010) Semblance response to a ground-penetrating radar wavelet and resulting errors in velocity analysis. *Near Surface Geophysics*.

Booth AD, Mercer A, Clark RA, Murray T, Jansson P and Axtell C (2013) A comparison of seismic and radar methods to establish the thickness and density of glacier snow cover. *Annals of Glaciology*, 73-82.

Bouchon M and Aki K (1977) Discrete wave-number representation of seismic-source wave fields. *Bulletin of the Seismological Society of America*, 259-277.

Christoffersen P, Bougamont M, Carter SP, Fricker HA and Tulaczyk S (2014) Significant groundwater contribution to Antarctic ice streams hydrologic budget. *Geophysical Research Letters*, 2003-2010.

Diez A, Eisen O, Weikusat I, Eichler J, Hofstede C, Bohleber P, Bohlen T and Polom U (2014) Influence of ice crystal anisotropy on seismic velocity analysis. *Annals of Glaciology*, 97-106.

Dou S and Ajo-Franklin JB (2014) Full-wavefield inversion of surface waves for mapping embedded low-velocity zones in permafrost. *Geophysics*, 107-124.

Etzelmüller B, Berthling I and Sollid JL (2003) Aspects and concepts on the geomorphological significance of Holocene permafrost in southern Norway. *Geomorphology*, 52, 87 –104.

Etzelmüller B and Hagen JO (2005) Glacier–permafrost interaction in Arctic and alpine mountain environments with examples from southern Norway and Svalbard, edited by Harris, C. and Murton, J. B., *Cryospheric Systems: Glaciers and Permafrost*, Geological Society, London, Special Publication 242, pp. 11-27

Foti S, Cox B, Garofalo F, Hollender F, Bard P, Cornou C, Ohrnberger M and Sicilia D (2015) Uncertainties in *VS* profiles from geophysical tests and their influence on seismic ground response analyses: results from the InterPACIFIC blind Test. *6th*

International Conference on Earthquake Geotechnical Engineering,. Christchurch, NZ.

Gazetas G (1982) Vibrational characteristics of soil deposits with variable wave velocity. *International journal for numerical and analytical methods in Geomechanics*, 1-20.

Gucunski N and Woods RD (1992) Numerical simulation of the SASW test. *Soil Dynamics and Earthquake Engineering*, 213-227.

Hauck C, Bottcher M and Maurer H (2011) A new model for estimating subsurface ice content based on. *The Cryosphere*, 453–468.

Hayashi K and Suzuki H (2004) CMP cross-correlation analysis of multi-channel surface-wave data. . *Exploration Geophysics*, 7-13.

Hofstede C, Christoffersen P, Hubbard B, Doyle SH, Young TJ, Diez A, Eisen O and Hubbard A (2018) Physical conditions of fast glacier flow: 2. Variable extent of anisotropic ice and soft basal sediment from seismic reflection data acquired on Store Glacier, west Greenland. *Journal of Geophysical Research: Earth Surface*, 349-362.

Johansen TA, Digranes P, Van Schaack M and Lønne I (2003) Seismic mapping and modeling of near-surface sediments in polar areas. *Geophysics*, 566-573.

Killingbeck SF, Livermore PW, Booth AD and West LJ (2018) Multimodal Layered Transdimensional Inversion of Seismic Dispersion Curves with Depth Constraints. *Geochemistry, Geophysics, Geosystems*, 19(12), 4957-4971.

King EC and Jarvis EP (2007) Use of Shear Waves to Measure Poisson's Ratio in Polar Firn. *Journal of Environment and Engineering Geophysics* , 15-21.

Kneisel, C., Hauck, C., Fortier, R., & Moorman, B. (2008). Advances in geophysical methods for permafrost investigations. *Permafrost and Periglacial Processes*, *19*(2), 157-178.

Kulessa B, Hubbard A, Booth A, Bougamont M, Dow C, Doyle S, Christoffersen P, Lindbäck K, Pettersson R, Fitzpatrick AA and Jones G (2017) Seismic evidence for complex sedimentary control of Greenland Ice Sheet flow. *Science Advances*, 1603071.

Lindbäck K, Kohler J, Pettersson R, Nuth C, Langley K, Messerli A, Vallot D, Matsuoka K and Brandt O (2018) Subglacial topography, ice thickness, and bathymetry of. *Earth System Science Data*, 1769-1781.

Livermore PW, Fournier A, Gallet Y and Bodin T (2018) Transdimensional inference of archeomagnetic intensity change. *Geophysical Journal International* 215(3), 2008-2034. Doi 10.1093/gji/ggy383.

Murray T, Booth AD and Rippin DM (2007) Water-Content of Glacier-Ice: Limitations on Estimates from Velocity Analysis of Surface Ground-Penetrating Radar Surveys. *Journal of Environmental and Engineering Geophysics* , 87-99.

Park CB (2005) MASW horizontal resolution in 2D shear-velocity (*Vs*) mapping. *Open-File Report, Lawrence: Kansas Geologic Survey*.

Park CB, Miller RD and Xia J (1998) Imaging dispersion curves of surface waves on multi-channel record. *SEG Technical Program Expanded Abstracts*, 1377-1380.

Park CB, Miller RD and Xia J (1999) Multichannel analysis of surface waves. *Geophysics*, 800-808.

Park CB, Miller RD and Xia J (2001) Offset and resolution of dispersion curve in multichannel analysis of surface waves (MASW). *Symposium on the Application of Geophysics to Engineering and Environmental Problems*, SSM4-SSM4.

Peters LE, Anandakrishnan S, Holland CW, Horgan HJ, Blankenship DD and Voigt DE (2008) Seismic detection of a subglacial lake near the South Pole, Antarctica. *Geophysical Research Letters*.

Picotti S, Francese R, Giorgi M, Pettenati F and Carcione JM (2017) Estimation of glacier thicknesses and basal properties using the horizontal-to-vertical component spectral ratio (HVSR) technique from passive seismic data. *Journal of Glaciology*, 229-248.

Picotti S, Vuan A, Carcione JM, Horgan HJ and Anandakrishnan S (2015) Anisotropy and crystalline fabric of Whillans Ice Stream (West Antarctica) inferred from multicomponent seismic data. *Journal of Geophysical Research: Solid Earth*.

Podolskiy EA and Walter F (2016) Cryoseismology. *Reviews of geophysics*, 708-758.

Preiswerk LE and Walter F (2018) High-Frequency (>2 Hz) Ambient Seismic Noise on High-Melt Glaciers: Green's Function Estimation and Source Characterization. *Journal of Geophysical Research: Earth Surface*.

Reinardy BTI, Leighton I and Marx PJ (2013) Glacier thermal regime linked to processes of annual moraine formation at Midtdalsbreen, southern Norway, *Boreas*, 42, 896-911.

Reinardy BTI, Booth AD, Hughes ALC, Boston CM, Åkesson H, Bakke J, Nesje A, Giesen RH and Pearce DM (2019) Pervasive cold ice within a temperate glacier –

implications for glacier thermal regimes, sediment transport and foreland geometry. *The Cryosphere,* 13, 827-843.

Richart FE, Hall JR and Woods RD (1970) Vibrations of soils and foundations. *International Series in Theoretical and Applied Mechanics*.

Saintenoy A, Friedt JM, Booth AD, Bernard E, Laffly D, Marlin C and Griselin M (2013) Deriving ice thickness, glacier volume and bedrock morphology of the Austre Lovénbreen (Svalbard) using Ground-penetrating Radar. *Near Surface Geophysics*, 253-261.

Shen W, Wiens DA, Anandakrishnan S, Aster RC, Gerstoft P, Bromirski PD, Hansen SE, Dalziel IW, Heeszel DS, Huerta AD and Nyblade AA (2018) The crust and upper mantle structure of central and west Antarctica from Bayesian inversion of Rayleigh wave and receiver functions. *Journal of Geophysical Research: Solid Earth*, 7824-7849.

Siegert MJ, Kulessa B, Bougamont M, Christoffersen P, Key K, Andersen KR, Booth AD and Smith AM (2018) Antarctic subglacial groundwater: a concept paper on its measurement and potential influence on ice flow. *Geological Society, London, Special Publications*, 197-213.

Stearns LA and Van der Veen CJ (2018) Friction at the bed does not control fast glacier flow. *Science,* 361(6399), 273-277.

Stokoe KH, Wright GW, James AB and Jose MR (1994) Characterization of geotechnical sites by SASW method. *Geophysical characterization of sites: Oxford publications*.

Temminghoff M, Benn DI, Gulley JD and Sevestre H (2018) Characterization of the englacial and subglacial drainage system in a high Arctic cold glacier by speleological mapping and ground-penetrating radar. *Geografiska Annaler: Series A, Physical Geography,* 1-20.

Thiel E and Ostenso NA (1961) Seismic studies on Antarctic ice shelves. *Geophysics*, 706-715.

Tsoflias GP, Ivanov J, Anandakrishnan S and Miller R (2008b) Use of active source seismic surface waves in glaciology. *21st EEGS Symposium on the Application of Geophysics to Engineering and Environmnetal Problems.*

Tsoflias GP, Ivanov J, Anandakrishnan S, Horgan H, Peters L, Voigt D and Winberry P (2008a) Firn and shallow ice profiling at Jakobshavn Glacier using dispersed seismic surface waves. *AGU Fall Meeting Abstracts*.

Tsuji T, Johansen TA, Ruud BO, Ikeda T and Matsuoka T (2012) Surface-wave analysis for identifying unfrozen zones in subglacial sediments. *Geophysics*, 17-27.

Walter F, Chaput J and Lüthi MP (2014) Thick sediments beneath Greenland's ablation zone and their potential role in future ice sheet dynamics. *Geology*, 487-490.

Wathelet M (2005) Array recordings of ambient vibrations: surface-wave inversion. *PhD Diss., Liége University,* 161.

Wathelet M, Jongmans D and Ohrnberger M (2004). Surface wave inversion using a direct search algorithm and its application to ambient vibration measurements. *Near Surface Geophysics* 2, 211--221.Willis IC, Fitzsimmons CD, Melvold K, Andreassen LM and Giesen RH (2012) Structure, morphology and water flux of a subglacial drainage system, Midtdalsbreen, Norway. *Hydrological Processes,* 3810-3829.

Xia J, Miller RD and Park CB (1999) Estimation of near-surface shear-wave velocity by inversion of Rayleigh waves. . *Geophysics*, 691-700.

Xia J, Miller RD, Park CB and Tian G (2003) Inversion of high frequency surface waves with fundamental and higher modes. *Journal of Applied Geophysics*, 45-57.

Yan P, Li Z, Li F, Yang Y, Hao W and Bao F (2018) Antarctic ice sheet thickness estimation using the. *The Cryosphere*, 795–810.

Young Kim K, Lee J, Ho Hong M, Kuk Hong J, Keun Jin Y and Shon H (2010) Seismic and radar investigations of Fourcade Glacier on King George Island, Antarctica. *Polar Research*, 298-310.

Zimmerman RW and King MS (1986) The effect of the extent of freezing on seismic velocities in unconsolidated permafrost. . *Geophysics*, 1285-1290.

Åkesson H, Nisancioglu K., Giesen R and Morlighem M (2017) Simulating the evolution of Hardangerjøkulen ice cap in southern. *The Cryosphere*, 281-302.

Chapter 5 Characterisation of subglacial water using a constrained transdimensional Bayesian Transient Electromagnetic Inversion

Siobhan F. Killingbeck[1], Adam D. Booth[1], Philip W. Livermore[1], Charles R. Bates[2], Landis J. West[1]

[1]School of Earth and Environment, University of Leeds, Leeds, LS2 9JT, UK

[2]Earth and Environmental Sciences, University of St Andrews, St Andrews, KY16 9AL, UK

Correspondence to: Siobhan F. Killingbeck (eespr@leeds.ac.uk)

Accepted to Solid Earth, doi: doi.org/10.5194/se-2019-126

5.1 Abstract

Subglacial water modulates glacier-bed friction and therefore is of fundamental importance when characterising the dynamics of ice masses. The state of subglacial pore water, whether liquid or frozen, is associated with differences in electrical resistivity that span several orders of magnitude, hence liquid water can be inferred from electrical resistivity depth profiles. Such profiles can be obtained from inversions of transient (time-domain) electromagnetics (TEM) soundings, but these are often non-unique. Here, we adapt an existing Bayesian transdimensional algorithm ('MuLTI') to the inversion of TEM data using independent depth constraints to provide statistical properties and uncertainty analysis of the resistivity profile with depth. The method was applied to ground-based TEM data acquired on the terminus of the Norwegian glacier Midtdalsbreen, with depth constraints provided by co-located ground penetrating radar data. Our inversion shows that the glacier bed is directly underlain by material of resistivity 10^2 Ωm ±1000 %, with thickness 5-40 m, in turn underlain by a highly conductive basement (10^0 Ωm ±15 %). High resistivity material, $5x10^4$ Ωm ±25 %, exists at the front of the glacier. All uncertainties are defined by the interquartile range of the posterior resistivity distribution. Combining these resistivity profiles with those from co-located seismic shear-wave velocity inversions to further reduce ambiguity in the hydrogeological interpretation of the subsurface, we propose a new 3D interpretation in which the Midtdalsbreen subglacial material is partitioned into partially frozen sediment, frozen sediment/permafrost and weathered/fractured bedrock with saline water.

5.2 Introduction

Subglacial structure and material properties are one of several important controls on ice flow, both through composition and ice/material interactions. The potential for subglacial sediments to store and pressurise water is a key element in predicting the evolution of ice masses of all sizes, from small mountain glaciers to large polar ice-sheets (Christoffersen et al., 2014; Siegert et al, 2018). Currently, the ability to develop accurate ice flow models is limited by poor understanding of processes acting at the ice/bed interface, and the composition of subglacial material. With increased knowledge of subglacial structure and sediment liquid water content, our ability to predict glacier retreat patterns would be greatly increased.

Non-invasive geophysical imaging methods are widely and successfully applied to characterise the internal properties of glacier ice and its immediate basal environment. Such methods (including reflection seismology and ground-penetrating radar) can

underperform when characterising material properties beyond the first few metres of the glacier bed (Booth et al., 2012), yet subglacial aquifers, sediment accumulations and permafrost can extend to much greater depths (e.g., Mikucki et al., 2015 and Hauck et al., 2001). Further still, inversions of isolated geophysical datasets are unconstrained and non-unique, with many models of the subsurface matching the observed dataset. Joint inversions using multiple independent datasets can constrain the model space, combining depth and resolution sensitivities from multiple datasets. Glaciological surveys often involve the acquisition of multiple geophysical datasets: given the typical absence of ground-truth data, imaging the target with several methods provides a more robust interpretation (e.g., Merz et al., 2016). However, these datasets are seldom combined numerically. In this paper, we provide a mechanism for the constrained inversion of transient electromagnetics (TEM), with depth constraints derived from ground penetrating radar (GPR), to provide geophysical insight into the structure and water characteristics of the subglacial environment. This method is adapted from a transdimensional Bayesian framework, termed 'MuLTI' and described in Killingbeck et al. (2018), originally applied to characterise subglacial sediment distribution from seismic surface wave data (Killingbeck et al., 2019). Here, we explore a similar concept for the TEM method.

Time domain electromagnetic methods use electromagnetic fields to sound the subsurface structure. Here we use the transient time-domain method (TEM) which indirectly probes the subsurface resistivity structure by measuring transient eddy currents induced by current transmitted through either a grounded-wire, coincided loop or offset coil. The method has a depth sensitivity ranging from a few meters to kilometres, depending on the survey parameters used. Of particular relevance here is that electrical resistivity increases by several orders of magnitude when water in pores freezes (Hoekstra and McNeill, 1973), allowing resistivity methods to indicate the liquid water content of subsurface materials. TEM methods have been extensively applied for hydrogeophysical exploration to map groundwater resources (Auken et al., 2003), mapping permafrost on mountainous regions under debris covered glaciers (Hauck et al., 2001), mapping arctic permafrost in Alaska (Minsley et al., 2012), and more recently mapping deep saline groundwater zones in Antarctica's Taylor Valley (Mikucki et al., 2015). These studies illustrate that characterising the resistivity of the subsurface offers a promising means of distinguishing material type and water content within the subglacial environment.

In common with most geophysical inversions, such resistivity profiles are non-unique: many profiles fit the data within error tolerance, and smoothing is usually employed to recover a single solution. Early inversion techniques for TEM data included non-

linear least squares (Barnett, 1984) and an Occam-type regularization method to obtain a smooth solution (Constable et al., 1987), but these were prone to being trapped in local minima with any large resistivity variations becoming smoothed. More recent inversion methods include laterally- and spatially-constrained algorithms to regularize the inversion and obtain solutions that agree with the expected geological variations (e.g., Christensen and Tølbøll, 2009; Vignoli et al., 2015; Auken et al., 2015). Yet, these methods do not provide detailed uncertainty analysis of the estimated model parameters and require a fixed number of layers in the model. The maximum depth of investigation (DOI) is generally estimated using methods, such as half-space skin depth (Spies, 1989) or the Jacobian sensitivity matrix (Christiansen and Auken, 2012), though these do not consider the non-linear sensitivity of the DOI to conductivity structure. These limitations in uncertainty quantification, fixed model space and DOI estimation can be mitigated by transdimensional Bayesian sampling-based inverse methods. These produce an ensemble of models from which statistical properties of the model parameters, including model dimensions, can be inferred (Mosegaard and Tarantola, 1995, Blatter et al., 2018). The computed posterior probability density function (pdf) provides a robust measure of DOI, highlighting model uncertainty at each depth (Blatter et al., 2018). To further reduce the parameter space and improve vertical resolution, the inversion can be constrained with complementary depth information (e.g., from borehole records or other geophysical sources), which is most useful in the case that any internal layer represents a discontinuity in properties to which all techniques are sensitive.

In this paper, we derive the implementation of 'MuLTI-TEM' (Multimodal Layered Transdimensional Inversion of Transient ElectroMagnetics) and its use for characterising the subglacial environment. After testing the method on a synthetic dataset, we analyse a TEM dataset acquired on the Norwegian glacier Midtdalsbreen, an outlet of the Hardangerjøkulen ice cap, using complementary GPR data for constraining the ice thickness. Since the glacier bed represents a transition in both dielectric constant and electrical resistivity, the GPR depth constraint can be used directly in the TEM inversion. Recent results from Killingbeck et al. (2019) interpret the Midtdalsbreen subsurface from seismic shear wave velocity (*Vs*) profiles, as local accumulations of soft material (partially frozen glacial till) and permafrost overlying bedrock. Finally, we show a combined 3D interpretation of previous shear wave inversions (Killingbeck et al., 2019) and results output from MuLTI-TEM, and suggest the development of a joint resistivity-*Vs* depth-constrained inversion strategy.

5.3 Method

5.3.1 Transient electromagnetics

In TEM surveying, an electromagnetic field is generated by sending a periodic, modified square-wave, current through a transmitter coil. When the current is on, a static electromagnetic field is established in the ground. The electromagnetic field is varied by terminating the current abruptly at the first quarter-period, being reduced to zero for the second quarter-period, the current is then reversed for the third quarter-period before being reduced to zero again for the final quarter-period. This switch off induces eddy currents in the subsurface, initiating within the immediate vicinity of the transmitter then spreading downwards. The eddy currents produce a secondary electromagnetic field which propagates back up through the subsurface, inducing a current in a receiver coil located at some distance from the transmitter. The receiver typically measures the induced secondary electromagnetic field in the transmitter-off periods. The response of the subsurface is measured in terms of the decaying amplitude of the secondary electromagnetic field. This is recorded as a function of time, with later responses originating from greater depths. With regards to conductivity of the subsurface, the more conductive the subsurface, the larger the eddy currents and the larger the measured secondary electromagnetic field will be, implying a slower transient decay. By taking repeated measurements a sounding curve, similar to DC resistivity soundings, is obtained (Geonics, 1994). The measured voltages versus time from the receiver coil are then used to constrain the resistivity profile with depth.

The maximum depth of investigation (DOI) (h), in meters, can be approximated by:

$$h \approx 0.55 \left(\frac{I\,A\,\rho}{\eta_v}\right)^{1/5} \tag{5.1}$$

where I is the transmitter current, A is the loop area, η_v is the voltage noise level and ρ is the average resistivity, in Ωm, of the underlying section (Spies, 1989). Equation 5.1 shows the transmitter loop size is an important acquisition parameter controlling depth of investigation. Large loop soundings (e.g., > 40x40 m), where the receiver coil is located in the centre of the large transmitter coil, have been conducted on thick permafrost regions by Rozenberg and others (1985) and Todd and Dallimore (1998). Our depth of target (0 - 80 m) allows for a smaller, more portable loop size to be used. In this study, we use an efficient 10 x 10 m loop, with the receiver 15 m offset from the centre of the transmitter loop (to stop electromagnetic interference with the receiver) shown and discussed further in section 5.4.

5.3.2 MuLTI-TEM

MuLTI-TEM is a Bayesian inversion Matlab code that determines the posterior distribution of resistivity as a function of depth. It is adapted from the MuLTI algorithm ('Multimodal Layered Transdimensional Inversion), developed for seismic surface wave inversions (see detailed in Killingbeck et al. (2018)). The data input, *d*, to MuLTI-TEM are the voltages (v) at each of the N timegates, measured as the mean recording in a stack window. The mean, through central limiting, is assumed to be normally distributed with a variance σ^2, the variance of the measurements divided by the number of measurements in the stack window, so that the data and uncertainties can be written as:

$$d = [v_1, v_2 \ldots . v_N]$$

$$\sigma = [\sigma_1, \sigma_2 \ldots . \sigma_N] \quad (5.2)$$

The method used to find the posterior distribution of the resistivity profile

$$p(m|d) \propto p(d|m)p(m) \quad (5.3)$$

is outlined below, where $p(m|d)$ is the posterior probability of the model (m) given d, $p(m)$ is the prior information known about the model before the introduction of data, and $p(d|m)$ is the likelihood.. A Markov Chain Monte Carlo methodology is used to sample the posterior distribution, traversing the space of admissible models with the statistics of the ensemble converging to the underlying posterior distribution, provided the chain of models is long enough.

We describe the 1D variation of resistivity with depth as a piecewise constant function using Voronoi nuclei (see Killingbeck et al., 2018). Any available depth constraints separate the resistivity into different depth layers. In our case, in which constraints are drawn from high resolution GPR data, we consider depth constraints to be exact since the accuracy of GPR depth estimation is decimetre scale (Killingbeck et al., 2019), compared to the meter scale resolution of the TEM. Within each layer, we define a single confined nucleus; aside from being confined to the given layer, this nucleus is otherwise unconstrained in depth. The number of confined layers, l, is equal to the number of layered depth constraints applied with the addition of an assumed half space of constant resistivity extending to infinite depth. If no depth constraints are applied then $l = 1$, corresponding to a half space. We add in an additional k nuclei in the model that are unconstrained in depth, termed *floating*. Our transdimensional framework allows the data to self-determine the required number of layers k (e.g., Bodin and Sambridge, 2009; Bodin et al., 2012, Livermore et al., 2018), thus k is also an unknown that we determine.

The model vector, that describes the resistivity profile, is then

$$m = [dp_1, dp_2 \ldots . dp_k, \log(R_1), \log(R_2) \ldots . \log(R_k), k, dpc_1, dpc_2 \ldots . dpc_l, \log(Rc_1), \log(Rc_2) \ldots . \log(Rc_l)] \quad (5.4)$$

where dp_i are the floating nuclei depths, $\log(Rc_i)$ are the base-e log of the their respective resistivities, dpc_i are the confined nuclei depths and $\log(Rc_i)$ are the base-e log of their respective resistivities. In our transdimensional framework the number of floating nuclei (k) is a free parameter and self-determined in the algorithm.

For the choice of prior distribution in transdimensional calculations, it is worth noting that usually the geophysical properties of the cells (here the resistivity) and the cell depths are assumed independent, allowing a simple separated analytic form for the prior distribution (e.g. Bodin and Sambridge, 2009). This is followed in our simplest geometry with no GPR constraints, for which the prior distribution on the resistivity is depth-independent and uniform with wide bounds on log(R) (e.g., R between 10^0-10^5 Ωm), to convey the fact that no prior information (beyond that which can be reasonably assumed for typical materials) is known about the subsurface. However, by interpreting any GPR-derived layers as different materials (Table 5.2) with much more narrowed ranges of resistivity, it is clear that a broad depth-independent prior distribution is no longer appropriate. Here we allow the prior distribution of resistivity to depend on depth, by defining for each layer a different uniform distribution that reflects the tightened bounds from lithological information. This restricted prior distribution then significantly decreases the number of permissible models describing resistivity with depth, reducing model ambiguity from any given set of data. In terms of the model parameters, the prior of the resistivity for any nucleus is given by the specific layer that the nucleus is within (Killingbeck et al. (2018). Although a closed form expression for the depth-dependent prior distribution cannot be easily formulated, in the algorithm only the ratios of prior distributions are needed.

Lastly, the likelihood is defined by assuming that the measurements are normally distributed about values calculated from a forward model of TEM response (assuming a given resistivity profile) and the estimated standard deviation σ, where σ is dataset specific and defined for each different dataset. MuLTI-TEM uses the Leroi algorithm of the CSIRO and AMIRA project P223F (CSIRO and AMIRA, 2019) as a forward modeller to compare proposed subsurface models to the observed data. The Leroi algorithm is written in Fortran 95 and has a wide range of electromagnetic modelling capabilities, for more information see Raiche (2008). We have used a simplified version of this algorithm and created a MEX file to call the code in Matlab from within

the MuLTI-TEM algorithm. See Table B1 and Figure B1, in the appendix, for detailed TEM survey parameters input to MuLTI-TEM, defined from the Leroi forward modelling algorithm.

MuLTI-TEM numerically approximates the posterior distribution by creating an ensemble of models, traversing the model space and sampling the models with greater likelihood more often than models with a poor fit to the observed data. Provided the ensemble is sufficiently sampled the numerically-obtained posterior distribution will converge to the true posterior. This is achieved by constructing a Markov-chain, each model in the chain being based on the previous model but randomly perturbed, the size of the perturbation being controlled by the user. We thin the Markov chain by using every 100th model when computing the distribution statistics, which suppresses any localised correlations of neighbouring models and speeds up convergence. MuLTI-TEM produces a variety of statistics of the resistivity ensemble including, but not limited to: the mean and mode (the most likely) solution and 95% credible intervals as an estimate of its uncertainty, thus giving a profile with a quantified uncertainty.

5.4 Data acquisition

Data acquisition was performed on Midtdalsbreen, a NE-flowing outlet glacier of the Hardangerjøkulen ice cap in central-southern Norway (60.59ºN, 7.52ºE; Figure 5.1a) in April-May 2018. Midtdalsbreen is surrounded by mountains of phyllite, crystalline granite and gneiss suggesting this as the underlying bedrock. The glacier is well-suited to methodological development as it is logistically accessible, especially with multiple types of geophysical surveying equipment. More detailed information on previous glaciological and geophysical studies on Midtdalsbreen can be found in Andersen and Sollid 1971; Etzelmüller and Hagen, 2005; Reinardy et al., 2013, 2019; Willis et al., 2012.

GPR, seismic and TEM surveys were performed around and over the glacier front (Figure 5.1). All methods were acquired at each line highlighted, A-D, in the same field season. Lines B and C are located entirely on the glacier, whereas Line A shows no glacier ice. Line D traverses through each of Lines A, B and C and extends beyond the glacier terminus. At the time of acquisition, the subsurface comprised snow (2-4 m thick) overlying a varying thickness (0-25 m) of glacier ice, and a substrate of unknown subglacial material. This layered interpretation is based on the interpretation of the GPR dataset, which also suggest that the snow and ice layers show little variation in any of lines A, B and C.

Killingbeck et al. (2019) used MuLTI to jointly interpret the seismic and GPR data, defining regions of partially frozen sediment and hard bedrock based on subglacial shear wave velocities (*Vs* < 1000 m/s for the former, > 2000 m/s for the latter). Figure 5.1b shows the seismic *Vs* results obtained at the glacier bed along all survey lines. This paper focuses initially on the joint inversion of the TEM and GPR data, and thereafter integrates the observations with the existing *Vs* distributions.

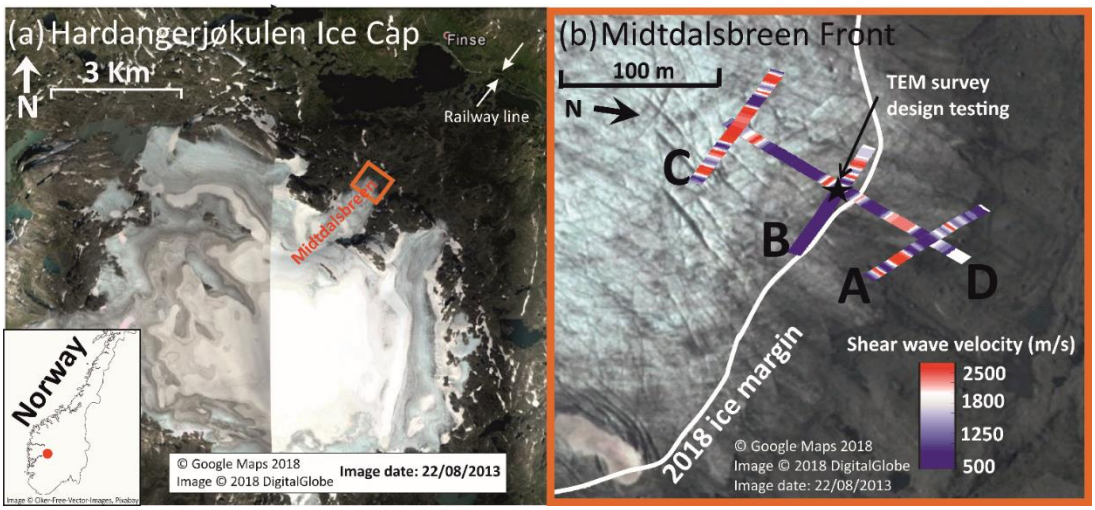

Figure 5.1 a) Location of Hardangerjølken ice cap in Norway and Google Earth image of Midtdalsbreen, survey area, with nearest sources of TEM noise (town and railway line) highlighted. b) Survey lines acquired during 2018 field season with the seismic *Vs* results obtained at the top rock horizon displayed. The orange border around (b) identifies the same area as the orange box in (a), note (b) is rotated away from North to enable optimal data comparison in later figures.

TEM data were acquired with a Geonics PROTEM 47 system, consisting of a 3 channel digital time-domain receiver, a TEM-47 battery powered transmitter and a 3D multi-turn receiver coil. All survey parameter are listed in Table 5.1. For cross-glacier lines A, B and C, the system was moved along the lines in 4 m intervals; for the longer down-glacier line D, this was increased to 8 m. Multiple survey configurations were initially tested at the intersection of lines B and D to determine the optimal survey configuration for imaging the subglacial environment at Midtdalsbreen. These tests comprised the following (the maximum DOI of each test is estimated using Equation 5.1, with voltage noise level 1 nV/m^2 (Figure 5.2d) and average underlying resistivity range as 0.1 to 1000 Ωm):

a) 37 m x 37 m square transmitter with receiver in centre, with estimated DOI 110 to 680 m (Figure 5.2a)

b) 10 m x 10 m square transmitter with receiver 15m away from centre of transmitter square, with estimated DOI 64 to 400 m (Figure 5.2b.)

c) 5 m x 5 m square transmitter with receiver 12.5m away from centre of transmitter square, with estimated DOI 45 to 300 m (Figure 5.2c.)

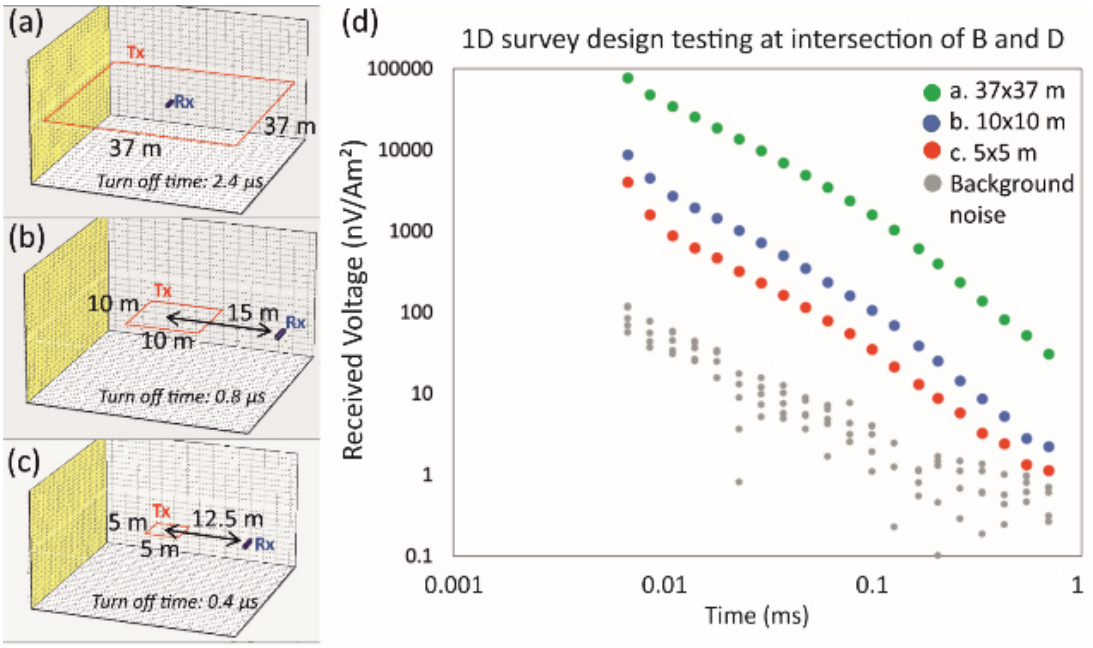

Figure 5.2 Survey configuration testing at the intersection of B and D. a) 37m x 37m transmitter coil with receiver in the centre. b) 10m x 10m transmitter coil with receiver 15m offset. c) 5m x 5m transmitter coil with receiver 12.5m offset. d) Raw data acquired at the intersection of B and D (237.5Hz), from each survey configuration, plotted with background noise recorded with transmitter turned off.

For accurate resistivity soundings, the raw signal should be above background noise levels (Figure 5.2d). Background noise, measured with the transmitter coil turned off, is considered low at Midtdalsbreen since there are no large sources of electrical noise e.g. power lines, buildings, roads, metal infrastructure for ~5 km (where the nearest town, Finse, is located, Figure 5.1). The 10 m x 10 m square transmitter (Figure 5.2b, Figure 5.3) was chosen as the optimum survey configuration because:

i) it had a fast turn off time (for imaging the shallow surface),

ii) the raw signal (received voltage) recorded was sufficiently greater than the background noise (Figure 5.2d),

iii) it was easily deployed on the glacier, and could be moved rapidly between the points of the survey lines (Figure 5.3), and

iv) the estimated DOI (ranging from 64 m to 400 m depending on the underlying resistivity) is sufficient for imaging our target depth, subglacial sediments below ~25 m thick ice.

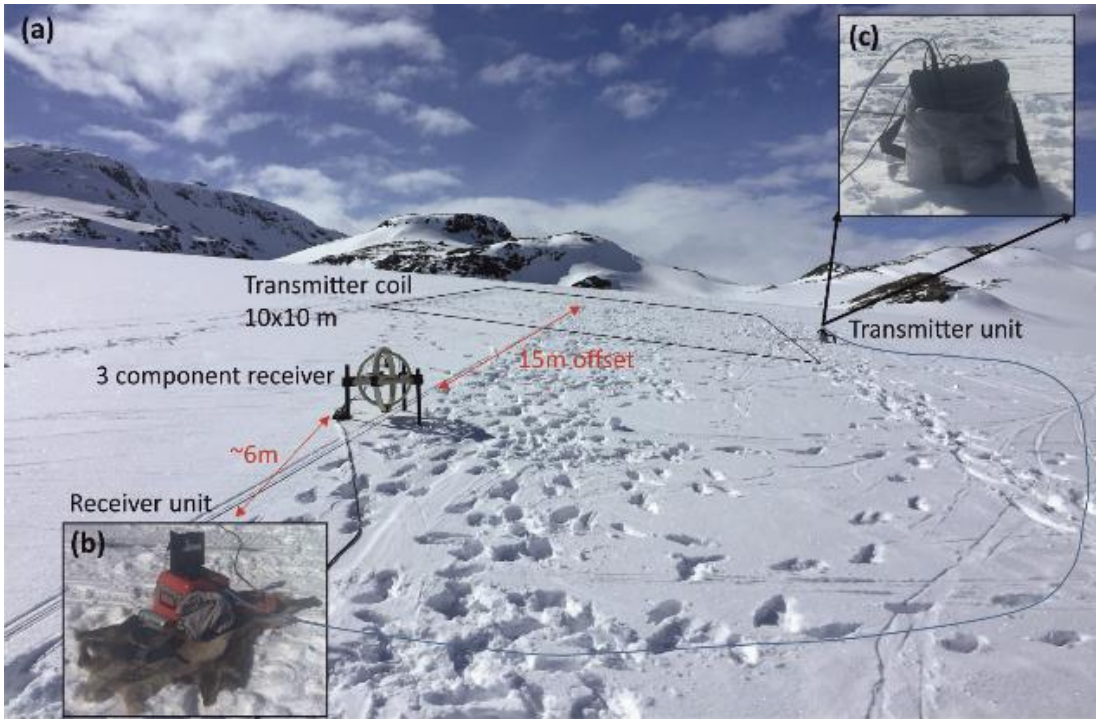

Figure 5.3 a) Survey configuration used for acquiring lines A, B, C and D on the glacier. b) Image of the receiver unit on top of a rug to protect unit from snow and easily drag along the lines. c) Image of transmitter unit sitting in bubble-wrap pocket used to protect unit and batteries from snow and cold.

Table 5.1 TEM survey parameters

Fixed Survey Parameters	
Transmitter coil	10 m x 10 m
Transmitter – receiver offset	15 m
Turn off time	0.8 us
Gain	4
Frequency	237.5 Hz
Orientation of Tx and Rx	220 degrees
Gate	20
Integration Time	15 seconds
Repetition Base	50 Hz
Receiver effective area	31.4 m^2
Number of repeat readings stacked	3
Transmitter current	2 A

5.5 Application of MuLTI-TEM to a synthetic dataset

Synthetic TEM responses from a variety of models representing different possible glacial and subglacial structures of the Midtdalsbreen glacier were input into MuLTI-TEM for validation (models (a)-(e) in Figure 5.4). Each model included layers of snow, ice, and bedrock, with models (b)-(e) also including saturated subglacial sediment. Each layer was populated with representative resistivities from previous TEM studies (Mikucki et al., 2015). Certain models were designed to test particular aspects of the inversion: model (b) tested the maximum DOI using our specified survey design and synthetic, and model (c) tested whether the inversion can resolve a 5 m-thin layer.

Synthetic TEM responses were calculated from the 1D block models using the Leroi forward modelling algorithm (Raiche, 2008), then normally distributed random noise, with a magnitude of 5% of the signal at each timegate, was applied to all time gates, a similar noise model to Blatter et al. (2018), see Figure 5.5. The simulated TEM survey configuration assumed a 10 m x 10 m square transmitter with receiver 15m away, consistent with the field acquisition.

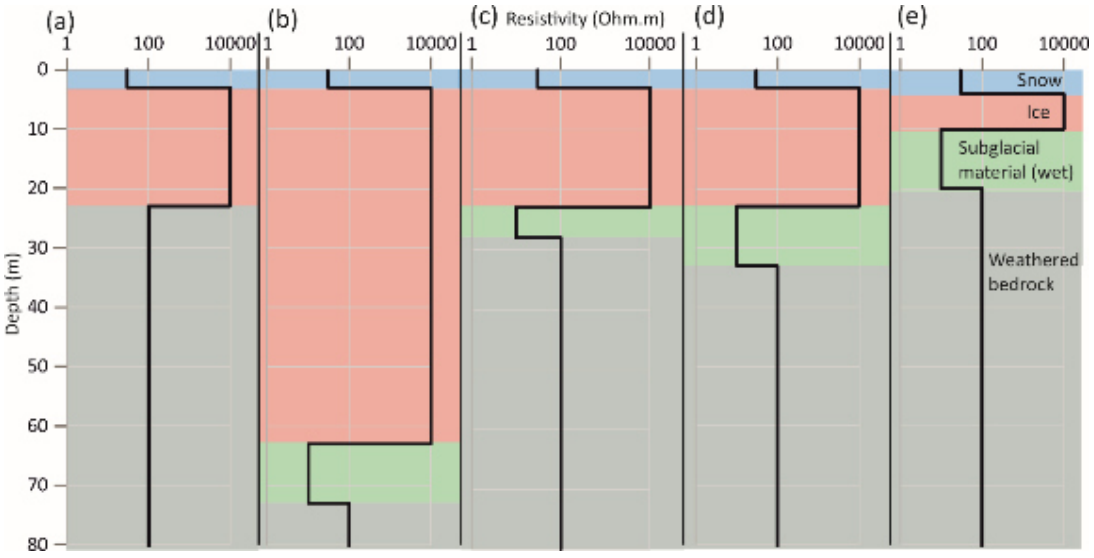

Figure 5.4 1D synthetic block models created to simulate different subsurface scenarios expected at Midtdalsbreen.

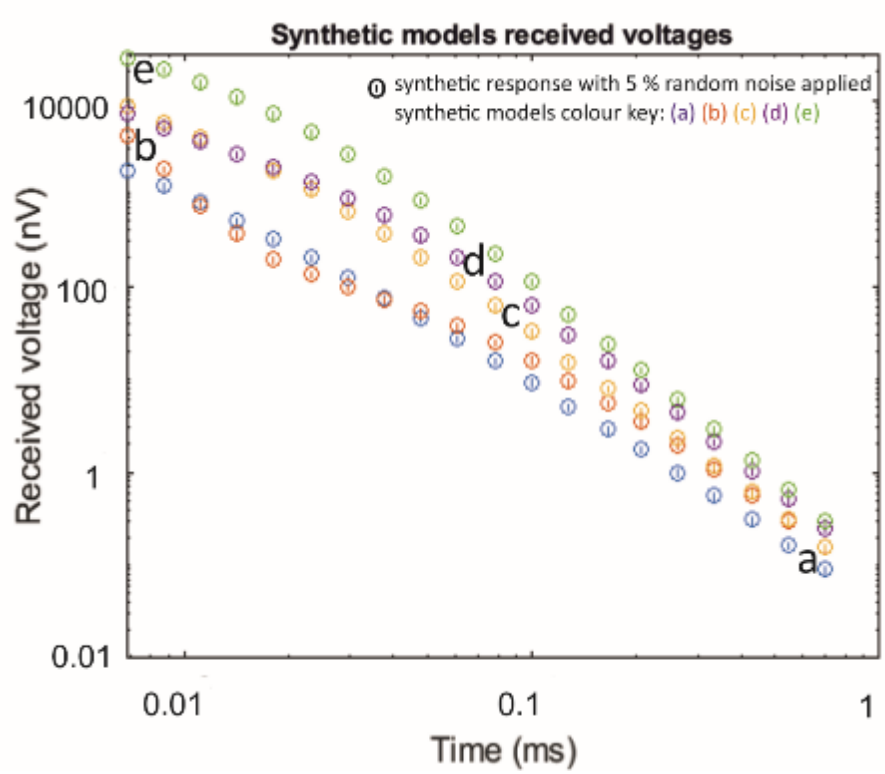

Figure 5.5 Forward modelled responses for 1D synthetic block models a-e with 5 % random noise applied. The lines within the circles represent the 5% error bars.

The inversions were run using resistivity ranges shown in Table 5.2 using a maximum depth of 80 m, consistent with the estimated maximum DOI for this configuration. To highlight the benefit of additional depth constraints, MuLTI-TEM is separately run for an unconstrained case, and a case in which the depths of snow-ice and ice-bed horizons are fixed. One million iterations were sufficient for the posterior distribution to converge (a test of 2 million iterations produced the same posterior, some example test results are shown in Figure B2). Additional figures in B3 show that the modal model from the depth constrained inversion fits the data better than that from the non-constrained inversion, with, in general, a lower data misfit. Multiple chains were also tested with one million iterations using different initial conditions. For the constrained case, these produced similar posterior distributions with identical interpretation, indicating that only one chain was needed. For the unconstrained case, the posterior distributions differ slightly but are nevertheless qualitatively the same, suggesting that the unconstrained case is not yet converged (Figure B4). More detailed inversion parameters used are documented in Table B2.

Table 5.2 Resistivity parameter boundaries used in MuLTI-TEM for the glacier feasibility study.

Material	Resistivity boundaries (Ωm)
Snow	10^0-10^3
Ice	10^3 - 10^5
Subglacial material	10^0 - 10^5
Non constrained material	10^0 - 10^5

Posterior probability density distributions (pdf) of the synthetic resistivity profiles produced from MuLTI-TEM are shown in Figure 5.6. These are shown, within their 95% credible interval, as coloured contours, where red indicates the most likely values. Consistent with many previous studies, both the unconstrained and constrained inversions indicate that the TEM method can resolve conductive structures much more accurately than resistive ones, highlighted by the much tighter pdf over the conductive sediment layer compared to the resistive ice layer. The unconstrained inversions (Figure 5.6a) capture a similar structure to the true model, but they struggle to resolve true layer depths. The simple synthetic model (a) and thick resistive layered model (b) are relatively well resolved, however the more complicated synthetic models with thin layers and large resistivity contrasts (c, d and e) are not. The depth-averaged resistivity errors within the subglacial layer (calculated from the difference of the modal and true solutions) of each synthetic non-constrained solution are: a) 275 Ωm, b) 14 Ωm, c) 30 Ωm, d) 21 Ωm and e) 2000 Ωm. The addition of depth constraints (Figure 6b) improves the match throughout. The resistivity of the thin snow layers and conductive sediment layers are well-resolved in all synthetics, with depth-averaged resistivity errors within the subglacial layer reduced to: a) 8 Ωm, b) 14 Ωm, c) 23 Ωm, d) 10 Ωm and e) 25 Ωm (a factor of 34, 1, 1.3, 2.1 and 80 improvement on their unconstrained equivalents). Note, imaging beneath a conductive structure is difficult for the TEM method due to the attenuated signal (Blatter et al., 2018); however our constrained inversion results show the bottom of the conductive layers (in (b) – (e) to be much better resolved, i.e. to within < 10 meters.

The TEM method is generally more sensitive to conductance (the product of conductivity and thickness) rather than the layer conductivity or thickness alone (Geonics, 1994). Therefore, modelling is challenged by a non-unique problem, for example with thinner more conductive layers producing a similar TEM signal to thicker less conductive layers. The addition of depth constraints greatly reduces this

non-uniqueness enabling more accurate solutions to be obtained at all depths. However, an example where this TEM inversion struggles is when a thin conductive layer exists above a resistive basement (Figure B6). In this example (Figure B6 left panel), a thin layer 1 m thick and resistivity 1 Ωm has conductance of 1 S, equivalent to a 10 m thick semi-conductive layer of 10 Ωm resistivity. Inverting this synthetic example with depth constraints in MuLTI-TEM shows that such a thin conductive layer above resistive basement cannot be fully resolved even by the constrained inversion, appearing as a much thicker, less conductive layer.

This feasibility study highlights the significant added value of depth constraints when a complex resistivity structure is expected. It demonstrates MuLTI-TEM is promising for the potential distributions of resistivity beneath Midtdalsbreen.

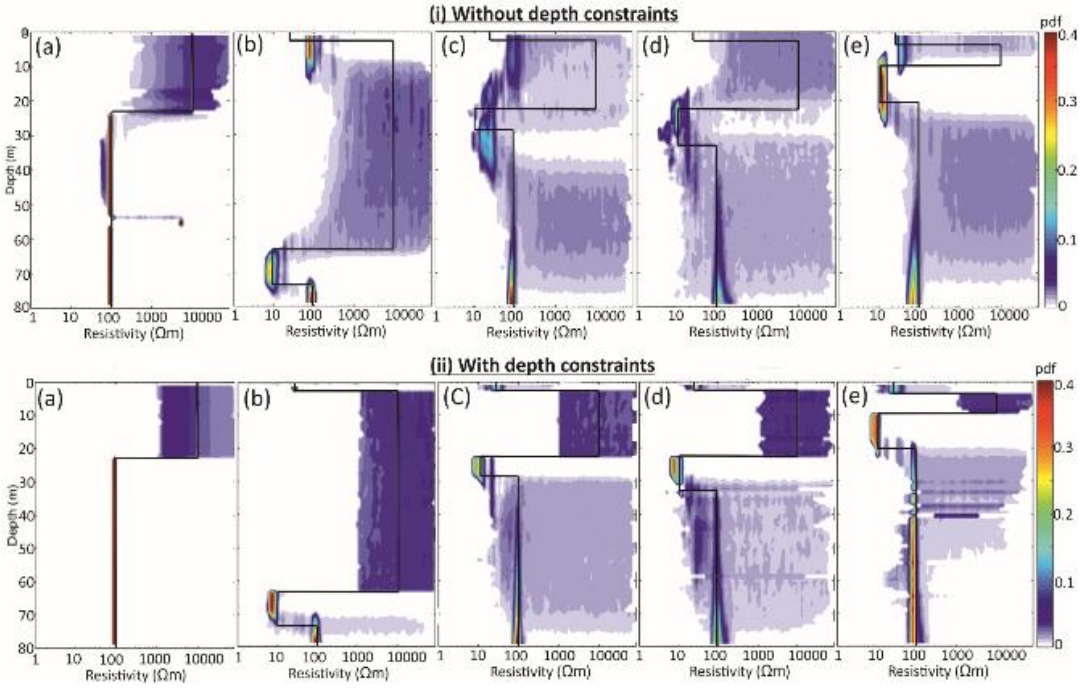

Figure 5.6 Posterior distributions of resistivity determined from MuLTI-TEM inversion. Top: i) without depth constraints. Bottom: ii) with depth constraints. The models correspond to those shown in Figure 5.4a-e, highlighted by the black line. The colour scale represents the probability density distribution of resistivity within the 95% credible interval.

5.6 Application of MuLTI-TEM to the Midtdalsbreen dataset

5.6.1 1D resistivity profiles

Using the data collected at Midtdalsbreen, we produced 1D resistivity profiles for the soundings acquired at the midpoint of lines A, B and C (Figure 5.7). Anomalous data points either induced by residual current still in the transmitter (at early timegates) or

below the background noise level (at later timegates) were removed, shown as "X" in Figure 5.7(ii). Inversions were run with depth constraints taken from the GPR dataset for the snow-ice and glacier bed interfaces (red and blue horizons, respectively, in Figure 5.7). The same inversion parameters were used as the synthetic study (Table B2), but with the maximum depth extended to 160 m to test the limit of DOI. The data variance (σ) was kept at 5% of the signal at each timegate as this was a good representation of the data variance of each data point calculated from the 3 stack recordings acquired in the field.

Posterior resistivity distributions are shown in Figure 5.7(i), comparison of data fit with 200 randomly chosen forward models from the model ensemble are shown in Figure 5.7(ii) and posterior distribution of the number of nuclei are shown in Figure 5.7(iii). The estimated uncertainty for the most likely solution is calculated as one-half of the interquartile range at each depth, used due to non-normal pdfs. As is clear from Figure 5.7(i), conductive layers identified within the subglacial material are well resolved with a tight pdf and low uncertainty. However, resistive layers (e.g., ice) have a wide pdf with large uncertainty estimates. For example, the uncertainty of the resistive ice layer is typically estimated as ~ ± 10^4 Ωm, whereas that of the conductive subglacial material is ~ ± 10^2 Ωm. The maximum DOI can also be identified in these distributions, expressed where the posterior distribution extends across the prior resistivity boundaries applied in a given layer (Table 5.2). This is 90 m for Line A, 87 m Line B and 76 m for Line C.

The 1D inversions show a ~10 m-thick layer, of 10^2 Ωm resistivity, directly under the ice, underlain in turn by conductive material of 10^0-10^1 Ωm for Line B and C. In contrast, Line A (off the ice margin, see Figure 5.1b) shows a ~70 m-thick resistive layer, 10^4-10^5 Ωm, immediately beneath the snow layer, underlain by either a very conductive thin layer (~1 Ωm) or a conductive material that extends to greater depth (these cannot be distinguished as it is close to the limit of DOI). We ensured that our methodology can discriminate the thick conductive layers observed in Lines B and C, and thin conductive layers underlain by resistive material approaching the DOI, using forward modelling. When compared (Figure B5) to the data at the midpoint of Line C, the thicker conductive model has the closest resemblance to the observed data. This analysis suggests a spatially varying pattern of subglacial resistivities from the front of the glacier up to Line C.

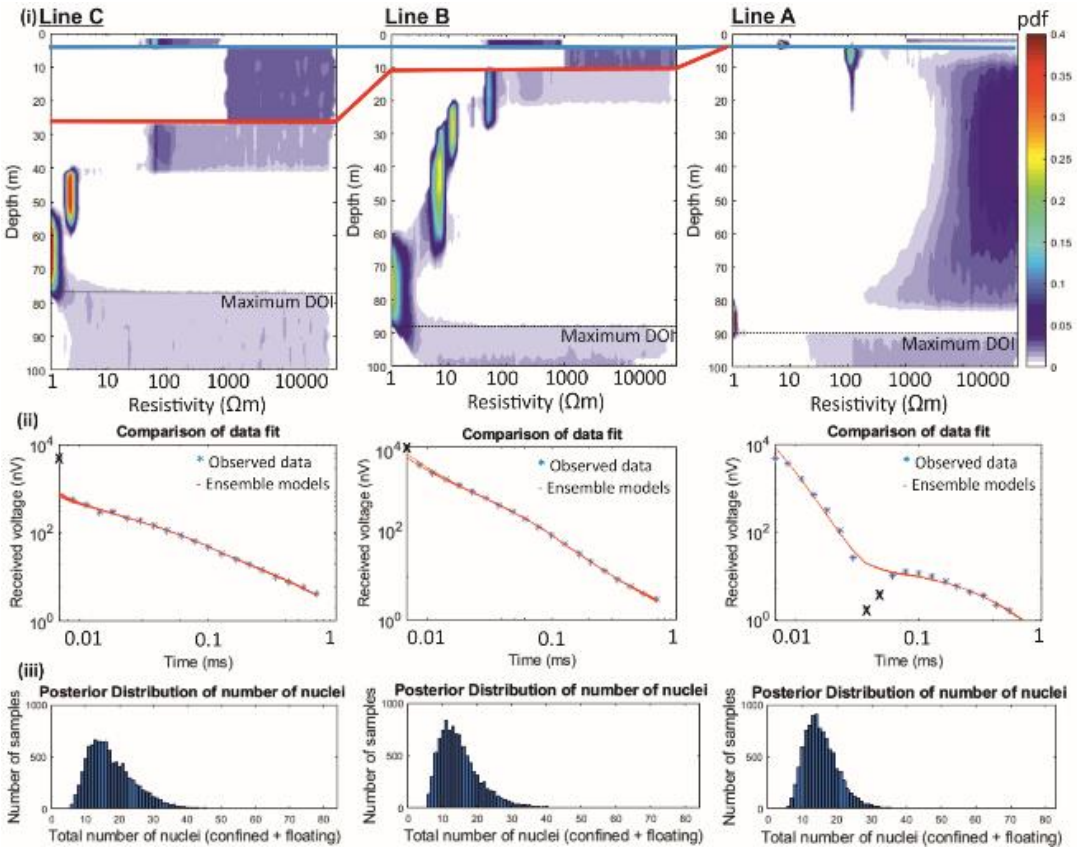

Figure 5.7 Results of the 1D soundings acquired at the midpoint of lines A, B and C inverted using MuLTI-TEM. i) resistivity posterior probability distributions, with the maximum depth of investigation (DOI) plotted as the black dotted line. The blue and red solid lines highlight the snow-ice and ice-material depths. ii) comparison of the observed data and 200 randomly chosen forward models from the model ensemble. The black X's show anomalous data points removed. iii) posterior distribution of number of nuclei.

5.6.2 2D resistivity profiles

MuLTI-TEM is used to invert multiple independent 1D soundings acquired along Lines A, B, C (4 m intervals) and D (8 m intervals). Again, anomalous data points either induced by residual current in the transmitter (at early timegates) or below the background noise level (at later timegates) were removed, shown as the grey regions in Figure 5.8 (left column). The raw signal acquired is generally above the background noise level for all time gates, except some anomalous points in the centre of Line A, corresponding with anomalous points at the NE end of Line D, highlighted in Figure 5.8 left column.

When using a central loop TEM survey configuration the 1D response is simply located at the centre of the transmitter, where the receiver is located. However, with an offset transmitter-receiver survey configuration, used in this study, the location of the 1D sounding is a subject of debate. Some place the location below the receiver

and others midway between the transmitter and receiver (Hoekstra and Blohm, 1990). The entire section between the transmitter and receiver is expected to influence the measurements, especially at late times as the current is diffuse. In what follows, we assume the 1D location of each sounding to be at the centre point between the transmitter and receiver, although we note subsurface conditions near the transmitter may have a slightly larger influence on the received voltage measure at early times, when the current loop radius is approximately the same as the transmitter loop radius and not overlapping the receiver offset position.

Inversions were run with depth constraints supplied from snow and ice horizons picked from the GPR data and using the same parameters as the synthetic study. We verified convergence of the solutions by running another Markov-chain and increasing the chain length to 1.5 million iterations: all tests reproduced the same posterior distribution. Consistent with initial observations in the 1D analysis, the 2D resistivity profiles (Figure 5.8, central column) highlight a wide range of subglacial resistivity values, from 10^0 to 10^5 Ωm, both along- and cross- glacier profiles, however there are some key consistent observations between these profiles, including

- a ~ 10^2 Ωm layer directly below the ice, for ice thicknesses < 20 m (mainly observed in Line B), which varies in thickness,
- a high resistive layer, 10^4-10^5 Ωm, in line A which matches line D at their intersection, and
- a lowermost layer of highly conductive material, ~10^0-10^1 Ωm, that generally extends to the DOI

The estimated uncertainties for the mode resistivity solutions are displayed in Figure 5.8 (rightmost column). This reiterates previous observations made from the synthetic study and 1D analysis, that conductive layers identified within the subglacial material are well resolved by the TEM method with low uncertainty, however TEM methods struggle to fully resolve the more resistive layers which therefore have a larger uncertainty. We note that marginal uncertainties along a 2D line can also be displayed as a 3D probability cube, with axes representing resistivity, line distance and depth, and colour bar representing the probability (e.g., Ray et al., 2014). This aids visualisation of the Bayesian solution and its uncertainty, particularly useful when characterising an anomalous target from a constant background resistivity e.g., a subglacial aquifer or lake underlain by bedrock.

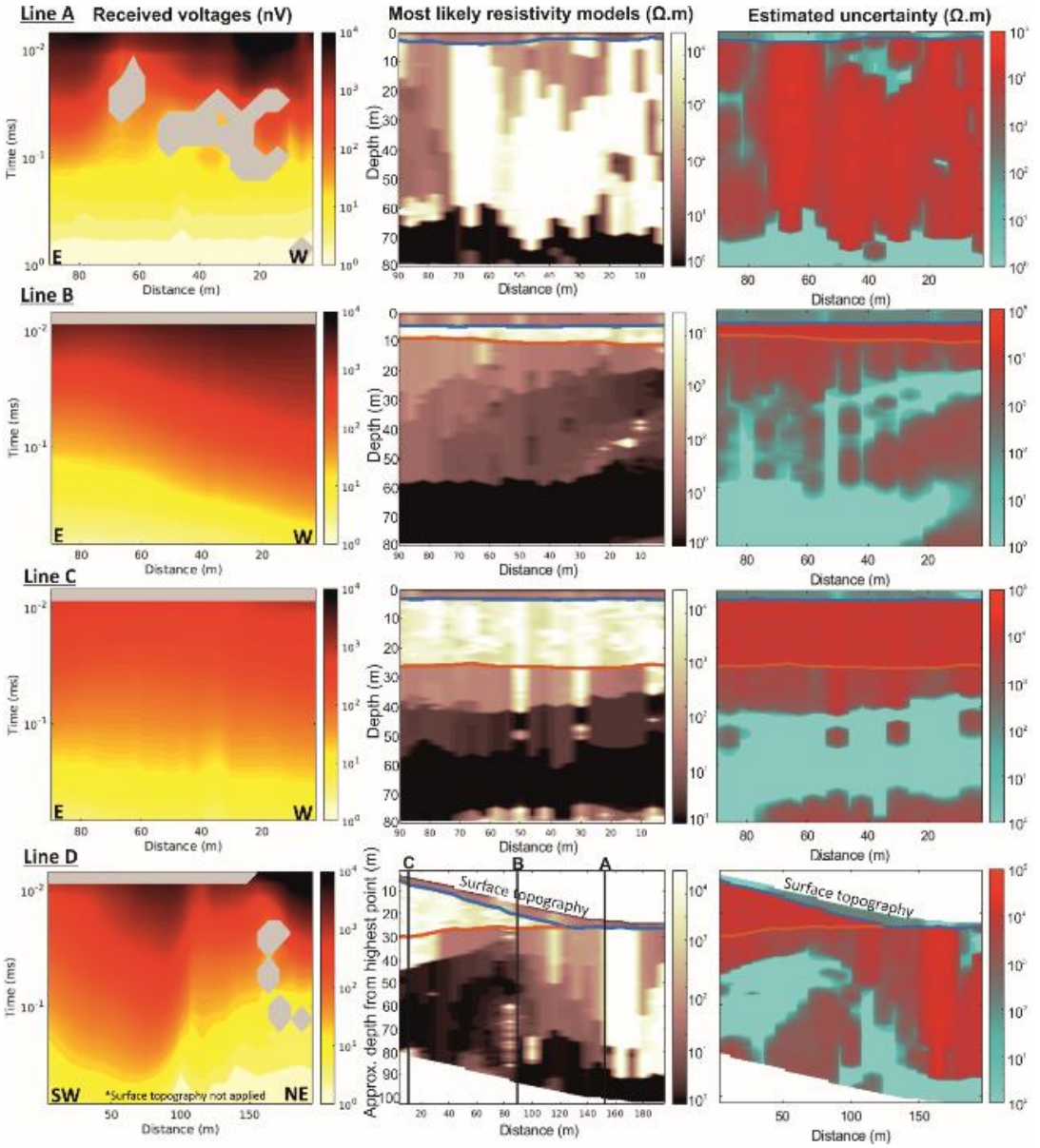

Figure 5.8 2D inversion outputs for Lines A-D from multiple 1D MuLTI-TEM inversions. Left column: received voltages input to MuLTI-TEM; central column: most likely 2D resistivity profiles; right column: estimated uncertainty (half the interquartile range of the posterior distribution). Snow and ice horizons are plotted in blue and red respectively.

5.7 Interpretation and Discussion

5.7.1 Joint interpretation of MuLTI-TEM with MuLTI seismic results

The variability of resistivity (10^0 – 10^5 Ωm) in our TEM profiles suggests a complex subsurface structure, in which subglacial water may be in liquid and frozen states. However, the nature of the matrix – whether sediment or bedrock – cannot be determined from resistivity alone. Resistivity is related to the resistivity of the pore

fluids divided by the fractional porosity. A commonly used approximation is given by Archie's law, which states that:

$$R = aR_W/\Phi^m \quad (5.5)$$

where R is the bulk resistivity of a saturated porous medium, Φ is the porosity, R_W is the pore fluid resistivity and m and a are empirical quantities determined by the geometry of the pores (Archie, 1942). A modified version can be used for clay-mineral bearing subglacial sediments e.g. Kulessa et al., 2006. However, it is difficult to distinguish material type, such as sediment or bedrock, from resistivity alone. By contrast, seismic shear wave methods are sensitive to the shear modulus, or stiffness, of a material but are insensitive to water content. However, a combined interpretation of resistivity and *Vs* profiles can be used to define a mutually-consistent system to characterise the material properties and water content of the subglacial environment. We do this using complementary seismic data, acquired alongside our TEM acquisitions in 2018.

The initial interpretation of the seismic data was presented in Killingbeck et al. (2019). This study excluded certain phase velocities on the grounds that they were too high (Figure B7); but this merit re-evaluation when compared with the co-located observation of high resistivity. Therefore, in this integrated interpretation, the high phase velocities are include, thus providing broader bandwidth dispersion curves.

Observing trends of *Vs* and resistivity in our profiles, three clear patterns emerge within the subglacial material:

i) zones of low *Vs* and low resistivity,

ii) high *Vs* and high resistivity, and

iii) high *Vs* with low resistivity (Figure 5.9; leftmost and centre columns).

These patterns have been used to define 3 different material types (Table 5.3). From previous electromagnetic and seismic studies (e.g., King et al., 1988; Schneider et al., 2013; Wu at al., 2017), liquid water in the pores of unconsolidated material has a low resistivity and low *Vs* (we define this as partially frozen sediment), whereas frozen water in pores is very resistive with a high *Vs* (defined as frozen sediment/permafrost). We assume the bedrock comprises of phyllite, crystalline granite and gneiss with a high *Vs* and high resistivity. However, the resistivity profiles show the bedrock to have a very low resistivity suggesting it could be highly fractured and weathered with saline water in the fractures. The presence of saline water can decrease the electrical resistivity by as much as 9 orders of magnitudes (Olhoeft, 1981). An alternative explanation for this high *Vs*, low *R* lithology is consolidated sediment /till rich in clay-

minerals, although the presence of bedrock clasts and outcrops around the glacier foreland suggest the former.

Table 5.3 *Vs* and resistivity ranges for subglacial material lithologies, used in analysis of both MASW and TEM. Material types have been defined from King et al., 1988; Mikucki et al., 2015 and Killingbeck et al., 2019.

Material	***Vs* range (m/s)**	**Resistivity range (Ωm)**
Partial frozen sediment/till	$Vs < 1600$	$50 < R < 500$
Frozen sediment/permafrost	$Vs > 1900$	$R > 500$
Weathered/fractured bedrock with saline water	$Vs > 1900$	$R < 50$

The resistivity and *Vs* profiles are linearly interpolated such that they have mutually consistent sample intervals (1 m) and depth extents (40 m). The TEM and seismic were acquired in the same field season along the same lines, the acquisition parameters were chosen so the two methods could be directly comparable. However, the location of each 1D TEM sounding and seismic common midpoint gather are offset by 2 m, therefore, we linearly interpolated and resampled both the resistivity and *Vs* solutions, originally sampled every 4 m (Line A, B and C) and 8 m (Line D), to every meter thus making them directly comparable. Killingbeck et al. (2019) consider abrupt lateral variations in the *Vs* profiles to be noise, and interpret the broader variation in lateral and vertical character as the representative velocity structure. Therefore, since the lateral resolution of the *Vs* profiles (estimated from the length of the geophone spread; 30-40 m) is larger than that of the resistivity profiles (estimated from the horizontal spacing between 1D soundings; 4-8 m), we apply lateral smoothing to the *Vs* profiles during the joint analysis. After these steps, we obtain a smooth joint interpretation of the predicted subglacial material shown in Figure 5.9 (rightmost column) and Figure 5.10.

The joint interpretation shows zones of mainly sediment and thick permafrost (> 40 m) at the front of the glacier, along line A, matching observations at the corresponding intersection point with line D. Note the sparse, disconnected areas identified as bedrock in Line A are regarded as a misallocation, potentially due to abrupt lateral variations in *Vs* which we regard as noise. Unfrozen sediment occurs directly below the ice at line B, with a varying thickness of 30 m at the eastern end to 5 – 10 m towards the western end. In contrast, a mixture of frozen and unfrozen sediment is observed directly below the ice at line C, typically ~ 10 m thick. Underlying the ice

and sediment layers in all lines is the conductive bedrock with its structure shown clearly in the cross glacier line, D. This also highlights a thin zone of frozen sediment directly under the glacier tongue, matching observations from the GPR data shown in Reinardy et al. (2019), suggesting there is a frozen tongue.

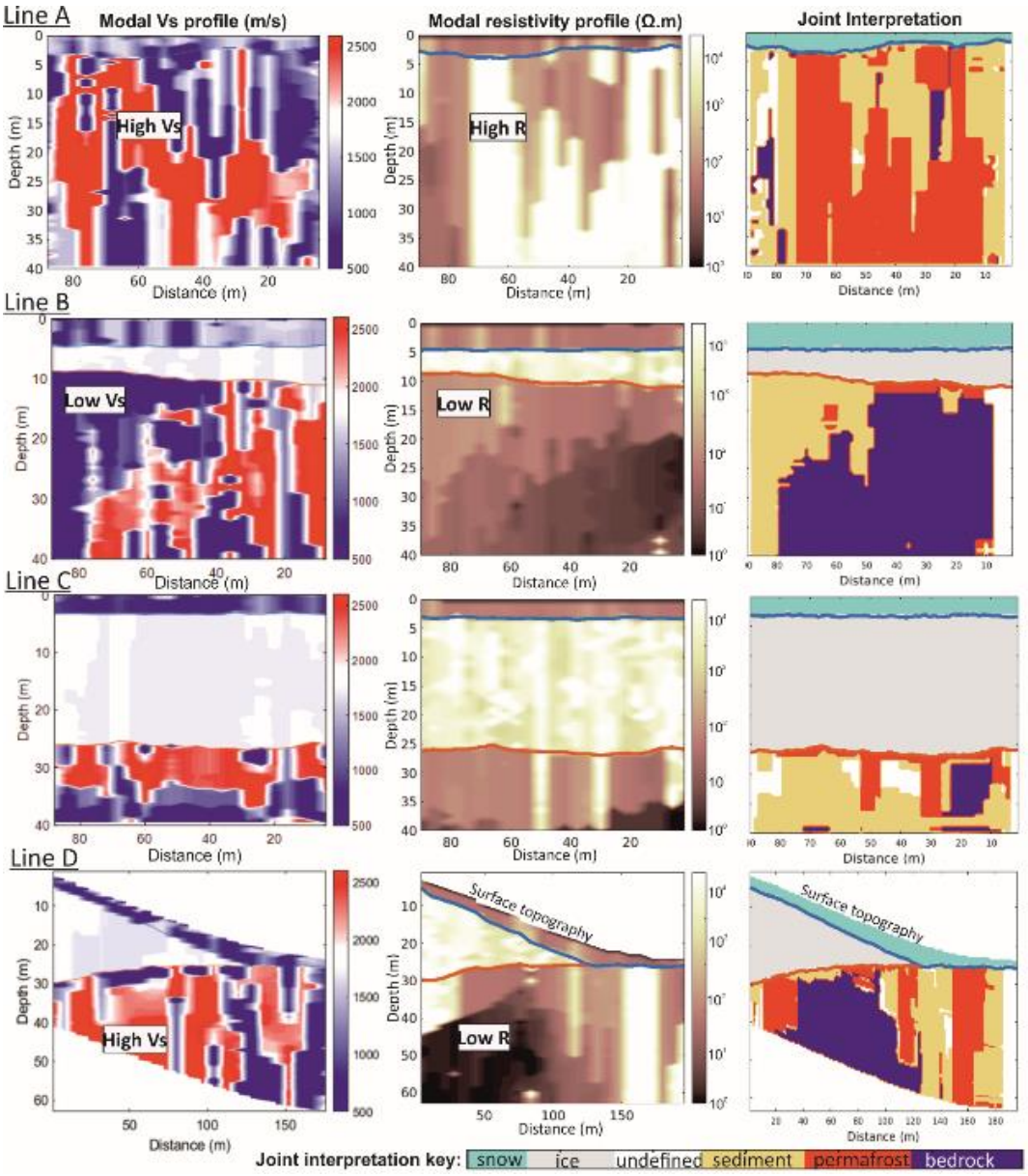

Figure 5.9 Joint interpretation of *Vs* and resistivity profiles for lines A-D. Left column: modal *Vs* solution. Central column: modal resistivity solution. Example of areas with high *Vs* and high *R* is shown in Line A, low *Vs* and low *R* is shown in Line B and high *Vs* with low *R* is shown in Line D. Right column: estimated subglacial material when applying *Vs* and resistivity conditions of Table 5.3. Note the sparse, disconnected areas identified as bedrock in Line A are regarded as a miss-allocation.

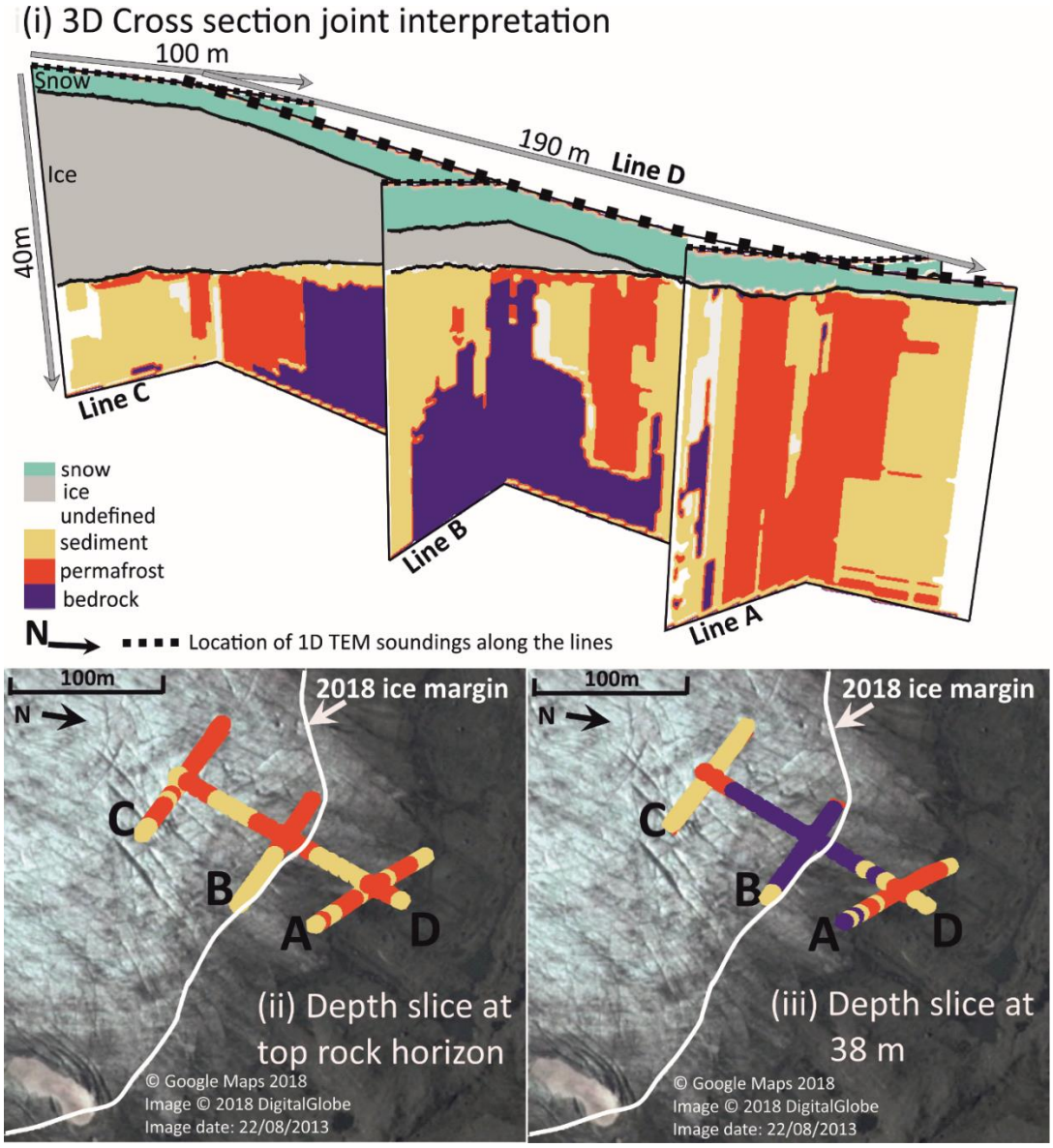

Figure 5.10 i) 3-D cross-section of lines A-D, showing the subglacial material estimated from applying *Vs* and resistivity conditions stated in Table 5.3. ii) Depth slice through 3-D cross at the top rock horizon. iii) Depth slice through 3-D cross-section at 38 m.

5.7.2 Discussion

MuLTI-TEM combines a probabilistic approach with external depth constraints to mitigate ambiguous, non-unique solutions found in conventional TEM inversions. It provides a robust quantitative uncertainty analysis of any chosen model at all depth levels, also providing an accurate estimate of DOI using the posterior distribution. The addition of depth constraints improves the characterisation of material, particularly beneath conductive layers and enables a faster convergence of the solution, as demonstrated in the synthetic study. We note other methods could be used to enhance the efficiency of the transdimensional inversion, potentially providing

better convergence rates, such as proposing the birth parameters from the prior (instead of a Gaussian distribution) e.g., Dosso et al., 2014. Further still, having access to the full posterior distribution enables subsets of the posterior model probabilities to be selected, testing various hypothesis about the model structure (Ray and Key, 2012).

Nevertheless, the success of MuLTI-TEM depends fundamentally on the input data quality and its suitability for the specific target imaged. With TEM methods, it is often not possible to determine separately the conductivity and thickness, only the conductance (product of thickness and conductivity) can be determined. Therefore, thorough synthetic modelling should be undertaken before acquiring data in the field to determine if the survey design and time range of measurements is sufficient and suitable to detect specific targets.

Although this paper focuses on the specific TEM survey design used in this study, ground based 10 x 10 m transmitter with receiver 15 m away, MuLTI-TEM can be used with most TEM datasets. The Leroi forward modelling code can be used in frequency or time-domain mode to model most TEM transmitter/receiver combinations, ground based or airborne, and needs only to be adapted to the user specific TEM configuration (Raiche, 2008). Equally, depth constraints are provided as numerical inputs and can therefore be supplied from any external source e.g., borehole measurements or any complementary inference from an external geophysical data source. In our Midtdalsbreen case study, the uncertainty in the depth constraints applied is negligible (decimetre-accuracy from GPR data) compared to the observed data uncertainty (meter accuracy from TEM), motivating us to fix the internal interface depths. However, there remains a finite resolution in GPR data hence we are considering a modification to the MuLTI-TEM code to make it compatible with uncertain interface depths. This would also benefit depth constraints supplied from more uncertain data sources, thus making MuLTI-TEM more broadly applicable.

This paper has presented how a joint analysis of three geophysical datasets can increase our understanding of the material in the subsurface and provide a more detailed interpretation. Using GPR information as a depth constraint, we have combined insight from TEM and seismic shear wave methods to provide a detailed characterisation of the material beneath the margins of Midtdalsbreen. Critically, TEM data reveal hydrological properties to which the seismic analysis was insensitive, whereas the seismic data indicate the varying stiffness of the subglacial material. Future extensions of this interpretative strategy could include petrophysical relationships to obtain and/or guide interpretations of the volumetric proportions of water, ice and air in the subsurface (e.g., Hauck et al., 2008). A further promising extension would be a modification to calculate the joint distribution of resistivity and

Vs (rather than only the marginal distributions discussed in this paper) which could lead to a more accurate understanding of the subsurface structure (utilizing the structural similarities between resistivity and seismic velocity (e.g., Wisén and Christiansen, 2005). Such a combined approach would also result in more detailed analysis of the Midtdalsbreen margin, including a probabilistic facies classification, leading to a framework by which aquifer properties, such as porosity, water content and pore fluid conductivity/salinity, beneath large ice masses could be quantified. This could have a direct impact on basal parameters used as input to ice-flow models for a better prediction of ice motion over time, and hence future sea level rise.

5.8 Conclusions

The material properties of the subglacial environment, in particular their water content and saturation, can be characterised by inferences of their resistivity, obtained from TEM measurements. However, conventional TEM inversions provide solutions that are non-unique with no quantification of uncertainty estimates in depth and resistivity. This paper has presented the inversion algorithm 'MuLTI-TEM', used to overcome such problems. Our method uses a transdimensional Bayesian inversion approach adapted from the MuLTI algorithm (Killingbeck et al., 2018), which incorporates independent depth constraints to limit the solution space reducing ambiguity. Synthetic testing of multiple different scenarios representing a small glacier underlain by sediment showed the addition of depth constraints greatly improves numerical convergence. This results in constrained solutions having a large improvement in the depth-average uncertainty of the output model, an average factor of 15 improvement on their unconstrained equivalents, with little computational power needed to obtain these results.

A joint interpretation, using *Vs* and resistivity boundaries, of the MuLTI-TEM results with MuLTI seismic surface wave results, presented in Killingbeck et al. (2019), considers three subglacial material classifications: sediment ($Vs < 1600$ m/s, $50\ \Omega m < R < 500\ \Omega m$), permafrost ($Vs > 1600$ m/s, $R > 500\ \Omega m$) and weathered/fractured bedrock with saline water in the fractures ($Vs > 1900$ m/s, $R < 50\ \Omega m$). Their spatial extent, within the Midtdalsbreen's subglacial environment, shows a mixture of sediment and permafrost directly below the ice, and in the moraine at the front of the glacier, underlain by bedrock.

MuLTI-TEM is highly versatile being compatible with most TEM survey designs, ground based or airborne, as the Leroi forward modelling code can model most transmitter/receiver combination, along with the depth constraints being provided

from any external source. This study presents novel methodologies, through MuLTI-TEM and MuLTI, by which other glacier and ice-sheets subglacial material can be explored, highlighting the importance of acquiring multiple geophysical datasets for accurately characterising the subglacial environment.

5.9 Code availability

MuLTI-TEM can be found at: https://github.com/eespr/MuLTI-TEM, DOI 10.5281/zenodo.3471638.

5.10 Acknowledgements

This project was funded by the UK NERC SPHERES DTP, grant NE/L002574/1. Fieldwork was funded by the research project 'Snow Accumulation Patterns on Hardangerjøkulen Ice Cap (SNAP)', itself funded by the European Union's Horizon 2020 project INTERACT, under grant agreement No 730938. The time domain electromagnetic equipment was supplied by NERC Geophysical Equipment Facility, loan 1090. Fieldwork was greatly assisted by Emma Pearce, James Killingbeck and Kjell Magne Tangen. Alan Hobbs and all NERC GEF staff are thanked for their support and advice throughout the project.

5.11 References

Andersen, J. L., and Sollid, J. L.: Glacial chronology and glacial geomorphology in the marginal zones of the glaciers Midtdalsbreen and Nigardsbreen, south Norway, Norsk Geogr. Tidsskr, 25, 1–38, 1971.

Archie, G. E.: Classification of carbonate reservoir rocks and petrophysical considerations, AAPG Bulletin, 36(2), 278-298, 1942.

Auken, E., Christiansen, A.V., Kirkegaard, C., Fiandaca, G., Schamper, C., Behroozmand, A.A., Binley, A., Nielsen, E., Effersø, F., Christensen, N.B. and Sørensen, K.: An overview of a highly versatile forward and stable inverse algorithm for airborne, ground-based and borehole electromagnetic and electric data, Exploration Geophysics, 46(3), 223-235, 2015.

Auken, E., Jørgensen, F., and Sørensen, K. I.: Large-scale TEM investigation for groundwater, Exploration Geophysics, 34(3), 188-194, 2003.

Barnett, C. T.: Simple inversion of time-domain electromagnetic data. Geophysics, 49(7), 925-933, 1984.

Blatter, D., Key, K., Ray, A., Foley, N., Tulaczyk, S. and Auken, E.: Trans-dimensional Bayesian inversion of airborne transient EM data from Taylor Glacier, Antarctica, Geophysical Journal International, 214(3), 1919-1936, 2018.

Bodin, T. and Sambridge, M.: Seismic tomography with the reversible jump algorithm, Geophysical Journal International, 178(3), 1411-1436, 2009.

Bodin, T., Sambridge, M., Tkalčić, H., Arroucau, P., Gallagher, K. and Rawlinson, N.: Transdimensional inversion of receiver functions and surface wave dispersion, Journal of Geophysical Research: Solid Earth, 117(B2), 2012.

Booth, A. D., Clark, *R*. A., Kulessa, B., Murray, T., Carter, J., Doyle, S. and Hubbard, A.: Thin-layer effects in glaciological seismic amplitude-versus-angle (AVA) analysis: implications for characterising a subglacial till unit, Russell Glacier, West Greenland, The Cryosphere, 909-922, 2012.

Christensen, N. B. and Tølbøll, *R*. J.: A lateral model parameter correlation procedure for one-dimensional inverse modelling. Geophysical Prospecting, 57(5), 919-929, 2009.

Christiansen, A. V. and Auken, E.: A global measure for depth of investigation. Geophysics, 77(4), WB171-WB177, 2012.

Christoffersen, P., Bougamont, M., Carter, S. P., Fricker, H. A. and Tulaczyk, S.: Significant groundwater contribution to Antarctic ice streams hydrologic budget, Geophysical Research Letters, 2003-2010, 2014.

Constable, S. C., Parker, *R*. L., and Constable, C. G.: Occam's inversion: A practical algorithm for generating smooth models from electromagnetic sounding data. Geophysics, 52(3), 289-300, 1987.

CSIRO and AMIRA: P223Suite Open source exploration geophysical electromagnetic modelling tools, online: http://p223suite.sourceforge.net/accessed on 1/02/2019.

Dosso, S. E., Dettmer, J., Steininger, G., and Holland, C. W. Efficient trans-dimensional Bayesian inversion for geoacoustic profile estimation. Inverse Problems, 30(11), 114018, 2014.

Etzelmüller, B. and Hagen, J. O.: Glacier–permafrost interaction in Arctic and alpine mountain environments with examples from southern Norway and Svalbard, in Harris C and Murton JB eds. Cryospheric systems: glaciers and permafrost. Geological Society, London, Special Publication, 242, 11–27, 2005.

Geonics.: PROTEM47D operating manual, Geonics Ltd., 1994.

Hauck, C., Bach, M. and Hilbich, C.: A 4-phase model to quantify subsurface ice and water content in permafrost regions based on geophysical data sets, Proceedings Ninth International Conference on Permafrost, Fairbanks, Vol. 1, Kane D.L. and Hinkel K.M. (eds), Institute of Northern Engineering, University of Alaska Fairbanks, 675-680, 2008.

Hauck, C., Guglielmin, M., Isaksen, K. and Vonder Mühll, D.: Applicability of frequency-domain and time-domain electromagnetic methods for mountain permafrost studies, Permafrost and Periglacial Processes, 12(1), 39-52, 2001.

Hoekstra, P., and Blohm, M. W.: Case histories of time-domain electromagnetic soundings in environmental geophysics, Geotechnical and environmental geophysics, 2, 1-15, 1990.

Hoekstra, P. and McNeill, D.: Electromagnetic probing of permafrost, in Proceedings of Second International Conference on Permafrost, 517–526, Yakutsk, Russia, 1973.

Killingbeck, S. F., Booth, A. D., Livermore, P. W., West, L. J., Reinardy, B. T. I. and Nesje, A.: Subglacial sediment distribution from constrained seismic inversion, using MuLTI software: Examples from Midtdalsbreen, Norway, Annals of Glaciology, 1-14 , 2019.

Killingbeck, S. F., Livermore, P. W., Booth, A. D. and West, L. J.: Multimodal Layered Transdimensional Inversion of Seismic Dispersion Curves with Depth Constraints, Geochemistry, Geophysics, Geosystems, 19(12), 4957-4971, 2018.

King, M. S., Zimmerman, *R*. W. and Corwin, *R*. F.: SEISMIC AND ELECTRICAL PROPERTIES OF UNCONSOLIDATED PERMAFROST, Geophysical Prospecting, 36(4), 349-364, 1988.

Kulessa, B. (2007), A Critical Review of the Low-Frequency Electrical Properties of Ice Sheets and Glaciers, *Journal of Environmental and Engineering Geophysics*, 12(1), 23-36, doi:doi:10.2113/JEEG12.1.23.

Kulessa, B., B. Hubbard, and G. H. Brown. (2006). Time-lapse imaging of subglacial drainage conditions using three-dimensional inversion of borehole electrical resistivity data. *Journal of Glaciology*, 52(176), 49-57, doi:10.3189/172756506781828854.

Livermore, P. W., Fournier, A., Gallet, Y. and Bodin, T.: Transdimensional inference of archeomagnetic intensity change, Geophysical Journal International, 215(3), 2008-2034, 2018.

Merz, K., Maurer, H., Rabenstein, L., Buchli, T., Springman, S. M. and Zweifel, M.: Multidisciplinary geophysical investigations over an alpine rock glacier. Geophysics, 81(1), WA1-WA11, 2016.

Mikucki, J. A., Auken, E., Tulaczyk, S., Virginia, *R*. A., Schamper, C., Sørenson, K. I., Doran, P. T., Dugan, H. and Foley, N.: Deep groundwater and potential subsurface habitats beneath an Antarctic dry valley, Nature Communicatoins, 6, 6381, 2015.

Minsley, B. J., Abraham, J. D., Smith, B. D., Cannia, J. C., Voss, C. I., Jorgenson, M. T., Walvoord, M. A., Wylie, B. K., Anderson, L., Ball L. B., Deszcz-Pan, M., Wellman, B. K. and Ager, T. A.: Airborne electromagnetic imaging of discontinuous permafrost, Geophys. Res. Lett., 39, L02503, 2012.

Mosegaard, K. and Tarantola, A.: Monte Carlo sampling of solutions to inverse problems, Journal of Geophysical Research: Solid Earth, 100(B7), 12431-12447, 1995.

Olhoeft, G. *R*.: Electrical properties of granite with implications for the lower crust, Journal of Geophysical Research: Solid Earth, 86(B2), 931-936, 1981.

Raiche, A.: Leroi version 8.0, Fortran 95 program, developed for AMIRA project P223F, 2008.

Ray, A. and Key, K. Bayesian inversion of marine CSEM data with a trans-dimensional self parametrizing algorithm. Geophysical Journal International, 191(3), 1135-1151, 2012.

Ray, A., Key, K., Bodin, T., Myer, D. & Constable, S. Bayesian inversion of marine CSEM data from the Scarborough gas field using a transdimensional 2-D parametrization. Geophys. J. Int. 199, 1847–1860, 2014.

Reinardy, B.T.I., Booth, A.D., Hughes, A.L.C., Boston, C.M., Åkesson, H., Bakke, J., Nesje, A., Giesen, *R*.H. and Pearce, D.M.: Pervasive cold ice within a temperate glacier – implications for glacier thermal regimes, sediment transport and foreland geometry, Cryosphere, 13, 827–843, 2019.

Reinardy, B. T. I., Leighton, I., and Marx, P. J.: Glacier thermal regime linked to processes of annual moraine formation at Midtdalsbreen, southern Norway, Boreas, 42, 896–911, 2013.

Rozenberg, G., Henderson, J. D., Sartorelli, A. N., and Judge, A. S.: Some aspects of transient electromagnetic soundings for permafrost delineation, In Workshop on Permafrost Geophysics (pp. 85-5). Hanover, NH: Cold Reg. Res. Lab, 1985

Schneider, S., Daengeli, S., Hauck, C., and Hoelzle, M.: A spatial and temporal analysis of different periglacial materials by using geoelectrical, seismic and borehole temperature data at Murtèl–Corvatsch, Upper Engadin, Swiss Alps, Geographica Helvetica, 68(4), 265-280, 2013.

Siegert, M. J., Kulessa, B., Bougamont, M., Christoffersen, P., Key, K., Andersen, K. *R*., Booth, A. D. and Smith, A. M.: Antarctic subglacial groundwater: a concept paper on its measurement and potential influence on ice flow, Geological Society, London, Special Publications, 197-213, 2018.

Spies, B.: Depth of investigation in electromagnetic sounding methods, Geophysics, 54, 872-888, 1989.

Todd, B. J., and Dallimore, S. *R*.: Electromagnetic and geological transect across permafrost terrain, Mackenzie River delta, Canada, Geophysics, 63(6), 1914-1924, 1998.

Vignoli, G., Fiandaca, G., Christiansen, A. V., Kirkegaard, C., and Auken, E.: Sharp spatially constrained inversion with applications to transient electromagnetic data. Geophysical Prospecting, 63(1), 243-255, 2015.

Willis, I. C., Fitzsimmons, C. D., Melvold, K., Andreassen, L. M., and Giesen, *R*. H.: Structure, morphology and water flux of a subglacial drainage system, Midtdalsbreen, Norway, Hydrol. Processes, 26, 3810–3829, 2012.

Wisén, *R*. and Christiansen, A. V.: Laterally and mutually constrained inversion of surface wave seismic data and resistivity data, Journal of Environmental & Engineering Geophysics, 10(3), 251-262, 2005.

Wu, Y., Nakagawa, S., Kneafsey, T. J., Dafflon, B., and Hubbard, S.: Electrical and seismic response of saline permafrost soil during freeze-Thaw transition, Journal of Applied Geophysics, 146, 16-26, 2017.

Chapter 6 Feasibility study for polar ice-sheet applications

This thesis has thus far considered applications of MuLTI and MuLTI-TEM on a glacier with ice thicknesses < 25 m. However, the dynamically-important regions of Antarctica and Greenland feature much thicker ice than the Midtdalsbreen example presented here. For example, Siegert et al. (2018) suggest that the subglacial aquifers which may underlie Antarctica's Institute Ice Stream (IIS) may be beneath 2 km of ice. Furthermore, subglacial water is an important consideration across a range of depth and time scales; while water directly at the glacier bed may influence present-day ice dynamics, thicker subglacial aquifers may act as a reservoir for prolonging and potentially buffering the supply of basal water over a longer time period. Therefore, development of geophysical techniques which can image deep within the subglacial environment is vital for monitoring and mapping such reservoirs.

In this Chapter I undertake a feasibility study for polar ice-sheet applications using MuLTI and MuLTI-TEM. I model different scenarios of the Institute Ice Stream, as presented in Siegert et al. (2018), where ice thicknesses are 2 km.

6.1 Synthetic ice-sheet models

Five different scenarios for IIS, based on models developed by Siegert et al. (2018), are constructed including:

(a) ice sheet directly underlain by bedrock (Figure 6.1a),
(b) ice sheet directly underlain by a high porosity, liquid groundwater, sedimentary basin (on top of bedrock) (Figure 6.1b),
(c) ice sheet directly underlain by permafrost 100 m thick, on top of sediment and basement (Figure 6.1c).
(d) ice sheet directly underlain by permafrost 500 m thick, on top of sediment and basement (Figure 6.1d).
(e) ice sheet directly underlain by permafrost 1000 m thick, on top of sediment and basement (Figure 6.1e).

Each layer is matched with the resistivity parameters defined in Siegert et al. (2018) and elastic parameters typical of each material (Chapter 4; King et al., 1988; Peters et al., 2008). Rayleigh wave and TEM synthetics are created from these models and inverted using MuLTI and MuLTI-TEM, with the depth constraint of the 2 km ice thickness (as could be defined from, e.g., low-frequency radar sounding; Siegert et

al., 2016), to assess their reliability at recovering the true models, within the deep subglacial environment.

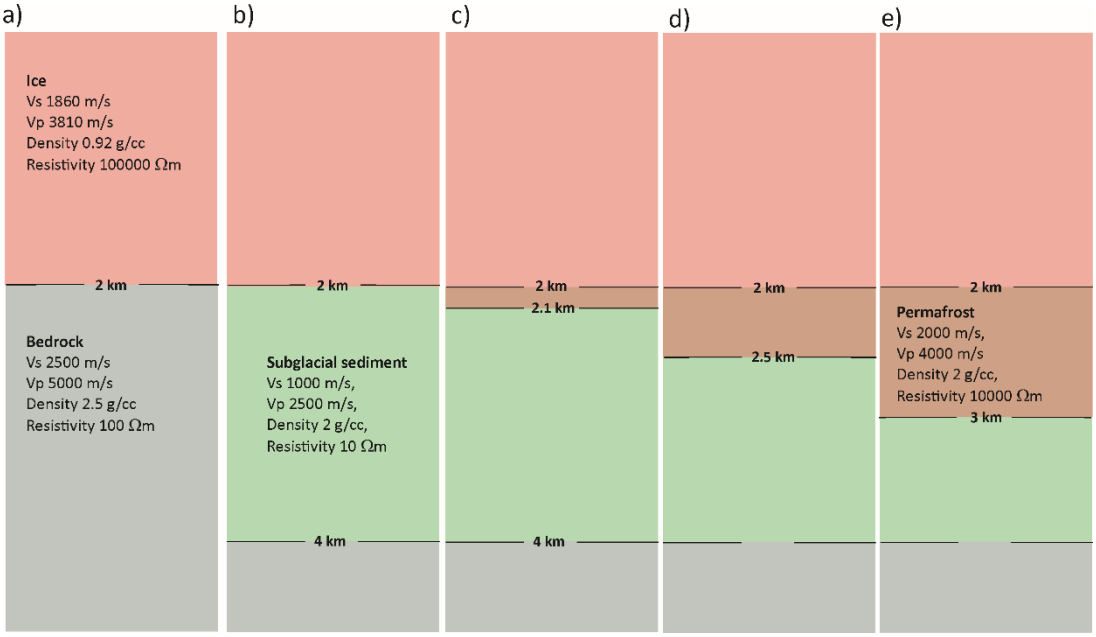

Figure 6.1 1-D synthetic models of different scenarios of the Institute ice stream, Antarctica, as presented in Siegert et al. (2018), with elastic and resistivity parameters typical of each material.

6.2 Feasibility of resolving *Vs* structure from Rayleigh waves using MuLTI

Synthetic Rayleigh wave dispersion curves were simulated using the modelling algorithm *mat_disperse*, for all 1-D models shown in Figure 6.1. The *mat_disperse* function solves the eigenvalue problem for Rayleigh waves in an elastic vertically heterogeneous halfspace and returns the modal phase velocities (Rix and Lai, 2003). The DWM method, described in Chapter 3 and 4, was not used, as this generates a full synthetic waveform based on MASW acquisition which would have to be converted to a dispersion curve. Here, the frequency information is used directly aiming to characterise the frequency ranges needed to resolve the *Vs* structure under thicker ice (2km).

Synthetic dispersion curves were generated from 0.01 Hz to 2 Hz, shown in Figure 6.2. Frequencies greater than 2 Hz are dominated by the ice velocity only, and therefore do not provide any extra information in the inversion for characterising the subglacial structure. In all models with a complex velocity structure and a low velocity zone, (b-e), multiple higher order modes dominate at frequencies > 0.5 Hz. The dispersion curves are also plotted with an approximate depth range, using the 1/3

wavelength approximation (Gazetas 1982), in Figure 6.2. This highlights that the lowest resolvable layer thicknesses are limited to ~ 500 m.

The dominant curve from either the fundamental or two higher order modes were used as input to MuLTI. This was to avoid higher order mode ambiguities at relatively high frequencies, shown in Chapter 3. The parameters listed in Table 6.1 were assigned, described in Chapter 3, and posterior distributions of *Vs* were derived using MuLTI.

Figure 6.3 shows the results from the *Vs* inversions for all synthetic models a-e. The simplest 2 layer synthetic model ((a) ice-basement) has a *Vs* structure recovered accurately, with mode solution 0.1 % within the true model. The 3 layer synthetic model ((b) ice-sediment-basement) has a *Vs* structure also recovered well, with mode solution 6.6 % within the true model, and identifies the unconstrained sediment-basement boundary to +/- 160 m. However, the added permafrost layer in models c-e is not recovered well. The 100 m permafrost layer, model c, is too thin to even be identified (the thinnest resolvable layer is ~ 500 m, Figure 6.2), yet the inversion still identifies the unconstrained sediment and basement layers, accurate to +/- 10 %. Inversions of models d and e have a large uncertainty range of +/- 1050 m/s, calculated from the 95 % credible interval, between 2 km and 4 km (which includes the permafrost and sediments layers). Their mode solutions are 22 % (model d) and 36 % (model e) to within the true model, note the 1000 m permafrost synthetic inversion does identify a high velocity layer directly under the ice. However, these solutions are not fully converged, highlighted by the posterior distribution of number of nuclei, and therefore need to be investigated further by running more chains and testing different inversion parameters.

Table 6.1 Inversion parameters used in MuLTI (MuLTI-TEM) for synthetic tests a-e in Figure 6.1.

Inversion parameters				
Maximum Depth			4500 m	
Number of floating nuclei			50	
Burn in			10000	
Number of iterations			500000	
Number of chains			3	
σ_{change}, σ_{move}, σ_{birth}			200 m/s (2) , 500 m, 400 m/s (2)	
Number of layers			2	
Material	**Resistivity prior boundaries (Ωm)**	**Density (g/cm^3)**	***Vp* (m/s)**	***Vs* (m/s) prior boundaries**
Ice	$5x10^3 – 5x10^5$	0.92	3810	1700-2000
Rock	$1 – 5x10^4$	2.3	3800	500-2800

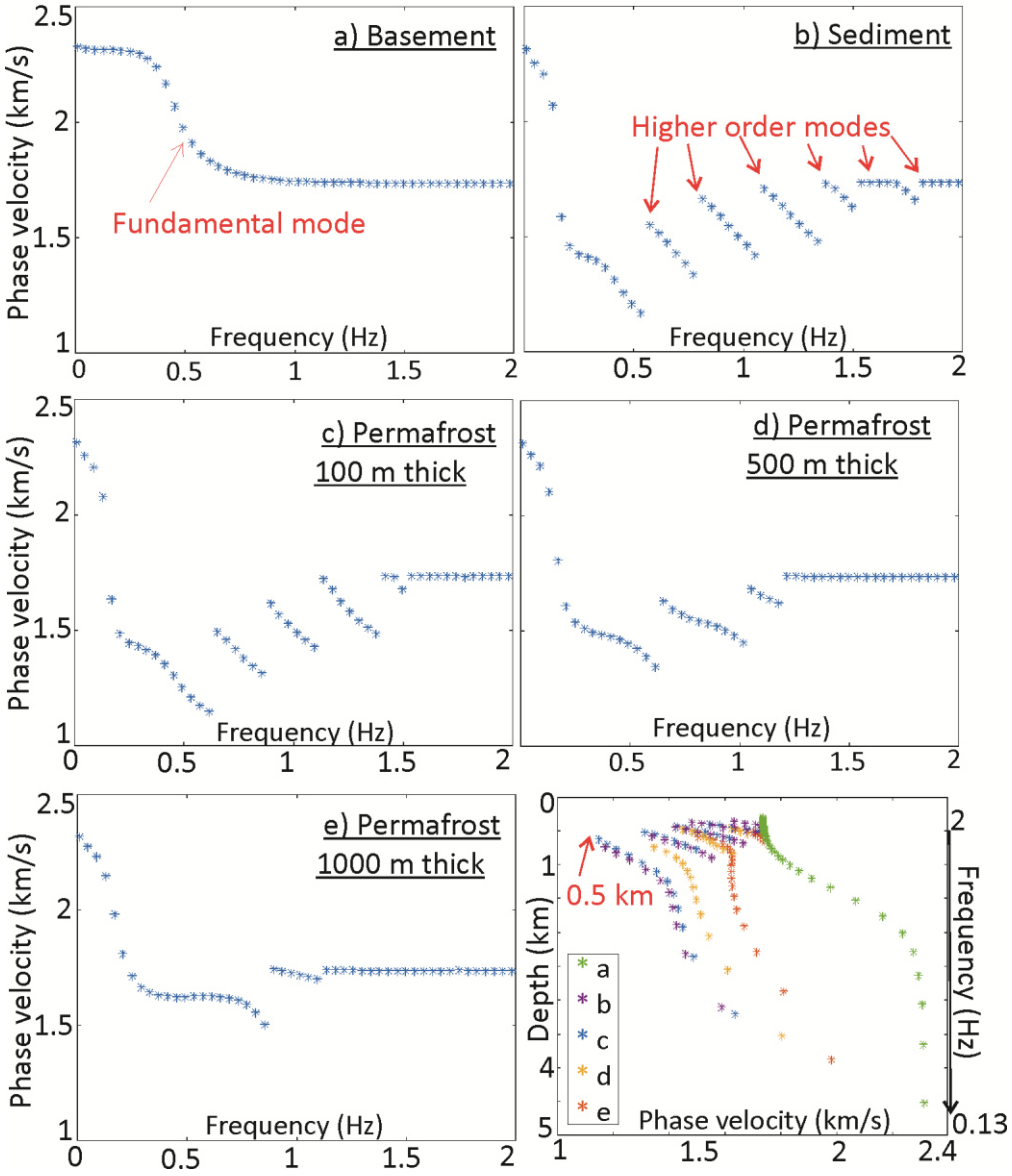

Figure 6.2 Dispersion curve analysis for synthetic models a – e, Figure 6.1, simulated using the modelling algorithm *mat_disperse*. Panel e shows the depth resolution (and so also the sounding depth), estimated using the one third wavelength approximation.

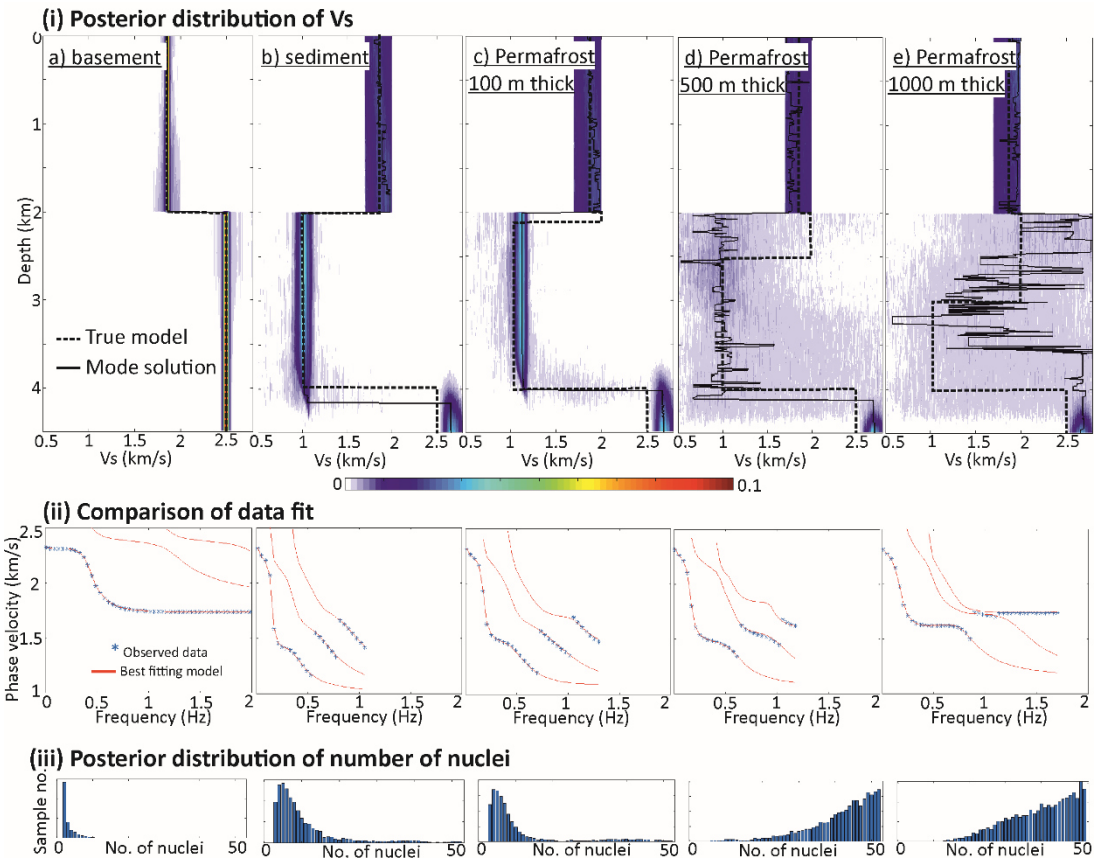

Figure 6.3 Results of synthetic models a - e inverted using MuLTI with fixed depth constraints at base-ice, 2 km. i) *Vs* posterior probability distributions with the true model plotted in the black dashed line and mode solution plotted in the black solid line. ii) Comparison of the observed data with the forward model of the best fitting ensemble model. iii) Posterior distribution of number of nuclei.

6.3 Feasibility of resolving resistivity structure from TEM using MuLTI-TEM

Key and Siegfried in 2017 showed for ice thicknesses > 1000 m airborne EM systems, previously used in Antarctica, would be poor at measuring the subglacial environment as the differentiating signal from the subglacial material would be below the system noise level. However, ground based systems can have a much larger loop size (up to 2000 m), than what is practically possible for helicopters (~ 22 m), therefore, the system noise floor is much smaller, e.g., a loop with an order of magnitude larger area would result in a noise floor ten times smaller. They suggest that ground-based TEM soundings made with powerful antennas could be useful for mapping subglacial conductivity beneath thick ice.

Therefore, synthetic TEM soundings were simulated with 1000 m x 1000 m transmitter loop, 10 Amps current and 3 Hz transmitter waveform frequency, using

the Leroi forward modelling algorithm (Raiche, 2008), for all models shown in Figure 6.1. The inversion parameters listed in Table 6.1 were assigned and MuLTI-TEM was run with depth constraints applied at the base of the ice, 2 km.

The results are shown in Figure 6.4. The simplest 2 layer synthetic model ((a) ice-basement) resistivity structure is recovered accurately, with mode solution 2.4 % within the true model. For the sediment layer in model b, resistivity value is recovered well, with mode solution 0.6 % within the true model, however the unconstrained sediment-basement boundary (from 10 to 100 Ωm) is not detected at 4 km, this occurs also for models c and d. Yet, the added permafrost layers in models c-e are identified and resolved in the inversion, with mode solution 39 % (c), 44 % (d) and 41 % (e) within the true model. Model e is the only model to detect a resistivity increase near the unconstrained sediment-basement boundary, +/- 300 m within the true model boundary.

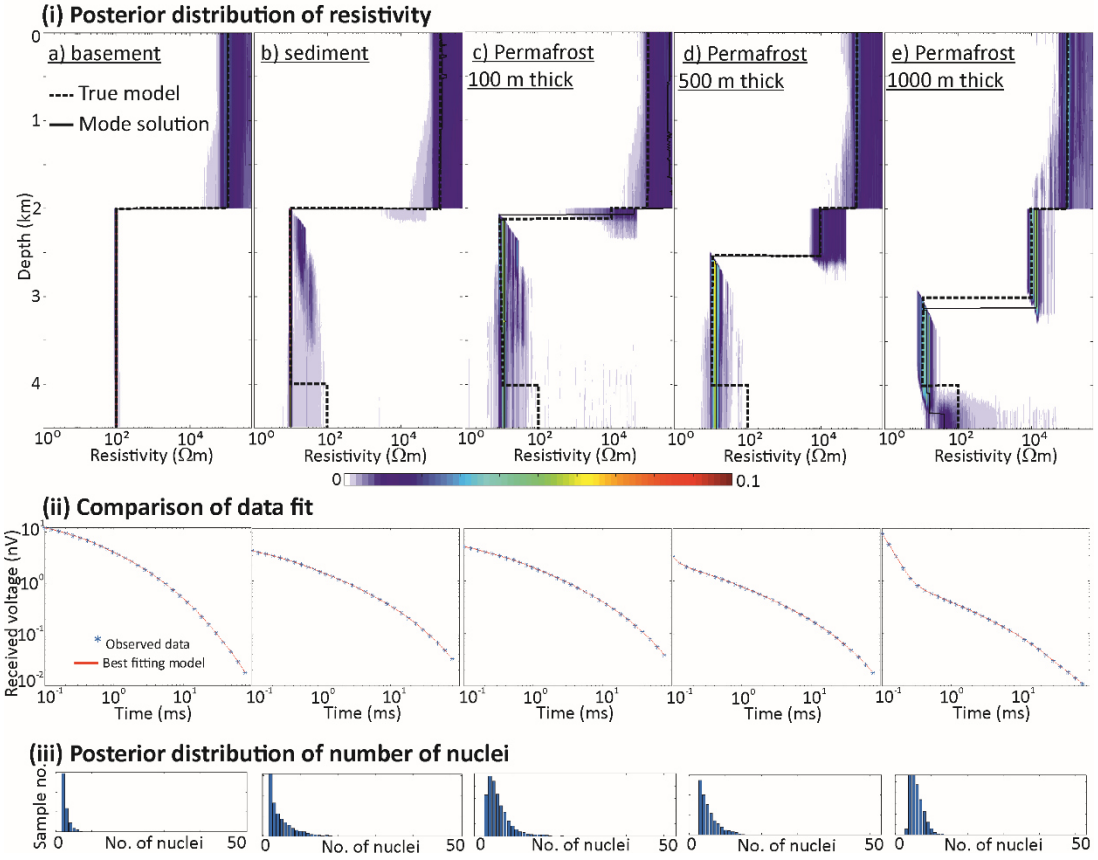

Figure 6.4 Results of synthetic models a - e inverted using MuLTI-TEM with fixed depth constraints at base-ice, 2 km. i) resistivity posterior probability distributions with the true model plotted in the black dashed line and mode solution plotted in the black solid line. ii) comparison of the observed data with the forward model of the best fitting ensemble model. iii) posterior distribution of number of nuclei.

6.4 Outlook for Antarctic and Greenland applications

6.4.1 Summary of feasibility study

Here, I have completed a preliminary feasibility study to understand some of the strengths and limitations using the MuLTI and MuLTI-TEM methods, by modelling similar structures for IIS as predicted in Siegert et al. (2018). Low frequency (< 2 Hz) dispersion curves from Rayleigh waves can resolve large scale (> 1 km) *Vs* structure under 2 km ice; all inversions detected the unconstrained sediment-basement boundary at 4 km depth. However, the inversions struggled to resolve *Vs* structures less than 1 km thick, highlighted in the permafrost models. On the other hand, TEM soundings from a high power system can recover smaller scale (< 1 km) resistivity structure under 2 km ice, the inversion of synthetic model c detected a permafrost layer only 100 m thick. However, the deeper unconstrained sediment-basement boundary (at 4 km) was not detected in most models. This highlights that Rayleigh wave dispersion curves and TEM soundings have different resolution sensitives, but that these are mutually complementary. Large scale structure can be identified using surface waves, whereas the smaller scale detail directly under the ice can be resolved with TEM. Such imaging could reconcile interpretative ambiguities in reflection seismic interpretations, e.g., Booth et al. (2012).

The next step in this study would be to test many more synthetic models, representing different ice thicknesses, subglacial material layer thicknesses and properties, and bedrock properties, to further test the resolution and limitation of each technique.

For MuLTI, further work could include passive seismic studies and the ability to resolve the dominant fundamental and higher order modes. Simulated receiver locations and sources could be used to find the optimum survey design for different subsurface models. Furthermore, the effect of anisotropic ice fabric on the seismic waves should be considered and modelled (e.g., Smith et al., 2017).

For MuLTI-TEM, a better understanding of the background electrical noise levels, expected from the data acquisition environment, should be sought and used for synthetic tests (as detailed in Key and Siegfried (2017)), including testing different transmitter loop sizes and current. This will provide a better understanding of how long one can realistically measure (late time measurements) before the signal is below the background noise level.

6.4.2 Potential seismic sources and TEM systems used on polar ice sheets

This feasibility study shows how MuLTI and MuLTI-TEM can be used to identify subglacial structure under 2 km thick ice. Both techniques rely on appropriate

frequency sampling of the data, (and power output in the TEM case) to enable them to resolve the targeted subglacial structure.

When seismic signals are coherent across a passive seismic recording network, array techniques can be used to calculate phase velocities of incoming waves (e.g., Rost and Thomas, 2002). Walter et al. (2015) used glacier seismicity and a match-field processing technique to obtain frequency-dependent phase velocity measurements on the Greenland ice sheet, with bandwidth 1 – 6 Hz. Diez at al. (2016) analysed Rayleigh wave dispersion curves (with bandwidth 4 - 18 Hz) on Antarctica's Ross ice shelf, using ambient seismic noise, by beamforming the passive-source seismic array data to obtain the main propagation direction of the surface waves. However, these frequency ranges are not low enough to penetrate under 2 km of ice. Here, in my example, frequencies < 2 Hz are sensitive to the subglacial environment, which in turn causes problems resolving layer thicknesses < 1 km. This low frequency range could most likely be generated from regional earthquake sources (Qian et al., 2019), volcano tectonic earthquakes (McNutt et al., 2015) and primary and secondary microseisms (Chevrot et al., 2007).

For TEM, to image deeper features requires a low frequency transmitter waveform (providing longer time measurements) and large current and transmitter loop (Equation 5.1). The Geonics TEM47 system, used in Chapter 4, is appropriate for shallow resistivity soundings down to 150 m and can use transmitter loops sizes 5 m to 100 m with current 1 to 3 Amps, ideal for the Midtdalsbreen case study. However in this Chapter, the Geonics TEM67 system is simulated for a deep resistivity sounding. The TEM67 is appropriate for resistivity soundings greater than 1000 m and can use transmitter loops sizes up to 2000 m with a maximum current of 25 Amps.

In summary, for these methods to be used successfully on thick ice sheets in Antarctica or Greenland, some of the key survey requirements are listed below.

For surface wave seismic:

- broadband seismometers which can measure the frequency range required,
- deployed in an array suitable for measuring wavelengths appropriate for the targeted depth. Where the array length should be at least equal to the maximum desired wavelength, which approximately corresponds to three times the desired investigation depth (Foti et al., 2018; Gazetas 1982),
- synthetic testing to model different array sizes and wavelengths recovered,
- a low frequency source which generates frequencies compatible for targeting depths under the ice thickness, e.g., primary and secondary microseisms (Chevrot et al., 2007).

For TEM:

- a powerful TEM system (e.g., Geonics TEM67),
- large transmitter loop and current. In this example 1000 x 1000 m was used, although a smaller loop with multiple turns can reproduce the same moment, providing a more efficient survey design.
- synthetic testing to model different transmitter loop sizes and current, including an estimate of background electrical noise levels expected from the data acquisition environment (generally low on thick ice sheets).

Chapter 7 Discussion

In this chapter, I first consider the current strengths and limitations of the MuLTI and MuLTI-TEM framework. I then discuss potential methodologies to directly combine these datasets in a joint *R-Vs* inversion/interpretation. Finally, further MuLTI developments are proposed, which address some of the current limitations of the framework, in particular, with regards to fixing and estimating unknown parameters.

A summary of all MuLTI methods presented in the thesis so far, and in this discussion chapter, are detailed in Table 7.1. This lists the family of MuLTI techniques in a hierarchy of increasing complexity, starting with: the simplest MuLTI and MuLTI-TEM (Chapter 3 and 5), MuLTI III then introduces Vp and density from a prescribed distribution (Section 7.3.1), MuLTI IV considers the effect of uncertain layer depths (Section 7.3.2) and finally MuLTI MASW+TEM considers a probabilistic joint *R-Vs* inversion (Section 7.2). All these developments will be discussed in this chapter.

Table 7.1 Summary table of all MuLTI methods presented and discussed in the thesis.

Method	**Choice of prior distribution**					**Posterior PDF output**
	Vs	***Vp***	**Density**	***R***	**Layer depths**	
MuLTI	Uniform	Single value	Single value	-	fixed	*Vs*
MuLTI-TEM	-	-	-	Uniform	fixed	*R*
MuLTI III	Uniform	Prescribed distribution	Prescribed distribution	-	fixed	*Vs, Vp,* density
MuLTI IV (TEM)	Uniform	Prescribed distribution	Prescribed distribution	(Uniform)	Prescribed distribution	*Vs, Vp,* density, (*R*) layer depths
MuLTI MASW+ TEM (joint *R-Vs* inversion)	Uniform	Prescribed distribution	Prescribed distribution	Uniform	Prescribed distribution	*Vs, Vp,* density, *R,* layer depths, facies classifications, petrophysical interpretations (e.g., f_w, f_i and f_{air})

7.1 Development of the Bayesian framework: strengths and limitations

The MuLTI Bayesian framework is easily adaptable to multiple different geophysical methods. In this thesis, I have presented MuLTI for the inversion of Rayleigh wave dispersion curves and MuLTI-TEM for the inversion of TEM soundings, to obtain posterior distributions on *Vs* and *R* structure of the subsurface. It could also be developed for (for example) seismic refraction methods (e.g., Montgomery et al., 2017) and electrical resistivity tomography methods (e.g. Andersen et al., 2003).

The Bayesian formulation within MuLTI is employed to produce a PDF of the posterior distribution enabling access to the whole ensemble of models. This allows multiple outputs, e.g., average, mode, and a variety of marginal posterior distributions, to be examined to provide a comprehensive uncertainty analysis. Further still, having access to the full posterior distribution enables subsets of the posterior model probabilities to be selected, making it possible to test various hypothesis about the model structure (Ray and Key, 2012). Along a 2D line, marginal uncertainties can be displayed as a 3D probability cube, with axes representing subsurface property, line distance and depth, and colour bar representing the probability (e.g., Ray et al., 2014). This aids visualisation of the Bayesian solution and its uncertainty, particularly useful when characterising an anomalous target from a constant background e.g., a subglacial aquifer or lake underlain by bedrock.

MuLTI adopts a transdimensional reverse jump approach, in which constraints for internal interface depths, provided numerically from external datasets, narrow the model space. For the choice of prior distribution required in the Bayesian transdimensional calculations, most authors assume that the prior subsurface structure is depth independent so that the prior PDF analytically separates completely into its constituent parts (e.g. Bodin & Sambridge, 2009). This is followed in the simplest geometry considered in this thesis in which no depth constraints are applied. However, as shown in Equation (3.7) such a depth-independent form is in fact not necessary and the prior distribution on the model (where the model includes both the depth and geophysical property value for each nucleus) can be written in terms of conditional probabilities. In this formulation, the prior distribution is completely specified (but does not have a straightforward analytic form) and the usual transdimensional methodology can be applied.

In the case studies discussed in Chapters 4 and 5, the uncertainty in the depth constraints applied is small compared to the observed data uncertainty (e.g., decimetre-scale depth accuracy from GPR data, vs. meter-scale accuracy from seismic

and TEM), motivating the internal interface depths taken to be fixed. Yet, this may not be the case for depth observations from other external datasets, for example seismic reflection (Anandakrishnan et al., 1998) and refraction data (Montgomery et al., 2017), therefore further development to add uncertainty bounds in depth constraint should be considered (Section 7.3.2).

MuLTI and MuLTI-TEM solve for structure in depth only. In Chapters 4 and 5, this has been extended to two spatial dimensions by running multiple 1-D inversions along the lines acquired at Midtdalsbreen. For MuLTI-TEM, each TEM sounding is recorded at single surface points along the line, therefore the inherent lateral resolution of MuLTI_TEM, extended to 2-D, is mainly driven by the measurement spacing. However, for MuLTI, the dispersion curve picked from CMPCC gathers (along a 2-D seismic line) represent an average of the geophone spread and assumes the subsurface directly beneath is horizontally homogeneous. This causes lateral smearing along the line, where the horizontal resolution is as large as the CMP spread length. Therefore, in Chapter 4 offsets of the CMPCC gathers are limited to minimise lateral smearing, although this reduces the resolution of the dispersion curves picked, especially at the low frequencies, highlighted in the test field campaign (Chapter 2). With current advances in 2-D and 3-D seismic modelling algorithms (e.g., Zhang et al., 2019; Cao et al., 2019), the development of a 2-D implementation of MuLTI could circumvent this limited lateral resolution issue.

The benefits gained from using a Bayesian sampling-based method comes at the price of significant computational cost. For each 1D inversion of MuLTI and MuLTI-TEM needed 1 million iterations for the posterior distribution to converge. Furthermore, if no depth constraints are applied, multiple chains are also required to prevent the unconstrained solution converging to a local minima. The speed of each iteration depends fundamentally on the speed of the forward model computation and the number of nuclei chosen in that iteration, with more nuclei taking longer, for example: a single iteration using MuLTI (gpdc forward modelling algorithm) takes 0.001 seconds with 2 fixed nuclei and 0.065 seconds with 22 fixed nuclei. Therefore, one million iterations can take between ~5 and ~20 hours, which is also very similar for MuLTI-TEM. This could be reduced further by breaking down the one million iterations, for example, into 5 chains of 200000 iterations and using parallel computing constructs to run the chains in parallel (e.g., the use of 5 processing cores would reduce the time by a factor of 5). Other methods could also be used to enhance the efficiency of the transdimensional inversion, potentially providing faster and better convergence rates, such as proposing the birth parameters from the prior (instead of a Gaussian perturbation from the current model) e.g., Dosso et al. (2014).

In the following sections, I discuss some strengths and limitations specific to the MuLTI and MuLTI-TEM algorithms.

7.1.1 MuLTI

Although this thesis focuses on Rayleigh wave dispersion curves derived from active source seismic data, with high-frequency sources and shallow depth penetration, MuLTI can be equivalently applied to dispersion curves from passive sources (e.g., Walter et al., 2014; Picotti et al., 2017). The Geopsy forward modelling code, used in MuLTI, has the capability to model dispersion curves with frequencies <1 Hz. MuLTI would allow such data to be inverted with depth constraints drawn from, for example, radio-echo sounding datasets. Chapter 6 presented a feasibility study for imaging deeper targets, specifically under polar ice sheets 2 km thick, using low frequency (0.01 - 2 Hz) dispersion curves. This study showed that large scale (> 1 km) *Vs* structure, under 2 km ice, can be resolved to within 6 % of the true model, however layers < 1 km thick proved more difficult to resolve, with results to within 36 % of the true model.

A potential criticism of the methodology is that it only inverts for *Vs* while holding *Vp* and density constant throughout. A further development of the algorithm would be to also consider inverting simultaneously for *Vp* and density. In addition to the increased computational cost of solving for two extra unknowns, there may be too many solutions in the model space which fit the data within its tolerance, so the uncertainties may be too large to be useful. In MuLTI, by deriving material-layer boundaries I am able to fix *Vp* and density appropriately in each layer according to the material expected. This is an improvement from inversions that have no defined layers, with *Vp* and density fixed throughout the model space (e.g. Hayashi, 2012). A further improvement is to use a prior distribution for both *Vp* and density that is far more refined (and possibly depth-dependent) than the uniform distribution adopted in MuLTI. This has been implemented in MuLTI III, discussed further in section 7.3.1.

7.1.2 MuLTI-TEM

MuLTI-TEM is compatible with any ground-based TEM survey design parameters. Chapter 6 presented a feasibility study for imaging under polar ice sheets 2 km thick using a simulated powerful TEM system with 1000 m x 1000 m transmitter loop, 10 Amps current and 3 Hz transmitter waveform frequency. This study showed TEM can recover smaller scale (< 1 km) resistivity structure under 2 km ice, detecting layers as thin as 100 m. However, the inversion struggled to detect the deeper sediment-basement boundary, at 4 km, in most models.

Furthermore, the original Leroi forward modelling code, developed in Fortran 95 (Raiche, 2008), can be used in frequency or time-domain mode to model most EM transmitter/receiver combinations, ground based or airborne. Such surveys include, for example, (i) moving loop surveys with one or more magnetic dipole receivers moving at fixed horizontal offsets with respect to a rectangular loop, (ii) surface magnetic dipole-dipole surveys, (iii) coincident loop surveys, (iv) borehole magnetic dipole-dipole surveys and (v) CSAMT (controlled source audio magnetotellurics). The configuration in the Leroi code used can be adapted to the user's specific EM configuration in MuLTI-TEM.

The success of MuLTI-TEM depends fundamentally on the input data quality and its suitability for the specific target imaged. In general, with TEM methods, it is often not possible to determine separately the conductivity and thickness, only the conductance can be determined. Therefore, synthetic modelling along with in-field survey design testing for the recovery of a 1-D subsurface profile (Chapter 5) should be completed to determine if the survey design and time range of measurements are sufficient.

7.2 Joint *R*-*Vs* inversion strategy

Although the MuLTI and MuLTI-TEM frameworks integrate different data types in constrained inversions, it would be valuable to integrate MASW and TEM datasets into a fully-coupled joint inversion (MuLTI MASW+TEM). In this section, I firstly discuss a methodology for presenting the facies classifications (of Chapter 5) of the subglacial environment in a probabilistic manner, using the joint probabilistic outputs of *Vs* and *R*, from MuLTI and MuLTI-TEM. I then apply a petrophysical inversion, using derived petrophysical relationships which directly combine *R* and *Vs* to obtain the volumetric proportions of water, ice and air in the subsurface.

7.2.1 Probabilistic facies classification

The Midtdalsbreen facies classification shown in Figure 5.9 and 5.10, and defined in Table 5.3, uses the mode solutions of *Vs* and *R* individually, to identify the different facies in a relatively qualitative sense. It is possible to combine the facies classification in a probabilistic manner but, for this, the joint probability distribution of *Vs* and *R* is needed. If I assume *Vs* and *R* were independent variables, the normalised PDFs for *Vs* and *R* may be combined, by calculating the product,

$$P(Vs = v_s \; and \; R = r) = P(Vs = v_s).P(R = r) \tag{7.1}$$

for all *Vs* and *R* (an example of this analysis is shown in Figure 7.1). However, although I can readily calculate the mode of this distribution to assess the facies classification, the uncertainty (however quantified) is a numerical value which is difficult to translate into a probability of miss-classification. Also realistically, *Vs* and *R* are not independent variables with depth, as they both depend on the same underlying subsurface structure. The joint probability density function ($f_{Vs,R}(v_s, r)$) for two continuous random variables is given by,

$$f_{Vs,R}(v_s, r) = f_{R|Vs}(r|v_s) f_{Vs}(v_s) = f_{Vs|R}(v_s|r) f_R(r) \quad (7.2)$$

where $f_{R|Vs}(r|v_s)$ and $f_{Vs|R}(v_s|r)$ are the conditional distributions of *R* given $Vs=v_s$ and of *Vs* given *R=r.* Currently, I do not have access to these conditional distributions but only to the marginal distributions for each separate variable, $f_{Vs}(vs)$ and $f_R(r)$. A direct joint *Vs-R* Bayesian inversion would provide an estimate of this joint probability distribution and output the facies classifications in a probabilistic manner.

This probabilistic facies classification could be achieved by sampling models populated with both elastic and resistivity parameters and combining the likelihood functions from the seismic and TEM forward models, e.g., Hou et al. (2006). The model vector would therefore be given by,

$$m = [dp_1 \dots, dp_k, Vs_1 \dots, Vs_k, R_1 \dots, R_k, k, dpc_1 \dots, dpc_l, Vsc_1 \dots, Vsc_l, Rc_1 \dots, Rc_l] \quad (7.3)$$

where *dp* is the depth of each nucleus, *k* is the number of unconfined nuclei and *l* is the number of confined (*c*) nuclei, as described in Chapter 3. Forward modelling of the seismic dispersion curve g_1, using the models' elastic parameters and the gpdc algorithm, and TEM response g_2, using the models' resistivities and Leroi algorithm, can be combined to estimate the joint *Vs-R* likelihood probability $p(d|m)$. Since the seismic and TEM techniques are sampling different geophysical properties (seismic wave velocity and resistivity), I can consider them independent (Hou et al, 2006). Thus, the joint *Vs-R* likelihood probability is given by,

$$p(d|m) = p_1(d_1|m).p_2(d_2|m) \quad (7.4)$$

where $d_1 = g_1(m) + \varepsilon_1$ and $d_2 = g_2(m) + \varepsilon_2$ represents the observations of the seismic surface waves and TEM responses (ε denotes the difference between observations and forward model responses), respectively. I assume the probability of the *i*th datum $PV_i(f_i)$ and $R_i(t_i)$ is normally distributed about the nearest modal value, $c_{gpdc}(f_i)$ and $c_{Leroi}(t_i)$, at frequency f_i and time t_i, with standard deviation $\sigma_{PVi}(f_i)$ and $\sigma_{Ri}(t_i)$, respectively. Assuming that each datum for the seismic (indexed by $i = 1, 2 \dots N_{data}$) and TEM (indexed by $j = 1, 2 \dots M_{data}$) datasets is independent, the likelihood $p(d|m)$ of the joint *Vs-R* model m is then proportional to:

$$\prod_{i=1}^{N_{data}} e^{-\frac{(PV_i - c_{gpdc}(f_i))^2}{2\sigma_{PV}(f_i)^2}} \cdot \prod_{j=1}^{M_{data}} e^{-\frac{(R_j - c_{Leroi}(t_j))^2}{2\sigma_R(t_j)^2}} \quad (7.5)$$

The prior information for *Vs*, *R* and any depth constraints can be input and applied in the same way as described in Chapter 3. During sampling of the posterior distribution, using the MCMC algorithm, at each step, a new model *m′* can be proposed that differs from the current model by one of five perturbations, which depends on a set of user specified parameters ($\sigma_{changeVs}$, $\sigma_{changeR}$, σ_{move}, $\sigma_{birthVs}$ and σ_{birthR}) whose values affect the speed of convergence to the posterior distribution, i.e.:

- change *Vs*: same as MuLTI, defined in Chapter 3.
- change *R*: perturb the resistivity of a randomly chosen nucleus by a random amount distributed as $N(0,\sigma_{changeR}^2)$.
- move nucleus: same as MuLTI, defined in Chapter 3. Note, *Vs* and *R* stay the same for the randomly chosen nucleus.
- birth: add a floating nucleus to the existing model whose depth is uniformly distributed $U[0, dp_{max}]$ and whose *Vs* is distributed $N(Vs, \sigma_{birthVs}^2)$, where *Vs* is the value of *Vs* based on the current nuclei distribution, and *R* is distributed $N(r, \sigma_{birthR}^2)$, where r is the value of *R* based on the current nuclei distribution.
- death: same as MuLTI, defined in Chapter 3.

Each proposed model would be tested to see if it satisfies a certain acceptance criterion, shown in Equation 3.8, with all accepted models (including prior models when a proposed model is not accepted) added to the model ensemble. The facies classifications, detailed in Table 5.3, can also be applied to all models in the chain and added to an ensemble of facies classifications. This methodology would provide a posterior distribution of *Vs*, *R* and the facies classification, all with the same model space (in depth) and posterior distribution of number of nuclei.

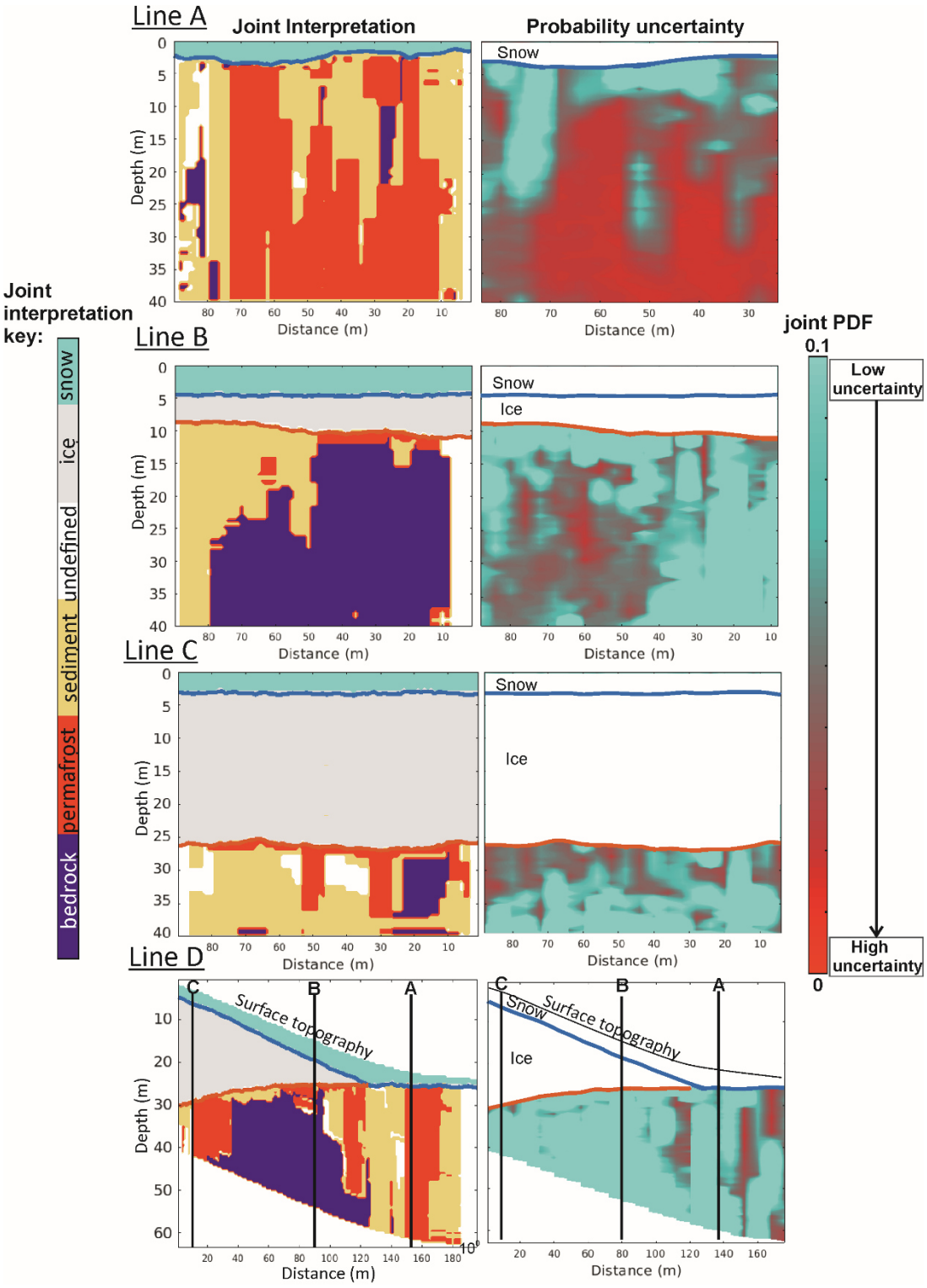

Figure 7.1 Left column: Facies classifications for lines A-D at Midtdalsbreen (Chapter 5), colour bar on the left. Right column: joint probability of *Vs* and *R* calculated from the product of the normalised PDF values (Equation 7.1), assuming *Vs* and *R* are independent. Note this is calculated for the subglacial material only with colour bar on the right.

7.2.2 Petrophysical interpretation

In this joint approach, petrophysical relationships are derived, from seismic velocity and resistivity empirical relationships, to obtain and/or guide interpretations of the volumetric proportions of water, ice and air in the subsurface. Here, the four-phase model of Hauck et al. (2011) is applied, to determine the volumetric fractions of rock (f_r), water (f_w), air (f_a) and ice (f_i) of the Midtdalsbreen subglacial environment. This model is based on geophysical mixing rules for electrical resistivity (Archie 1942) (Equation 7.6) and an extension of the time-averaged formula for seismic P-wave velocities, *Vp*, (Timur 1968) (Equation 7.7):

$$\rho = a\rho_w \Phi^{-m} S_w^{-n} \tag{7.6}$$

$$\frac{1}{V_p} = \frac{f_w}{V_w} + \frac{f_r}{V_r} + \frac{f_i}{V_i} + \frac{f_a}{V_a} \tag{7.7}$$

using $\Phi = 1 - f_r$ and $S_w = {f_w}/{\Phi}$ and assuming

$$f_w + f_r + f_i + f_a = 1 \tag{7.8}$$

equations for the ice-, water- and air content can be written as

$$f_i = \frac{V_i V_a}{V_a - V_i}\left[\frac{1}{V_p} - \frac{f_r}{V_r} - \frac{1-f_r}{V_a} + \left(\frac{a\rho_w(1-f_r)^n}{\rho(1-f_r)^m}\right)^{1/n}\left(\frac{1}{V_a} - \frac{1}{V_w}\right)\right] \tag{7.9}$$

$$f_a = \frac{V_i V_a}{V_i - V_a}\left[\frac{1}{V_p} - \frac{f_r}{V_r} + \frac{f_r - 1}{V_i} - \left(\frac{a\rho_w(1-f_r)^n}{\rho(1-f_r)^m}\right)^{1/n}\left(\frac{1}{V_w} - \frac{1}{V_i}\right)\right] \tag{7.10}$$

$$f_w = \left(\frac{a\rho_w(1-f_r)^n}{\rho(1-f_r)^m}\right)^{1/n} \tag{7.11}$$

where ρ and ρ_w are the electrical resistivities (Ωm) of the bulk material and the pore water, Φ is the porosity, S_w is the water saturation, n, m and a are empirical constants, and Vp, V_w, V_r, V_i and V_a are the seismic P wave velocities (m/s) of the bulk material, water, rock, ice and air. In general, the empirical constants and material properties (n, m, a, ρ_w, V_w, V_r, V_i and V_a) can be estimated from laboratory results and literature (e.g. Hauck and Kneisel, 2008; Kneisel et al., 2008; Hauck et al., 2011). Provided *R*, *Vp* and a suitable porosity model can be derived or estimated for the subsurface, ice- (f_i), air- (f_a) and unfrozen water content (f_w) can be explicitly computed using Equations 7.6, 7.7 and 7.8.

In this section, the petrophysical analysis is applied to the Midtdalsbreen subglacial material, where *Vs* and *R* solutions have been derived from MuLTI and MuLTI-TEM, Chapters 4 and 5. Here, an estimated Poisson's ratio is used to approximate *Vp* from the derived *Vs*, however further developments of MuLTI (presented in Section 7.2.1

and 7.3) aim to address limitations associated to fixing and approximating parameters, such as *Vp* and density, by solving for them in a probabilistic manner also.

7.2.2.1 Input Parameters

Poisson's ratio (ν) is the measure of material deformation response when subject to uniaxial stress and is commonly used in seismology to understand the elastic parameters of a material, where *Vp* can be derived from *Vs* (or vice versa) by,

$$Vp = \sqrt{Vs^2 \frac{2(1-\nu)}{1-2\nu}} \tag{7.12}$$

Poisson's ratio was estimated for the Midtdalsbreen subglacial material using literature presented in Vásárhelyi (2009), Mavko et al. (2019) and Simonsen et al. (2002), detailed in Table 7.2. Table 7.2 also details the parameters *n*, *m*, *a*, ρ_w, V_w, V_r, V_i and V_a estimated from literature presented in Hauck and Kneisel, (2008), Kneisel et al., (2008) and Hauck et al., (2011). These parameters were supplied as constants throughout the whole model, however, it is noted that these values may vary strongly over the model domain.

Vp was approximated using equation 7.12 and the smoothed modal *Vs* solution (used in Chapter 5 for the facies classification). A 2D porosity model was approximated using the facies classifications, by populating each facies with an estimated porosity. Figure 7.2 shows the 2D parameters input to the four-phase petrophysical model, including *Vp*, *R* and porosity (for the subglacial material only).

Hauck et al. (2011) showed in a sensitivity testing study, that *n* and *m* have a small effect on ice, water and air contents estimated. However, ρ_w and V_r were shown to have a larger effect on the ice content estimated where low bulk velocities were measured. Also, Φ was shown to have a large effect on the ice content especially where high bulk velocities were measured. Further sensitivity testing of ρ_w, V_r, Φ and ν could be completed to better understand the uncertainty in the observed ice content estimated and the derived *Vp* profile.

Table 7.2 Model parameters input to petrophysical four phase model based on the literature studies Hauck and Kneisel (2008), Kneisel et al. (2008) and Hauck et al. (2011). The Poisson's ratio was increased where very low *Vs* values (< 500 m/s) exist (Vásárhelyi 2009; Mavko et al., 2019; Simonsen et al., 2002).

Model input parameters	
a	1
n	2
m	2
V_i	3800 m/s
V_a	330 m/s
V_r	4000 m/s
V_w	1500 m/s
ρ_w	10 Ωm
v	0.33 except 0.45 if Vs < 500 m/s

7.2.2.2 Four-phase model interpretations

The results from the petrophysical four-phase model, for lines A-D, are shown in Figure 7.3. Within the subglacial material, the area below the base-ice (red) horizons, ice-, water- and air contents are normalised by the porosity showing the percentage of pore space which is filled by the respective material. All lines show a similar pattern to those observed in the facies interpretations (Figure 5.9). The zones of permafrost identified in the facies classification all show a high fraction of ice and a low fraction of water in the pores, particularly highlighted in line A and D. The areas of wet sediment identified in the facies classification all show a high fraction of water and a low fraction of ice in the pores, highlighted in Lines B and C. The interpreted fractured bedrock facies is associated with a 100% estimate of water content in its pores/fractures, highly influenced by the low resistivities observed at depth. The fractional air content, for all lines, shows anomalously high values in deep pores (arrows in Figure 7.2), most likely a consequence of estimating *Vp* from *Vs* using *v*, rather than measuring *Vp* directly. The anomalous high air content arises where there are zones of very low *Vs* (< 500 m/s). These low velocity zones are likely caused by wet unconsolidated material (soft), with a low shear modulus compared to the (hard) underlying bedrock. Even though Poisson's ratio is increased (to 0.45) in these areas to attempt to account for this, some anomalously low *Vp* values are still obtained, relatively close to the seismic velocity in air (330 m/s).

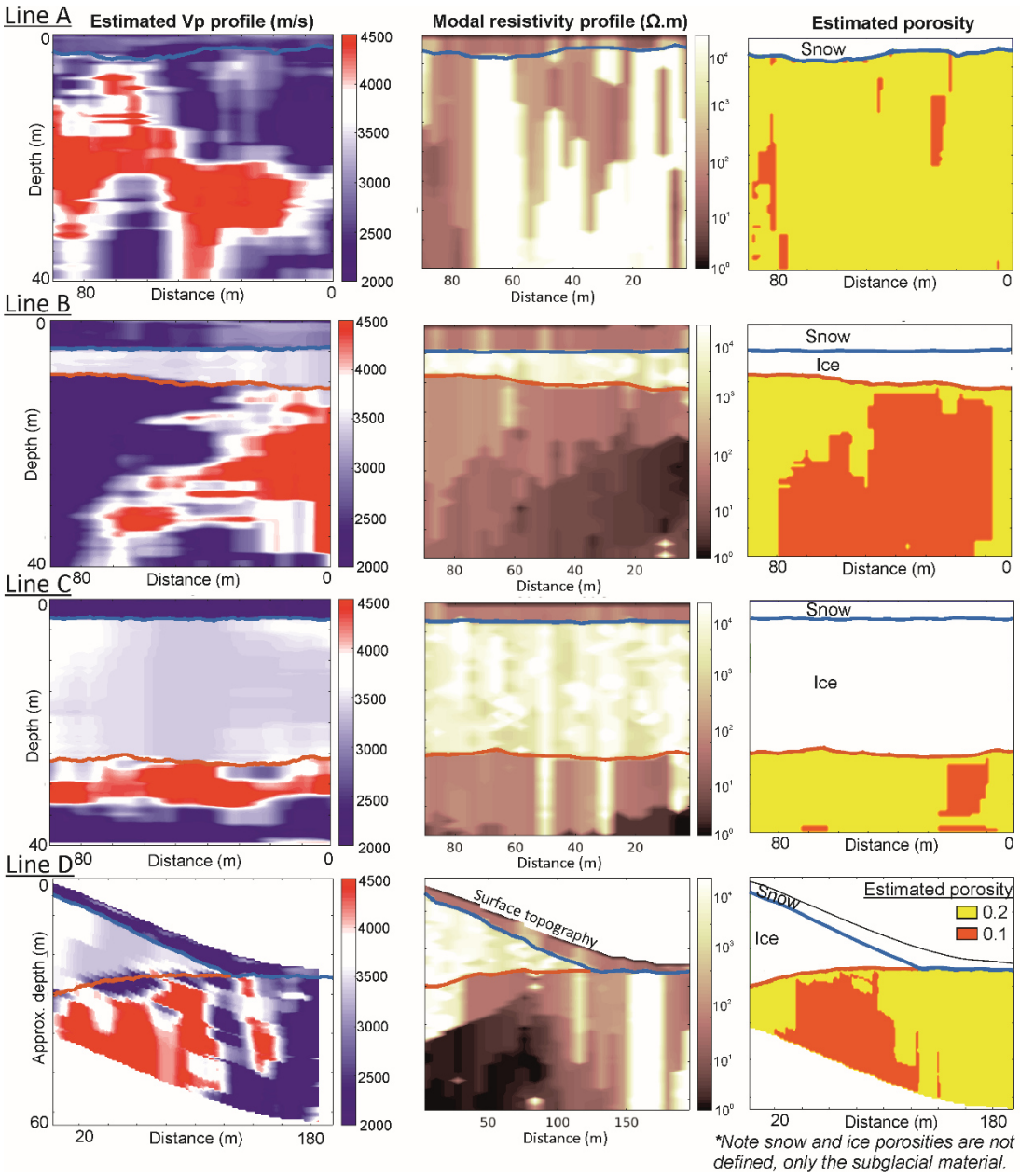

Figure 7.2 2D model parameters input to the petrophysical four phase model for lines A-D. Left column: estimated *Vp* profiles derived from the smoothed modal *Vs* profiles (Chapter 4) and estimated ν (Table 6.1) using equation 7.12. Centre column: modal resistivity profiles, detailed in Chapter 5. Right column: estimated porosity model using the facies classifications shown in Figure 5.9, Chapter 5, for subglacial material only. Blue and red lines are the base snow and ice horizons, respectively.

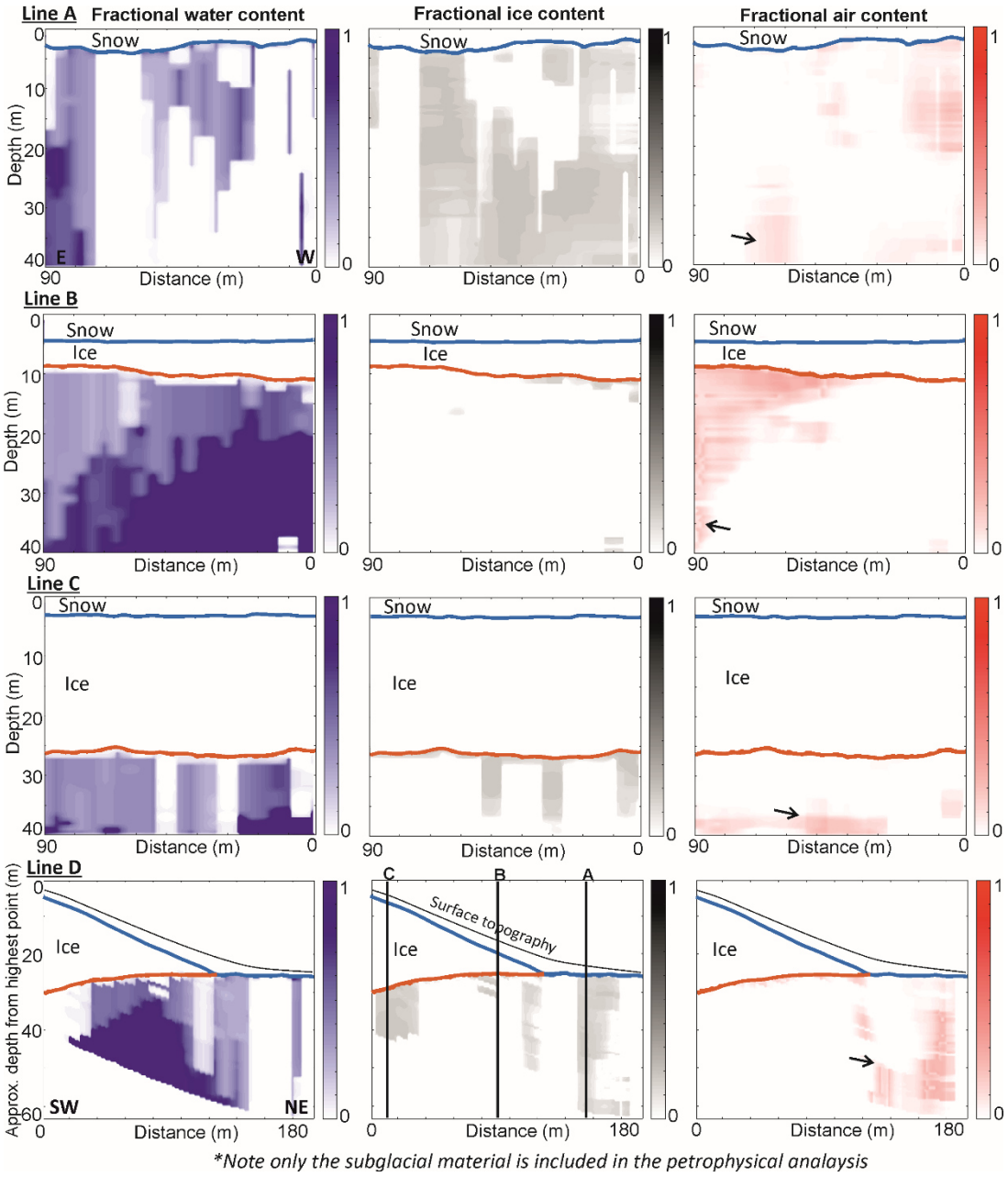

Figure 7.3 Petrophysical four-phase model outputs for lines A-D at Midtdalsbreen. Left column: fraction of water content. Centre column: fraction of ice content. Right column: fraction of air content. The arrows in the right column point to anomalously high air content at depth, arising from anomalously low *Vp* values derived from observed low *Vs*, using equation 7.12. Note only the subglacial material is included in this analysis, the white snow and ice layers are not representative of the colour bars shown.

7.2.2.3 Further petrophysical analysis

This section presents a methodology (developed by Hauck et al. (2011)) for which a petrophysical analysis of the subglacial material can be completed. However, there are limitations with approximating important parameters such as *Vp*, Poisson's ratio

and porosity, as well as having a poor knowledge of their uncertainty. Further developments of MuLTI (presented in 7.3) aim to address these limitations by solving for such parameters (e.g., *Vp* and density) directly using the Bayesian approach. Thereafter, through use of (e.g.) the Biot-Gassman theory (Biot 1941; Gassmann 1951), the probabilistically derived *Vp*, *Vs* and density parameters could provide a more justifiable estimate of porosity and quantify its uncertainty.

Furthermore, this four-phase model could be combined within a probabilistic joint *Vs*-*R* inversion, approach detailed in Section 7.2.1, to provide a posterior distribution of *Vs*, *R*, (f_i), (f_a) and (f_w), with all model parameters being defined in the same physical space (in depth), and posterior distribution of number of nuclei. Thus, also providing detailed uncertainty analysis for each fractional content (water, ice and air) enabling a more reliable interpretation of this analysis.

7.3 Further MuLTI development

Currently, MuLTI and MuLTI-TEM can be applied to many other glaciological, environmental and engineering applications, targeting shallow (e.g., Chapter 4 and 5) or deep (e.g., Chapter 6) structure. Yet, as with any software or algorithm, there are many different routes I could follow to continue and further develop the work presented in this thesis. In this section I discuss, in detail, some of the potential options for future development of the MuLTI framework, highlighted previously in the discussion, Section 7.1. This involves a preliminary study of an evolution of MuLTI, termed MuLTI III), in which *Vp* and density are allowed to vary, whereas they were fixed in the original MuLTI code. This feasibility study was funded by the Antarctic Science Bursaries, which supported a 3 week research visit to the University of Maryland, where full analysis and *Vs* inversions of a new dataset was completed. While these results are not yet finalised, nor their implications fully integrated with glaciological implications, they show promise for the future development of the MuLTI framework.

7.3.1 MuLTI III

MuLTI III has been developed to address a key limitation in the original MuLTI code, specifically that *Vp* and density must be fixed. MuLTI III overcomes this limitation by allowing both *Vp* and density to vary, together with estimates of their uncertainty. In this section, I therefore describe the new model parameterisation and sampling methodology, of *Vp* and density, and present an example case study using MuLTI III to derive the *Vs* structure of a firn aquifer in south eastern Greenland.

7.3.1.1 Model parameterisation

Here, I describe the 1-D variation of *Vp* and density with depth as a piecewise constant function using Voronoi nuclei, in which each layer is divided into a variable number of sublayers with constant velocities, similar to the way *Vs* is described. At each depth, the value of *Vp* and density is determined by its nearest nucleus within the same layer, see Figure 7.4 for an illustration of this model parameterisation. The model vector for *Vs*, *Vp* and density is then

$$m = [m_{vs}, m_{vp}, m_{den}] \tag{7.13}$$

$(m_{Vs} = [dp_1, dp_2, \dots, dp_k, Vs_1, Vs_2, \dots, Vs_k, k, dpc_1, dpc_2 \dots dpc_l, Vsc_1, Vsc_2, \dots, Vsc_l])$

$(m_{Vp} = [dp_1, dp_2, \dots, dp_k, Vp_1, Vp_2, \dots, Vp_k, k, dpc_1, dpc_2 \dots dpc_l, Vpc_1, Vpc_2, \dots, Vpc_l])$

$(m_{den} = [dp_1, dp_2, \dots, dp_k, den_1, den_2, \dots, den_k, k, dpc_1, dpc_2 \dots dpc_l, denc_1, denc_2, \dots, denc_l])$

where *k* is the number of floating nuclei, Vs_i, Vp_i and den_i are the *Vs*, *Vp* and density of the floating nuclei, *l* is the number of confined nuclei, *dpc* are the depths of the confined nuclei and Vsc_i, Vpc_i and $denc_i$ are the *Vs*, *Vp* and density of the confined nuclei, respectively.

7.3.1.2 Prior information

The prior distribution of *Vp* and density as a function of depth is taken to be normally distributed with both depth-dependent mean (μ_{vp} and μ_{den}) and standard deviation (σ_{vp} and σ_{den}), Figure 7.4c. These depth-dependent parameters are interpolated between a discrete set of values read in by the code.

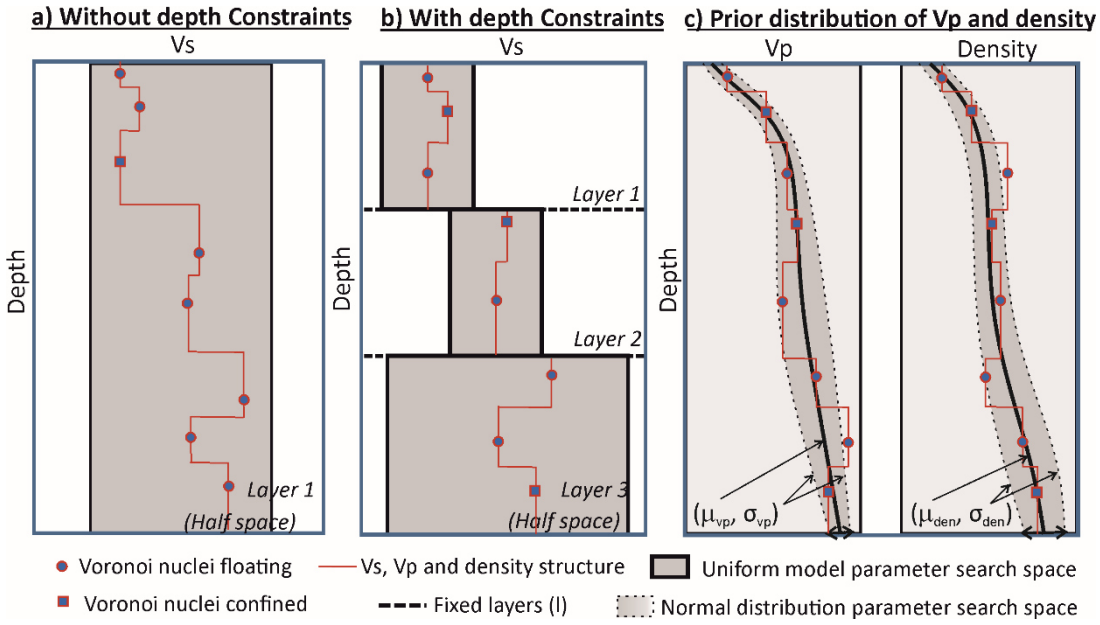

Figure 7.4 Illustration of MuLTI III model parameterization using Voronoi nuclei (floating and confined) and prior distributions, reformed from the original MuLTI parameterization shown in figure 2.1. a) Prior distribution of *Vs* without depth constraints; b) prior distribution of *Vs* with depth constraints; c) prior distribution of both *Vp* and density.

7.3.1.3 Numerical sampling of the posterior

As explained in Chapter 3, I sample the posterior distribution using the MCMC algorithm. At each step, a new model *m'* is proposed that differs from the current model by, now, one of six perturbations (Figure 7.5), which depend on a set of user specified parameters ($\sigma_{changeVs}$, $\sigma_{changeVp}$, $\sigma_{changeDen}$, σ_{move}, $\sigma_{birthVs}$, $\sigma_{birthVp}$ and $\sigma_{birthDen}$) whose values affect the speed of convergence to the posterior distribution:

- change *Vs*: same as MuLTI, defined in Chapter 3.
- change *Vp*: perturb the velocity of a randomly chosen nucleus by a random amount distributed as $N(0,\sigma_{changeVp}^2)$.
- change density: perturb the density of a randomly chosen nucleus by a random amount distributed as $N(0,\sigma_{changeDen}^2)$.
- move nucleus: same as MuLTI, defined in Chapter 3. Note, *Vs*, *Vp* and density stay the same for the randomly chosen nucleus.
- birth: add a floating nucleus to the existing model whose depth is uniformly distributed $U[0, dp_{max}]$ and whose *Vs* is distributed $N(Vs, \sigma_{birthVs}^2)$, where *Vs* is the value of *Vs* based on the current nuclei distribution, *Vp* is distributed $N(Vp, \sigma_{birthVp}^2)$, where *Vp* is the value of *Vp* based on the current nuclei distribution and density is distributed $N(den, \sigma_{birthDen}^2)$, where den is the value of density based on the current nuclei distribution.

- death: same as MuLTI, defined in Chapter 3.

Each proposed model is tested to see if it satisfies a certain acceptance criterion, which is amended from the original acceptance criterion of Equation 3.8, to account for these extra perturbations. The same methodology is applied thereafter to that in MuLTI, described in Chapter 3.

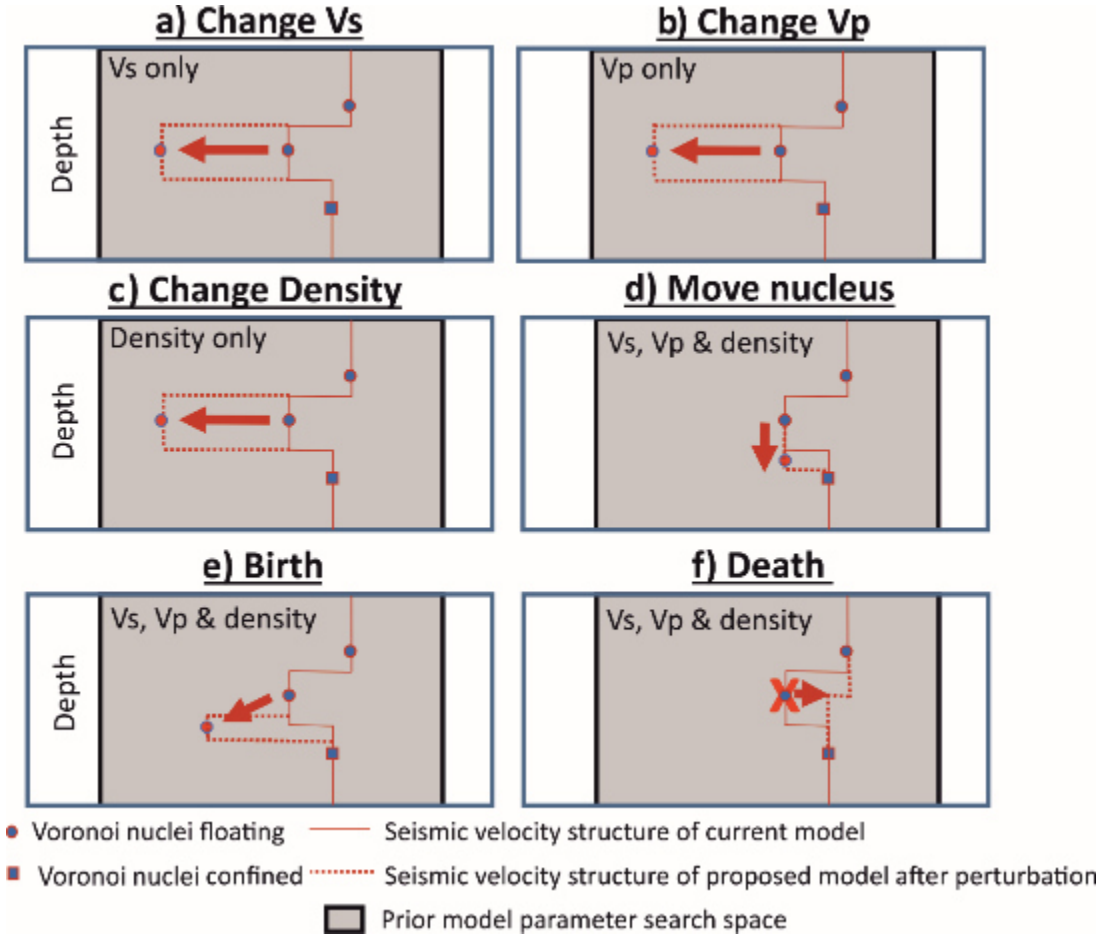

Figure 7.5 Illustration of six possible perturbations to a current model in MuLTI III, adapted from the original MuLTI perturbations shown in figure 2.2. a) change *Vs* of a nucleus, b) change *Vp* of a nucleus, c) change density of a nucleus, d) move a nucleus to a different depth, e) give birth to a new floating nucleus, and f) remove a floating nucleus.

7.3.1.4 Test application of MuLTI III

Active source seismic, GPR and borehole data was acquired along a flow line at Helheim Glacier, south east Greenland (Figure 7.6), to investigate the structure of a firn aquifer, a perennial store of liquid water. The main goal of the survey was to constrain the local thickness of the aquifer layer and provide seismological estimates for the volume of water, for comparison to estimates derived from other geophysical

and hydrological measurements. The seismic acquisition is detailed in Montgomery et al., 2017, which presents a seismic refraction experiment conducted to determine the *Vp* structure of the aquifer, estimating the depth of the firn-ice transition to be on average 28 m below the surface (Figure 7.6). The density structure of the aquifer, determined from ice cores, are detailed in Miller at al., 2018. Here, I present a seismic Rayleigh wave study completed using the active source seismic dataset (Montgomery et al., 2017) and MuLTI III to obtain the *Vs* structure of the aquifer, thus, enabling elastic parameters such as the bulk and shear moduli, and the *Vp*/*Vs* ratio to be calculated. Additionally, through the use of (e.g.) the Biot-Gassman theory (Biot 1941; Gassmann 1951), these parameters could be related to the water volume stored in the firn aquifer providing a more complete hydrological characterisation of the aquifer and its total water content.

The *Vs* structure of the firn was evaluated using a constrained inversion of the Rayleigh wave dispersion curves in MuLTI III. For this trial analysis, I apply MuLTI III to Array 1 from Site 7 (Figure 7.6), as described in Montgomery et al. (2017). This array uses 24 geophones with a 5 m geophone interval. These data were transformed into frequency-phase velocity domain where the Rayleigh wave dispersion curve was picked (Figure 7.7b). Combined with the mean and standard deviation of distributions of *Vp* (derived from a Bayesian implementation of P-wave refraction tomography; Montgomery et al., 2017) and density (measured from ice cores; Miller et al., 2018), plus GPR- and seismic-derived depth constraints for the boundaries of the aquifer (Montgomery et al., 2017), this curve was input to MuLTI III. The *Vs* layer boundaries applied were:

i) 500 – 2000 m/s in the firn above the aquifer (layer 1),
ii) 500 – 1700 m/s in the firn aquifer (layer 2) and
iii) 1200 – 2300 m/s in the ice (layer 3).

The maximum number of floating nuclei was set to 50 and 1 million iterations (including the burn-in) were found to be enough for convergence of the posterior distribution sampled by the single Markov chain, although multiple chains were run to check they converged on the same posterior distribution.

Figure 7.7c shows the results from MuLTI III. The posterior distribution of *Vp* and density are comparable to their prior distributions, although the marginal posterior distribution of *Vs* identifies a decrease through the aquifer, which could be due to an increase in density, caused by the storage of liquid water in the firn pores, Equation 1.1.

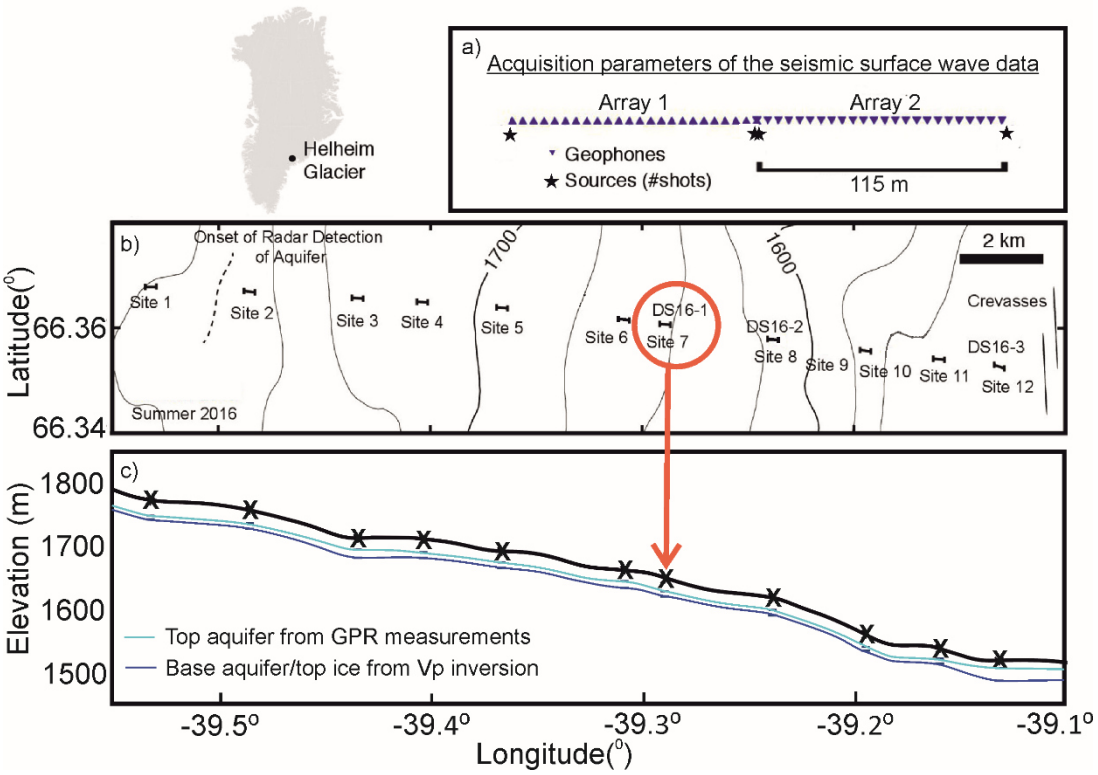

Figure 7.6 Location of the firn aquifer field site in Greenland, adapted from Montgomery et al. (2017). a) Seismic acquisition parameters used for the surface wave study. b) Location of seismic surveys, sites 1-12, with drill sites indicated as DS16-1, DS16-2 and DS16-3. Here, only data from Site 7 are considered (highlighted in the red circle). c) Elevation profile along the glacier's flow line (down slope) with all site locations marked by "X". The top and base of the aquifer are shown, respectively, by the light and dark blue lines.

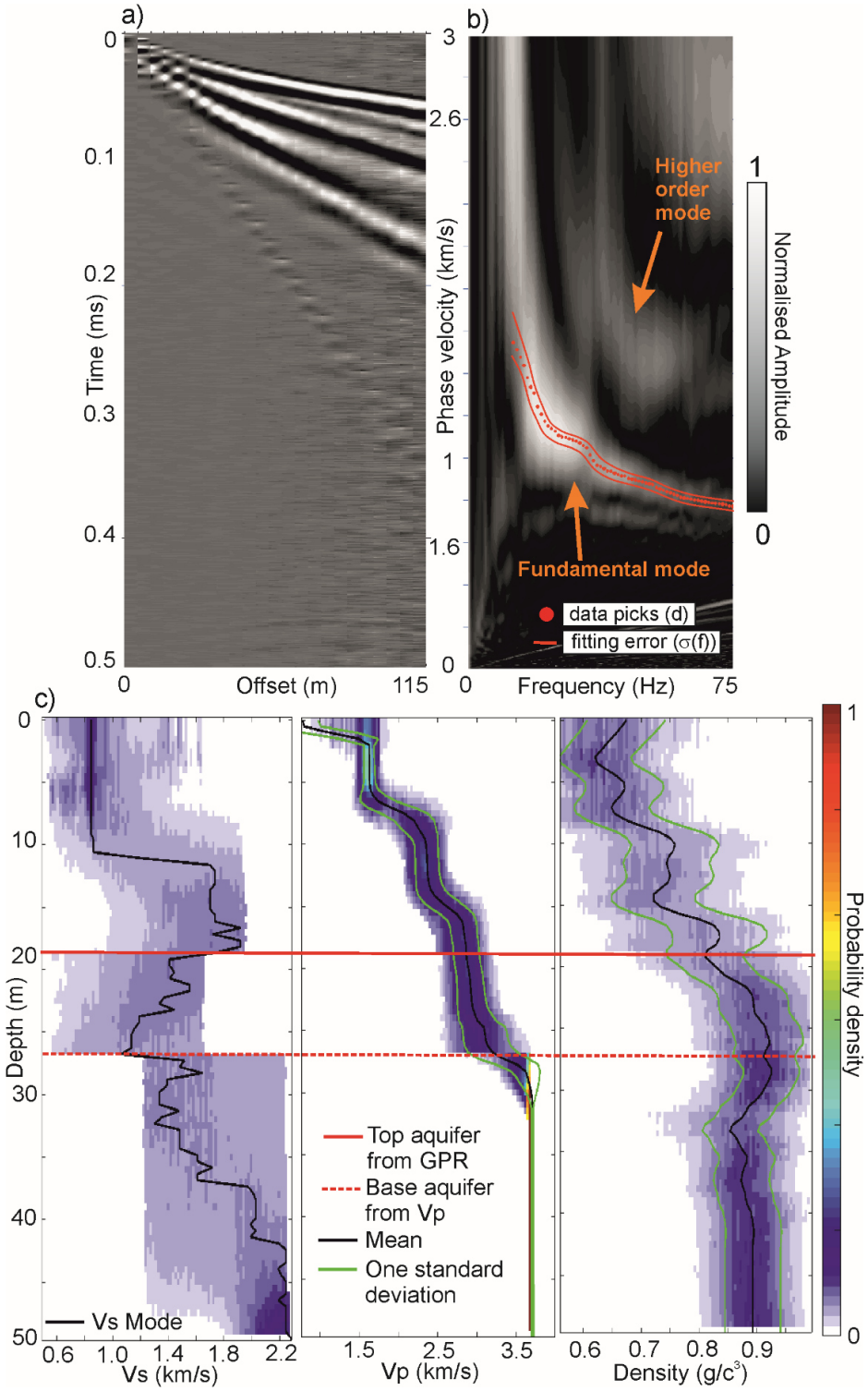

Figure 7.7 Site 7 dispersion curve analysis and inversion results. a) Zero offset shot gather. b) Dispersion curve picked. c) *Vs*, *Vp* and density posterior distributions output using MuLTI III. The depths of the top and base aquifer are plotted in the red and red-dashed lines. The prior mean and spread of one standard deviation of *Vp* and density are plotted in the black and green lines, respectively. The mode *Vs* solution is plotted in the black line in the *Vs* PDF image.

7.3.2 MuLTI IV with variable layer depths

The next progression for the MuLTI framework, including both MuLTI and MuLTI-TEM, is to address the limitation of fixed internal interfaces at layer boundaries. Currently, layer depths are input as a single numerical value, fixed to that depth, with no methodology in place to reflect their associated uncertainty. One way this could be achieved is to alter the prior distribution so that the layer depths themselves are drawn from a distribution rather than being assumed constant. For example, they may be assumed to be normally distributed with given mean and standard deviation during numerical sampling of the posterior.

The approach would involve input, to MuLTI as prior information, a mean (μ_z) and standard deviation (σ_z) for each layer depth (l_{dp}),

$$l_{dp} = [\mu_{z1}, \mu_{z2}, \dots \mu_{zn}, \sigma_{z1}, \sigma_2, \dots \sigma_{zn}] \quad (7.14)$$

where *n* is the number of layers. I would then add a new perturbation step, sampling the posterior distribution using the MCMC algorithm, to perturb a randomly chosen layer depth using a normal distribution, derived from the mean (μ_z) and standard deviation (σ_z) of the chosen layer depth (l_{dp}). This new perturbation step would be called "change layer depth". Any nuclei in the vicinity of this movement, causing a change in the nuclei's originally defined layer, may therefore have a significant modification to the value of their prior distribution.

Chapter 8 Conclusions

8.1 Summaries of objectives and results

This thesis has presented a novel constrained inversion methodology (MuLTI) for further development of the geophysical techniques: MASW and TEM used in cryosphere studies. The algorithms have been made publicly available via GitHub to motivate other users and continue development of these methods. Here, I recap my objectives set out in Chapter 1, along with a summary of my results directly related to each objective, presented in this thesis.

Objective 1. *The development of a novel inversion methodology, easily adaptable for different geophysical techniques, enabling multiple geophysical observations to be integrated into a single inversion.*

Result: The constrained Bayesian inversion framework: MuLTI has been developed for the inversion of Rayleigh wave dispersion curves (Chapter 3) and MuLTI-TEM (Chapter 5) for the inversion of TEM soundings, with the ability to constrain layer depths from other geophysical datasets. Furthermore, the algorithm has been made publicly available via GitHub.

Objective 2. *To evaluate the feasibility of using MASW and TEM techniques on glacier ice, to obtain the shear-wave and resistivity properties of the subglacial environment.*

Result: Synthetic studies (presented in Chapter 4 and 5), including a test field campaign (presented in Chapter 2) were completed to evaluate the feasibility of these techniques.

Objective 3. *To deploy MASW, TEM and complementary GPR surveys on Midtdalsbreen, an outlet glacier of the Hardangerjøkulen ice cap in Norway, using observations from (2) to inform and optimise acquisition design.*

Result: The main field campaign was completed in spring 2018, where active source seismic, TEM and GPR were all acquired, along all profiles. Knowledge from the test field campaign , in 2017 (Chapter 2), aided the decision making on the seismic survey design. The TEM equipment was kindly loaded from the NERC GEF, where 1-D TEM survey testing was completed at the start of the field campaign (Chapter 5).

Objective 4. *To apply the novel inversion methodology developed in (1) to derived shear-wave and resistivity models of the Midtdalsbreen subglacial environment.*

Result: The final shear-wave velocity and resistivity profiles of the Midtdalsbreen subglacial environment are presented in Chapter 4 and 5.

Objective 5. *To develop a joint inversion strategy for combining observations from the seismic and TEM data.*

Result: A methodology for presenting the facies classifications (of Chapter 5) of the subglacial environment in a probabilistic manner, using the joint probabilistic outputs of *Vs* and *R*, from MuLTI and MuLTI-TEM is presented in Chapter 7. Along with, a petrophysical inversion approach, using derived petrophysical relationships which directly combine *R* and *Vs* to obtain the volumetric proportions of water, ice and air in the subsurface.

Objective 6. *In discussion, to evaluate the applicability of these approaches for characterising larger ice sheets, for example in Antarctica and Greenland, where the evolution of the subglacial environment is an important consideration in predictions of future sea-level rise.*

Result: A feasibility study for a polar ice mass is presented in Chapter 6. This highlights the different resolution sensitives of both the Rayleigh wave dispersion curves and TEM soundings, which complement each other if used together. Large scale structure (> 2 km) can be identified using surface waves and the smaller scale detail (< 2 km), directly under the ice, can be resolved using TEM. Furthermore, I have shown that these methods could be applied with existing survey systems and energy sources.

Additionally, I have shown the applicability of an advanced formulation of MuLTI for evaluating meaningful hydrological properties of polar firn aquifers.

8.2 Overall conclusions

Non-invasive geophysical techniques can be used to explore the inaccessible, widely unknown, basal environment of glaciers and ice masses. An improved understanding of this environment, including its material composition and hydrology, has profound implications for predictions of glacier flow and dynamic evolution. The work presented in this thesis has developed two geophysical techniques for cryospheric applications, specifically seismic surface waves (MASW) and TEM, to gain insight into the material composition and water content of subglacial material.

In particular, the composition and water content of the subglacial environment can be characterised by joint inferences from *Vs* and *R* structure. This thesis has presented a novel constrained Bayesian inversion framework MuLTI (Multimodal Layered Transdimensional Inversion; https://github.com/eespr), which uses a Markov chain Monte Carlo implementation of Bayesian inversion to produce a probability distribution of geophysical properties as a function of depth. The framework is easily adaptable to multiple different geophysical methods; here, I have presented MuLTI for the inversion of Rayleigh wave dispersion curves and MuLTI-TEM for the inversion of TEM soundings, respectively to obtain posterior distributions of subsurface *Vs* and *R* structures. A novel aspect of the methodology allows independent depth constraints, drawn from any external data source (for example, GPR and borehole data), to be directly input to MuLTI. This mitigates recurring problems identified in isolated inversions of single datasets, such as poor depth sensitivity, low resolution, and ambiguous, non-unique solutions. Furthermore, the transdimensional Bayesian sampling-based method employed, produces an ensemble of models from which statistical properties of the model parameters, including model dimensions, are inferred, providing a robust quantitative uncertainty analysis of any chosen model at all depth levels.

The method was applied to seismic and electromagnetic data acquired on the terminus of the Norwegian glacier Midtdalsbreen. By combining the resistivity and seismic shear-wave velocity profiles, a new 3D interpretation of the Midtdalsbreen subglacial structure was proposed. Three subglacial material classifications were considered using *Vs* and *R* boundaries from the MuLTI and MuLTI-TEM outputs: sediment ($Vs < 1600$ m/s, 50 Ωm $< R <$ 500 Ωm), permafrost ($Vs > 1600$ m/s, $R >$ 500 Ωm) and weathered/fractured bedrock with saline water in the fractures ($Vs > 1900$ m/s, $R <$ 50 Ωm). Their spatial extent, within Midtdalsbreen's subglacial environment, showed a

mixture of sediment and permafrost directly below the ice, and in the moraine at the front of the glacier, all underlain by bedrock.

Through synthetic studies and real-data applications, this study showed how joint analysis of three geophysical datasets can increase our understanding of the material in the subsurface and thus provide a more detailed interpretation. Critically, in the application presented, TEM data reveal hydrological properties to which the seismic analysis was insensitive, whereas the seismic data indicate the varying stiffness of the subglacial material.

The adaptable and versatile MuLTI framework offers a promising platform for further methodological development and use in other glaciological applications. For example, directly combining MuLTI and MuLTI-TEM in a probabilistic joint facies classification would enable access to the joint distribution of subsurface R and Vs, which could lead to a more accurate understanding of the subsurface structure (utilizing structural similarities between resistivity and seismic velocity). Also, the development of MuLTI III (where independent Vp and density profiles along with their standard deviations are input) has enabled reliable characterisation of the Vs structure of a firn aquifer in South East Greenland, with important implications on the estimated volume of water stored in the aquifer. Furthermore, the feasibility study for polar ice sheet applications presented how MuLTI and MuTLI-TEM could be adapted and applied on polar ice sheets, up to 2 km thick, to characterise the deep subglacial environment.

In summary, this thesis has presented novel methodologies to benefit the exploration of subsurface materials. By developing an integrative set of frameworks, the MuLTI and MuLTI-TEM approaches highlight the advantages of acquiring and combining multiple geophysical datasets for characterising the stiffness and electrical properties of the glaciated subsurface. The algorithms have been made publicly available via GitHub to motivate other users in the cryosphere and other (e.g., industrial engineering) settings, and to continue further development of these valuable geophysical techniques.

References (Chapters 1, 2, 6 and 7)

Åkesson H., Nisancioglu K., Giesen R. & Morlighem M. (2017). Simulating the evolution of Hardangerjøkulen ice cap in southern Norway since the mid-Holocene and its sensitivity to climate change. *Cryosphere*, 11, 281–302

Anandakrishnan S. (2003). Dilatant till layer near the onset of streaming flow of Ice Stream C, West Antarctica, determined by AVO (amplitude *Vs* offset) analysis. *Ann. Glaciol*., 36, 283–286

Anandakrishnan, S., Blankenship, D. D., Alley, R. B., & Stoffa, P. L. (1998). Influence of subglacial geology on the position of a West Antarctic ice stream from seismic observations. *Nature*, 394(6688), 62-65.

Andreassen L. M. & Winsvold H. (2012). Inventory of Norwegian Glaciers. *Norwegian Water Resources and Energy Directorate*, rapport 38-2012, 236 pp

Andersen, K. E., Brooks, S. P., & Hansen, M. B. (2003). Bayesian inversion of geoelectrical resistivity data. *Journal of the Royal Statistical Society: Series B* (Statistical Methodology), 65(3), 619-642.

Archie, G. E. (1952) Classification of carbonate reservoir rocks and petrophysical considerations, *AAPG Bulletin*, 36(2), 278-298.

Armstrong M. (2009). Multichannel Analysis of Surface Waves (MASW) determined surface-wave velocity profile and its relation to observation of the near-surface polar firn layers. *Supervised Project Report, University of Canterbury*, https://ir.canterbury.ac. nz/handle/10092/14187 (Accessed: December 2018)

Aster, R. C., & Winberry, J. P. (2017). Glacial seismology. *Reports on Progress in Physics*, *80*(12), 126801.

Auken, E., & Christiansen, A. V. (2004). Layered and laterally constrained 2D inversion of resistivity data. *Geophysics*, *69*(3), 752-761.

Auken, E., Christiansen, A. V., Jacobsen, B. H., Foged, N., & Sørensen, K. I. (2005). Piecewise 1D laterally constrained inversion of resistivity data. *Geophysical Prospecting*, *53*(4), 497-506

Auken, E., Jørgensen, F., & Sørensen, K. I. (2003). Large-scale TEM investigation for groundwater, *Exploration Geophysics*, 34(3), 188-194.

Bamber, J., & Riva, R. (2010). The sea level fingerprint of recent ice mass fluxes. *The Cryosphere*, 4(4), 621-627.

Bartholomaus, T. C., R. S. Anderson, & S. P. Anderson (2008), Response of glacier basal motion to transient water storage, *Nat. Geosci*., 1(1), 33–37, doi:10.1038/ngeo.2007.52.

Bartholomew, I., Nienow, P., Mair, D., Hubbard, A., King, M. A., & Sole, A. (2010). Seasonal evolution of subglacial drainage and acceleration in a Greenland outlet glacier. *Nature Geoscience*, *3*(6), 408.

Bell R. (2008). The role of subglacial water in ice-sheet mass balance. *Nat. Geosci*., 1, 297–304

Benjumea, B., & Teixidó, T. (2001). Seismic reflection constraints on the glacial dynamics of Johnsons Glacier, Antarctica. *Journal of Applied Geophysics*, *46*(1), 31-44.

Bentley, C. R., and H. Kohnen (1976), Seismic refraction measurements of internal friction in Antarctic ice, *J. Geophys. Res*., 81, 1519– 1526, doi:10.1029/JB081i008p01519

Bingham, R.G., Vaughan, D.G., King, E.C., Davies, D., Cornford, S.L., Smith, A.M., Arthern, R.J., Brisbourne, A.M., De Rydt, J., Graham, A.G. & Spagnolo, M. (2017). Diverse landscapes beneath Pine Island Glacier influence ice flow. *Nature communications*, 8(1), p.1618.

Blankenship, D.D., Morse, D.L., Finn, C.A., Bell, R.E., Peters, M.E., Kempf, S.D., Hodge, S.M., Studinger, M., Behrendt, J.C. and Brozena, J.M. (2001). Geologic controls on the initiation of rapid basal motion for West Antarctic ice streams: A geophysical perspective including new airborne radar sounding and laser altimetry results. *The West Antarctic ice sheet: behavior and environment*, 77, pp.105-121.

Bodin, T., & Sambridge, M. (2009). Seismic tomography with the reversible jump algorithm. Geophysical Journal International, 178(3), 1411–1436. doi.org/10.1111/j.1365-246X.2009.04226.x

Bodin, T., Sambridge, M., Tkalčić, H., Arroucau, P., Gallagher, K., & Rawlinson, N. (2012). Transdimensional inversion of receiver functions and surface wave dispersion. Journal of Geophysical Research, 117, B02301. doi.org/10.1029/2011JB008560

Bohleber, P., Sold, L., Hardy, D.R., Schwikowski, M., Klenk, P., Sirguey, P., Cullen, N.J., Potocki, M., Hoffmann, H. & Mayewski, P. (2017). Ground-penetrating radar reveals ice thickness and undisturbed englacial layers at Kilimanjaro's Northern Ice Field. *The Cryosphere*, 11(1), pp.469-482.

Booth, A.D., Clark, R.A., Kulessa, B., Murray, T., Carter, J., Doyle, S.H. & Hubbard, A.L. (2012). Thin-layer effects in glaciological seismic amplitude-versus-angle (AVA) analysis: implications for characterising a subglacial till unit, Russell Glacier, West Greenland. *Cryosphere*, 6, pp.909-922.

Booth, A. D., Mercer, A., Clark, R., Murray, T., Jansson, P., & Axtell, C. (2013). A comparison of seismic and radar methods to establish the thickness and density of glacier snow cover. *Annals of Glaciology*, 54(64), 73-82.

Biot, M. A. (1941). General theory of three-dimensional consolidation. *Journal of applied physics*, 12(2), 155-164.

Brisbourne, A.M., Smith, A.M., Vaughan, D.G., King, E.C., Davies, D., Bingham, R.G., Smith, E.C., Nias, I.J. & Rosier, S.H. (2017). Bed conditions of Pine Island Glacier, West Antarctica. *Journal of Geophysical Research: Earth Surface*, *122*(1), pp.419-433.

Budd, W. F., Keage, P. L., & Blundy, N. A. (1979). Empirical studies of ice sliding. *Journal of glaciology*, *23*(89), 157-170.

Buselli, G., Barber, C., & Zerilli, A. (1988). The mapping of groundwater contamination with TEM and DC methods. *Exploration Geophysics*, *19*(2), 240-243.

Cao, R., Earp, S., de Ridder, S. A., Curtis, A., & Galetti, E. (2019). Near-real time near-surface 3D seismic velocity and uncertainty models by wavefield gradiometry and neural network inversion of ambient seismic noise. *Geophysics,* 85(1), 1-57.

Chevrot, S., Sylvander, M., Benahmed, S., Ponsolles, C., Lefevre, J. M., & Paradis, D. (2007). Source locations of secondary microseisms in western Europe: Evidence for both coastal and pelagic sources. *Journal of Geophysical Research: Solid Earth*, 112(B11).

Christoffersen, P., Bougamont, M., Carter, S. P., Fricker, H. A., & Tulaczyk, S. (2014). Significant groundwater contribution to Antarctic ice streams hydrologic budget. *Geophysical Research Letters*, 41(6), 2003-2010.

Church, J.A., P.U. Clark, A. Cazenave, J.M. Gregory, S. Jevrejeva, A. Levermann, M.A. Merrifield, G.A. Milne, R.S. Nerem, P.D. Nunn, A.J. Payne, W.T. Pfeffer, D. Stammer and A.S. Unnikrishnan. (2013), Sea Level Change. In: Climate Change 2013: The Physical Science Basis. Contribution of Working Group I to the Fifth Assessment Report of the Intergovernmental Panel on Climate Change [Stocker, T.F., D. Qin, G.-K. Plattner, M. Tignor, S.K. Allen, J. Boschung, A. Nauels, Y. Xia, V. Bex and P.M. Midgley (eds.)]. *Cambridge University Press*, Cambridge, United Kingdom and New York, NY, USA.

Chandler, D.M., Wadham, J.L., Lis, G.P., Cowton, T., Sole, A., Bartholomew, I., Telling, J., Nienow, P., Bagshaw, E.B., Mair, D. and Vinen, S., (2013). Evolution of the subglacial drainage system beneath the Greenland Ice Sheet revealed by tracers. *Nature Geoscience*, 6(3), p.195.

Clair, J. S., & Holbrook, W. S. (2017). Measuring snow water equivalent from common-offset GPR records through migration velocity analysis. *The Cryosphere*, 11(6), 2997-3009.

Constable, S. C., Parker, R. L., & Constable, C. G. (1987). Occam's inversion: A practical algorithm for generating smooth models from electromagnetic sounding data. *Geophysics*, *52*(3), 289-300.

Cooper, M. D., Estop-Aragonés, C., Fisher, J. P., Thierry, A., Garnett, M. H., Charman, D. J., Murton, J.B., Phoenix, G.K., Treharne, R., Kokelj, S.V. & Wolfe, S.A. (2017). Limited contribution of permafrost carbon to methane release from thawing peatlands. *Nature Climate Change*, 7(7), 507.

Crary, A. P. (1963). Results of United States traverses in east Antarctica, 1958-1961. *IGY World Data Center A: Glaciology, American Geographical Society*.

Cuffey, K. M., & Paterson, W. S. B. (2010). The physics of glaciers. *Academic Press*. 693 pp

deGroot-Hedlin, C., & Constable, S. (1990). Occam's inversion to generate smooth, two-dimensional models from magnetotelluric data. *Geophysics*, *55*(12), 1613-1624.

Diez, A., Bromirski, P.D., Gerstoft, P., Stephen, R.A., Anthony, R.E., Aster, R.C., Cai, C., Nyblade, A. & Wiens, D.A. (2016). Ice shelf structure derived from dispersion curve analysis of ambient seismic noise, Ross Ice Shelf, Antarctica. *Geophysical Journal International*, *205*(2), pp.785-795.

Diez, A., Eisen, O., Hofstede, C., Lambrecht, A., Mayer, C., Miller, H., Steinhage, D., Binder, T. and Weikusat, I. (2015). Seismic wave propagation in anisotropic ice-Part 2: Effects of crystal anisotropy in geophysical data. *The Cryosphere*, 9(1), pp.385-398.

Dosso, S. E., Dettmer, J., Steininger, G., & Holland, C. W. (2014). Efficient trans-dimensional Bayesian inversion for geoacoustic profile estimation. *Inverse Problems*, 30(11), 114018.

Dou S. & Ajo-Franklin J.B. (2014). Full-wavefield inversion of surface waves for mapping embedded low-velocity zones in permafrost. *Geophysics*, 79, 107–124

Ellis, R. G., & Oldenburg, D. W. (1994). Applied geophysical inversion. *Geophysical Journal International*, *116*(1), 5-11.

Foti, S., Comina, C., Boiero, D., & Socco, L. V. (2009). Non-uniqueness in surface-wave inversion and consequences on seismic site response analyses. *Soil Dynamics and Earthquake Engineering*, *29*(6), 982-993.

Foti, S., Hollender, F., Garofalo, F., Albarello, D., Asten, M., Bard, P.Y., Comina, C., Cornou, C., Cox, B., Di Giulio, G. and Forbriger, T. (2018). Guidelines for the good practice of surface wave analysis: A product of the InterPACIFIC project. *Bulletin of Earthquake Engineering*, 16(6), pp.2367-2420.

Gagliardini, O., Cohen, D., Råback, P., & Zwinger, T. (2007). Finite-element modeling of subglacial cavities and related friction law. *Journal of Geophysical Research: Earth Surface*, *112*(F2).

Gallardo, L. A., & Meju, M. A. (2003). Characterization of heterogeneous near-surface materials by joint 2D inversion of dc resistivity and seismic data. *Geophysical Research Letters*, 30(13).

Gassmann, F. (1951). Elasticity of porous media. *Vierteljahrsschrder Naturforschenden Gesselschaft*, 96, 1-23.

Gazetas, G. (1982). Vibrational characteristics of soil deposits with variable wave velocity. *International Journal for Numerical and Analytical Methods in Geomechanics*, 6(1), 1–20. https://doi.org/10.1002/nag.1610060103

Geonics. (1994) PROTEM47D operating manual, Geonics Ltd.

Glasser, N.F. & Scambos, T.A. A structural glaciological analysis of the 2002 Larsen B ice shelf collapse. *Journal of Glaciology* 54, 3-16 (2008).

Godio, A., & Rege, R. B. (2015). The mechanical properties of snow and ice of an alpine glacier inferred by integrating seismic and GPR methods. *Journal of Applied Geophysics*, *115*, 92-99.

Haeberli, W., Schaub, Y., & Huggel, C. (2017). Increasing risks related to landslides from degrading permafrost into new lakes in de-glaciating mountain ranges. *Geomorphology*, 293, 405-417.

Hauck, C., Bach, M., & Hilbich, C. (2008). A 4-phase model to quantify subsurface ice and water content in permafrost regions based on geophysical datasets. In *Proceedings Ninth International Conference on Permafrost, June* (pp. 675-680).

Hauck, C., Böttcher, M., & Maurer, H. (2011). A new model for estimating subsurface ice content based on combined electrical and seismic data sets. *The Cryosphere*, 5(2), 453-468.

Hauck, C., Guglielmin, M., Isaksen, K., & Vonder Mühll, D. (2001). Applicability of frequency-domain and time-domain electromagnetic methods for mountain permafrost studies. *Permafrost and Periglacial Processes*, *12*(1), 39-52.

Hauck, C., Isaksen, K., Vonder Mühll, D. & Sollid, J.L. (2004). Geophysical surveys designed to delineate the altitudinal limit of mountain permafrost: an example from Jotunheimen, Norway. *Permafrost and Periglac. Process*. 15 (3), 191-205.

Hauck, C., & Kneisel, C. (2008). Quantifying the ice content in low-altitude scree slopes using geophysical methods. *Applied Geophysics in Periglacial Environments, edited by: Hauck, C. and Kneisel, C., University Press, Cambridge*, 153-164.

Hauck, C., Vieira, G., Gruber, S., Blanco, J., & Ramos, M. (2007). Geophysical identification of permafrost in Livingston Island, maritime Antarctica. *Journal of Geophysical Research: Earth Surface*, *112*(F2).

Hayashi K (2012) Analysis of surface-wave data including higher modes using the genetic algorithm. *GeoCongress 2012: State of the Art and Practice in Geotechnical Engineering*, 2776-2785.

Hering, A., Misiek, R., Gyulai, A., Ormos, T., Dobróka, M., & Dresen, L. (1995). A joint inversion algorithm to process geoelectric and surface wave seismic data. Part I: basic ideas. *Geophysical Prospecting*, *43*(2), 135-156.

Hoekstra, P. & McNeill, D. (1973). Electromagnetic probing of permafrost, in Proceedings of Second International Conference on Permafrost, 517–526, Yakutsk, Russia.

Hoffman, M. J., G. A. Catania, T. A. Neumann, L. C. Andrews, and J. A. Rumrill (2011), Links between acceleration, melting, and supraglacial lake drainage of the western Greenland Ice Sheet, *J. Geophys. Res*., 116(F4), F04035, doi:10.1029/2010JF001934.

Hofstede, C., Christoffersen, P., Hubbard, B., Doyle, S.H., Young, T.J., Diez, A., Eisen, O. & Hubbard, A. (2018). Physical conditions of fast glacier flow: 2. Variable extent of anisotropic ice and soft basal sediment from seismic reflection data acquired on Store Glacier, West Greenland. *Journal of Geophysical Research: Earth Surface,* 123(2), pp.349-362.

Holland, C. W., & Anandakrishnan, S. (2009). Subglacial seismic reflection strategies when source amplitude and medium attenuation are poorly known. *Journal of Glaciology*, 55(193), 931-937.

Holland, J. H. (1965). Adaptation in natural and artificial systems. Ann Arbor: *The University of Michigan press*.

Holt, T.O., Glasser, N.F., Quincey, D. & Siegfried, M.R. (2013). Speedup and fracturing of George VI Ice Shelf, Antarctic Peninsula. *The Cryosphere* 7, 797-816

Horgan, H. J., Anandakrishnan, S., Alley, R. B., Peters, L. E., Tsoflias, G. P., Voigt, D. E., & Winberry, J. P. (2008). Complex fabric development revealed by englacial seismic reflectivity: Jakobshavn Isbræ, Greenland. *Geophysical Research Letters*, 35(10).

Hou, Z., Rubin, Y., Hoversten, G. M., Vasco, D., & Chen, J. (2006). Reservoir-parameter identification using minimum relative entropy-based Bayesian inversion of seismic AVA and marine CSEM data. *Geophysics*, 71(6), O77-O88.

Hoversten, G.M., Cassassuce, F., Gasperikova, E., Newman, G.A., Chen, J., Rubin, Y., Hou, Z. & Vasco, D. (2006). Direct reservoir parameter estimation using joint inversion of marine seismic AVA and CSEM data. *Geophysics*, *71*(3), pp.C1-C13.

Iken, A., H. Röthlisberger, A. Flotron, & W. Haeberli (1983), The uplift of Unteraargletscher at the beginning of the melt season—A consequence of water storage at the bed?, *J. Glaciol*., 29(101), 28–47.

Iverson, N. R. (2010). Shear resistance and continuity of subglacial till: hydrology rules. *Journal of Glaciology*, *56*(200), 1104-1114.

Julià, J., Ammon, C. J., Herrmann, R. B., & Correig, A. M. (2000). Joint inversion of receiver function and surface wave dispersion observations. *Geophysical Journal International*, 143(1), 99–112. doi.org/10.1046/j.1365-246x.2000.00217.x

Key, K. and Siegfried, M.R., 2017. The feasibility of imaging subglacial hydrology beneath ice streams with ground-based electromagnetics. *Journal of Glaciology*, 63(241), pp.755-771.

King, E. C., & Jarvis, E. P. (2007). Use of shear waves to measure Poisson's ratio in polar firn. *Journal of Environmental and Engineering Geophysics*, *12*(1), 15-21.

King, M. S., Zimmerman, R. W., & Corwin, R. F. (1988). SEISMIC AND ELECTRICAL PROPERTIES OF UNCONSOLIDATED PERMAFROST 1. *Geophysical Prospecting*, 36(4), 349-364.

Kneisel, C., Hauck, C., Fortier, R., & Moorman, B. (2008). Advances in geophysical methods for permafrost investigations. *Permafrost and Periglacial Processes*, 19(2), 157-178.

Kohnen, H., 1972. On the relationship between seismic velocities and density in firn and ice. Z. *Geophys*. 38, 925-925.

Kopp, R.E., R.M. DeConto, D.A. Bader, C.C. Hay, R.M. Horton, S. Kulp, M. Oppenheimer, D. Pollard, and B.H. Strauss. (2017). Evolving understanding of Antarctic Ice-Sheet physics and ambiguity in probabilistic sea-level projections. *Earth's Future* 5: 1217-1233.

Kopp, R.E., R.M. Horton, C.M. Little, J.X. Mitrovica, M. Oppenheimer, D.J. Rasmussen, B.H. Strauss, and C. Tebaldi. 2014. Probabilistic 21st and 22nd century sea-level projections at a global network of tide-gauge sites. *Earth's Future* 2: 283-406.

Kulessa, B., Hubbard, A.L., Booth, A.D., Bougamont, M., Dow, C.F., Doyle, S.H., Christoffersen, P., Lindbäck, K., Pettersson, R., Fitzpatrick, A.A. & Jones, G.A. (2017). Seismic evidence for complex sedimentary control of Greenland Ice Sheet flow. *Science advances*, *3*(8), p.e1603071.

Larour, E., Ivins, E. R., & Adhikari, S. (2017). Should coastal planners have concern over where land ice is melting?. *Science advances*, *3*(11), e1700537.

Levenberg, K. (1944). A method for the solution of certain non-linear problems in least squares. *Quarterly of applied mathematics*, 2(2), 164-168.

Lindbäck, K., Kohler, J., Pettersson, R., Nuth, C., Langley, K., Messerli, A., Vallot, D., Keniche, M. & Brandt, O. (2018). Subglacial topography, ice thickness, and bathymetry of Kongsfjorden, northwestern Svalbard. *Earth System Science Data 10*, no. 4.

Livermore, P. W., Fournier, A., Gallet, Y., & Bodin, T. (2018). Transdimensional inference of archeomagnetic intensity change. *Geophysical Journal International*, 215(3), 2008–2034. doi.org/10.1093/gji/ggy383

Mair, D., P. Nienow, M. J. Sharp, T. Wohlleben, and I. Willis (2002), Influence of subglacial drainage system evolution on glacier surface motion : Haut Glacier d'Arolla, Switzerland, *J. Geophys. Res*., 107(B8), EPM 8-1–EPM 8-13, doi:10.1029/2001JB000514.

Marquardt, D. W. (1963). An algorithm for least-squares estimation of nonlinear parameters. *Journal of the society for Industrial and Applied Mathematics*, 11(2), 431-441.

Mavko, G., Mukerji, T., & Dvorkin, J. (2019). The rock physics handbook. *Cambridge university press*.

McNutt, S. R., & Roman, D. C. (2015). Volcanic seismicity. In The Encyclopedia of Volcanoes (pp. 1011-1034). Academic Press.

Meier, M.F., M.B. Dyurgerov, U.K. Rick, S. O'Neel, W.T. Pfeffer, R.S. Anderson, S.P. Anderson, & A.F. Glazo*Vs*ky. (2007). Glaciers dominate eustatic sea-level rise in the 21st century. *Science* 317: 1064-1067.

Menzies, J., & Shilts, B. W. (2002). Subglacial environments. In *Modern and past glacial environments* (pp. 183-278). Butterworth-Heinemann.

Mikucki, J.A., Auken, E., Tulaczyk, S., Virginia, R.A., Schamper, C., Sørensen, K.I., Doran, P.T., Dugan, H. & Foley, N. (2015). Deep groundwater and potential subsurface habitats beneath an Antarctic dry valley. *Nature communications*, *6*, p.6831.

Miller, O., Solomon, D. K., Miège, C., Koenig, L., Forster, R., Schmerr, N., ... & Montgomery, L. (2018). Direct evidence of meltwater flow within a firn aquifer in southeast Greenland. *Geophysical Research Letters*, 45(1), 207-215.

Minsley, B.J., Abraham, J.D., Smith, B.D., Cannia, J.C., Voss, C.I., Jorgenson, M.T., Walvoord, M.A., Wylie, B.K., Anderson, L., Ball, L.B. & Deszcz-Pan, M. (2012). Airborne electromagnetic imaging of discontinuous permafrost. *Geophysical Research Letters*, 39(2).

Montgomery, L.N., Schmerr, N., Burdick, S., Forster, R.R., Koenig, L., Legchenko, A., Ligtenberg, S., Miège, C., Miller, O.L. and Solomon, D.K. (2017). Investigation of firn aquifer structure in southeastern Greenland using active source seismology. *Frontiers in Earth Science*, 5, p.10.

Murray T., Booth A. D. & Rippin D. M. (2007). Water-content of Glacier-Ice: limitations on estimates from velocity analysis of surface ground-penetrating radar surveys. *J. Environ. Eng. Geophys*., 12, 87–99

Murray, T. (1997). Assessing the paradigm shift: deformable glacier beds. *Quaternary Science Reviews*, 16(9), 995-1016.

Park, C. B., Miller, R. D., & Xia, J. (1999). Multichannel analysis of surface waves. *Geophysics*, *64*(3), 800-808.

Park, C. B., Miller, R. D., & Xia, J. (2001). Offset and resolution of dispersion curve in multichannel analysis of surface waves (MASW). *In Proceedings of the SAGEEP*.

Pedersen, J. B., Schaars, F. W., Christiansen, A. V., Foged, N., Schamper, C., Rolf, H., & Auken, E. (2017). Mapping the fresh-saltwater interface in the coastal zone using high-resolution airborne electromagnetics. *First Break*, *35*(8), 57-61.

Penumadu, D., & Park, C. B. (2005). Multichannel analysis of surface wave (MASW) method for geotechnical site characterization. In *Earthquake engineering and soil Dynamics* (pp. 1-10).

Peters, L. E., Anandakrishnan, S., Holland, C. W., Horgan, H. J., Blankenship, D. D., & Voigt, D. E. (2008). Seismic detection of a subglacial lake near the South Pole, Antarctica. *Geophysical Research Letters*, 35(23).

Picotti S., Francese R., Giorgi M., Pettenati F. & Carcione J.M. (2017). Estimation of glacier thicknesses and basal properties using the horizontal-to-vertical component spectral ratio (H*VS*R) technique from passive seismic data. *J. Glaciol*., 63, 229–248

Picotti, S., Vuan, A., Carcione, J. M., Horgan, H. J., & Anandakrishnan, S. (2015). Anisotropy and crystalline fabric of Whillans Ice Stream (West Antarctica) inferred from multicomponent seismic data. *Journal of Geophysical Research: Solid Earth*, *120*(6), 4237-4262.

Podolskiy, E. A., & Walter, F. (2016). Cryoseismology. *Reviews of geophysics*, *54*(4), 708-758.

Preiswerk L.E. & Walter F. (2018). High-frequency (>2 Hz) ambient seismic noise on high-melt glaciers: green's function estimation and source characterization. *J. Geophys. Res. Earth Surf*., 123, 1667–1681

Qian, Y., Wei, S., Wu, W., Zeng, H., Coudurier-Curveur, A., & Ni, S. (2019). Teleseismic waveform complexities caused by near trench structures and their impacts on earthquake source study: application to the 2015 Illapel aftershocks (Central Chile). *Journal of Geophysical Research: Solid Earth*, 124(1), 870-889.

Raiche, A. (2008). Leroi version 8.0, Fortran 95 program, developed for AMIRA project P223F, online at http://p223suite.sourceforge.net/descriptions.html, accessed on 01.02.2019

Ray, A. and Key, K. (2012) Bayesian inversion of marine CSEM data with a trans-dimensional self parametrizing algorithm. *Geophysical Journal International*, 191(3), 1135-1151

Ray, A., Key, K., Bodin, T., Myer, D. & Constable, S. (2014) Bayesian inversion of marine CSEM data from the Scarborough gas field using a transdimensional 2-D parametrization. *Geophys. J. Int*. 199, 1847–1860

Reinardy, B., Booth, A., Hughes, A., Boston, C., Akesson, H., Bakke, J., Nesje, A., Giesen, R. & Pearce, D. (2019). Pervasive cold ice within a temperate glacier-implications for glacier thermal regimes, sediment transport and foreland geomorphology. *The Cryosphere*.

Reinardy, B., Leighton, I., and Marx, P. (2013). Glacier thermal regime linked to processes of annual moraine formation at Midtdalsbreen, southern Norway. *Boreas*, 42, 896–911, 2013.

Rignot, E., Mouginot, J. & Scheuchl, B. (2011). Antarctic grounding line mapping from differential satellite radar interferometry. *Geophys. Res. Lett.* 38, L10504

Rippin, D. M., Vaughan, D. G., & Corr, H. F. (2011). The basal roughness of Pine Island Glacier, West Antarctica. *Journal of Glaciology*, 57(201), 67-76.

Rix G. J. and Lai C. G. (2003). *Mat_disperse*, Matlab function, online at https://github.com/yiran06/mat_disperse, assessed on 01/02/2018

Ronczka, M., Wisén, R., & Dahlin, T. (2018). Geophysical pre-investigation for a Stockholm tunnel project: Joint inversion and interpretation of geoelectric and seismic refraction data in an urban environment. *Near Surface Geophysics*, 16(3), 258–268.

Rost, S., and C. Thomas (2002). Array seismology: Methods and applications. *Rev. Geophys*., 40(3), 1008, doi:10.1029/2000RG000100.

Rutishauser, A., Blankenship, D.D., Sharp, M., Skidmore, M.L., Greenbaum, J.S., Grima, C., Schroeder, D.M., Dowdeswell, J.A. & Young, D.A. (2018). Discovery of a hypersaline subglacial lake complex beneath Devon Ice Cap, Canadian Arctic. *Science advances*, *4*(4), p.eaar4353.

Schoof, C. (2005). The effect of cavitation on glacier sliding. *Proceedings of the Royal Society A: Mathematical, Physical and Engineering Sciences*, *461*(2055), 609-627

Shen, W., Ritzwoller, M. H., Schulte-Pelkum, V., & Lin, F. C. (2012). Joint inversion of surface wave dispersion and receiver functions: A Bayesian Monte-Carlo approach. *Geophysical Journal International*, 192(2), 807–836.

Siegert, M.J., Kulessa, B., Bougamont, M., Christoffersen, P., Key, K., Andersen, K.R., Booth, A.D. & Smith, A.M. (2018). Antarctic subglacial groundwater: a concept

paper on its measurement and potential influence on ice flow. *Geological Society, London, Special Publications*, *461*(1), pp.197-213.

Siegert, M.J., Ross, N., Li, J., Schroeder, D.M., Rippin, D., Ashmore, D., Bingham, R. and Gogineni, P. (2016). Subglacial controls on the flow of Institute Ice Stream, West Antarctica. *Annals of Glaciology*, 57(73), pp.19-24.

Simonsen, E., Janoo, V. C., & Isacsson, U. (2002). Resilient properties of unbound road materials during seasonal frost conditions. *Journal of Cold Regions Engineering*, 16(1), 28-50.

Sisson, S. A. (2005). Transdimensional Markov chains: A decade of progress and future perspectives. *Journal of the American Statistical Association*, *100*(471), 1077-1089.

Smith, E. C., Baird, A. F., Kendall, J. M., Martín, C., White, R. S., Brisbourne, A. M., & Smith, A. M. (2017). Ice fabric in an Antarctic ice stream interpreted from seismic anisotropy. *Geophysical Research Letters*, 44(8), 3710-3718.

Smith, A. M. (2007). Subglacial bed properties from normal-incidence seismic reflection data. *Journal of Environmental and Engineering Geophysics*, *12*(1), 3-13.

Socco, L. V., Boiero, D., Foti, S., & Wisén, R. (2009). Laterally constrained inversion of ground roll from seismic reflection records. *Geophysics*, *74*(6), G35-G45.

Stearns, L. A., & Van der Veen, C. J. (2018). Friction at the bed does not control fast glacier flow. *Science*, 361(6399), 273-277.

Stokoe, K. H., & Santamarina, J. C. (2000, November). Seismic-wave-based testing in geotechnical engineering. In *ISRM International Symposium*. International Society for Rock Mechanics and Rock Engineering.

Stokoe, K. H. II, Wright, G. W., James, A. B., & Jose, M. R. (1994). Characterization of geotechnical sites by SASW method. In R. D. Woods (Ed.), Geophysical characterization of sites. New Delhi: Oxford Publisher.

Sundal, A. V., Shepherd, A., Nienow, P., Hanna, E., Palmer, S., & Huybrechts, P. (2011). Melt-induced speed-up of Greenland ice sheet offset by efficient subglacial drainage. *Nature*, 469(7331), 521.

Thiel E. & Ostenso N. A. (1961). Seismic studies on Antarctic ice shelves. *Geophysics*, 26, 706–715

Timur, A. (1968). Velocity of compressional waves in porous media at permafrost temperatures. *Geophysics*, 33(4), 584-595.

Tsoflias, G. P., Ivanov, J., Anandakrishnan, S., Horgan, H., Peters, L., Voigt, D., & Winberry, P. (2008, December). Firn and shallow ice profiling at Jakobshavn Glacier using dispersed seismic surface waves. In *AGU Fall Meeting Abstracts*.

Tsuji, T., Johansen, T. A., Ruud, B. O., Ikeda, T., & Matsuoka, T. (2012). Surface-wave analysis for identifying unfrozen zones in subglacial sedimentsS-wave velocity in subglacial sediment. *Geophysics*, *77*(3), EN17-EN27.

Vallée, M. A., & Smith, R. S. (2009). Application of Occam's inversion to airborne time-domain electromagnetics. *The leading edge*, *28*(3), 284-287.

Vaughan, D. G., Comiso, J. C., Allison, I., Carrasco, J., Kaser, G., Kwok, R., Mote P., Murray T., Paul F., Ren J. & Rignot E. (2013). Observations: cryosphere. *Climate change, 2103*, 317-382.

Vaughan, D. G., Smith, A. M., Nath, P. C., & Le Meur, E. (2003). Acoustic impedance and basal shear stress beneath four Antarctic ice streams. *Annals of Glaciology*, 36, 225-232.

Vásárhelyi, B. (2009). A possible method for estimating the Poisson's rate values of the rock masses. *Acta Geodaetica et Geophysica Hungarica*, 44(3), 313-322.

Walter F, Chaput J and Lüthi MP (2014) Thick sediments beneath Greenland's ablation zone and their potential role in future ice sheet dynamics. *Geology*, 487-490.

Walter, F., P. Roux, C. Roeoesli, A. Lecointre, D. Kilb, and P.-F. Roux (2015). Using glacier seismicity for phase velocity measurements and Green's function retrieval. *Geophys. J. Int*., 201(3), 1722– 1737, doi:10.1093/gji/ggv069.

Weertman, J. (1957). Steady-state creep through dislocation climb. *Journal of Applied Physics*, 28(3), 362-364.

Willis, I. C., Fitzsimmons, C. D., Melvold, K., Andreassen, L. M., & Giesen, R. H. (2012). Structure, morphology and water flux of a subglacial drainage system, Midtdalsbreen, Norway. *Hydrological Processes*, *26*(25), 3810-3829.

Winberry, J. P., Anandakrishnan, S., Wiens, D. A., Alley, R. B., & Christianson, K. (2011). Dynamics of stick–slip motion, Whillans Ice Stream, Antarctica. *Earth and Planetary Science Letters*, 305(3-4), 283-289.

Wisén, R., & Christiansen, A. V. (2005). Laterally and mutually constrained inversion of surface wave seismic data and resistivity data. *Journal of Environmental and Engineering Geophysics*, 10(3), 251–262. doi.org/10.2113/JEEG10.3.251

Xia, J., Miller, R. D., & Park, C. B. (1999). Estimation of near-surface shear-wave velocity by inversion of Rayleigh waves. *Geophysics*, *64*(3), 691-700.

Yamanaka, H., & Ishida, H. (1996). Application of genetic algorithms to an inversion of surface-wave dispersion data. *Bulletin of the Seismological Society of America*, *86*(2), 436-444.

Yilmaz, Ö. (2001). Seismic data analysis: Processing, inversion, and interpretation of seismic data. *Society of exploration geophysicists.*

Young Kim, K., Lee, J., Ho Hong, M., Kuk Hong, J., Keun Jin, Y., & Shon, H. (2010). Seismic and radar investigations of Fourcade Glacier on King George Island, Antarctica. *Polar Research*, 29(3), 298-310.

Zhang, X., Hansteen, F., Curtis, A., & de Ridder, S. (2019) 1D, 2D and 3D Monte Carlo ambient noise tomography using a dense passive seismic array installed on the North Sea seabed. *Accepted to: Journal of Geophysical Research: Solid Earth*. Doi 10.1029/2019JB018552

Appendices

Appendix A

Supplementary material for: Chapter 4 Subglacial sediment distribution from constrained seismic inversion, using MuLTI software: Examples from Midtdalsbreen, Norway

Table A1. Inversion parameters used in MuLTI for the synthetic feasibility study and 1D and 2D real data inversions, explained further in Killingbeck et al., 2018.

Inversion Parameter	Value
Number of Layers	3
Minimum number of total nuclei	3
Maximum number of total nuclei	33
Maximum depth	40 m
Burn in number	10 000
Number of Iterations (including burn in)	1 000 000
Number of MCMC chains	1
Sigma change	20 m/s
Sigma move	1 m
Sigma birth	400 m/s

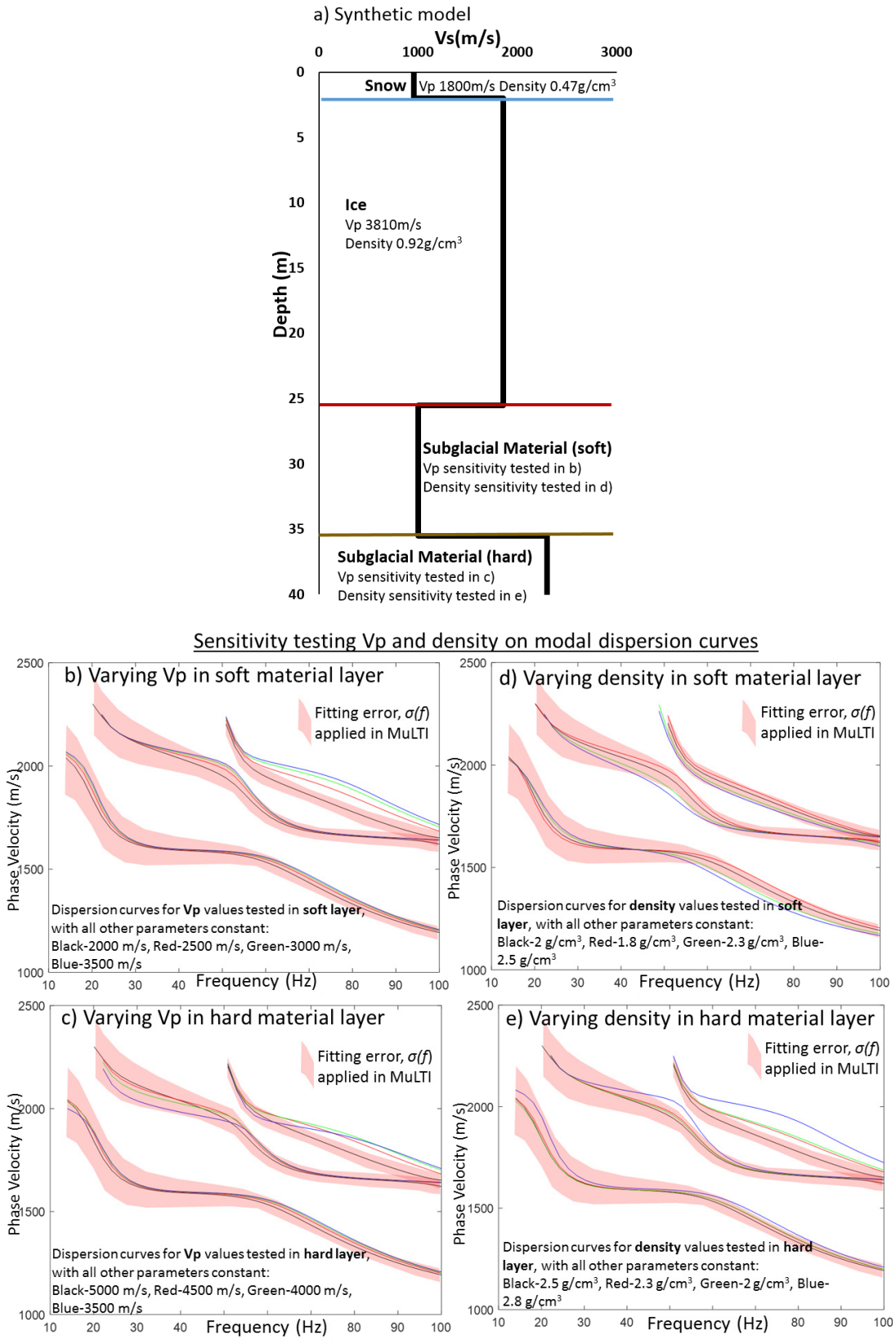

Figure A1. Sensitivity testing *Vp* (b and c) and density (d and e) on modal dispersion curves for the synthetic model shown in a).

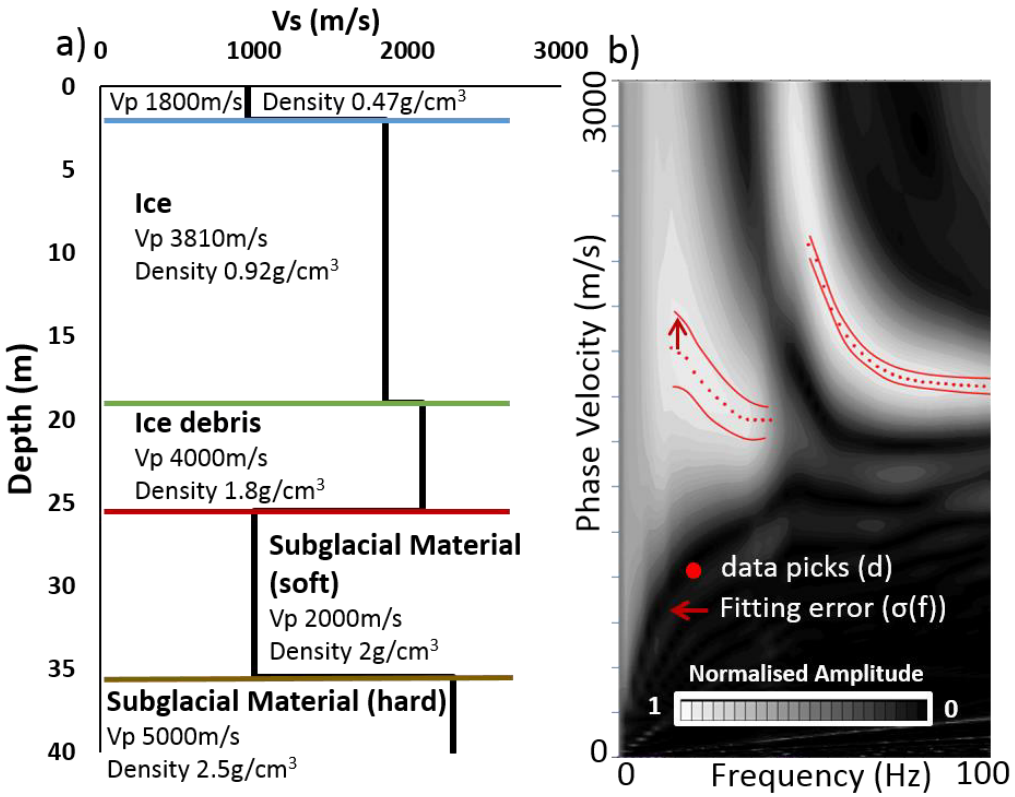

Figure A2. a) Complex synthetic model with added ice-debris layer and b) corresponding DWN synthetic dispersion curve.

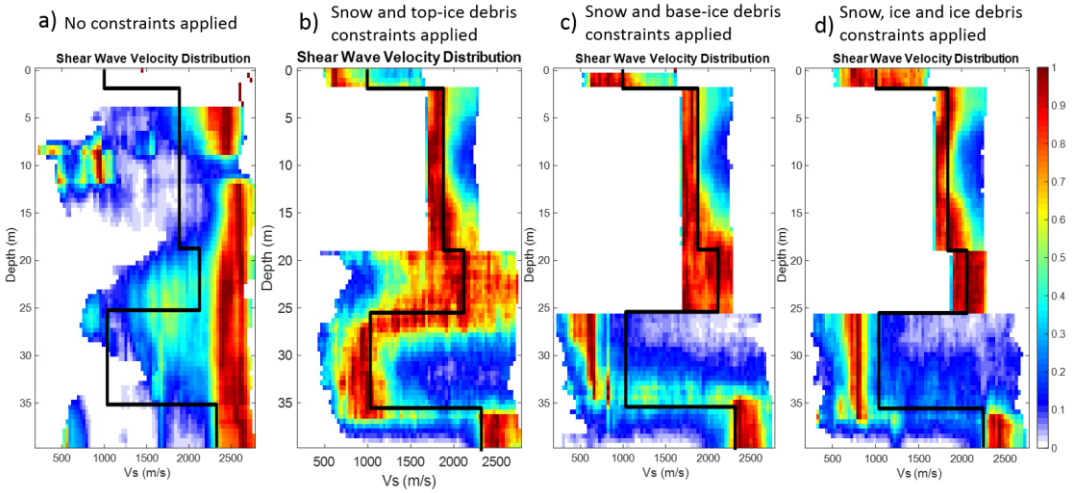

Figure A3. MuLTI inversion results from the ice-debris synthetic model (Figure A1) with a) no constraints applied, b) snow and top-ice debris depth constraints applied, c) snow and base-ice debris depth constraints applied and d) snow, top-ice debris and base-ice debris depth constrains applied.

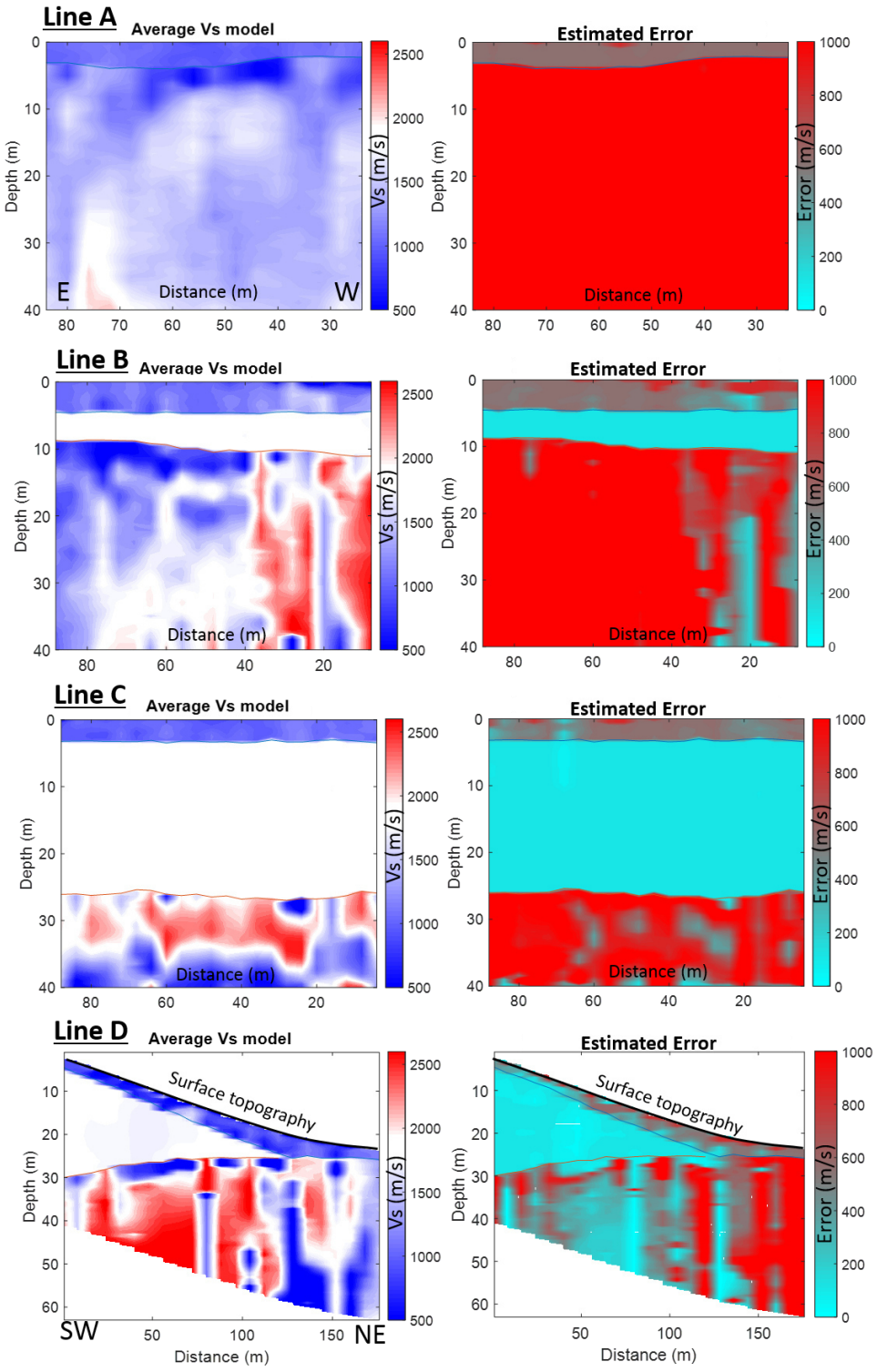

Figure A4. Resulting 2D average *Vs* profiles after applying multiple 1D MuLTI inversions, with GPR constraints, at each CMPCC along the seismic lines A-D (diverging colour scale centred, in white, on *Vs* of ice (1750-1900m/s)) and corresponding estimated error plots, calculated from the 95% credible interval half width. The snow and ice depth horizons are plotted in blue and red respectively.

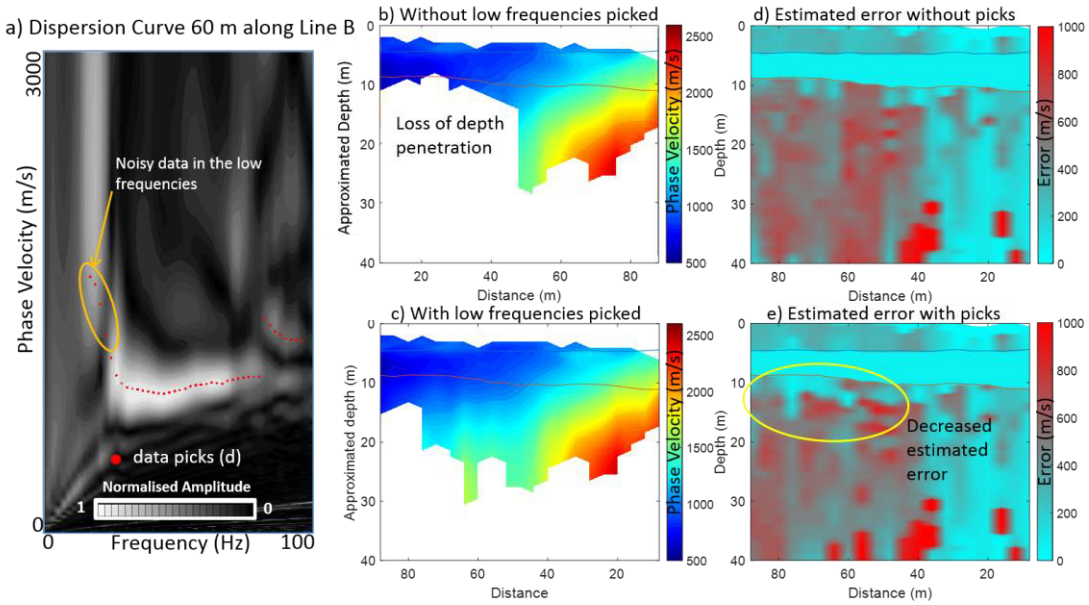

Figure A5. a) Example dispersion curve from Line B highlighting the noisy low frequency picks. We believe these high phase velocities at the low frequencies are real and associated with the thin (4 m thick) ice layer at this location in Line B. Approximated depths of picked phase velocities without noisy low frequencies picked (b) and with noisy low frequencies picked (c). Corresponding estimated errors, calculated from half the interquartile range, using dispersion picks without noisy low frequencies (d) and with noisy low frequencies (e).

Appendix B

Appendix for Chapter 5: Characterisation of subglacial water using a constrained transdimensional Bayesian Transient Electromagnetic Inversion.

Table B1 (continued overleaf). TEM survey parameters input to MuLTI-TEM, defined from the Leroi forward modelling algorithm.

Parameter name	Unit	Parameter description	Midtdalsbreen parameters
REFTYM	msec	Time from which TOPN & TCLS are measured. For example, this could be signal off-time or start of downward ramp.	1.05
OFFTYM	msec	Time between end of one pulse and the start of the next pulse (of opposite sign) since a bipolar waveform is assumed. This is most likely equal to ¼ period of the complete waveform. For systems which have a signal which is always on, OFFTIME = 0.	1.05
TXON	msec	Digitised time of each point in the waveform (fixed at 4 points). In most cases, TXON(1) = 0, TXON(2) = pulse on-time, TXON(3) = pulse off-time, TXON(4) = REFTYM where TXON(4) - TXON(3) = turn off time.	[0.0, 0.001, 1.0492, 1.05]
TXAMP	amps	Transmitter current at time TXON(J). If signal is normalised, this should be 1.	[0.0, 1.0, 1.0, 0.0]
TOPN	msec	Start times of receiver windows, the number of time gates is fixed at 20 (1x20).	[0.006000, 0.007625, 0.009750, 0.012500, 0.015880, 0.020250, 0.025880, 0.033000, 0.042130, 0.053750, 0.068500, 0.087380, 0.111400, 0.151700, 0.181100, 0.231000, 0.294600, 0.375900, 0.479500, 0.611600]
TCLS	msec	End times of receiver windows, the number of time gates is fixed at 20 (1x20).	[0.007625, 0.009750, 0.012500, 0.015880, 0.020250, 0.025880, 0.033000, 0.042130, 0.053750, 0.068500, 0.087380, 0.111400, 0.151700, 0.181100, 0.231000, 0.294600, 0.375900, 0.479500, 0.611600, 0.780100]
			(continued overleaf)

SXE	meters	East coordinate of vertex I for loop position J, fixed at 4 vertices. Note the transmitter is fixed on the ground (Z=0) in this adapted Leroi code, for airborne data more parameters will need to be passed through the mex file to model.	[5, -5, -5, 5]
SXN	meters	North coordinate of vertex I for loop position J, fixed at 4 vertices.	[5, 5, -5, -5]
RXE	meters	Receiver easting.	15
RXN	meters	Receiver northing.	0
RXZ	meters	Receiver z (always be 0 for ground based TEM).	0

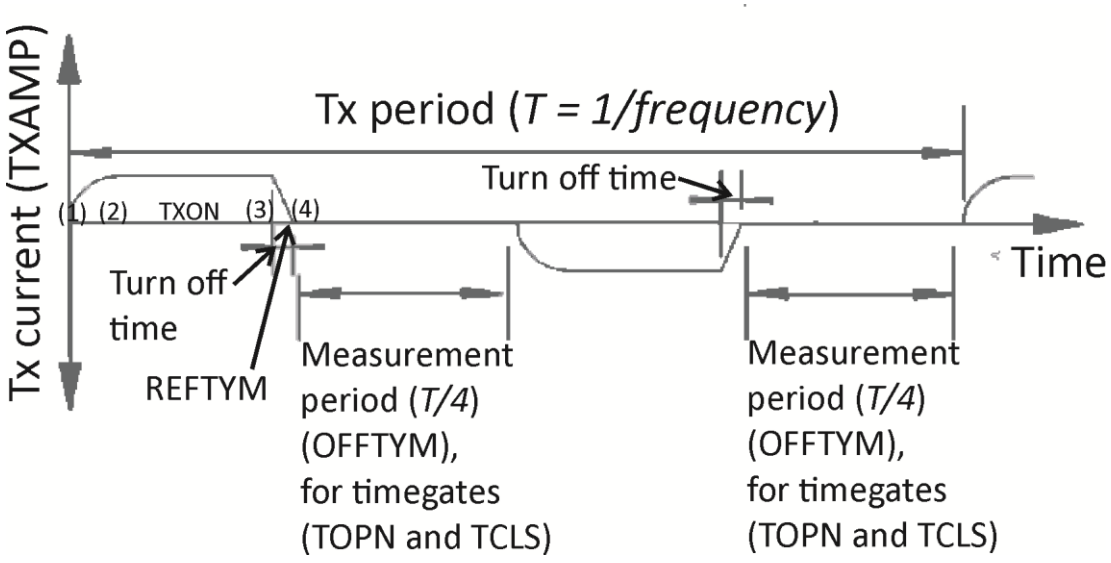

Figure B1. Schematic image of the transmitter waveform, highlighting the waveform parameters defined in MuLTI-TEM described in Table B1.

Table B2. Inversion parameters used in MuLTI-TEM for the synthetic feasibility study and 1D and 2D real data inversions, explained further in Killingbeck et al. (2018). Burn in number is the number of iterations discounted at the start of the chain to remove any dependencies of the initial conditions. Sigma resistivity, change, move and birth are user specified parameters that determine the magnitude of the four different perturbations that can be applied (change resistivity, move nucleus, give birth to a new nucleus, and remove a nucleus).

Inversion Parameter	**Value**
Number of Layers (non-constrained)	1
Number of Layers (constrained)	3
Weighting (data variance, σ)	5% of the signal at each timegate
Minimum number of total floating nuclei	0
Maximum number of total floating nuclei	80
Maximum depth	80 m
Burn in number	10 000
Number of Iterations (including burn in)	1 000 000
Number of MCMC chains	1
Sigma resistivity change (log(R))	2
Sigma move (meters)	10
Sigma birth (log(R))	2

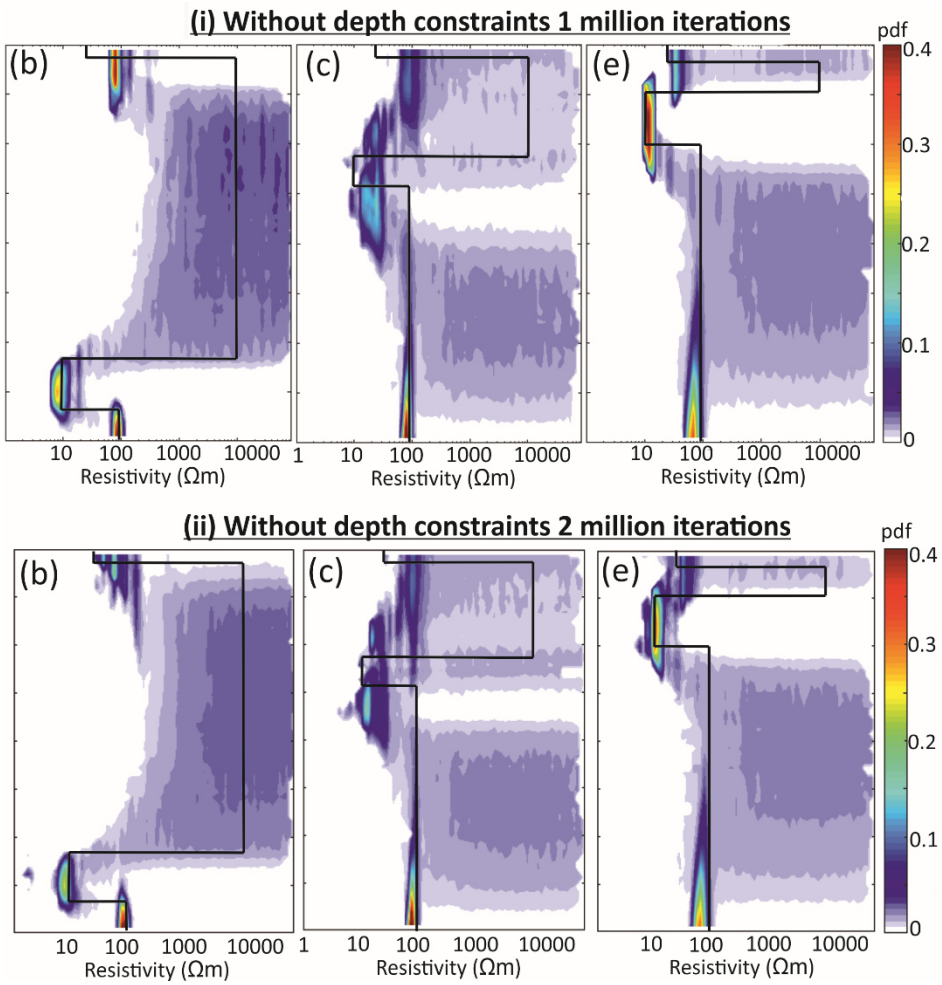

Figure B2. Posterior distributions of resistivity determined from MuLTI-TEM inversion for the synthetic models b, c and e without depth constraints applied and with i) 1 million iterations (top) and ii) 2 million iterations (bottom).

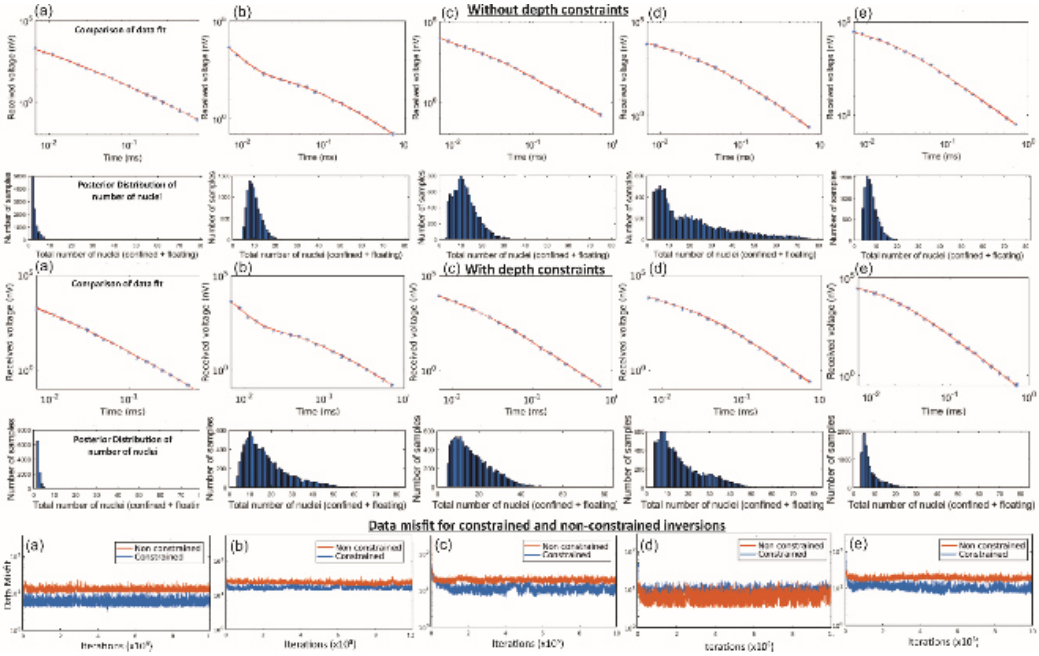

Figure B3. Synthetic inversion results for all models in Figure 4 (a-e), showing comparison of data fit and posterior distribution of number of nuclei plots.

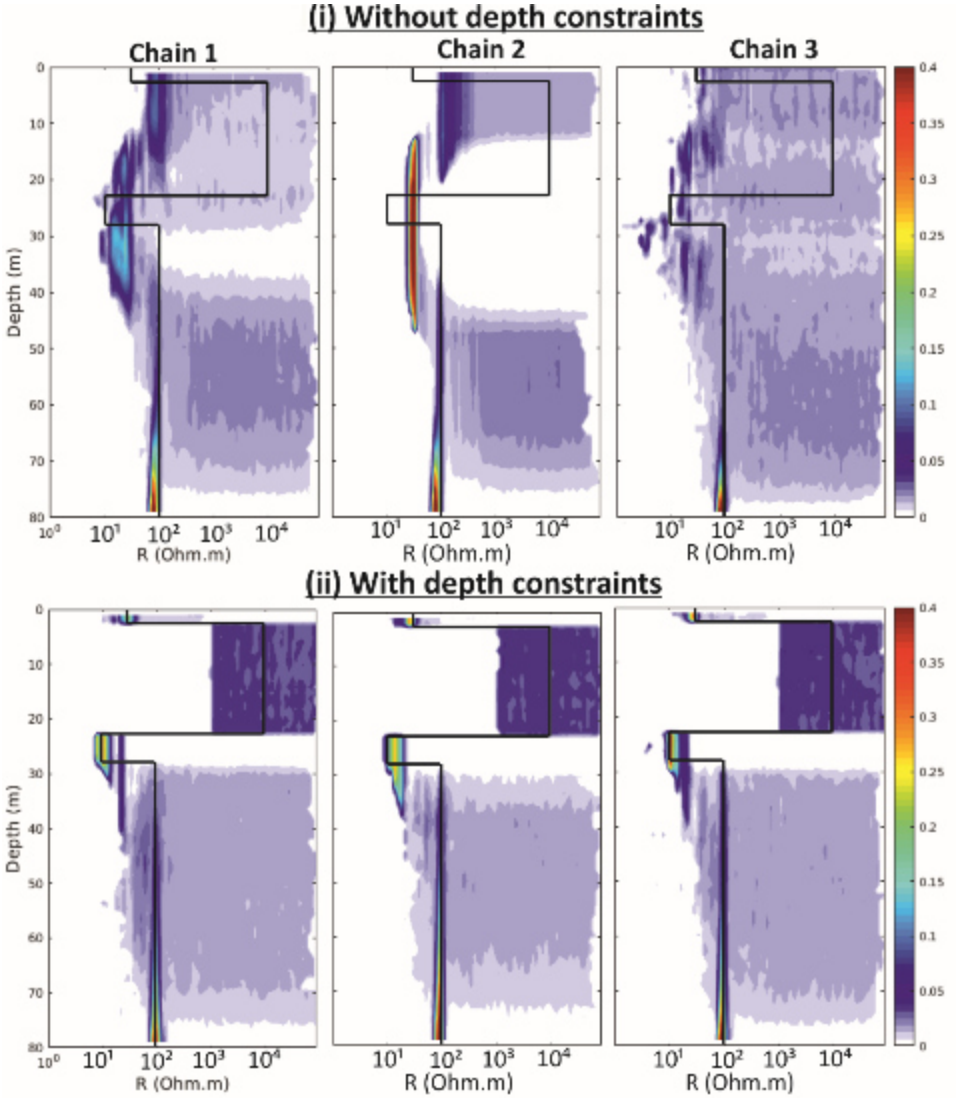

Figure B4. Posterior distribution of resistivity for synthetic model d using 3 different chains for the non-constrained and constrained inversions with MuLTI-TEM, highlighting the independence of the constrained solutions on chain index, whereas the non-constrained distributions show a weak variation across chains.

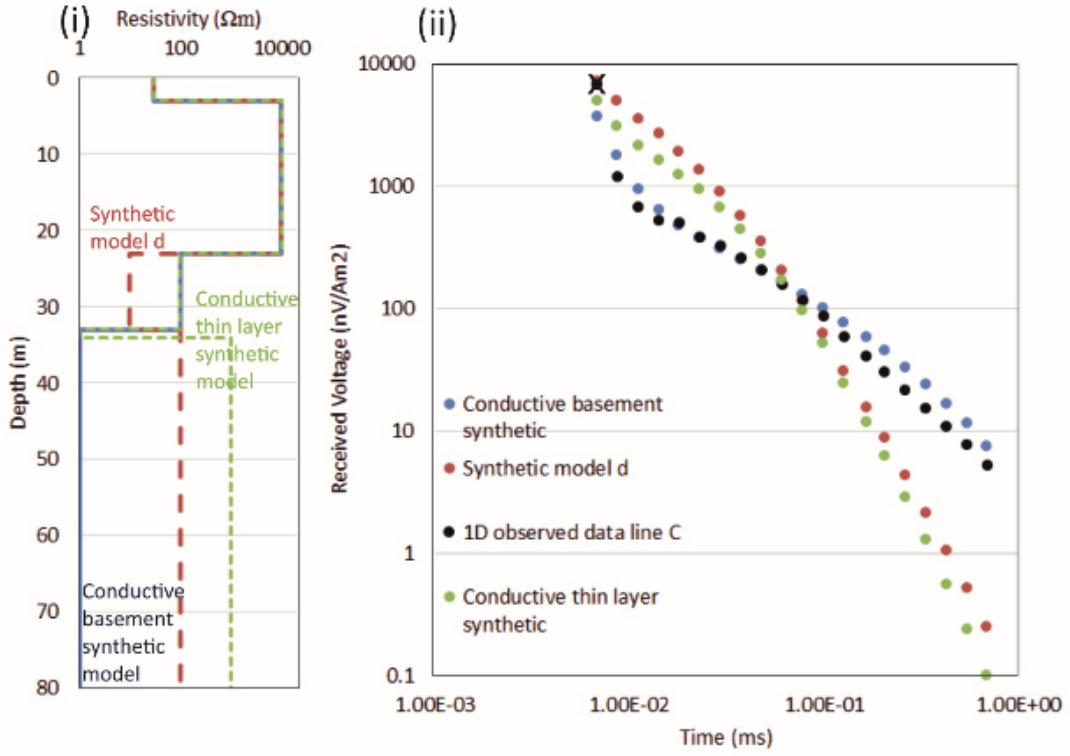

Figure B5. i) Example synthetic models created with a conductive thin layer on top of a resistive basement (green) and a conductive basement (blue), compared to the original synthetic model d. ii) Calculated responses, using the Leroi forward modelling code, of the synthetics compared to the observed data at the midpoint of line C.

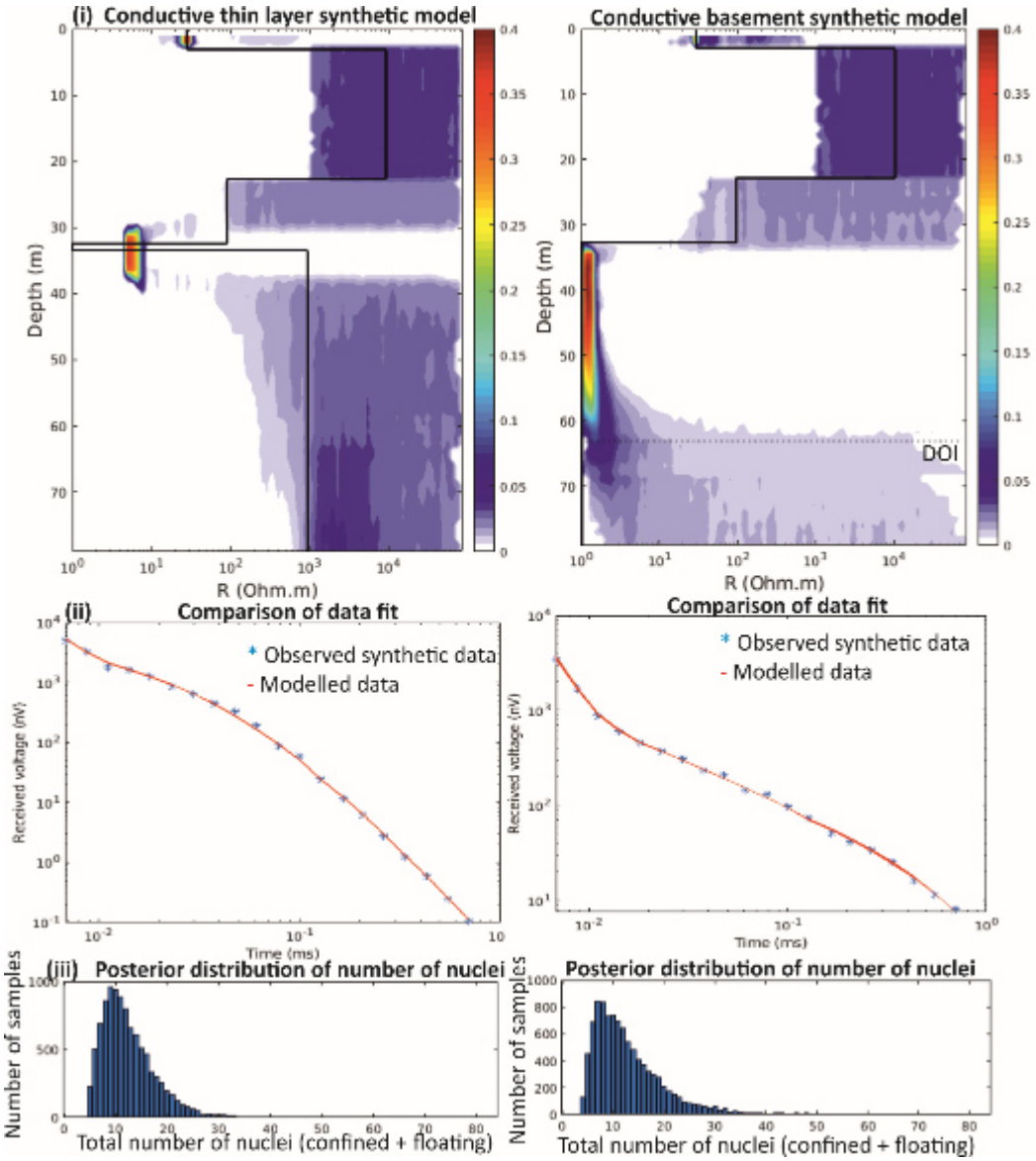

Figure B6. MuLTI-TEM inverted result for the a) conductive thin layer synthetic model and the b) conductive basement synthetic model, shown in Figure B5.

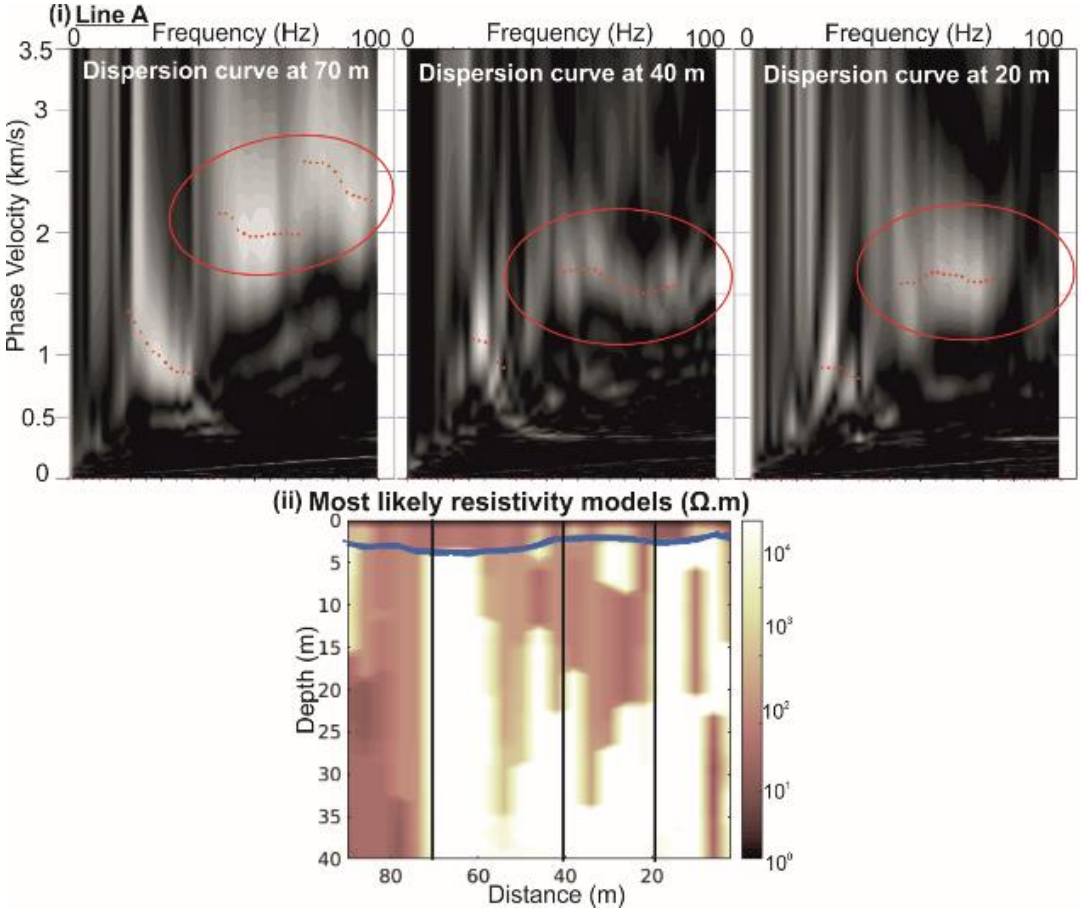

Figure B7. i) Example of re-picked dispersion curves along line A at 20 m, 40 m and 70 m. The noisy high phase velocities observed > 55 Hz (originally not picked) are now thought to be real, matching the high resistivity observations along Line A. Red circles highlight the extra high frequencies picked. ii) Most likely resistivity profile with locations of dispersion curves marked by the black lines.

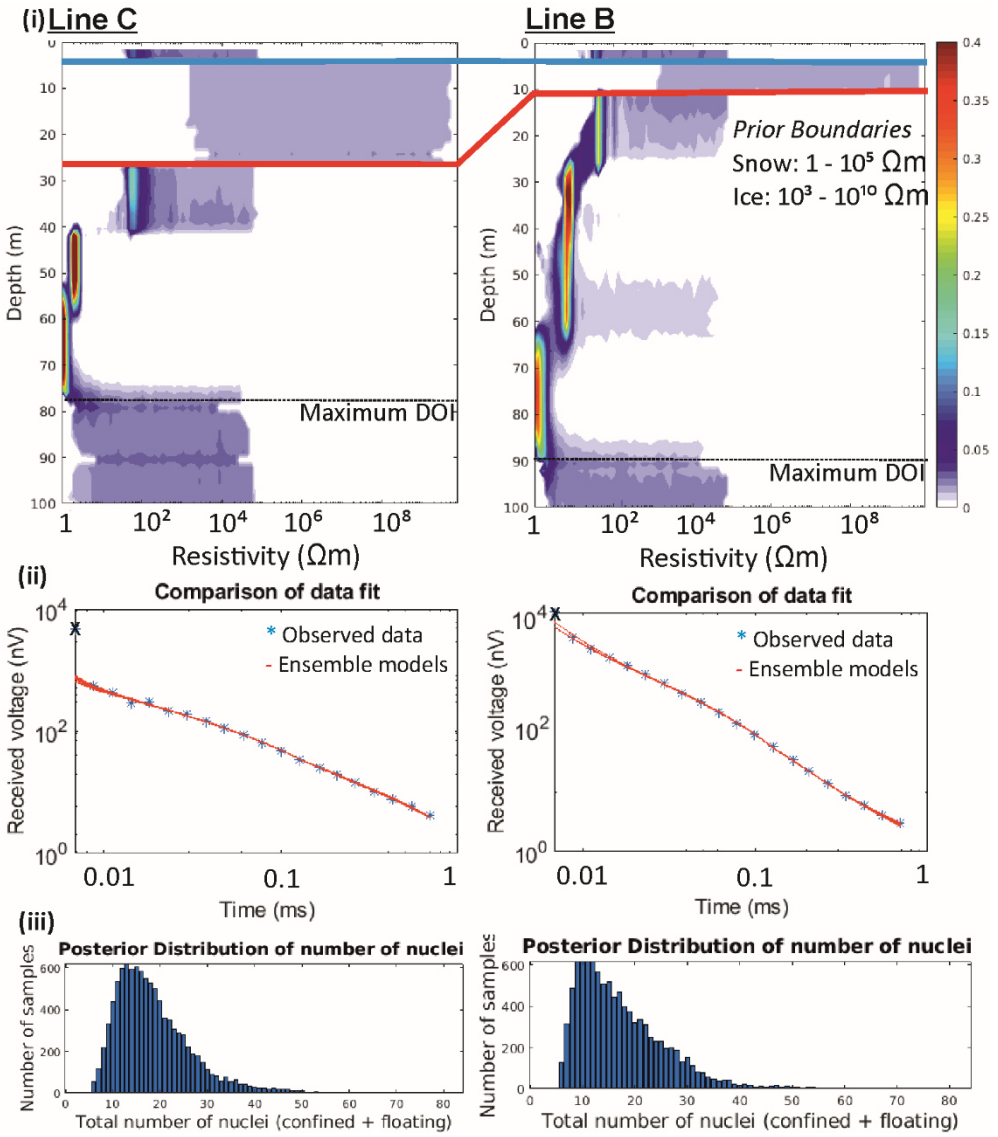

Figure B8. Results of 1D soundings acquired at the midpoint of lines B and C inverted with extended prior boundaries of the snow and ice layers, to represent temperate ice resistivities (e.g. Kulessa, 2007). The mode solution and PDF of the subglacial *R* structure is identical to the results shown in Figure 5.7.